

MODELING OF POROUS POLYMER MEMBRANE FORMATION

Von der Fakultät Energie-, Verfahrens- und Biotechnik und dem Stuttgart Research
Centre for Simulation Technology der Universität Stuttgart zur Erlangung der
Würde eines Doktors der Ingenieurwissenschaften (Dr.-Ing.) genehmigte
Abhandlung

vorgelegt von

Manuel Hopp-Hirschler

geboren in Nürtingen

Prüfungsvorsitzender: Prof. Dr.-Ing. Joachim Gross
Hauptberichter: Prof. Dr.-Ing. Ulrich Nieken
Mitberichter: Prof. Dr.-Ing. Matthias Wessling

Tag der mündlichen Prüfung: 06.11.2017

Institut für Chemische Verfahrenstechnik der Universität Stuttgart
2017

Vorwort

Diese Arbeit entstand im Rahmen meiner Tätigkeit als Wissenschaftlicher Mitarbeiter am Institut für Chemische Verfahrenstechnik (ICVT) der Universität Stuttgart.

Ich bedanke mich herzlichst bei Prof. Nicken für die Betreuung der Arbeit und sein Vertrauen in die neuen Lösungsansätze auf dem Weg zu dieser Arbeit. Prof. Wessling danke ich für das Interesse an der Arbeit und den Mitbericht.

Mein besonderer Dank gilt Prof. Strathmann für zahlreiche Diskussionen zur Entstehung von Polymermembranen. Prof. Eigenberger danke ich für seine kritischen Fragen und sein Interesse an der Arbeit. Dr. Grabowski danke ich für die Diskussion der experimentellen Ergebnisse. Dr. Sorescu danke ich für seine Unterstützung in der numerischen Umsetzung.

Ich bedanke mich bei meinem Betreuer der Masterarbeit, Franz, der mir einen guten Einstieg in die Simulationsmethode ermöglicht hat. Ein besonderer Dank gilt meinen Bürokollegen Winni und Philip, die mit mir durch alle Höhen und Tiefen gegangen sind und mir stets mit motivierenden und anerkennenden Worten zur Seite gestanden sind. Ich danke meinen Kollegen Christian Z. und Manuel H. für die zahlreichen Diskussionen. Matthias, Rene und Sebastian danke ich für die entspannten Mittagspausen bei einer Runde Skat. Außerdem danke ich Katrin, Holger und Herrn Lorenz, stellvertretend für die Mitarbeiter des Instituts, für ihre Unterstützung während meiner Tätigkeit.

Ich danke Fynn, Marina, Christian W., Mike und Pascal, die durch herausragende Abschlussarbeiten und Hiwi-Tätigkeiten zu dieser Arbeit beigetragen haben. Ein besonderer Dank gilt Steffen, der meine Ideen zu Tropfenkollisionen umgesetzt hat. Ich danke der Deutschen Forschungsgemeinschaft für die finanzielle Förderung meiner Arbeit im Rahmen des Sonderforschungsbereichs 716.

Ich danke meinen Eltern für die finanzielle Unterstützung während des Studiums,

durch die mir diese Arbeit erst möglich wurde. Zuletzt danke ich meiner Frau Madlen für ihre Geduld und Unterstützung während der Arbeit. Es war manchmal schwer mich von packenden Ideen abzubringen und den Feierabend zu genießen.

Contents

Zusammenfassung	j
Abstract	n
List of Symbols	i
Acronyms	vii
1 Introduction	1
1.1 Motivation	3
1.2 Aim of the thesis	4
1.3 Outline	5
2 Phenomenology of membrane formation	7
2.1 Observations in experiments	7
2.2 Empirical theory on polymer membrane formation in literature . . .	10
2.2.1 Shrinkage and cracks due to mechanical stress	10
2.2.2 Gradients in surface tension	11
2.2.3 Delayed and spontaneous demixing	12
2.2.4 Viscous fingering instability	13
2.2.5 Further theories on macrovoids	14
2.3 Experiments on membrane formation	15
2.3.1 Material and Properties	17
2.3.2 Experimental setup and procedure	18
2.3.3 Investigation of pore shape	21
2.3.4 Influence of viscosity ratio on pore shape	24

2.3.5	Analysis of the dynamics of different pore shapes	28
2.4	Conclusion	30
3	Theory	33
3.1	Physical picture	33
3.2	Thermodynamics	36
3.2.1	Equation of state	39
3.3	Balance equations	41
3.3.1	Continuity equation	43
3.3.2	Component equation	43
3.3.3	Momentum equation	44
3.3.4	Stochastic terms	46
3.4	Simplified model	47
3.4.1	Models for porous polymer membrane formation in literature .	48
3.4.2	Assumptions	51
3.4.3	Compact model equations	54
4	Numerical method	55
4.1	Numerical approaches to study morphology evolution in literature . .	55
4.2	Smoothed Particle Hydrodynamics method	57
4.3	Discrete balance equations	62
4.3.1	Continuity equation	63
4.3.2	Component balance	63
4.3.3	Momentum balance	65
4.3.4	Stochastic terms	67
4.3.5	Estimation of pressure	68
4.4	Boundary conditions	70
4.4.1	Periodic boundary conditions	70
4.4.2	Solid wall boundary conditions	71
4.4.3	Open boundary conditions	74
4.5	Numerical stability	76
4.5.1	Corrected kernel function and corrected gradient of kernel function	77
4.5.2	Density-invariant divergence-free approach	79
4.5.3	Particle Shifting	80

4.6	Time integration	84
4.7	Validation of implementation	85
4.8	Delimitation from Smoothed Dissipative Particle Dynamics	85
4.9	Compact discrete model equations	86
5	Viscous fingering	89
5.1	Current state on modeling of viscous fingering in literature	90
5.2	Hele-Shaw cell	91
5.3	Immiscible viscous fingering	92
5.3.1	Limit of stability of displacement	96
5.3.2	Analysis of the dynamics of displacement	98
5.3.3	Influence of diffuse interface on immiscible fingering	102
5.3.4	Influence of different diffusion coefficients on the shape of fingers	104
5.4	Miscible Fingering	109
5.4.1	Limit of stability of displacement	111
5.4.2	Analysis of the dynamics of displacement	112
5.5	Comparison of fingering dynamics to experiments	116
5.6	Conclusion	120
6	Liesegang pattern	123
6.1	Simplification of ternary to binary system	124
6.1.1	Recap of realistic ternary system	124
6.1.2	Simplified binary model	127
	Definition of auxiliary quantities	127
	Mass transport in the polymer solution outside of the miscibility gap	128
	Mass transport inside of the miscibility gap	131
	Compact balance equations of simplified model	135
6.2	Characteristics of the system	136
6.3	Computational setup	139
6.3.1	Example of evolution of morphology behind moving front	141
6.4	Influence of Hi and A on pore shape	144
6.5	Transition of pore shapes	146
6.5.1	Transition from sponge pores to finger pores	146

6.5.2	Transition from lamella layer to finger pores	149
6.6	Influence of fluctuations in composition on pore shape	152
6.7	Influence of hydrodynamics on pore shape	154
6.7.1	Influence of surface tension	154
6.7.2	Influence of gradient in the surface tension	157
6.8	Conclusion	159
7	Conclusion and Outlook	161
7.1	Conclusion	161
7.2	Outlook	162
	Bibliography	165
	Appendix	191
A	Measurements of viscosity	191
B	Review of proof of sharp interface limit from diffuse interface	207
C	Validation of thermodynamic consistent fluctuations of concentration	213
D	Phase separation	215
D.1	Validation of binary phase separation model	215
D.1.1	Influence of smoothing length	220
D.1.2	Influence of resolution	222
D.1.3	Influence of energy parameter κ'	223
D.1.4	Influence of particle distribution	225
D.1.5	Consistent fluctuations in the Cahn-Hilliard model	227
D.1.6	Influence of symmetric boundary conditions	230
E	Ternary phase separation and Stefan–Maxwell Diffusion in SPH	233
E.1	Generalized Fickian approach	233
E.2	Stefan-Maxwell approach	240
F	Validation of diffusive transport of a scalar property in SPH	241

G	Surface tension	245
G.1	Lid-driven cavity	246
G.2	Buoyancy-driven cavity	250
G.3	Validation of surface tension	254
G.3.1	Static capillary stress normal to interface	256
G.3.2	Dynamic capillary stress normal to interface	259
G.3.3	Static capillary stress tangential to interface	262
G.4	Thermocapillary droplet migration	264
H	Review of limit of instability in immiscible viscous fingering	271
I	Reduction of dimension of the shear stress	275
J	Numerical convergence in immiscible viscous fingering	285
K	Derivation of phase separation front velocity	287
	Publications	291

Zusammenfassung

Poröse Polymermembranen kommen in verschiedenen Trennprozessen wie z.B. der Dialyse oder Wasseraufbereitung zum Einsatz. Dabei beeinflusst die Porenstruktur nicht nur die Trenneigenschaften sondern auch die mechanische Stabilität der Membran. Um gezielt Einfluss auf die Porenstruktur im Herstellungsprozess nehmen zu können, muss daher zunächst der Mechanismus, der zur Porenstruktur führt, verstanden werden. Für eine Vorhersage der Porenstruktur ist ein numerisches Modell zur Abschätzung der Porenmorphologie wünschenswert.

Ein typischer Herstellungsprozess von porösen Polymermembranen ist das Ausfällen einer Polymerlösung mit einem flüssigen Fällungsmittel. Dabei werden eine Polymerlösung und ein Fällungsmittel in Kontakt gebracht. Ausgehend von der Kontaktfläche zerfällt die Polymerlösung aufgrund einer Mischungslücke in eine polymerreiche und eine polymerarme Phase, wobei die polymerreiche Phase sich verfestigt und die Membranstruktur bildet. Obwohl dieser Prozess bereits seit Jahrzehnten industriell verwendet wird, ist der Mechanismus, der zur Bildung der Porenstruktur führt, bis heute noch nicht zweifelsfrei belegt. Die Motivation dieser Arbeit ist es daher die Lücke zwischen der meist experimentellen Membrantechnik und der theoretischen Beschreibung zu schließen und den Mechanismus der Porenbildung aufzuzeigen.

In Kapitel 2 werden zunächst die phänomenologischen Erkenntnisse aus experimentellen Arbeiten zusammengestellt. Eine zentrale Rolle spielt dabei der sogenannte Porenbildner. Wird dieser Stoff der Polymerlösung zugegeben, verändert sich die Porenstruktur von Fingerporen zu Schaumporen. In den meisten Anwendungsfällen ist die gewünschte Struktur die Schaumstruktur, da diese eine höhere mechanische Stabilität aufweist. Dahingegen können Defekte in Form von Fingerporen zum Versagen der Membran führen und sind unerwünscht. In den letzten Jahrzehnten wurden einige Theorien zur Entstehung dieser Defekte postuliert, jeweils basierend auf Experimenten. Die Mechanismen, die den Theorien zugrunde liegen, unterscheiden sich sehr. Als maßgebliche Effekte werden Gradienten in der Oberflächenspannung, die hydrodynamische Instabilität des "viskosen Fingerring" und unterschiedliche Zerfallsgeschwindigkeiten der Polymerlösung postuliert. In ausgewählten, eigenen Experimenten wird daher zunächst untersucht, wie schnell der Porenbildungsprozess bei unterschiedlichen Polymerlösungen voranschreitet. Eine Analyse der Geschwindigkeit der Porenentstehung deutet sowohl auf viskoses Finger-

ing also auch auf einen rein diffusiven Mechanismus mit alternierenden Strukturen hin. Dies könnten sogenannte "Liesegang patterns" sein.

In Kapitel 3 wird ein mathematisches Modell zur Beschreibung der Porenbildung bei Polymermembranen formuliert. Zunächst wird die physikalische Vorstellung eines kontinuierlichen Übergang der Grenzfläche zwischen zwei Fluiden rekapituliert. Unter der Annahme eines van-der-Waals Fluids lässt sich dabei die freie Energie eines Systems in einen lokalen Beitrag und einen Beitrag aufgrund von Gradienten der Dichte an der Grenzfläche unterteilen. Basierend hierauf lassen sich die Bilanzgleichungen eines Mehrphasen-Mehr-

komponenten-Systems aufstellen. Die Komponentenbilanz entspricht der sogenannten Cahn-Hilliard Gleichung, bei der im chemischen Potential der Gradient der Dichte an der Grenzfläche auftritt. Somit ist eine partielle Differentialgleichung 4. Ordnung zu lösen. Um den Einfluss thermischer Fluktuationen auf der Nanoskala zu erfassen, werden diese in der Komponentenbilanz berücksichtigt. Das isotherme Modell, bestehend aus Komponentenbilanz und Impulsbilanz, wird abschließend auf eine binäre Mischung eines Modellsystems vereinfacht, um eine effiziente numerische Lösung zu ermöglichen.

In Kapitel 4 wird die Smoothed Particle Hydrodynamics Methode zur Diskretisierung der Bilanzgleichungen eingeführt. Die Smoothed Particle Hydrodynamics Methode ist eine gitterfreie, Lagrange'sche Diskretisierungsmethode. Vorteile dieser Methode zeigen sich besonders bei Strömung in komplexen Geometrien mit freien Phasengrenzen. Mit Hilfe der diskreten Formulierung der 1. und 2. Ableitung im Ort werden anschließend die in Kapitel 3 eingeführten, reduzierten Bilanzgleichungen diskretisiert. Abschließend werden verschiedene Randbedingungen und die numerische Stabilität diskutiert. Eine ausführliche Validierung des diskreten Modells ist im Anhang zu finden.

In den letzten beiden Kapiteln werden zwei relevante Mechanismen zur Porenentstehung bzw. zum Porenwachstum untersucht. In Kapitel 5 wird zunächst die hydrodynamische Instabilität des viskosen Fingerring diskutiert. Viskoses Fingerring kann auftreten, wenn ein nieder-viskoses Fluid ein höher-viskoses Fluid verdrängt. Dieses Verhalten wird meist in sogenannten Hele-Shaw Zellen untersucht, die durch eine Strömung in einem sehr schmalen Spalt charakterisiert sind. In Abhängigkeit von Oberflächenspannung (im Falle zweier nicht-mischbarer Fluide) bzw. Diffusion (im Falle zweier mischbarer Fluide) entstehen fingerförmigen Strukturen, die wachsen,

sich verzweigen oder terminieren. Diese Strukturen finden sich häufig im Querschnitt einer porösen Polymermembran.

In Kapitel 5 wird zunächst in einer Hele-Shaw Zelle untersucht, ob das in Kapitel 3 eingeführte Modell die Charakteristika des viskosen Fingering, wie z.B. die Ausbreitungsgeschwindigkeit eines Fingers für mischbare und nicht-mischbare Fluide abbildet. Es wird gezeigt, dass für beide Fälle gute Ergebnisse erzielt werden können. Ein Vergleich mit den Experimenten aus Kapitel 2 zeigt, dass die Ausbreitungsgeschwindigkeit der Finger in den Experimenten vergleichbar mit denen eines nicht-mischbaren Systems ist. Abschließend lässt sich sagen, dass viskoses Fingering lediglich bei Flachmembranen relevant scheint, da bei Kapillarmembranen kein Pendant zur Hele-Shaw Zelle existiert weil keine konvektive Triebkraft auftritt, die das Fällungsmittel in die Polymerlösung treibt.

In Kapitel 6 werden sogenannte "Liesegang pattern" untersucht. Liesegang pattern sind alternierende Strukturen, die sich hinter einer bewegenden Grenzfläche bilden. Diese Strukturen entstehen z.B. in reaktiven Systemen, wenn eine Reaktionsfront durch das Gemisch der Edukte wandert und dabei alternierend unterschiedliche Produkte gebildet werden. Bei der Fällung von porösen Polymermembranen wandert die Grenzfläche, ausgehend vom Fällungsbad, in die Polymerlösung hinein. In Abhängigkeit der Zusammensetzung des Stoffsystems und der Geschwindigkeit der Grenzfläche in der polymerreichen Phase bildet sich unterschiedliche Porenstrukturen aus.

Das vereinfachte Modell aus Kapitel 3 wird auf ein Modellfluid angewandt. Dabei wird, anstelle der ternären Mischung aus Polymer, Lösungsmittel und Fällungsmittel, ein binäres Ersatzmodell betrachtet und die entstehende Strukturbildung untersucht. Das System kann durch zwei dimensionslose Größen A und Hi charakterisiert werden. Dabei kann A als thermodynamischer und Hi als kinetischer Parameter interpretiert werden. In Abhängigkeit dieser beiden Größen lassen sich die entstehenden Porenstrukturen in Schaum- und Fingerporen sowie dichte Schichten und Defekte unterteilen. Der Übergang von Schaumporen zu Fingerporen, der in industriellen Anwendungen von sehr großer Bedeutung ist, lässt sich auf eine Verringerung des Verhältnissen von Diffusion im Fällungsbad zur Diffusion in der Polymerlösung zurückführen.

Abschließend werden weitere Einflussfaktoren auf die Porenstruktur untersucht. Thermische Fluktuationen haben dabei nur minimalen Einfluss auf die Porenstruktur, da

sich der Porentyp nicht ändert. Hydrodynamische Effekte sind nur in nieder-viskosen Systemen relevant und Gradienten in der Oberflächenspannung sind nur bei sehr großen Gradienten, wie sie im realen System aber selten auftreten, relevant. Das Fazit dieser Arbeit ist, dass "Liesegang patterns" der entscheidende Mechanismus bei der Entstehung von Porenstrukturen bei porösen Polymermembranen sind.

Abstract

Porous polymer membranes are used in several separation processes, e.g. in dialysis or in water purification. The morphology of the membrane affects the quality of separation, e.g. selectivity, as well as the mechanical stability of the membrane. To control the morphology of the membrane during the preparation process we first need to understand the mechanism that leads to different pore structures. It is desirable to use a numerical model to predict the pore type and detailed structure. Wet-casting is a very common preparation process for porous polymer membranes where a liquid precipitation agent is used. Herein, a polymer solution and a coagulation bath is brought into contact. After contact the polymer solution is driven into a miscibility gap and starts to phase separate into a polymer lean and a polymer rich phase. Starting from the contact area between polymer solution and coagulation bath a pore structure grows where the polymer rich phase leads to the pore matrix. Although the process is used frequently in the last decades, its mechanism is still not fully understood. Therefore, the motivation in this thesis is to bridge experimental observations from membrane science to theoretical physics where concepts exist to understand the formation of pore structures in porous polymer membranes.

In chapter 2 we first review the phenomenology of pore formation and experimental observations. A key component is the so-called pore builder. If this component is present in the polymer solution then the morphology changes from finger pores to sponge pores. In most cases a sponge pore structure is desired because of its higher mechanical stability. Defects, such as macrovoids, are undesirable because the membrane may collapse. In the last decades several theories to explain the presence of defects are postulated based on experimental observations. But the responsible mechanism is diverse. For example, gradients of the surface tension, viscous fingering instability or different phase separation dynamics in the polymer solution are postulated. Therefore we present selected experiments to analyze the speed of formation of the pores in different polymer solutions. An analysis of the speed of pore formation adumbrates that viscous fingering as well as a purely diffusive mechanism, e.g. Liesegang patterns, may be responsible for the formation of finger pores.

In chapter 3 we formulate a mathematical model to predict the formation of pores in polymer membranes. First we introduce the physical concept of a diffusive interface

between two fluids. Assuming a van-der-Waals fluid we may divide the free energy of a system into a local and a non-local part where the non-local part accounts for a gradient in the density near the interface. Based on this concept we formulate the balance equations for a multi-phase, multi-component system. As a result, the component balance equals the so-called Cahn-Hilliard equation with a chemical potential that includes a gradient of the density near the interface. Therefore we have to solve a fourth-order partial differential equation. On the nanoscale thermal fluctuations may be important. We account for thermal fluctuations of the partial density in the component balance. Finally we simplify the model to an isotherm model for a binary mixture to reduce computational effort. This model represents the most simple model to study pore formation in porous polymer membranes.

In chapter 4 we introduce the Smoothed Particle Hydrodynamics method and formulate the discrete form of the balance equations. The Smoothed Particle Hydrodynamics method is a Lagrangian mesh-free method to discretize partial differential equations. Advantages of the method are flow in complex geometry and the movement of interfaces. We discretize the balance equations, introduced in chapter 3, using the discrete operator of the 1st and 2nd spatial derivative. Finally we discuss different boundary conditions and numerical stability. A detailed validation of the discrete model is attached in the Appendix.

In the last two chapters we investigate two relevant mechanisms for the origin of pores and its growth. In chapter 5 we discuss viscous fingering instability. Viscous fingering is a hydrodynamic instability and may be present if a less viscous fluid displaces a more viscous fluid. A typical system to investigate viscous fingering is a so-called Hele-Shaw cell. Its characteristic is a flow in a small gap. Fingers originate depending on surface tension (in case of two immiscible fluids) or diffusion (in case of two miscible fluids). These kind of morphology is often found in the cross-section of a porous polymer membrane.

In chapter 5 we investigate a Hele-Shaw cell using the discrete model. We show that the model describes the characteristics of viscous fingering, e.g. the evolution dynamics of a viscous finger, for both miscible and immiscible fluid mixtures. In both cases we find good agreement. We compare the characteristics of viscous fingering with the experiments introduced in chapter 2 to demonstrate that immiscible viscous fingering is present in the experiments. Finally we conclude that viscous fingering may only be relevant in the preparation process for flat sheet membranes

because there doesn't exist a representative equivalent to the Hele-Shaw cell in the preparation process of capillary membranes.

In chapter 6 we investigate so-called Liesegang patterns. Liesegang patterns are alternating structures formed behind a moving interface. These structures arise, for example, in reactive systems. When a reaction front moves through a mixture of reactants, alternating layers of products may result. During precipitation of porous polymer membranes an interface between a stable and unstable polymer solution moves into the stable polymer solution. Diverse pore structures are formed in the unstable polymer solution depending on the composition of the polymer solution and the velocity of the interface between the stable and unstable polymer solution. We apply the reduced model introduced in chapter 3 for a representative model-fluid. Thereby we replace the ternary mixture, consisting of polymer, solvent and non-solvent, by a binary system and investigate the kind of structures. To characterize these structures we introduce two dimensionless numbers A and Hi . Here A and Hi may be interpreted as a thermodynamic parameter and a kinetic parameter. Depending on A and Hi we are able to characterize the morphology into sponge pores and finger pores as well as dense layers and defects. The transition between sponge pores and finger pores is of major importance in industry. We find that this transition is caused by a reduction of the ratio of diffusion in the coagulation bath and polymer solution.

Finally we investigate additional influences on the pore structure. We find that thermal fluctuations are of minor importance because they do not change the type of pores. Hydrodynamic effects are only relevant in less viscous systems and gradients of the surface tension are only relevant if the gradients are very large. But this is not the case in typical systems.

We conclude that Liesegang patterns is the mechanism that is responsible for pore formation in porous polymer membranes.

List of Symbols

Latin letters

A	dimensionless mass fraction
A_a	Quantity of particle a
A	dimensionless mass fraction of polymer
A	dimensionless viscosity ratio
A_w	amplitude of the thermal fluctuation
$A(\vec{x})$	general quantity at position x
B	dimensionless surface tension
b	gap in Hele-Shaw cell
C	color
Ca	capillary number
c_p	specific heat capacity at constant pressure
$[C]$	color jump
d	dimension
Δt	discrete time step
D_i	diffusion coefficient of component i
D_{ij}	binary diffusion coefficient
dt	time step

e	internal energy density
F	free energy
F	Free energie
\bar{F}_i	total long-range attractive interaction force
\vec{F}_{body}	body force
f_w	normalization constant
\vec{g}	gravity
Ga	Gay-Lussac number
h	smoothing length
Hi	dimensionless number, ratio of binary diffusion coefficients
J_{ab}	random number
\vec{j}_i	mass flux of component i
\vec{j}_q	heat flux
k	conductibility of temperature
k_B	Boltzmann constant
L	length
L_0	initial particle spacing
m_b	mass of particle b
\tilde{M}_i	mobility of component i
mc_p	chain length of polymer
mc_i	chain length of component i
MW	molar weight
N	total number of mole
\hat{n}	unit normal
\vec{n}	normal vector
p	pressure

Pe	Peclet number
Pr	Prandtl number
q	non-dimensional smoothing length
R	ideal gas constant
Ra	Rayleigh number
r_{ab}	distance between particle a and b
\vec{r}_{ab}	distance vector between particle a and b
r_c	support radius
R_d	radius of droplet
Re	Reynolds number
R	radius
S_a	shepard kernel
S_i	source of component i
T	temperature
t	time
\vec{u}	Velocity vector
U^*	dimensionless velocity
u_w	absolute velocity of the wall
u_x^*	dimensionless velocity in x direction
u_y^*	dimensionless velocity in y direction
V	volume
V	absolute velocity (in analysis of viscous fingering only)
W	width
W_{ab}	kernel function evaluated between particle a and b
$d\tilde{W}$	increment of a Wiener process
\vec{x}	position vector

x^*	dimensionless position in x direction
y^*	dimensionless position in y direction

Greek letters

α	constant
χ_{12}	Flory-Huggins interaction parameter for component 1 und 2
δ	Dirac-Delta function
ε	relative error
η	dynamic viscosity
γ	shear rate
κ'	gradient energy parameter
κ	curvature
λ	thermal conductivity
λ_m	maximal wave length
λ	wave length
μ_i	chemical potential of component i
ν	kinematic viscosity
Ω	surface area
ω_i	mass fraction of component i
$\Pi_{capillary}$	capillary stress tensor
$\Pi_{viscous}$	viscous stress tensor
Ψ	general variable
ρ	Mass density
ρ_a^0	initial density of particle a
ρ_i	partial density of component i
σ	surface tension coefficient

τ	time step
τ	shear stress
ϑ	distance
φ	volume fraction
ϑ^*	dimensionless distance

Subscripts

a	index of particle
b	index of particle
i	index of component
j	index of component
p	polymer
s	solvent
*	intermediate time
**	in corrector step

Superscripts

'	index
---	-------

Acronyms

biCGStab	biConjugate Gradient
CFL	Courant-Friedrichs-Lewy
CSF	Continuum Surface Force
DIDF	density-invariant and divergence-free approach
DPD	Dissipative Particle Dynamics
FP	finger-like structures
ISPH	incompressible SPH
KHI	Kelvin-Helmholtz instability
LBM	Lattice Boltzmann method
LP	alternating structures
NMP	1-Methyl-2-pyrrolidone
PEG	polyethylglycol
PGF	interface
PSf	Ultrason S 6010
PVP	polyvinylpyrrolidone

RTI	Rayleigh-Taylor instability
SDPD	Smoothed Dissipative Particle Dynamics
SP	sponge-like structures
SPH	Smoothed Particle Hydrodynamics
TIPS	thermal-induced phase separation
WCSPH	weakly-compressible SPH

CHAPTER 1

Introduction

Separation units are present in many industrial processes. In process engineering applications, the separation of liquid or gas mixtures can be a crucial task when thermal separation is very energy consumptive. One alternative separation unit to conventional columns is a membrane. A membrane separates different fluid phases as a semi-permeable barrier and controls the transport of components between the phases [Wan11]. Depending on the kind of membrane the transport mechanism through the membrane differs. There exist a wide range of membranes e.g. hollow fiber and flat membranes, ceramic and polymer membranes or porous and dense membranes. There are different ways to classify them, e.g. by geometry, material, membrane structure or application [Str11]. Here we focus on porous polymer membranes.

Porous polymer membranes are used in desalination, wine filtration, food processing, hazardous substance removal, artificial kidney, medical and pharmaceutical industry [Wan11]. Depending on the application of the separation process, different properties of the membrane, like pore size, porosity or membrane material, are required. For example the pore size at the separation layer needs to be much smaller in nano filtration than in micro filtration. In addition an asymmetric pore structure with small pores at the permselective separation layer and larger pores in the sublayer is often preferred to reduce the total resistance of transport through the membrane. Most of the commercial porous polymer membranes are prepared by the mechanism of phase inversion. A polymer-solvent mixture is driven into a thermodynamic miscibility gap where the mixture spontaneously phase separates into a polymer rich

and a polymer lean phase. The polymer rich phase forms the polymer matrix of the membrane and the polymer lean phase forms the pores of the membrane. This process was pioneered by Loeb and Sourirajan [Loe63] for asymmetric membranes without defects.

There are 3 different established preparation processes for porous polymer membranes [Str11; Wan11]. The first process is the so-called thermal-induced phase separation (TIPS) process. A polymer-solvent mixture is normally cooled down until the mixture gets unstable and starts to phase separate [Can85]. With the TIPS process high porosity and anisotropic membrane structures can be obtained. The second process is the so-called dry-casting process. In this process a polymer-solvent mixture is in contact with a gas phase and the solvent evaporates from the polymer mixture into the gas phase. Because of the change in composition, the polymer-solvent mixture enters a miscibility gap and starts to phase separate. As a result we obtain an open-porous structure. The third process is the so-called wet-casting process. In contrast to the dry-casting process the polymer-solvent mixture is in contact with a coagulation bath that contains a liquid non-solvent. In this process the solvent diffuses from the polymer mixture into the coagulation bath while non-solvent diffuses into the polymer mixture. The polymer mixture enters a miscibility gap because of the change in composition and starts to phase separate. In this process we normally obtain an asymmetric membrane with an almost dense separation layer and porous sublayers. The received pore structure strongly depends on the very complex interaction of thermodynamics and kinetics during the preparation process of the membrane. Therefore, in this thesis we focus on the thermodynamics and kinetics that lead to structure formation in the wet-casting process.

In the history of membrane science diverse membranes based on different polymers are prepared and investigated. The polymer was selected because of product quality, economy or legal issues for special applications. At the beginning Loeb and Sourirajan [Loe63] and Strathmann et al. [Str75] investigated cellulose acetate. Nowadays [Yu14] polysulfone and polyethersulfone is used because of its high product quality and USP Class VI permission for medical devices. The constitutional formula of polysulfone is shown in Fig. 1.1. In addition different additives, e.g. polymers or solvents, are used to obtain a specific pore structure [Str75; Str11]. This leads to an even more complex system and it is more difficult to identify the mechanisms of pore formation in experiments.

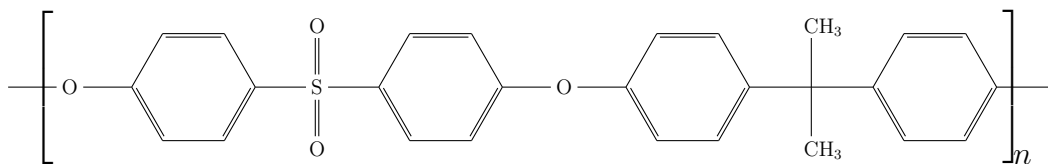


Figure 1.1: Constitutional formula of polysulfone.

1.1 Motivation

In the last 50 year comprehensive experimental studies on the formation of polymer membranes have been reported [Wit96]. These studies enlarge empirical knowledge of the preparation process of polymer membranes. In the same period no prediction of morphology from first principles was possible due to a lack of understanding in membrane science and possibly due to computational limitations [Boo92]. Therefore only simple mathematical models were used to explain different types of membrane structures in comparison with experiments [Lee10]. Morphology and process conditions were correlated to predict the outcome of pore structure in a specific preparation process. But these models are unable to predict morphology from first principles because they don't reflect the complex dynamics during formation of pores and therefore are not very useful to identify the mechanism of pore formation. To understand the formation of pores in polymer membranes it is essential to first clarify the major phenomena that lead to different pore structures, depending on the interaction between thermodynamics and kinetics during pore formation, and then formulate an appropriate mathematical model that is able to reproduce experimental findings. Such a model should allow to support the development of new polymer membranes in the future.

The major challenge to identify the mechanism of pore formation in polymer membranes is understanding the physics of the nanoscale. In theoretical physics a comprehensive theory [Grm97a; Ött05] of polymer systems on the nanoscale was developed and formulated only 20 years ago, even if the principles point back to the early work of Gibbs and van-der-Waals. An example is the picture of an interface between two fluids. Already van-der-Waals realized that the transition between two fluids is smooth and continuous instead of sharp as often assumed in macroscopic models used by engineers. But this continuous transition, a so-called diffuse interface, is essential to formulate consistent models, e.g., for the kinetics of phase

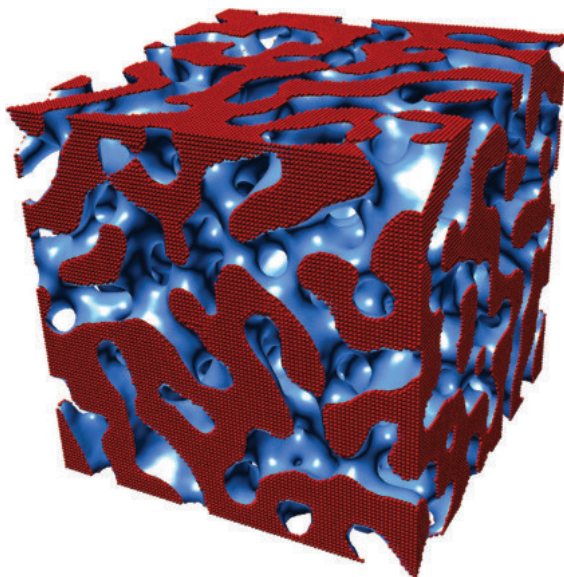


Figure 1.2: 3-dimensional porous structure calculated with the model presented in this thesis. Material indicates the matrix. Void spaces indicate the pores.

separation as we will see later. Unfortunately, even today the access to the physical models of complex polymer systems, as used in membrane science, is very difficult because of the mathematics involved. Although, an access for engineers to the physics of the nanoscale is highly desirable.

So far, the physics of the nanoscale was only rarely applied in engineering applications. Only a few investigations of pore formation in polymer membranes are available in literature [Akt05; He11; Tan12; Tan15; Tan13; Wan08; Zho06b]. In these works the physical balance equations (component, momentum, energy) are discretized and solved using mesoscopic methods, like Lattice-Boltzmann method (LBM) or Dissipative Particle Dynamics (DPD) method. The aim of these works is to demonstrate that it is possible to predict morphology in polymer systems using the equations from physics on the nanoscale. Therefore mainly phase separation of a fluid mixture was investigated. A own example of porous structures emerging during phase separation is shown in Fig. 1.2. Only one fluid phase is shown for visibility.

1.2 Aim of the thesis

Concluding from the aforementioned short literature survey, an attempt is made to solve the balance equations on the nanoscale to investigate pore formation from first

principles. In literature, a comprehensive study on the mechanism of different pore structures is still pending. Therefore in this thesis we provide an access to the physics on the nanoscale from an engineers' point of view. We discuss the thermodynamics and kinetics in terms of balance equations in a system assuming a diffuse interface between two fluid phases. This will lead us to a model that is capable of predicting morphology of polymer membranes from first principles. It also reflects the major mechanism that leads to different pore structures during phase inversion.

1.3 Outline

The thesis is organized as follows.

In chapter 2 we start with a review from the phenomenological mechanisms that lead to the formation of porous structures in polymer membranes. Then we present experiments on membrane formation, similar to that of Strathmann et al. [Str75], but with extended time resolution to identify these possible mechanisms strongly affecting the evolution of the morphology. We compare these findings with observations reputed in literature and evaluate their relevance on pore formation.

In chapter 3 we review the thermodynamics and kinetics and derive the balance equations. For an isotherm phase separating fluid mixture we use the component balance (so-called Cahn-Hilliard equation) and momentum balance. Since structure formation in polymer membranes occurs on the nanoscale, we extend the averaged component balance by a stochastic contribution to account for thermal fluctuations. Finally we simplify the model and consider only the reduced model in the remainder of the thesis.

In chapter 4 we present the Smoothed Particle Hydrodynamics (SPH) method that is used to solve the model equations. We first review the basics of SPH and formulate the discrete balance equations. Then we introduce the boundary conditions, numerical stability approaches and the time integration scheme.

In chapter 5 we focus on viscous fingering instability. Since it is found in literature that viscous fingering could be responsible for macrovoids in flat sheet membrane formation [Ren04] we test our model to reproduce viscous fingering instability for an immiscible and a miscible fluid mixture. We compare the dynamics of both systems with the dynamics found in experiments. Finally we investigate the influence of the diffusion on the morphology during viscous fingering instability.

In chapter 6 we investigate Liesegang pattern formation behind a phase separation front. A similar setup was developed by Foard and Wagner [Foa12b]. We first compare our results qualitatively with the literature [Foa12b]. Then we focus our investigation on the transition of different pore structures as found in experiments on polymer membrane formation [Yu14]. Finally we investigate the effect of thermal fluctuations and hydrodynamics on the morphology.

CHAPTER 2

Phenomenology of membrane formation

In this chapter we review the phenomenological point of view on polymer membrane formation. We first summarize empirical observations and theories derived from experiments over the last 50 years. In most of the experiments presented in literature only the morphology at the end of the preparation process is analyzed. To identify possible transport mechanisms of pore formation time-resolved experiments are necessary. Therefore we present additional own experiments on polysulfone membranes. Then we analyze the dynamics of pore formation. Finally we identify possible transport mechanisms that are involved in the formation of the pore structure.

2.1 Observations in experiments

The most simple preparation process of porous polymer membranes consists of the following consecutive steps:

1. A homogeneous mixture of a polymer and a solvent is prepared. Therefore the granular polymer (e.g. polysulfone, abbreviated as PSf) is dissolved in a suitable solvent (e.g. N-Methylpyrrolidone, abbreviated as NMP). In this sense "suitable" means that the polymer totally dissolves in the solvent. The homogeneous polymer mixture (often called polymer solution) is limpid and not cloudy.
2. Then the homogeneous polymer solution is cast in the geometric shape of the membrane. For example, if flat membranes are prepared, the polymer solution is cast on a plate.

3. In the next step we bring the polymer solution in contact with a non-solvent (e.g. water). This is the step where the pore structures are formed because of transport of solvent from the polymer solution into the non-solvent phase. The non-solvent should be miscible with the solvent but immiscible with the polymer. In membrane science this behavior is expressed in differences of the Hansen solubility parameters [Han67]. The Hansen solubility parameter is a measure for the cohesive energy density of a molecule and expresses how much energy is required to remove a molecule from a system, roughly speaking. Hansen found that the miscibility of two substances correlate with the difference in the solubility parameters. If the difference is small then the substances mix well and if the difference is large they don't mix at all. Therefore, when choosing a non-solvent to precipitate a membrane, the difference of the solubility parameter of the polymer and non-solvent should be large. On the other side the difference of the solubility parameter of the solvent and non-solvent should be small.
4. After casting of the polymer membrane several post-processing steps like drying, stretching and flushing are performed. We skip these steps in the discussion of structure formation in this thesis because the characteristic morphology is already formed during step 3.

In a technical preparation process of porous polymer membranes several additives (e.g. polymers and solvents) are used to control the pore structure. Therefore one may imagine that the terms polymer, solvent and non-solvent represent a mixture of several substances instead of a pure substance.

A special additive is the so-called pore builder. Normally a high molecular polymer (e.g. Poly-Vinylpyrrolidone, abbreviated as PVP) influences the pore structure. With the pore builder added to the polymer solution, the pore structure is of sponge type (spherical pore shape, often called sponge pores). The pore builder also suppresses defects in the membrane structure. Such defects, in literature called macrovoids, are much larger than the typical pore size of the membrane and often show an elongated shape (elliptical pore shape, also called finger pores). Generally, defects are undesired in polymer membranes because the mechanical stability and the separation properties of the membrane (e.g. at high pressure) decreases drastically. Therefore, in the last 50 years a lot of experimental research was conducted to suppress defects

by adding several substances to the polymer solution or the non-solvent, additionally to the pore builder [Loe63; Smo92; Str75]. Some experiments demonstrate the correlation of different polymers, polymer concentration, solvent concentration and effects of additives in the polymer solution and the coagulation bath with defects. For example, if pure water is used as non-solvent then the final polymer membrane consists of mostly finger pores. But if solvent is added to the non-solvent then finger pores are suppressed and the final polymer membrane consists of mostly sponge pores with some smaller defects. Similarly, if the polymer concentration in the polymer solution is increased, a transition from finger pores to sponge pores is observed [Fro73; Smo92; Str75; Yu14]. This transition is observed in several systems with different polymers and solvents. Besides, defects are found both at the surface and inside of the membrane [Yu14] and temperature and humidity influence the pore structure drastically.

In an extensive study in the 70s [Str75] the dynamics of pore formation was experimentally studied. Strathmann et al. studied the dynamics of the pore formation by observing the extension of the pore structure during the preparation process using a light microscope. They studied two representative systems where on one hand sponge pores and on the other hand finger pores are formed. To quantify the dynamics of these two systems, they introduced an effective diffusion coefficient D_e

$$D_e = \frac{\vartheta^2}{4 \cdot t} \quad (2.1)$$

where ϑ is the length of the pore structure already visible using the light microscope in the direction of precipitation. t is the time after initial contact of polymer solution and non-solvent.

For some time steps (in the order of a few seconds), Strathmann et al. calculated the effective diffusion coefficient for both systems. They found that the effective diffusion coefficient in the system where finger pores are formed is much larger than in the system where sponge pores are formed.

All these observations from experiments are hard to correlate. Nevertheless several theories are postulated based on experiments of different polymer/solvent/non-solvent systems. In the next section we give a review of these theories.

Note that in literature both terms, phase separation and phase decomposition, are used to describe demixing. The term immersion precipitation is used when phase

separation is initiated by contact of two fluids.

2.2 Empirical theory on polymer membrane formation in literature

In all theories postulated for the formation of pores in polymer membranes, the basic mechanism leading to a porous structure of polymer membranes is liquid-liquid phase separation of a polymer solution [Wit96], followed by solidification of the polymer rich phase. This follows from thermodynamics of the ternary phase diagram and a large miscibility gap between the polymer and the non-solvent. At contact of the polymer solution and the non-solvent, the polymer solution is driven into the miscibility gap by the change of composition at the contact between polymer solution and coagulation bath (in literature the non-solvent is sometimes called coagulation bath). Nuclei of a polymer rich phase spontaneously emerge and grow. Similarly to the experiments of Strathmann et al. [Str75], Koenhen et al. [Koe77] demonstrated by measuring the penetration distance of the coagulation front (see ϑ in Eq. 2.1) that the function $\vartheta(\sqrt{t})$ follows a diffusive mass transfer dynamics, indicated by a straight line in the ϑ vs. \sqrt{t} diagram (which follows from a stationary diffusion equation). The polymer solutions used were of 20%-40% polymer weight fraction. A comprehensive overview of phase separation in the preparation process of polymer membranes is found in [Wit96; Yu14].

After half a century of experimental observations and thermodynamic investigations of the system, it is generally accepted that diffusive mass transfer during phase separation of the polymer solution, followed by solidification, is the major mechanism that leads to formation of the sponge pores in porous polymer membranes [Boo92; Kim90; Koe77; Smo92; Str75; Wit96; Yu14]. Several theories were postulated to explain the formation of finger pores. These theories about the origin and growth mechanism of finger pores (or sometimes called macrovoids in literature) are summarized in the following sections.

2.2.1 Shrinkage and cracks due to mechanical stress

After contact of the polymer solution with the coagulation bath, non-solvent (typically water) diffuses into the polymer solution while solvent diffuses out of the polymer solution. This leads to a lower solvent concentration near the interface between the polymer solution and the coagulation bath. In the theory first proposed by

Strathmann et al. [Str77; Str75] this process is assumed to be very fast. At contact of the polymer solution and the coagulation bath, a polymer rich layer, called the separation layer, is rapidly formed at the interface between polymer solution and coagulation bath. As a result mechanical stresses and cracks of the separation layer evolve. These cracks are the origin of macrovoids. When a crack exists, macrovoids grow due to shrinkage of polymer rich phases, formed behind the separation layer. As a consequence, macrovoids are directly connected to the coagulation bath. Strathmann et al. [Str75] found that macrovoids propagate much faster than can be expected by diffusive transport. They found that the rate of growth of macrovoids is about 100 to 1000 times faster than diffusive transport in typical systems, where sponge pore structures are observed. Because of this faster formation of finger pores, they concluded that there is a convective contribution involved in the formation of finger pores, maybe due to shrinkage.

2.2.2 Gradients in surface tension

On contact of the polymer solution and the coagulation bath, phase separation starts at the interface between the polymer solution and the coagulation bath and propagates into the polymer solution. The solvent concentration in the polymer solution reduces near the interface and leads to differences in the surface tension (we will see this later in the so-called capillary stress). This is also known as Marangoni force in literature.

Matz [Mat72] and Frommer and Messalam [Fro73] proposed that variations in the surface tension due to different solvent concentrations initiate and promote macrovoids. They argued that gradients in the surface tension are present because Sternling and Scriven [Ste59] showed it using a mathematical model for similar situations.

A similar theory was proposed by Ray et al. [Ray85]. In contrast to Matz and Frommer & Messalam, Ray et al. proposed the reason for the differences in the surface tension more precisely as differences in the chemical potential due to concentration gradients in the polymer solution at the interface. This is the physical origin of the Marangoni force. As we will see later, this implies not only a convective contribution but also a diffusive contribution to the mass transport.

2.2.3 Delayed and spontaneous demixing

In the ternary system of polymer, solvent and non-solvent a miscibility gap exists. The binodal and spinodal define the meta-stable and unstable regions of the miscibility gap. At the critical point binodal and spinodal converge. When an initially miscible polymer mixture intersects the binodal, the mixture gets meta-stable and phase separation occurs only if a large enough perturbation in the mixture is present. When the mixture intersects the spinodal, the mixture gets unstable and will phase separate for any perturbation in the mixture. The size of the meta-stable region strongly depends on the properties of the fluids and the composition of the mixture. In the theory on membrane formation proposed by Reuvers and Smolders [Reu87b; Smo92] two terms, spontaneous and delayed demixing, are introduced. When polymer solution and coagulation bath are in contact, spontaneous demixing refers to an immediate start of the pore formation. The mixture near the contact of the polymer solution and the coagulation bath is driven, in this case, very rapidly into the miscibility gap and therefore phase decomposition is observed almost immediately after contact of polymer solution and coagulation bath. In contrast, delayed demixing refers to a decelerated start of the pore formation. It takes some time until the mixture near the contact of the polymer solution and the coagulation bath gets unstable.

Reuvers and Smolders proposed that delayed demixing refers to a fictitious time-dependent composition path of the polymer mixture that first intersects the binodal and, after some time period, the spinodal before the mixture starts to phase separate. They proposed that delayed demixing leads to sponge pores. In addition, they performed thermodynamic calculations of theoretical composition paths to characterize delayed demixing.

If the fictitious time-dependent composition path of the polymer mixture intersects the binodal and spinodal at almost the same time, e.g. if binodal and spinodal are very close to each other, Reuvers and Smolders observed finger pores. In many systems spontaneous demixing appears, if the fictitious composition path of the polymer mixture enters the miscibility gap near the critical point, where binodal and spinodal converge (see Fig. 2.1). In numerical simulations this was demonstrated assuming diffusive transport in the system assuming concentration dependent diffusion coefficients. In experiments, this is the case for low polymer concentrations.

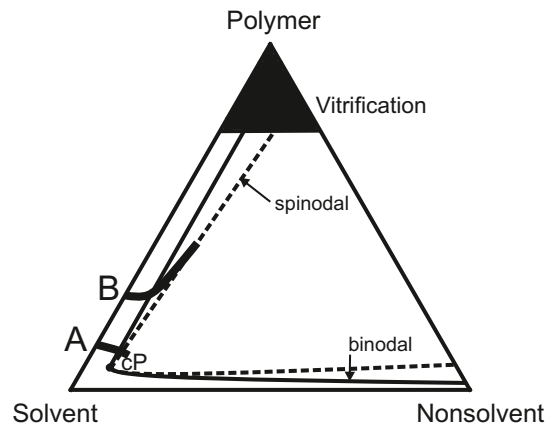


Figure 2.1: Ternary phase diagram of polymer, solvent and non-solvent. cP indicates the critical point. Binodal and spinodal are represented by the solid and dashed curves. *A* and *B* indicate composition paths for spontaneous and delayed demixing.

In contrast, delayed demixing appears if a pore builder (like PVP) is added to the polymer solution. Addition of PVP shifts the critical point to higher polymer concentration [Boo92]. Conclusively, they proposed that spontaneous demixing leads to finger pores and delayed demixing leads to sponge pores.

In addition, Reuvers and Smolders found in experiments that macrovoids (as defects in sponge pore structures) are initiated inside of a sponge structure. They stated that this is in contrast to the theory of Strathmann et al. [Str75]. Therefore they proposed that macrovoids are initiated when nuclei are formed next to existing nuclei. When a newly originated nucleus grows, influenced by the existing nuclei, it coalesces with an existing nucleus forms an elongated structure. In the highly viscous polymer solution the growth of nuclei is limited by diffusive mass transport of solvent and non-solvent. Therefore Reuvers and Smolders concluded that macrovoids grow only by diffusive transport of solvent and non-solvent.

2.2.4 Viscous fingering instability

Ren et al. [Ren04] reported experiments on flat sheet membranes between two parallel glass plates, similar to [Str75]. They stated that the experimental setup (fluid in a small gap between two solid phases) is a so-called Hele-Shaw cell. Hele-Shaw cells are normally used to study displacement of a fluid by another fluid. Especially the case where a more viscous fluid is displaced by a less viscous fluid (e.g. oil is displaced by

water) is typically studied. In the present system of polymer solution and coagulation bath we have a similar situation. If the less viscous coagulation bath displaces the more viscous polymer solution a hydrodynamic instability, called viscous fingering, arises. It is called viscous fingering because fingers of the less viscous fluid penetrate the more viscous fluid. This instability is known for immiscible and miscible fluid systems.

Ren et al. proposed that viscous fingering is responsible for the growth of macrovoids because there is typically a relative motion between the polymer solution and the coagulation bath. Originated from this motion, the coagulation bath is driven into the polymer solution. In addition, they found in the experiments that the pore structure is correlated to the viscosity of the polymer solution. For example, in high viscous polymer solutions (where viscous fingering propagates slower than in less viscous polymer solutions) sponge pores are observed while in less viscous polymer solutions finger pores are observed. Therefore they concluded that viscous fingering is responsible for the formation of macrovoids.

2.2.5 Further theories on macrovoids

Besides the above mentioned theories, different extensions of the above summarized theories can be found in the literature. They are in parts similar to the above theories. Therefore we summarize them below for the sake of completeness.

Broens et al. [Bro80] proposed a theory on the origin of macrovoids. They state that a heterogeneous distribution of polymers with distributed chain lengths or different defects in the molecule structure is responsible for the initiation of macrovoids. The former may be the case in undissolved micro-emulsions of polymer and solvent. In this theory, a macrovoid grows due to a diffusive flux of solvent from the polymer solution preferably into the macrovoid and therefore the polymer rich phase grows along the macrovoid.

An extension of the theory proposed by Reuvers and Smolders [Smo92] (delayed and spontaneous demixing, cf. Subsec. 2.2.3) was recently proposed by Yu et al. [Yu14]. In experiments they found that macrovoids originate inside the polymer solution after formation of a layer of sponge pores. Generally they agree to the theory of Reuvers and Smolders but proposed that there are local density variations during phase separation and compaction or shrinkage of the polymer rich phase, respectively, that influences the pore structure. This may lead to an influx of non-solvent into

the polymer lean phase and they call it a non-buoyancy, density-driven convection. Very recently Foard and Wagner [Foa12b] mathematically analyzed a model system that represents a polymer solution and a coagulation bath. Based on the assumption that only diffusion is responsible for mass transport, they showed that so-called Liesegang patterns [Lie96] are formed near the interface between polymer solution and coagulation bath. In 1896, Liesegang [Lie96] observed alternating patterns (periodic structures) in different systems. An example are chemical reaction systems where an electrolyte E_1 with low viscosity diffuses into another electrolyte E_2 or gel with a higher viscosity. At the mixing front a chemical reaction takes place. Liesegang pattern evolve with the moving reaction front and form alternating bands or rings [Ant99]. Foard and Wagner also observed these kind of structures in phase separating systems [Foa12b]. The characteristics of a chemical reaction system are very similar to an immersion precipitation system (polymer solution and coagulation bath) when a non-solvent diffuses into a more viscous polymer solution and the precipitation front moves toward the polymer solution. Therefore Foard and Wagner [Foa09] postulated that Liesegang patterns may be responsible for the formation of pores in polymer membranes.

An essential element in the evolution of Liesegang patterns is the formation and motion of an interface (or front) between different regimes in a mixture. In the present polymer/solvent/non-solvent system this front is the composition of the fluid that corresponds to the binodal because it represents the transition between stable and meta-/unstable fluid mixture. If solvent diffuses from the polymer solution into the coagulation bath, then the location of the composition on the binodal moves in the direction of the polymer solution. Behind this moving front different structures may evolve depending on the velocity of the front. For example, if the front moves very fast then we expect periodic polymer rich layers or droplets, depending on the amount of polymer in the system, because a nuclei that is formed near the front rapidly detaches.

2.3 Experiments on membrane formation

There are several observations on the pore characteristics in experiments and diverse theories were proposed to explain them. Therefore, we repeat some experiments with a different focus. In this thesis we simplify the experiments as much as possible

and focus only on aspects that enables us to identify the formation mechanism of the pores. Therefore we focus on time resolved data of the motion of the precipitation front for one polymer (PSf), one solvent (NMP), one pore builder (PVP) and pure water as non-solvent. The goals are identification of a possible convective transport mechanism and the influence of the viscosity on the pore structure.

In the last decades lots of experiments on polymer membrane formation were performed to identify the major mechanisms that lead to different pore shapes. Most of these experiments were done in the 70s and 80s on cellulose acetate membranes and polysulfone membranes with different solvents [Str75]. Most of the time resolved experiments on immersion precipitation are done using a pseudo two-dimensional setup and light microscopy. From these experiments, using different solvents and non-solvents, it turned out that different pore shapes are found classified in sponge-like and finger-like structures. In addition it was found that finger-like structures grow much faster than sponge-like structures. Therefore researchers believed that there is a convective flux involved. They found that finger-like structures grow perpendicular to the interface between polymer solution and non-solvent.

Later in the 90s [Smo92] analysis of the thermodynamics of the polymer system and cross sections of 3D capillary membranes indicate that there is no convective contribution that lead to finger-like structures. Quite contrary to Matz [Mat72], Smolders and Reuvers proposed that finger-like structures are the result of fast demixing and that sponge-like structures are the result of delayed demixing of the polymer solution. This means that the morphology is explainable only with mass transfer by diffusion and phase separation. As we will see later in Chap. 6 this is indeed the case. But before we do so we investigate the results of the pseudo two-dimensional experiments and explain why the observations of the 70s and 80s are deceptive and that the mechanism behind it is viscous fingering.

In the context of flat membranes, Ren et al. proposed that viscous fingering is responsible for finger-like structures [Ren04]. If flat membranes are cast on a plate then, under some conditions, viscous fingering may be present. They also proposed that viscous fingering could be responsible for finger-like structures in capillary membranes but never published detailed investigations. In this section we demonstrate that viscous fingering dynamics may be identified in pseudo two-dimensional experiments.

2.3.1 Material and Properties

In all experiments we use the polymer Ultrason S 6010 (PSf) from BASF SE delivered as granular. The solvent is 1-Methyl-2-pyrrolidone (NMP) delivered by Aldrich Chemicals Inc. We use purified water or polymers mixed with purified water as non-solvent in the coagulation bath. In the preparation process several additives may be dissolved in the polymer solution or coagulation bath to control the pore structure. One of the important additives is the pore forming material or so-called pore builder. A common pore builder is polyvinylpyrrolidone (PVP), e.g. PVP K90 powder, that is used here as delivered by BASF SE. In addition to PVP we use 2 other thicker, Agar and polyethylglycol (PEG) from Aldrich Chemicals Inc. as delivered, to increase the viscosity of the non-solvent. All relevant properties of the substances are summarized in Tab. 2.1.

The viscosity of the polymer solutions are not available in literature. Viscosity of the polymer solution and of the coagulation bath has been determined in dependence of composition. In total, 3 different polymer solutions plus 1 reference polymer solution and 3 different polymers in the coagulation bath are investigated. Viscosity is determined using the rotational rheometer RheoStress 600 from HAAKE with a titanium cone and a diameter of 35mm with an angle of 1° at constant temperature $T = 293.15\text{K}$. The shear stress τ is measured at constant rate γ for different rates. The dynamic viscosity η is calculated in the software RheoWin from HAAKE.

The polymer solutions of PSf and NMP shows viscoplastic behavior. Aqueous solutions of Agar also show viscoplastic behavior. Aqueous solutions of PVP show Newtonian behavior. This is in contrast to Ahmad et al. [Ahm95] who found Newtonian behavior only for high shear rates and viscoplastic behavior for low shear rates. In the relevant region of $\gamma \sim 10\text{s}^{-1}$ the behavior is Newtonian. Aqueous solutions of PEG show slightly viscoplastic behavior. All measurements are documented in detail in Appendix A.

For simplicity, in our simulations we consider the viscosity at a shear rate $\gamma = 10\text{s}^{-1}$ since this value is a good approximation for flow in a small gap between two plates [Mez12]. We also assume Newtonian behavior for the polymer solution and the coagulation bath, even if it is different from the real rheology to reduce computational effort later on. A summary of viscosity for all polymer solutions is given in Tab. 2.2. We find that the viscosity increases with concentration of additive polymer.

Table 2.1: Summary of properties of substances used in the experiments.

	ρ [kgm^{-3}]	MW [$gmol^{-1}$]	η [mPas]
PSf	1230 ^a	60,000 ^a	-
PVP	1200 ^a	1400,000 ^a	-
PEG	1128 ^b	35,000 ^c	-
Agar (E406)	550 ^b	120,000 ^b	-
NMP	1028 ^b	99.13	1.65 ^b (2.5) ^d
H ₂ O	1000	18	1
	σ [mNm^{-1}]	α [°] with H ₂ O	T _g [°C]
PSf	70.5 ^b	42.1 ^b	187 ^b
PVP	32 ^b	85 ^b	180 ^a
PEG	43 ^a	63 ^a	-
Agar (E406)	-	-	-
NMP	40.7 ^b	-	-
H ₂ O	72.8 ^b	-	-

^a BASF datasheet

^b This is only a typical value.

^c Aldrich Chemicals Inc. datasheet

^d own measurement, with +/- 1mPas error

Especially in solutions with Agar, the viscosity increases drastically when we added small amounts of Agar.

In addition to the viscosity of the polymer solution and the coagulation bath, we need diffusion coefficients for the polymer system. Unfortunately diffusion coefficients in polysulfone systems are very rare. In Tab. 2.3 we summarized typical values of diffusion coefficients to indicate the typical magnitude in stable mixtures. During phase separation the diffusion coefficient typically decreases due to higher polymer concentration.

2.3.2 Experimental setup and procedure

The experimental setup and procedure is similar to the pseudo experiments done in [Str75]. First we prepare a polymer solution. We use the chemicals as delivered without any preconditioning. At ambient temperature we mix PSf and NMP on a mass fraction basis using a electronic balance with a precision of 1mg. The total amount of polymer solution is always 10g. The polymer solution is stirred for a

Table 2.2: Summary of viscosity of different polymer solutions at shear rate $\gamma = 10s^{-1}$.

#	Composition [wt %]						Units	Value
	PSf	PVP	PEG	Agar	NMP	H ₂ O		
1	15	-	-	-	85	-	mPas	783.1 ^a
2	15	1	-	-	84	-	mPas	568.0 ^a
3	15	2	-	-	83	-	mPas	2140 ^a
4	15	3	-	-	82	-	mPas	3149 ^a
5	15	6	-	-	79	-	mPas	12169 ^a
6	15	-	1	-	84	-	mPas	863.6 ^a
7	15	-	2	-	83	-	mPas	1061 ^a
8	15	-	3	-	82	-	mPas	2402 ^a
9	15	-	6	-	79	-	mPas	1608 ^a
10	15	-	-	0.01	84.99	-	mPas	832.3 ^a
11	15	-	-	0.025	84.975	-	mPas	943.4 ^a
12	15	-	-	0.05	84.95	-	mPas	714.6 ^{a b}
13	15	-	-	0.1	84.9	-	mPas	873.2 ^{a b}
14	-	1	-	-	-	99	mPas	3.77
15	-	2	-	-	-	98	mPas	10
16	-	3	-	-	-	97	mPas	15.7
17	-	6	-	-	-	94	mPas	54.7
18	-	-	1	-	-	99	mPas	1.2 ^c
19	-	-	2	-	-	98	mPas	2.0 ^c
20	-	-	3	-	-	97	mPas	2.4 ^c
21	-	-	6	-	-	94	mPas	2.8 ^c
22	-	-	-	0.01	-	99.99	mPas	17
23	-	-	-	0.025	-	99.975	mPas	48.2
24	-	-	-	0.05	-	99.95	mPas	249.3
25	-	-	-	0.1	-	99.9	mPas	927.7

^a Precipitation during measurement.

^b Sample colored, indicates non-homogeneous suspension. Measurements not reliable.

^c Large errors during measurements.

Table 2.3: Diffusion coefficients in binary mixtures. The diffusion coefficient of PSF-NMP are highly concentration dependent.

component 1	component 2	D [cm^2/s]
PSf	NMP	$10^{-8} - 10^{-12}$ [Bal01; Koo98]
PSf	H ₂ O	$2.2 \cdot 10^{-6}(200^\circ)$ [Bal01]
NMP	H ₂ O	$6.0 \cdot 10^{-6}(20^\circ)$ [Amb95]

minimum of 24h before usage until it is transparent and homogeneous. After that the thickener is added to vary the viscosity of the polymer solution. If the thickener is added to the non-solvent, it is also dissolved and stirred for at least 24h until the solution is homogeneous.

We prepare two glass slides (Menzel-Gläser, Thermo Scientific, 76x26mm) with small stripes of tape to approximate a thickness between the glass slides of approximately $50\mu\text{m}$. Then the polymer solution is cast on one glass slide with a small scoop (see Fig. 2.2 on the left side). Immediately after casting of the polymer solution the second glass slide is put on top so that the polymer solution is covered and at least 30mm away from the edge of the glass plates where the non-solvent (coagulation bath) is put on the bottom glass slide (see Fig. 2.2 on the right side). Then we put the non-solvent on the bottom glass slide using a pipette. The amount of non-solvent added on the glass slide is much larger than the amount of polymer solution between the glass slides so that we may assume that the coagulation bath is very large. Therefore the concentration of solvent during precipitation in the coagulation bath is very small compared to the concentration of non-solvent.

A few moments after contact of the polymer solution with the coagulation bath the membrane structure gets visible. We observe the evolution of the membrane structure with a light microscope with a 4x optical zoom and digitize the images in real time. From these images we prepare a video to visualize the dynamics of the precipitation and the evolution of the morphology. For quantitative comparison we also insert a scale on every image.

We analyze two different properties of each sample. The first property is the developed shape of the membrane structure. Here we differentiate between finger-like structures, that are visible with the microscope, sponge-like structures that are in

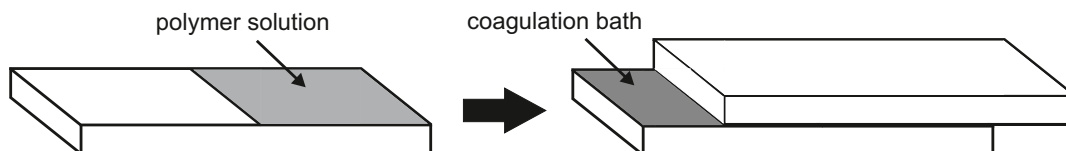


Figure 2.2: Sketch up of pseudo two-dimensional experimental setup.

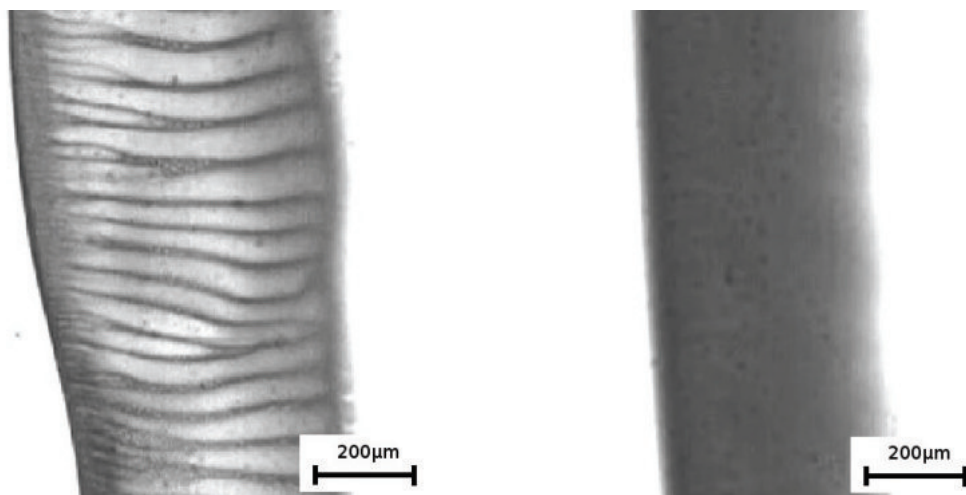
the range of a few micrometers and only visible in microscopes with at least 50x optical zoom, and alternating structures that may not fit in the previous categories. The second property is a dynamic property. We estimate the depth of the precipitation front over time and compare the growth of the membrane structure with different transport mechanisms.

2.3.3 Investigation of pore shape

We first demonstrate that our experiments match typical pore shapes found in literature [Str75]. Typical pore shapes are finger pores and sponge pores. The difference originates from the polymer solution used in the preparation process. For finger pores the polymer solution consists of the polymer and the solvent. For sponge pores a second polymer, the pore builder, is added to the polymer solution.

We prepare two polymer solutions with 25 wt% PSf content. We add 6 wt% PVP as a pore builder to one polymer solution. Then we precipitate both polymer solutions with pure water as non-solvent in the coagulation bath. The pore structures are shown in Fig. 2.3. Dark parts represent the polymer matrix and white parts represent the pores. In both images the coagulation bath is on the left side of the image. Only in the right structure a pore builder is added.

In Fig. 2.3a finger pores are observed. We observe that the fingers merge during



(a) 25 wt% PSf - 75 wt% NMP precipitated in H_2O , $t = 20\text{s}$

(b) 25 wt% PSf - 6 wt% PVP - 69 wt% NMP precipitated in H_2O , $t = 120\text{s}$

Figure 2.3: Light microscope images of two polysulfone membranes. Left: Without pore builder PVP. Right: With pore builder PVP.

precipitation and their thickness increases from left to right. The image is taken after approx. 20 s after contact of polymer solution and coagulation bath. The structure grows very fast.

In Fig. 2.3b smaller pores are observed. In images with much higher resolution sponge-like pores with a pore size of approximately $2 - 10\mu m$ are identified. The pores have homogeneous size in different parts of the membrane. The image is taken after approx. 120 s after contact of polymer solution and coagulation bath. The dynamics of precipitation is much lower than for finger pores.

As recognized in [Str75] the dynamics in both cases are very different and indicate different type of transport mechanisms. In [Str75] they proposed that convective flow is present when finger pores are formed because the speed of the precipitation front is much faster than typical diffusive transport in the polymer system. We investigate the dynamics of precipitation in detail in Sec. 2.3.5.

Next we investigate the influence of different polymer content in the polymer solution without pore builders and analyze characteristics of the finger pores. We consider 3 different polymer solutions with polymer mass fraction of 12 wt%, 20 wt% and 25 wt% PSf. The morphology of the membranes are shown in Fig. 2.4. We observe finger pores for all polymer solutions but of different shape. For the lowest polymer concentration in Fig. 2.4a the pore space (white space between the dark polymer matrix) is very large compared to the polymer matrix. It seems that less fingers are initially formed that merge to a few larger fingers. If we increase the polymer concentration in the polymer solution then the pore space decreases and the thickness of polymer fingers increases as shown in Fig. 2.4b. Again we observe that polymer fingers merge during precipitation to only a few large fingers. In both cases (Fig. 2.4a and b) we observe dead ends of pore space when polymer fingers merge.

This kind of morphology is very similar to what is observed in viscous fingering instability (displacement of a more viscous fluid by a less viscous fluid). During precipitation the viscosity of the polymer rich phase increases because solvent diffuses into the polymer lean phase and therefore the solvent concentration in the polymer rich phase decreases. As can be seen in the measurements of the viscosity (Tab. 2.2) that the viscosity of the polymer solution (and the ratio of viscosity between polymer solution and coagulation bath) increases. According to the numerical investigations of Tryggvason & Aref [Try83] less fingers are formed for a larger viscosity ratio. This

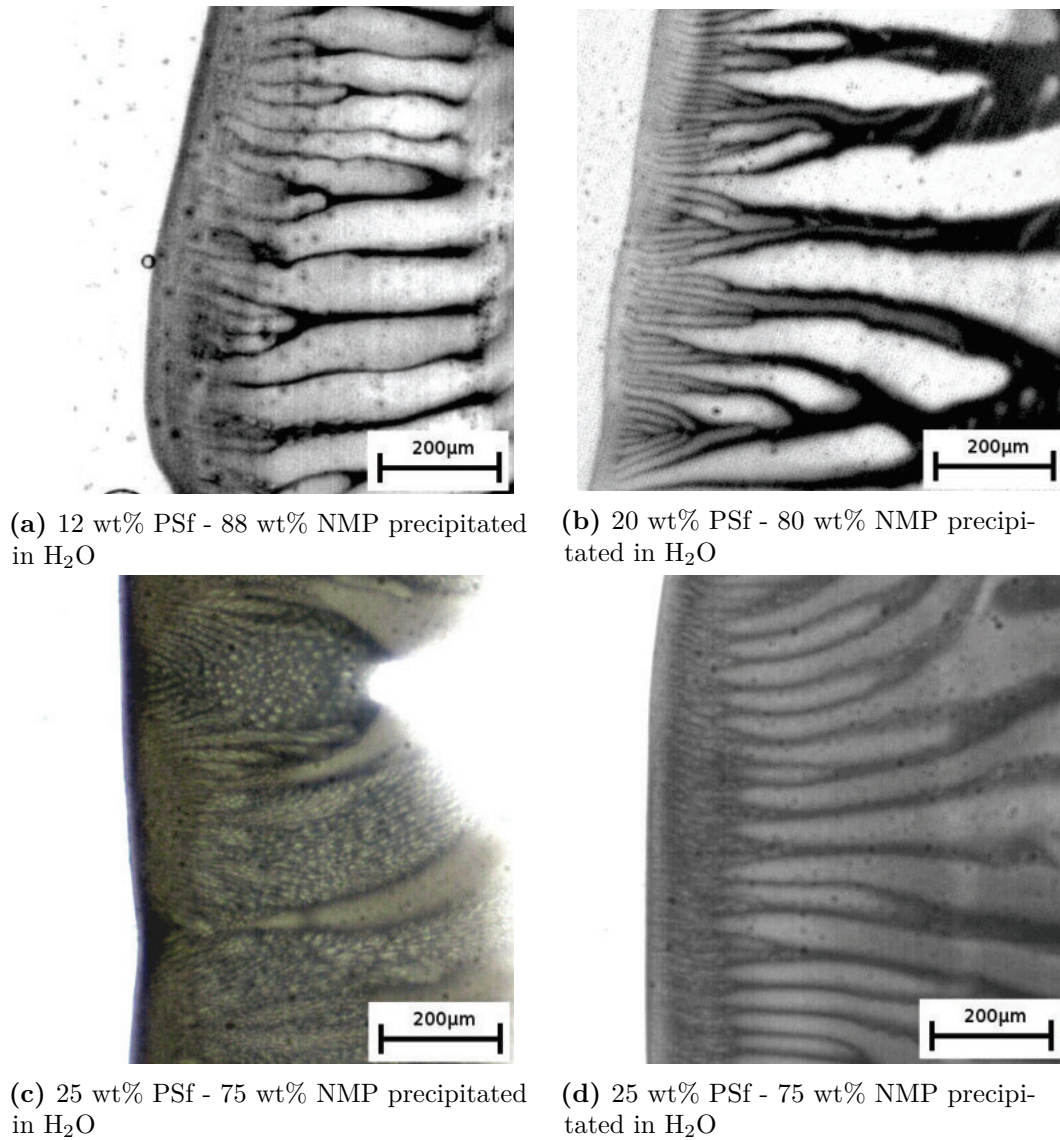


Figure 2.4: Light microscope images of polysulfone membranes with different polymer content precipitated in purified water. White represents the pore space and dark indicates the polymer matrix.

may explain that for increasing viscosity of the polymer phase less stable fingers remain.

When we increase the polymer concentration to 25 wt% the morphology differs from the previous ones (Fig. 2.4c and d). In some experiments we find mixed pore shapes of finger pores and sponge pores. The reason is that the polymer concentration is near to a critical value where heterogeneity during the precipitation may affect the morphology because the polymer solution is near to the limit of dissolution. Therefore we find finger pores or sponge pores or a mixture of them. The mixed structures are observed also in similar experiments in literature [Yu14]. In the remaining of this thesis we will not deal with mixed structures.

In the case where only finger pores are observed, see Fig. 2.4d, the polymer fingers and pore spaces grow in parallel. We rarely observe merging of polymer fingers. This is in agreement with observations by Tryggvason & Aref [Try83] for systems with very large viscosity ratio. The results indicate that viscous fingering may be the dominating effect.

In the next two sections we present further evidences for viscous fingering.

2.3.4 Influence of viscosity ratio on pore shape

We investigate the influence of the viscosity ratio between polymer solution and coagulation bath on the morphology because this is one of the main parameters affecting viscous fingering. In addition we may observe different pore shapes because the ratio between convective and diffusive transport ($\eta \propto D^{-1}$) may change.

We investigate the morphology of membranes with different polymer solutions and mixtures of polymer and non-solvent in the coagulation baths. We categorize the morphology in finger-like structures (FP), sponge-like structures (SP) and alternating structures (LP), that may indicate Liesegang patterns (cf. Subsec. 2.2.5). We vary the composition of the polymer solution and coagulation bath by adding small amounts of PVP, PEG and Agar to increase the viscosity. The mass fraction of PSf is fixed at 15 wt%. When we add thickener, we reduce the mass fraction of solvent (NMP). The results are summarized in Tab. 2.4. On the left side the pore structure, in the middle the composition of the polymer solution and on the right the composition of the coagulation bath are shown. Each line represents one combination of polymer solution and coagulation bath. The structures indicated in the first column represent the type of structures found in at least 3 experiments

Table 2.4: Analysis of pore shape for different polymer solutions and coagulation baths.

#	FP/SP/LP	Composition polymer solution [wt %]					Composition coagulation bath [wt %]				
		PSf	PVP	PEG	Agar	NMP	PVP	PEG	Agar	H ₂ O	
1	FP	15	-	-	-	85	-	-	-	100	
2	FP	15	-	-	-	85	1	-	-	99	
3	FP	15	-	-	-	85	2	-	-	98	
4	FP	15	-	-	-	85	3	-	-	97	
5	FP	15	-	-	-	85	6	-	-	94	
6	FP	15	-	-	-	85	-	1	-	99	
7	LP	15	-	-	-	85	-	2	-	98	
8	FP/SP ^a	15	-	-	-	85	-	3	-	97	
9	FP/SP ^l	15	-	-	-	85	-	6	-	94	
10	FP	15	-	-	-	85	-	-	0.01	99.99	
11	FP	15	-	-	-	85	-	-	0.025	99.975	
12	FP	15	-	-	-	85	-	-	0.05	99.95	
13	FP/SP ^a	15	-	-	-	85	-	-	0.1	99.9	
14	FP/SP ^a	15	1	-	-	84	-	-	-	100	
15	FP/SP ^a	15	2	-	-	83	-	-	-	100	
16	SP	15	3	-	-	82	-	-	-	100	
17	FP/SP ^a	15	6	-	-	79	-	-	-	100	
18	FP	15	-	1	-	84	-	-	-	100	
19	FP	15	-	2	-	83	-	-	-	100	
20	FP/SP ^b	15	-	3	-	82	-	-	-	100	
21	SP	15	-	6	-	79	-	-	-	100	
22	FP/SP ^c	15	-	-	0.01	84.99	-	-	-	100	
23	FP/SP ^a	15	-	-	0.025	84.975	-	-	-	100	
24	FP/SP ^a	15	-	-	0.05	84.95	-	-	-	100	
25	FP/LP/SP ^{a, d}	15	-	-	0.1	84.9	-	-	-	100	

a Some defect may be interpreted as finger-like pore structure but dynamics of formation is less than typical for finger-like pores.

b Very small finger-like pores.

c First sponge-like pores then finger-like pores.

d First sponge-like pores then formation of defects and then Liesegang patterns.

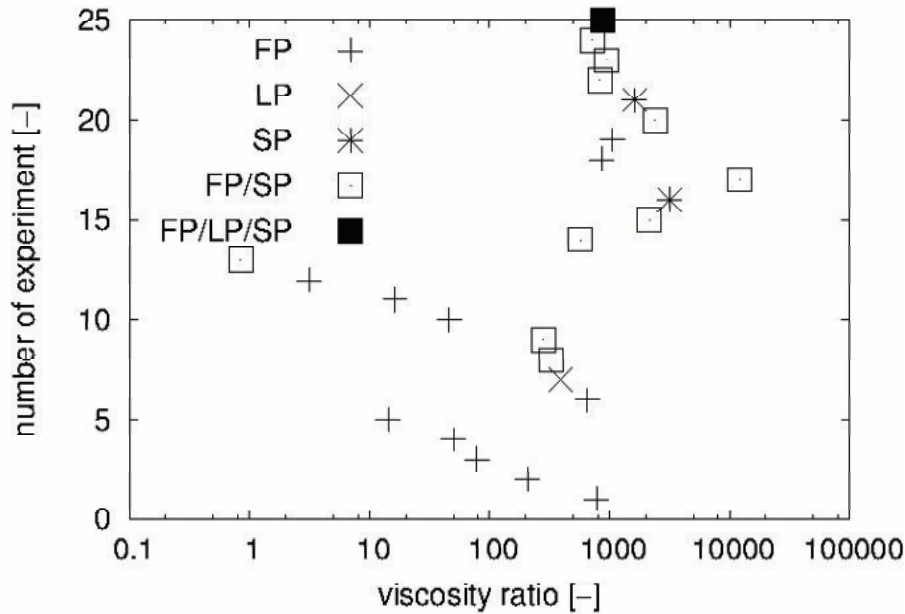
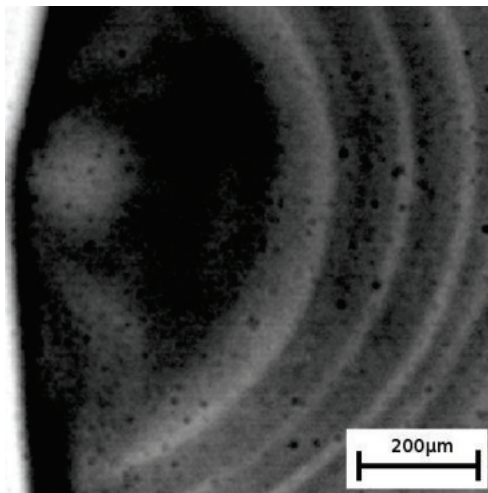


Figure 2.5: Categorization of pore structures depending on the viscosity ratio between polymer solution and coagulation bath. Vertical axis indicates number of experiment according to Tab. 2.4. Horizontal axis indicates ratio of viscosity. Symbols indicate pore structure.

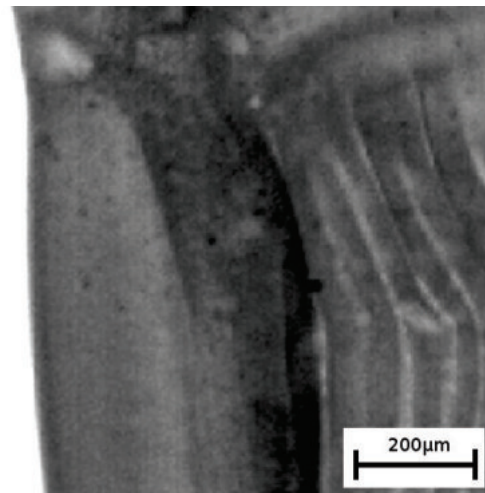
using the same composition. Cases of multiple pore structures are indicated. The table is visualized in Fig. 2.5.

We observe finger-like pores when the dynamics of precipitation is very fast compared to structures with sponge-like pores. We observe finger-like pores (FP) for most of the polymer solutions without thickener and for different compositions of solvent/non-solvent/thickener in the coagulation bath. Only a few samples show different behavior. These are samples with PEG (> 1 wt%) and Agar (> 0.05 wt%) added to the coagulation bath. Here we observe a slower dynamics of precipitation and sponge-like pores. In these cases we may interpret finger-like structures as defects in the sponge structure.

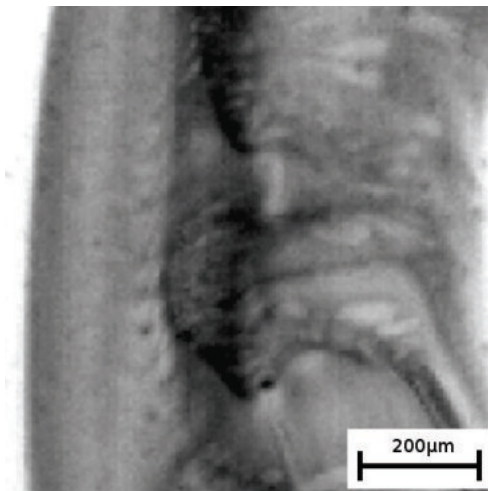
When thickener is added to the polymer solution instead of the coagulation bath we only rarely observe finger-like structures. Only in the cases of small amount of PEG in the polymer solution we observe finger-like structures. In most other cases we observe sponge-like structures or sponge-like structures with defects as is shown in Fig. 2.6c. Sometimes first sponge-like structures followed by finger-like defects are observed (shown in Fig. 2.6d). These observations match the experimental findings



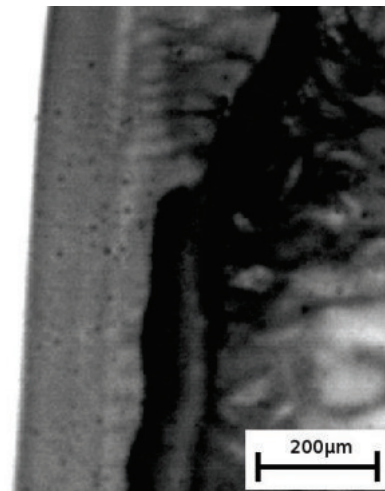
(a) 15 wt% PSf - 85 wt% NMP precipitated in 2 wt% PEG - 98 % H₂O



(b) 15 wt% PSf - 84.9 wt% NMP - 0.1 wt% Agar precipitated in H₂O



(c) 15 wt% PSf - 82 wt% NMP - 3 wt% PEG precipitated in H₂O



(d) 15 wt% PSf - 85 wt% NMP precipitated in 3 wt% PEG - 97 wt% H₂O

Figure 2.6: Light microscope images of polysulfone membranes with different polymer composition and coagulation composition.

reported in literature [Smo92; Str75; Yu14].

We made a special observation in the case of a coagulation bath with 2 wt% PEG (Fig. 2.6a). Here we repeatably found alternating lamella-like structures. The precipitation dynamics is faster than for sponge-like structures. This structure is typically observed in the context of Liesegang patterns. Similar structures are observed for high amounts of Agar in the coagulation bath (Fig. 2.6b) where first sponge-like pores, then finger-like defects and finally alternating structures are observed. We will have a closer look on Liesegang patterns in Chap. 6 as an alternative mechanism that may explain the morphology in polymer membranes because this is only theoretically discussed in literature [Foa12b] but not experimentally investigated so far.

In Fig. 2.5 we categorize the experiments depending on the viscosity ratio between polymer solution and coagulation bath. For low viscosity ratio typically finger pores are found while sponge pores are found for large viscosity ratio. Except for one experiment (# 13), this indicates that there may be a correlation between viscosity ratio and morphology. But for large viscosity ratio also mixed structures, e.g. sponge pores with defects, are found. Therefore it seems that there is still something missing to clearly categorize morphology.

Besides, the categorization in Fig. 2.5 doesn't enable us to identify the mechanism that is responsible for different morphology. Based on the theory of viscous fingering we would expect that sponge pores are only formed if the viscosity ratio is smaller than 1. Nevertheless it is reasonable that we don't find finger pores for very large viscosity ratio because the formation of fingers by viscous fingering is very slow and other effects may dominate.

One other effect may be diffusive transport. The viscosity ratio approximates the ratio of diffusive resistance in the polymer solution and the coagulation bath. In this context we may interpret Fig. 2.5 as low diffusive resistance for low viscosity ratio and large diffusive resistance for large viscosity ratio. Again, for large diffusive resistance there is still a property of the system missing because different kind of morphology is observed for similar diffusive resistance.

2.3.5 Analysis of the dynamics of different pore shapes

In the last section we observed different kind of structures for different polymer solution-coagulation bath combinations. We classified them in finger-like pores (FP), sponge-like pores (SP) and alternating lamella-like structures (LP). In this section

we analyze the propagation speed of these 3 patterns.

Strathmann et al. [Str75] estimated the distance between the interface of coagulation bath and polymer solution to analyze the dynamics of the formation of morphology. Similarly we measure the distance ϑ between coagulation bath and precipitation front in the homogeneous polymer solution over time t . We assume that the precipitation front is located at the point where the morphology gets visible. According to literature we expect that finger-like structures evolve more rapid than sponge-like structures [Str75].

We analyze the experiments presented in Sec. 2.3.3 in Fig. 2.3 (finger pores (FP) and sponge pores (SP)) and the experiment presented in Sec. 2.3.4 in Fig. 2.6a (lamella-like structures (LP)). The distance ϑ is measured as the distance between the interface of coagulation bath and polymer structure and the interface between polymer structure and polymer solution. At least 3 different points in the experiment are averaged to estimate ϑ . A plot of ϑ over time is shown in Fig. 2.7. We find the lowest propagation speed for sponge-like pores (SP). The dynamics is in good agreement with the dynamics of diffusive transport ($\vartheta \sim \sqrt{t}$). Similar results are presented by Strathmann et al. [Str75].

Finger pores (FP) evolve more rapid than sponge pores (SP). At the beginning of precipitation we find $\vartheta \sim t^{1.6}$. This behavior is highlighted in the close-up in Fig. 2.7. It indicates viscous fingering dynamics [Mah85]. For later times we find $\vartheta \sim t$. This indicates convective viscous transport in a confined domain. It was presented in literature [Str75] that finger pores grow much faster than sponge pores. But we found for the 25 wt% PSf solutions that finger pores grow faster by a factor of only 3 which is in contrast to what is reported in literature [Str75].

For alternating lamella-like structures (LP) we find a much larger growth rate than for the other two structures. This may depend on the lower polymer concentration (15 wt% PSf) compared to the sponge and finger pores in Fig. 2.7 (25 wt% PSf and 25 wt% PSf - 6 wt% PVP, respectively). In addition, we find in this case $\vartheta \sim \sqrt{t}$. This is similar to Eq. 2.1 and indicates a diffusive transport process for the motion of the precipitation front.

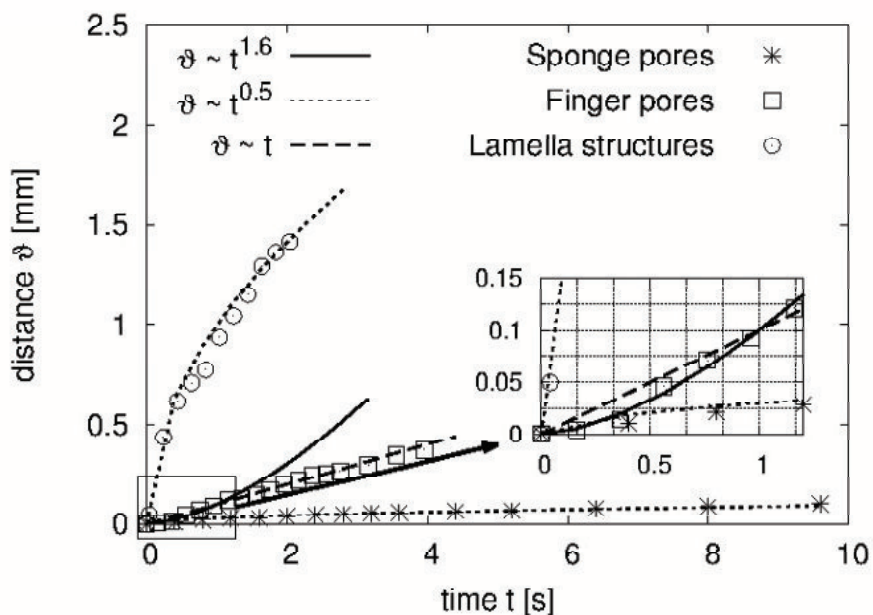


Figure 2.7: Comparison of dynamics of different pore types during preparation. Sponge pores are found for polymer solution 25 wt% PSf - 6 wt% PVP - 79 wt% NMP and water as coagulation bath. Finger pores are found for polymer solution 25 wt% PSf - 75 wt% NMP with water as coagulation bath. Lamella structures are found for polymer solution 15 wt% PSf - 85 wt% NMP with 2 wt% PEG - 98 wt% H₂O as coagulation bath.

2.4 Conclusion

In this chapter we first reviewed experimental observations and proposed theories on the formation of pores during the preparation process of polymer membranes. The theories are diverse because they rely on one hand on diffusive transport and on the other hand on convective transport of solvent and non-solvent. Therefore we reproduced some experiments, similar to the experiments published by Strathmann et al. in the 70s with higher time resolution, to investigate the dynamics of finger and sponge pore formation. We found that by adding a pore builder (PVP) to the polymer solution a transition from finger pores to sponge pores is possible. Addition of PVP affects the thermodynamics because it shifts the critical point to larger polymer concentrations.

For PSf in the polymer solution without PVP and different PEG concentrations in the coagulation bath, we found finger pores, sponge pores and also lamella-like structure. Depending on the viscosity ratio between polymer solution and coagulation

bath, we find that finger pores are observed for low viscosity ratio and sponge pores or sponge pores with defects are observed for larger viscosity ratio. Because defects represent finger-like structures we conclude that there is still something missing in the correlation between viscosity ratio and pore structure.

In the last part we analyzed the motion of the precipitation front and found evidences on viscous fingering and diffusive transport for lamella-like structures. Both phenomena are mentioned in the phenomenological theories (cf. Subsecs. 2.2.4 and 2.2.5). Interestingly, viscous fingering may only be present in the first moments of contact between polymer solution and coagulation bath, even though finger pores evolve. At later times other effects may dominate, e.g. convective flow in a channel or diffusive transport.

Based on this findings, we focus on viscous fingering and diffusive transport, that may lead to lamella-like structures in the remaining of this thesis. We assume that viscous fingering may only be relevant in the first moments of contact between polymer solution and coagulation bath and that diffusive transport dominates for later times.

CHAPTER 3

Theory

In this chapter we first discuss the physical picture of a phase separating fluid and its thermodynamics. Then we formulate the balance equations for mass and momentum. Since we restrict ourselves to isotherm systems we skip the energy balance. For the sake of completeness the energy balance is presented in Appendix G. Finally we condensate the thermodynamics and the balance equations to the most simple case and end up with the simplified model used in the remainder of this thesis.

3.1 Physical picture

Prior to a review of the thermodynamics, we shortly recapitulate the physical pictures of a fluid interface and the phase separation of a fluid mixture.

Let us start with the molecular picture of an interface between two fluids. For simplicity we assume an immiscible system, e.g. water and oil (note that this is not necessary but helps to get the important points) and a planar interface. On the left side we have only water molecules and on the right side only oil molecules (cf. Fig. 3.1a). These regions are called bulk phases. In the bulk phases only molecules of the same kind interact (e.g. an oil molecule is surrounded only by other oil molecules). These molecular interactions can be attractive or repulsive depending on the distance between two molecules. We do not need to go into details about the interactive forces at this point but just keep in mind that the interaction between molecules can be attractive or repulsive depending on the kind of the molecules and the distance between the molecules.

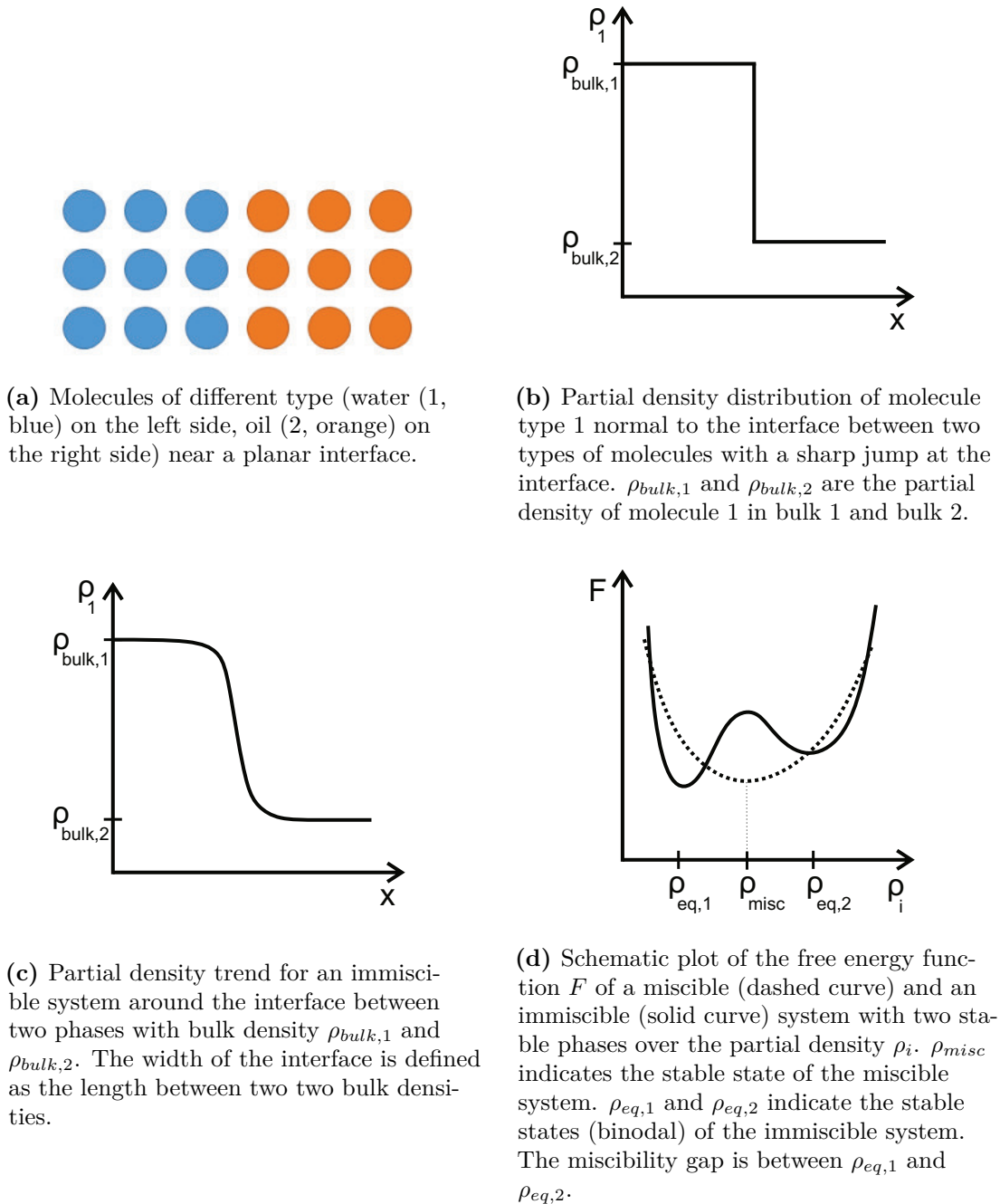


Figure 3.1: Representations of a fluid interface (a-c) and a plot of the free energy (d).

At the interface between these bulk phases an oil molecule interacts with oil molecules and water molecules. In the system water-oil, roughly speaking, for the same distance between the molecules, the oil molecules tends to interact more attractively with other oil molecules than with water molecules. Therefore, at the interface between the bulk phases, the molecules are ordered along the interface in a way that they do not mixing with molecules of the other type. This means that oil molecules and water molecules are separated from each other (this is not the case in real systems, because the interface between the bulk phases is not sharp, but we keep that picture for the moment).

Now we drop out of the molecular picture and consider the same system from a coarser scale where molecules are small compared to the scale. In this scale we consider a distribution of partial density instead of each single molecule. For example, we consider the partial density distribution of each kind of molecule in normal direction to the interface between the bulk phases. Inside the bulk phases the partial density distribution is constant because only one kind of molecules are present. At the interface a jump in the partial density distribution exists (Fig. 3.1b). Let us now go back to the molecular picture and consider a more realistic interface. Previously we assumed a sharp interface between the bulk phases. A realistic fluid interface is not sharp because the molecules slightly mix near the interface because of thermal fluctuations. Therefore the interface is somehow diffuse. If we go back to the coarser scale and again consider the partial density distribution (or partial mass density distribution ρ_i) we find that the jump at the interface in the molecule density distribution smooths out and we get a continuous transition from one bulk phase to another bulk phase (Fig. 3.1c). In the remainder of this thesis we use the term diffuse interface for this smooth transition in the density distribution.

Next we go back to the molecular picture and have a look at the energy involved in the interaction of the molecules. We only consider internal energy (just for simplicity, potential and kinetic energy are neglected). Say that the energy arises from the interaction between molecules. Clearly, the interaction of two oil molecules is different from the interaction of an oil and a water molecule.

Back on the coarser scale, we consider the free energy distribution, analog to the partial density distribution. The energy density distribution inside the bulk phase is constant because only molecules of the same kind interact. But near the interface we again find a smooth transition between the bulk phases. This smooth transition

of the energy density may have a complex shape for real multi-component systems, e.g. if electrolytes are involved. In literature it is common to plot the energy versus mass density instead of position in normal direction to the interface. As shown in Fig. 3.1d the energy F may vary strongly with the mass density. Therefore the energy differs from the bulk energy in the diffuse interface. This deviation is called surface energy or gradient energy, respectively, and is the origin of the macroscopic surface tension [Jam02]. We will see the relation between surface tension and partial density in the next section.

In the remaining part of this section we project a picture for phase separating fluids. As known from several textbooks on thermodynamics each physical system tends to minimize its free energy. For example, expressed in the total free energy F , $\min(F)$ represents the equilibrium of the system for constant temperature and volume. For simplicity we neglect meta-stable equilibrium states in the present discussion. Each energetic contribution in a system, e.g. the gradient energy of an interface, originated by unequal molecular interactions between molecules of different kind, locally increases F .

Now, consider a phase separating fluid mixture. When a fluid mixture gets unstable and nuclei arise, locally many interfaces originate in the fluid mixture. The fluid mixture is in non-equilibrium and the total free energy is far away from its minimum. Then there are two possible options to minimize the total free energy. One option is a collapse of nuclei, e.g. the mixture gets stable again. In this way the energetic contributions from interfaces vanish. An other option is to minimize the area of interfaces. The latter option is the case during phase separation when nuclei grow and coalesce until an equilibrium state, where the total free energy is minimized, is reached.

Now, we have a physical picture of a real, microscopic interface and the process during phase separation. Next we use this picture to review the thermodynamics of phase separating fluids.

3.2 Thermodynamics

In this section we review the thermodynamics of phase separating fluid mixtures based on the theory of van der Waals [Waa93] and Cahn and Hilliard [Cah58]. Van der Waals stated that it is necessary to consider the local environment at

a diffuse interface if we want to describe the surface energy contribution to the free energy. Cahn and Hilliard presented the derivation of a diffusion equation (so-called Cahn-Hilliard equation) for a binary mixture of solids including effects of the environment through higher order spatial derivatives of the density. It turned out that this approach, extended for liquid mixtures, describes both nucleation and diffusion-dominant coarsening dynamics very well [Tan00a].

A polymer solution for the preparation of polymer membranes is a liquid mixture of at least two components, polymer and solvent. For simplicity we consider a binary mixture to review the thermodynamics.

We start our discussion by considering the free energy F of a binary miscible (single-phase) and an immiscible (multi-phase) polymer mixture (cf. Fig. 3.1d). The free energy of the miscible system has one minimum. We bring in contact component 1 (ρ_1) and 2 (ρ_2). Since each physical system tends to minimize its free energy the miscible mixture tends to mix until it is perfectly mixed with a uniform mass density ρ_{misc} . In contrast the free energy of an immiscible system has two minima $\rho_{eq,1}$ and $\rho_{eq,2}$ (cf. Fig. 3.1d). The region between the minima is called the miscibility gap where the mixture is meta-stable or unstable. If a system is driven into the miscibility gap it phase separates into two phases with partial mass densities $\rho_{eq,1}$ and $\rho_{eq,2}$. Herein both densities could be equal.

Van der Waals postulated the following form of the free energy density [Jam08]

$$f = f^0 + \frac{\kappa'}{2} (\nabla \rho_i)^2. \quad (3.1)$$

f^0 is the local free energy density and the gradient term represents the additional free energy contribution due to the presence of a gradient in the partial density. κ' in Eq. 3.1 is the gradient energy parameter. The gradient term in Eq. 3.1 vanishes if the gradient in the partial density of one component vanishes or if the gradient of all components are equal because κ' is a function of the gradient of the partial density of each component to the partial density of a reference component. In the latter, $\kappa' = 0$. This is only the case in a perfectly homogeneous mixture when the partial density is constant throughout the mixture. The gradient energy term is also a measure for the width of the interface because it vanishes in the bulk phases where the partial density of each component is constant. We skip a detailed discussion of the thermodynamics here because later we use κ' as a numerical parameter. Further

details are found in literature [Kah00; Pla13; Sch13; Vin14].

Cahn and Hilliard presented a similar form of the free energy [Cah58] but they derived the free energy density from a Taylor series expansion of the free energy around f^0 . Note that the linear term vanishes due to symmetry reasons.

We can interpret the free energy in Eq. 3.1 composed of a local contribution and a non-local contribution that represents the influence of the spatial vicinity on the total free energy. It can be interpreted as the energy contribution due to the gradient of the partial density that is zero in the bulk [Kah00] because of the homogeneous density in the bulk.

The local part may be calculated using an equation of state for the local free energy F^0 and therefore represents a classical thermodynamic contribution. The non-local part is formally directly related to the surface tension [Kah00; Vin14]

$$\sigma = \int_{\rho_{bulk,1}}^{\rho_{bulk,2}} \sqrt{\kappa' \Delta \rho_i} d\rho_i \quad (3.2)$$

with the Laplace operator Δ . Note that Eq. 3.2 is only formally written here for simplification of the thermodynamic principles. Nevertheless, this demonstrates the importance of the gradient energy term for a consistent thermodynamic description of the interface. As we will see later the gradient energy term arises not only in the balance equation of momentum as surface tension but also in the component balance. Besides, it was mathematically proven that the second-order term is necessary for a stable solution in Hilbert space [Fif00].

Next we formulate the chemical potential based on the formal form of the free energy density (Eq. 3.1). Integrating the free energy density f over the volume V is

$$F = \int_V \left(f^0(T, V, \rho_i) + \frac{\kappa'}{2} (\nabla \rho_i)^2 \right) dV. \quad (3.3)$$

Later we will use the chemical potential to formulate the driving force in the balance equations. For a free energy as shown in Eq. 3.3 the chemical potential μ_i of a component i , using the functional variance¹ [Zho06a], and in analogy to the

¹ The function $Z[x(y), \nabla x(y)]$ with $x(y)$ as a continuous function depends on the function x and its derivative $\nabla x(y)$ and $\nabla = [\partial/\partial y]$ for all elements of y . The mathematical rule for the derivative of function Z (the so-called functional variance) is $\frac{\delta Z[x(y), \nabla x(y)]}{\delta x(y)} = \frac{\partial Z}{\partial x} - \nabla \cdot \frac{\partial Z}{\partial \nabla x}$.

derivation of the Euler-Lagrange equation is

$$\mu_i = \frac{\delta F}{\delta \rho_i} = \frac{\partial f}{\partial \rho_i} - \nabla \cdot \frac{\partial f}{\partial \nabla \rho_i}. \quad (3.4)$$

The chemical potential has the form

$$\mu_i = \mu_i^0 - \kappa' \nabla^2 \rho_i. \quad (3.5)$$

The first term is the local chemical potential (not the reference state) and may be calculated using an equation of state. The second term represents a spatial Laplacian and we get it from spatial discretization of the density normal to the interface. That means that we need to resolve the diffuse interface.

In the next section we introduce the equation of state used for μ_i^0 and discuss the properties of the ternary system (polymer, solvent and non-solvent).

3.2.1 Equation of state

The most simple fluid mixture that is involved in the preparation of porous polymer membranes in the wet-casting process consists of at least 3 components (polymer, solvent and non-solvent). For simplicity we neglect additives because their amount is very low compared to the 3 main components. The influence of additives are

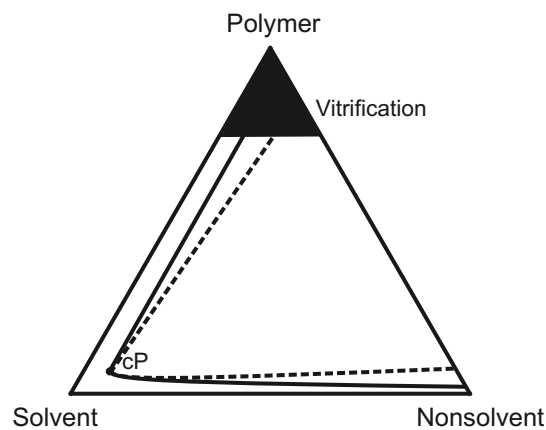


Figure 3.2: Schematic plot of a ternary phase diagram of polymer, solvent and non-solvent with a miscibility gap, an area of vitrification, the critical point cP, binodal (solid line) and spinodal (dashed line).

discussed in several literature on experiments and thermodynamics, e.g. [Boo92] and references therein. Before we introduce the equation of state used in this thesis, we discuss the general properties of the ternary mixture using the common ternary phase diagram.

A typical phase diagram for a ternary polymer/solvent/non-solvent mixture, as it is involved in the preparation process of porous polymer membranes, is shown in Fig. 3.2. We find the critical point located at large solvent amount in the mixture. Typically, the solvent completely dissolves in the polymer (up to the limit of dissolution of polymer) as well as in the non-solvent. The non-solvent is usually water. There exists a large miscibility gap between the polymer and the non-solvent. As indicated by the miscibility gap the polymer is almost insoluble in the non-solvent. The miscibility gap is separated from the miscible region through the binodal and spinodal that indicate the transition from the stable to meta-stable and meta-stable to unstable region, respectively. Between the binodal and the spinodal a meta-stable region exist where a finite perturbation leads to phase decomposition. In typical polymer systems this meta-stable region is small (binodal and spinodal are very close). Therefore, phase decomposition of polymer systems in literature is often referred to spinodal decomposition rather than binodal decomposition.

Typical polymer systems for polymer membranes have a region of vitrification for very high polymer concentrations. It is assumed that the structure during preparation of porous polymer membranes no longer changes when the vitrification point, in literature also called Bergman's point, is reached because the phase separation process slows down due to increasing transport resistance.

Next we need an equation of state for the local chemical potential μ_i^0 (not the reference state) and κ' . Firstly, we focus on μ_i^0 . For a polymer system the Flory-Huggins equation of state [Flo42; Hug42] provides a first approximation of the fluid behavior. Also, in literature some experimentally fitted parameters for typical polymer solutions used in the preparation process of porous polymer membranes are available. Therefore, we use the Flory-Huggins equation of state. The dimensionless molar Gibbs free enthalpy for a multi-component mixture in the Flory-Huggins theory is [Zho06a]

$$\frac{\Delta G}{NRT} = \sum_i \frac{\varphi_i}{mc_i} \ln \varphi_i + \sum_{ij} \chi_{ij} \varphi_i \varphi_j. \quad (3.6)$$

G , R and N are the Gibbs free enthalpy, ideal gas constant and total number of mole. φ_i and mc_i are the volume fraction and the chain length of component i in the mixture. Note that $mc_i = 1$ for non-polymers, e.g. solvents and non-solvents. χ_{ij} is the interaction parameter between fluid i and j . For example, the dimensionless chemical potential for a binary mixture of polymer and solvent with respect to the solvent s (assuming that the chain length of the solvent $mc_s = 1$) is [Zho06a]

$$\frac{\Delta\mu_s}{RT} = \frac{1}{RT} \frac{\partial(\Delta G)}{\partial n_s} = \ln(\varphi_s) - \frac{1}{mc_p} \ln(1 - \varphi_s) + \chi_{sp}(1 - 2\varphi_s) - mc_p + 1 \quad (3.7)$$

mc_p is the chain length of the polymer p . The chemical potential in Eq. 3.7 is a chemical potential relative to a standard state. Note that for polymer mixtures more accurate equations of state like PC-SAFT [Gro01] may be used to calculate the chemical potential of each component in the mixture.

In this thesis we focus on the development of a model for polymer membrane formation. It is difficult to calculate gradients of the chemical potential [Koo98], especially in the polymer lean phase when the concentration of polymer tends to zero. Therefore we need to simplify the chemical potential for numerical reasons. In the remaining of this thesis we only use the Flory-Huggins equation of state for a model-fluid. As a result, we use only the mathematical form of the Flory-Huggins equation to describe the chemical potential.

As shown in Eq. 3.2, κ' is directly related to the surface tension. If the surface tension of the mixture is known, e.g. from density functional theory (DFT), molecular simulations or experiments, we may use Eq. 3.2 and recursively calculate the constant energy parameter κ' (in the isotherm case). This is very similar to the density gradient theory used in thermodynamic calculations of the surface tension, e.g. [Vin14]. It is necessary to resolve the spatial density distribution over the diffuse interface between two bulk phases. Since the energy parameter is directly connected to the length scale of the diffuse interface we need to resolve this length scale in the simulations. Typical length scales are in the range of a few angstrom to a few nanometers.

3.3 Balance equations

In this section we present the balance equations. It is important to start with a complete description of a system because we don't want to exclude possible effects a

priori. A complete thermodynamic consistent form of the component, momentum and energy balance, as found in Thieulot et al. [Esp03b], is very complex and has parameters that are not known for the polymer system under consideration. Therefore we make the following assumptions to only reduce complexity without neglecting important mechanisms.

First, we assume that heterogeneous molecular configurations, e.g. orientation of a polymer molecule, is less important and that a balance of average quantities like partial mass and momentum density is sufficient on the mesoscale, ranging from nanometers to micrometers. This implies that a nuclei originated at the molecular level arises as thermal fluctuation of the average quantity. Therefore a balance of the average density of a quantity extended by a stochastic contribution is regarded. Second, we assume an isotherm system. This implies that Soret effects due to the presence of a temperature gradient are negligible in the component and momentum balance and we don't have to consider an energy balance.

The free energy of a realistic polymer/solvent/non-solvent mixture is very complex especially if we consider the chain length of the polymer. There are large spatial gradients of the chemical potential. Numerically it is very difficult to resolve the gradients of the chemical potential in the diffuse interface because the diffuse interface is very thin compared to the bulk phases. Therefore we restrict the present model to a Newtonian model-fluid mixture where all components, including the polymer, have equal molar mass with moderate spatial gradients of the chemical potential. Obviously the use of a Flory-Huggins equation of state (FH-EOS) for the free energy is questionable for equal molar mass. Therefore we use a FH-EOS-like equation of state for the model-fluid with a binary interaction parameter that controls the state of the system, e.g. stable or unstable. In this case moderate spatial gradients of the chemical potential are defined by efficiency of numerical solution. This implies that the molar average and mass average velocities are identical and we only need to formulate the momentum balance for the average momentum of the multi-component system. Since we consider a liquid fluid only, we assume an incompressible fluid and neglect solidification.

Using these assumptions we introduce the balance equations. We review the derivation of the balance equations in Lagrangian form for our Lagrangian numerical framework and introduce thermal fluctuations of the partial density that may be relevant on the nanoscale. Finally, we summarize the balance equations used in the

remainder of this thesis and discuss additional simplifications from numerical point of view.

3.3.1 Continuity equation

The continuity equation is [Lan87]

$$\frac{d\rho}{dt} + \nabla \cdot (\rho \vec{u}) = 0. \quad (3.8)$$

ρ and \vec{u} are the mass density and the mass average velocity of the fluid. We formulate the continuity equation in a Lagrangian reference frame. Therefore we rewrite Eq. 3.8 using the material derivative

$$\frac{D\rho}{Dt} + \rho \nabla \cdot \vec{u} = 0. \quad (3.9)$$

We define an incompressible system with constant density as

$$\nabla \cdot \vec{u} = 0 \quad (3.10)$$

where the density is independent of the pressure and therefore the divergence of the velocity is zero. Here we neglect the change of density on the mass average velocity.

3.3.2 Component equation

The component balance of component i is [Bir07]

$$\frac{d\rho_i}{dt} + \nabla \cdot (\rho \vec{u}) + \nabla \cdot \vec{j}_i + S_i = 0 \quad (3.11)$$

with the partial mass density ρ_i , the diffusive mass flux \vec{j}_i and a source term S_i , respectively. In our model we focus on non-reactive, incompressible, multi-component, multi-phase systems of fluids with equal molar mass. Therefore the source term $S_i = 0$ vanishes. We assume linear driving force relationship for the diffusive mass flux

$$\vec{j}_i = -\rho \frac{\tilde{M}_i}{RT} \nabla \mu_i \quad (3.12)$$

with the chemical potential μ_i consisting of a local and non-local part, as introduced in Sec. 3.2, and the mobility \tilde{M}_i of a component. R and T are the ideal gas constant and the absolute temperature. The mobility is related to the diffusion coefficient D_i as

$$D_i = \tilde{M}_i \frac{\delta^2 F}{\delta \rho_i^2} \quad (3.13)$$

with the free energy of the system F .

We again write Eq. 3.11 in Lagrangian form using the material derivative and Eq. 3.10

$$\frac{D\rho_i}{Dt} + \nabla \cdot \left(-\rho \frac{\tilde{M}_i}{RT} \nabla \mu_i \right) = 0. \quad (3.14)$$

Eq. 3.14 in terms of the mass fraction $\omega_i = \rho_i/\rho$ is

$$\frac{D\omega_i}{Dt} + \nabla \cdot \left(-\frac{\tilde{M}_i}{RT} \nabla \mu_i \right) = 0. \quad (3.15)$$

Finally, we get the component balance using Eq. 3.5

$$\frac{D\omega_i}{Dt} + \nabla \cdot \left(-\frac{\tilde{M}_i}{RT} \nabla (\mu_i^0 - \kappa' \nabla^2 \omega_i) \right) = 0. \quad (3.16)$$

Eq. 3.16 represents a fourth-order partial differential equation and is known as the Cahn-Hilliard equation.

3.3.3 Momentum equation

The momentum balance of the multi-phase system is [Esp03b; Jac99; Low98]

$$\frac{d(\rho \vec{u})}{dt} + \nabla \cdot (\rho \vec{u} \vec{u}) = -\nabla p + \nabla \cdot \mathbf{\Pi}_{viscous} + \vec{F}_{body} + \nabla \cdot \mathbf{\Pi}_{capillary} \quad (3.17)$$

with the pressure p , the viscous stress tensor $\mathbf{\Pi}_{viscous}$, a body force, e.g. gravity $\vec{F}_{body} = \rho \vec{g}$, and the capillary stress tensor $\mathbf{\Pi}_{capillary}$. The first three terms on the right hand side are classical terms in the momentum balance as in single-phase flow [Lan87]. The last term in Eq. 3.17 accounts for the presence of interfaces. With the continuity equation (Eq. 3.8) the momentum balance for an incompressible,

Newtonian fluid reduces to

$$\rho \frac{d\vec{u}}{dt} + \rho (\vec{u} \cdot \nabla) \vec{u} = -\nabla p + \eta \nabla^2 \vec{u} + \rho \vec{g} + \nabla \cdot \mathbf{\Pi}_{capillary} \quad (3.18)$$

with the dynamic viscosity η .

The capillary stress tensor in Eq. 3.18 arises due to the presence of the interface. We already introduced the physical picture of a diffuse interface in Sec. 3.1 as a smooth transition in the density between two bulk phases. This physical concept was developed by Rayleigh [Ray92] and van der Waals [Waa93] in the late 19th century. They proposed a theory of gradient energy contributions in the free energy due to the smooth transition in the density between two phases [And98] as introduced in Sec. 3.2 in Eq. 3.1. Van der Waals also recognized that it is necessary to consider the gradient energy term for a valid description of the dynamic contributions of the interface [Jam08]. The ansatz for the last term in Eq. 3.18, the divergence of the capillary stress tensor, is [Jam08]

$$\nabla \cdot \mathbf{\Pi}_{capillary} = \nabla \cdot \left(\kappa' \rho_i \nabla^2 \rho_i + \frac{\kappa'}{2} (\nabla \rho_i)^2 \right) - \nabla \cdot (\kappa' \nabla \rho_i \otimes \nabla \rho_i) \quad (3.19)$$

with the gradient energy parameter κ' . Analog to the structure of the viscous stress tensor (cf. Eq. I.5), the capillary tensor in Eq. 3.19 has the structure

$$\mathbf{\Pi}_{capillary} = \begin{pmatrix} xx & yx & zx \\ xy & yy & zy \\ xz & yz & zz \end{pmatrix}. \quad (3.20)$$

and consists of two parts. The first term on the right hand side of Eq. 3.19, in brackets, results in diagonal entries in the stress tensor. It reduces or increases the bulk pressure. The second term on the right hand side of Eq. 3.19 is the so-called Korteweg tensor [Kor01]. It results in diagonal and off-diagonal elements (similar to the shear stress) and implies a tangential surface tension force because the gradient of the partial density may vary along an interface. Note that the formulation of the capillary stress tensor is based on the ansatz of the free energy density (Eq. 3.1). This form of the capillary stress requires a diffuse interface to be consistent because the gradient of the partial density needs to be calculated across the interface. In

process engineering a diffuse interface is rarely resolved because the typical length scale is much larger than the width of the diffuse interface. It is more common to use the sharp interface limit of the capillary stress tensor to include surface tension in the momentum balance. The sharp interface limit may be seen as projecting the integral over the diffuse interface on the interface area (plane in 3D). A review of a mathematical derivation of the sharp interface limit from a diffuse formulation is shown in Appendix B. The main result is

$$\nabla \cdot \mathbf{\Pi}_{capillary} = \left(\sigma \kappa \vec{n} + \nabla_S \sigma \right) \delta \quad (3.21)$$

with the surface tension coefficient σ , the curvature κ and the gradient of the surface tension tangential to the surface $\nabla_S \sigma$. \hat{n} is the unit normal to the interface. δ is the Dirac-Delta function

$$\delta = \begin{cases} 1 & \text{at the interface} \\ 0 & \text{in the bulk.} \end{cases} \quad (3.22)$$

The momentum equation in Lagrangian form with a sharp interface is

$$\rho \frac{D\vec{u}}{Dt} = -\nabla p + \eta \nabla^2 \vec{u} + \rho \vec{g} + \left(\sigma \kappa \vec{n} + \nabla_S \sigma \right) \delta. \quad (3.23)$$

3.3.4 Stochastic terms

When the length scale of a problem is very small, continuum theory reaches a lower limit and thermal fluctuations in the average quantities are not negligible any more. For example, the width of a diffuse interface is typically only a few angstrom. We need to consider thermal fluctuations of the average quantities and formulate a consistent form that accounts for molecular degrees of freedom that are lost due to the continuum description (also called coarse grained level). As shown in Öttinger [Ött05] this may be done by considering stochastic contributions on the average quantities, like partial mass density, around a mean value with an amplitude that is directly related to the dissipative or irreversible dynamics of the system. A comprehensive discussion of thermal fluctuations in mass, momentum and energy is beyond the scope of this thesis. Discussions about consistent thermodynamics are found in [Esp03a; Ött05]. Here we only present the stochastic terms of the

component balance because we will use them to initialize our system.

A stochastic fluctuation of the partial mass density may be written as an amplitude A_w multiplied by an increment of a Wiener process $d\tilde{W}$

$$d\tilde{\rho}_i = A_w d\tilde{W}. \quad (3.24)$$

The increment of a Wiener process is a probability, e.g. a random number. As shown in [Esp03a; Ött05] the stochastic term is a source term. Roughly speaking Eq. 3.24 describes the stochastic appearance of a source of partial mass in the component balance. It is important to note that the amplitude is coupled to the irreversible part of the balance equation, e.g. the diffusive term of the component balance. Therefore the amplitude is [Don14]

$$A_w = \sqrt{\frac{2\tilde{M}_i \rho k_B T}{\frac{\partial \mu_i}{\partial \rho_i}}}. \quad (3.25)$$

k_B is the Boltzmann constant and \tilde{M}_i is the mobility of component i . Using Eqns. 3.24 and 3.25, the component balance (Eq. 3.14) is [Don14]

$$\frac{D\rho_i}{Dt} + \nabla \cdot \left(-\rho \frac{\tilde{M}_i}{RT} \nabla \mu_i \right) = d\tilde{\rho}_i \quad (3.26)$$

with

$$d\tilde{\rho}_i = \sqrt{\frac{2\tilde{M}_i \rho k_B T}{\frac{\partial \mu_i}{\partial \rho_i}}} d\tilde{W}. \quad (3.27)$$

We formulate the stochastic term explicitly later in the discrete form to ensure that the discrete equation is thermodynamically consistent [Esp03a].

3.4 Simplified model

In this section we first present the current state of models for polymer membrane formation in literature. Then we summarize the assumptions of our formulation of the balance equations. Herein, we highlight the differences of models in literature from the model used in this thesis. Finally we present the balance equations in

compact form. Since we use slightly different models in Chap. 5 and 6 we highlight the differences in this section as well.

3.4.1 Models for porous polymer membrane formation in literature

In literature, two classes of models exist to predict, or at least correlate, the morphology of polymer membranes. The first class represent 1-dimensional models based on the component balances of a polymer system. Hydrodynamic effects are neglected. The other class represents 2- or 3-dimensional models that include not only the component balance but also the momentum balance and therefore hydrodynamic effects like surface tension. We review models of both classes in the following.

1D models

The class of 1D models is pioneered by Cohen et al. [Coh79]. The model consists of a simple, effective diffusion equation (for example, Eq. 3.15) and the continuity equation for a ternary mixture of a binary polymer solution (polymer and solvent) and coagulation bath (non-solvent). Cohen et al. used Flory-Huggins thermodynamics to calculate the chemical potential of the polymer mixture in the bulk phases. Since then, models based on the work of Cohen et al. have been developed by Reuvers et al. [Reu87a], Tsay and McHugh [Tsa90], Cheng et al. [Che99] and Lee et al. [Lee06; Lee10]. All models consider ternary mixtures with thermodynamics of polymers, using the Flory-Huggins equation of state. The diffusion coefficients are calculated from the free volume theory. Input parameters of the model are thermodynamics, e.g. temperature and composition, and transport parameters like diffusion coefficients. An important development is reported by Lee et al. [Lee06], who considered density-induced convection and therefore extend the diffusion equation to a convection-diffusion equation. The models differ in the assumptions made, e.g. that the polymer does not dissolve in the coagulation bath in the model of Lee et al. [Lee10]. These models are used to calculate a so-called fictitious composition path in the ternary phase diagram during contact of polymer solution and coagulation bath. A fictitious composition path represents the change of composition at a specific point in the polymer solution during diffusive mass transport. With this information it is possible to identify the composition where the binodal and spinodal, respectively,

is reached and the period of time that it takes until phase separation may start. Both, the composition on the binodal and the time until phase separation starts, are correlated to final morphology. In most of the studied cases this correlation prove true. Nevertheless, since the models are limited to 1D they are unable to predict morphology from first principles.

These models are applied to different preparation processes like thermally-induced phase separation, dry-casting and wet-casting. The models predict the time between first contact of polymer solution and coagulation bath and the time when the binodal at a point in the polymer solution is reached very well. Phase separation didn't start with contact of polymer solution and coagulation bath because first small amounts of solvent need to diffuse out of the polymer solution and small amounts of non-solvent need to diffuse into the polymer solution. Note that the concentration of the binodal of the polymer rich phase indicates a ternary mixture (cf. Fig. 2.1). Therefore diffusive transport in a homogeneous polymer mixture is adequate to estimate the time until the binodal is reached.

As shown in a recent work by Foard and Wagner [Foa09] a 1D model, including the gradient energy term in the chemical potential, reproduces the distance between alternating structures, e.g. lamella-like structures as shown in Fig. 2.6a. In this model the Cahn-Hilliard equation (Eq. 3.16) is used. In simple cases, e.g. simple thermodynamics where the free energy is described by a fourth order polynomial, an analytic solution for the distance between alternating lamella as a function of the velocity of the phase separation front is possible. The phase separation front is the composition in the polymer solution where the binodal is reached for the first time. It moves into the polymer solution when solvent diffuses into the coagulation bath and its velocity may depend on the diffusive transport resistance in the homogeneous polymer solution and the coagulation bath.

2D/3D models

The first model to predict morphology from first principles was proposed by Akthakul et al. [Akt05]. They model immersion precipitation (wet-casting) using a continuum model, including gradient energy terms in the chemical potential to dynamically model phase separation. In their model, they used the Cahn-Hilliard equation (see Eq. 3.16) and the momentum balance. They model the coagulation bath explicitly by using a reservoir of non-solvent. They observed a compaction or shrinkage of

the membrane because the interface between the coagulation bath and the polymer solution is moving towards the polymer solution during phase separation because solvent diffuses into the coagulation bath.

At the same time Zhou and Powell [Zho06b] investigated a similar model. They observe similar results as Akthakul et al. In addition, they presented a morphology of a porous polymer membrane in 3D that is in qualitative agreement with the 2D simulations. Akthakul et al. and Zhou and Powell did not observe finger-like structures growing into the polymer solution and they did not observe clear asymmetric structures because they initially assumed an unstable polymer solution. Therefore they only modeled phase separation of the unstable polymer solution with a coagulation bath "as boundary condition". Conclusively they did not consider the transition from stable to unstable polymer solution when solvent diffuses into the coagulation bath. The same model was used by Mino et al. [Min15] to study thermal-induced phase separation.

Recently, Foard and Wagner [Foa12b] recognized that the morphology in immersion precipitation is similar to Liesegang patterns (see Subsec. 2.2.5). They linked this phenomena to the formation of pores in polymer membranes. Liesegang patterns are studied for several decades in physics, see Antal et al. [Ant99] or Hantz and Biro [Han06] and the references therein. An overview of the theory of phase-ordering kinetics is given in the review of Bray [Bra94]. The model proposed by Foard and Wagner is a 2D model based on the component balance (Cahn-Hilliard equation) and the continuity balance. They neglect hydrodynamic effects and stated that this should be investigated separately. They were able to predict sponge pores and finger pores with the same model depending on composition and the velocity of the phase separation front.

Differences of the present model to models from literature

The model used in this thesis is in parts similar to the model of Foard and Wagner [Foa12b] and Zhou and Powell [Zho06b]. We also use the Cahn-Hilliard equation. But in contrast to all models in literature, we include thermal fluctuations as stochastic contribution due to the small size of the system. In contrast to Foard and Wagner we consider the momentum balance. In contrast to Zhou and Powell we also include gradients of the surface tension in the momentum balance. Similar to Zhou and Powell we use Flory-Huggins equation of state but only for a model-fluid.

3.4.2 Assumptions

In this subsection we summarize the model assumptions in the present model. Note that we investigate the most simplified system that predicts morphology. The assumptions are:

- We consider an incompressible fluid.
- We assume an isotherm system. This implies that Soret effects due to the presence of a temperature gradient are neglected in the component and momentum balance and we don't consider the energy balance in our model.
- We do not model shrinkage of the polymer rich phase during phase separation.
- We do not model solidification but rather assume that the polymer rich phase is fixed after some time. We also neglect mechanical stress of the polymer rich phase.
- We assume that in the cases studied the diffusion coefficient or the mobility is constant. We argue that, only for simplicity of the discussion, the mobility in the component balance is equal to the diffusion coefficient $M_i = D_i$.
- We only consider thermal fluctuations in the component equation. We neglect thermal fluctuations in the momentum balance for simplicity.
- We study morphology in two dimensions. Therefore some results don't show

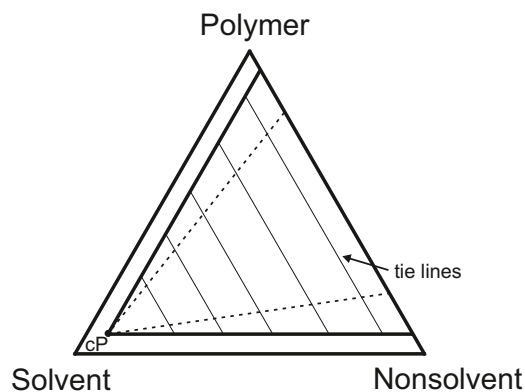


Figure 3.3: Schematic plot of a ternary phase diagram of polymer, solvent and nonsolvent with a large miscibility gap between polymer and non-solvent. The critical point is marked as cP in the left corner. The binodal (solid lines) is close to the binary mixtures. The dashed lines represent the spinodal.

all kind of possible structures. Nevertheless, the model may be extended to 3D in a straightforward way in future work.

- We assume that heterogeneous molecular configurations, e.g. orientation of a polymer molecule, is less important and that a balance of average quantities like partial mass and momentum density is valid on the mesoscale, ranging from nanometers to micrometers. This implies that nuclei originated at the molecular level arise as thermal fluctuations of the average quantity on the mesoscale.
- The free energy of a real polymer-solvent-non-solvent mixture is very complex. There are large gradients in the chemical potential [Koo98] especially at the interface between the polymer solution and the coagulation bath. Numerically it is very difficult to resolve these gradients in the diffuse interface because the diffuse interface is very thin. Therefore we restrict the present model to a Newtonian model-fluid mixture where all components, including the polymer, have equal molar mass with moderate spatial gradients in the chemical potential. In this case moderate spatial gradients in the chemical potential are justified by efficiency of numerical solution. This implies that the molar average and mass average velocities are identical and we only need to formulate the momentum balance for the average momentum of the multi-component system.
- We only use an equation of state similar to the Flory-Huggins equation of state for a binary model-fluid mixture. We assume that the chain length is unity and the interaction parameter $\chi_{12}=3$ for an unstable mixture and $\chi_{12}=1$ for a stable mixture.
- The miscibility gap in the real thermodynamics of PSf-NMP-water system is very large and the critical point is located at very low polymer and very high solvent concentration. The binodal is almost parallel to the binary polymer-solvent axis (cf. Fig. 3.2). Therefore we assume that the miscibility gap is large for the model-fluid (cf. Fig. 3.3). The location of the tie lines is parallel to the binary polymer/non-solvent axis. For completeness we present the balance equation for a ternary system and its discrete formulation in Appendix E.
- Since the energy parameter is directly connected to the length scale of the diffuse interface, we need to resolve this length scale in the simulations. Typical length

scales are in the range of a few angstrom to a few nanometers. Typical pore sizes are between nano- and micrometers. There is a large difference between the length scales and resolving it accurately increases the computational effort. A solution of this issue is motivated from a numerical technique called phase field. In this simulation technique an arbitrary energy function (the phase field) defines the phase distribution of a multi-component mixture. The basis for multi-phase phase field approaches is also a Cahn-Hilliard type of equation. The fourth-order differential equation is used to propagate the position of the interface. Therefore the (numerically) diffuse interface also needs to be resolved. In these models the interface is resolved within the numerical resolution for good numerical approximation of the diffuse interface. The gradient energy parameter κ' is scaled to correctly reproduce the surface tension. We use this technique here as well. Therefore we consider κ' as a numerical parameter that describes the dynamics of the interface. In the Appendix (D.1.3) we investigate the influence of κ' on the dynamics and the solution of the Cahn-Hilliard equation.

- If we directly use Eq. 3.19 in the simulations, we need to resolve the physical length scale of the interface accordingly as already mentioned in the former assumption. In our mesoscale model the interface is still thin compared to the typical length scale in the simulation. Resolving the interface is very inefficient. One solution is to increase the thickness of the interface in the simulation by adjusting κ' to reproduce the surface tension adequately. An alternative solution is to only consider a diffuse interface in the chemical potential of the component equation and use a sharp interface formulation for the capillary stress tensor in the momentum balance. The disadvantage of the latter solution is that the component balance (where we necessarily need at least a numerically diffuse interface) and momentum balance are decoupled. An advantage is that we can use established numerical models for the capillary stress tensor. We will use the sharp interface formulation and use established numerical methods in the momentum balance.

There are a few more assumptions but they are specific to the different cases studied in Chap. 5 and 6. We introduce them separately when needed.

3.4.3 Compact model equations

As mentioned earlier, there exist different theories in the literature on the formation of finger pores. Two prominent theories are based on the propagation of viscous fingers (Subsec. 2.2.4) and Liesegang patterns (Subsec. 2.2.5). In both theories gradients of the surface tension may appear. We use the following balance equations that represent the model for both cases.

Continuity equation:

$$\nabla \cdot \vec{u} = 0 \quad (3.28)$$

Component equation:

$$\frac{D\omega}{Dt} + \nabla \cdot \left(-\frac{\tilde{M}}{RT} \nabla \mu \right) = d\tilde{\omega} \quad (3.29)$$

with

$$d\tilde{\omega} = \frac{1}{\rho} \sqrt{\frac{2\tilde{M}\rho k_B T}{\frac{\partial \mu}{\partial \rho}}} d\tilde{W} \quad (3.30)$$

and

$$\mu = (\ln(\omega) - \ln(1 - \omega)) + (\chi_{12}(1 - 2\omega) - 1) - \kappa' \nabla^2 \omega. \quad (3.31)$$

We skip the index i here because we only consider binary mixtures.

Momentum balance:

$$\rho \frac{D\vec{u}}{Dt} = -\nabla p + \eta \nabla^2 \vec{u} + \rho \vec{g} + \left(\sigma \kappa \vec{\hat{n}} + \nabla_S \sigma \right) \delta. \quad (3.32)$$

Initial and boundary conditions are given in each study separately.

CHAPTER 4

Numerical method

In this chapter we introduce the numerical method to discretize the balance equations presented in Subsec. 3.4.3.

First, we review methods presented in literature to study the evolution of morphology with a focus on pore formation in polymer membranes. Then we introduce the Smoothed Particle Hydrodynamics (SPH) method. SPH is used in this thesis. We present the discrete balance equations, boundary conditions, approaches for numerical stability and the time integration scheme. Finally we summarize the discrete model equations.

4.1 Numerical approaches to study morphology evolution in literature

Akthakul et al. [Akt05] and Foard and Wagner [Foa12b] studied the formation of pores in polymer membranes. As introduced in Subsec. 3.4.1, they dynamically model phase separation using the Cahn-Hilliard equation. They used the Lattice Boltzmann method (LBM) to discretize the Cahn-Hilliard equation and studied pore formation in 2D. LBM is often used in the physics community for numerical flow simulations. It is based on the solution of the Boltzmann equation that is discretized using a finite grid. An advantage is its highly efficient parallelization due to the decoupled problems in each grid cell. A comprehensive review, especially for phase separating fluids, is found in [Che98].

Zhou and Powell [Zho06b] investigated membrane formation using the Cahn-Hilliard equation coupled to the momentum balance. They discretized the balance equations

using the finite volume method (FVM). The FVM is very popular in computational fluid dynamics in engineering applications. Herein, the computational domain is decomposed into finite volume elements for which a balance of a quantity (e.g. mass, momentum or energy) is formulated from the continuous equation. A comprehensive overview is found in [Fer96; Pat80].

Another numerical method was proposed very recently by Mino et al. [Min15] for thermally-induced phase separation. They discretize the Cahn-Hilliard equation using finite-volume method to model a phase-field. In a phase-field approach, typically used in multi-phase systems, each phase is represented by a unique value of an order parameter. For example, in a two-phase system, the order parameter is 1 and -1, respectively, and represents each bulk phase. Between the bulk phases a smooth transition of the order parameter, similar to the diffuse interface (see Sec. 3.2) exists. In contrast to FVM, in addition to the balance equations of mass, momentum and energy, a Cahn-Hilliard equation for the order parameter is solved to propagate the phase field. Therefore an additional equation for the motion of the interface between the phases is solved. A comprehensive overview of phase field methods is found in [Pro10]

The aforementioned numerical methods are similar in the fact that the physical balance equations are discretized directly. Contrary, an alternative method to study phase separation is the Dissipative Particle Dynamics (DPD) method, as introduced in the context of polymer morphology evolution in porous membranes by Wang et al. [Wan08]. DPD is a mesoscopic simulation method where molecules are coarse-grained to so-called particles that interact by using a soft potential. In DPD the interaction of the coarse-grained molecule clusters are expressed by a conservative, dissipative and random force between the clusters. They discretize the polymer, solvent and non-solvent in the mixture using 3 different types of particles with different interaction potential. It is also possible to directly include polymer behavior, e.g. the chain length of a polymer, by connecting single molecule clusters to a polymer chain. This is done by strongly connecting multiple particles to represent a polymer [He11; Tan12; Tan15; Tan13] using an additional interaction force so that the particles stick together.

In the present thesis we use the SPH method to discretize the balance equations. We introduce this method in detail in the next section. In the context of the SPH method, polymer membrane formation was not investigated yet. As reviewed

in the previous sections, the main mechanism of structure formation in polymer membranes is phase separation. In literature, two models for phase separating fluid mixtures are presented in the context of SPH. Okuzono [Oku97] first studied phase separation for a binary polymer mixture using a two-fluid model in SPH where different types of particles represent polymer and solvent. He didn't directly start the derivation from the Cahn-Hilliard equation. Instead, he derived the momentum balance equation for both fluids and included the interaction of both fluids as a source in the balance equations. Okuzono distributed different kinds of particles (e.g. particles of type A and B) and described the separation of the particles by viscous and surface tension forces. For the chemical potential, Okuzono used a simple fourth-order polynomial for the free energy of the system with an order parameter based on the type of particles (e.g. particles of type A represent -1 and particles of type B represent 1). The model's major disadvantage is that it only describes phase separation if a phase distribution is known a priori and a numerical diffuse interface is constructed (e.g. by smoothing of the order parameter).

Another approach is introduced by Thieulot and Espanol [Thi05] based on the Smoothed Dissipative Particle Dynamics (SDPD) method which is a consistent extension of SPH for mesoscale flow. We highlight the differences to SPH in Sec. 4.8. The model is based on the complete multi-component, multi-phase component, momentum and energy balance and therefore represents a model derived from first principles. They derived the chemical potential directly from the entropy of the fluid using a van-der-Waals equation of state. This model is similar to the model used in this work but differs in the main aspect that we include thermal fluctuations of the mass and neglect the energy balance.

4.2 Smoothed Particle Hydrodynamics method

Lagrangian discretization methods have advantages in dynamics of complex multi-phase systems because the interface position is tracked implicitly and mass is conserved. One example for a particle-based Lagrangian method is the SPH method. Introduced in 1977 independently by Monaghan and Gingold [Gin77] and Lucy [Luc77] for astrophysical problems, the method gained popularity in the 1990s for engineering problems in fluid dynamics [Cum99; Mon94; Mor97] and in the 2000s for multi-phase problems [Ada10b; Col03; Gre09; Hu09; Hu06; Le 08; Mon05; Sha03],

especially when free surfaces are present. The basics of the SPH method are well documented in review articles [Liu10; Mon92; Mon05; Mon12; Roo09] and two textbooks [Liu03; Vio12]. A complete list of current and past applications with focus on industrial applications is found in [Sha16]. We introduce the SPH method and review formulations for spatial derivatives in the following. We only highlight the major basics and the discrete operators for the partial differential equations. A derivation may be found in the early publications and the reviews of Monaghan [Gin77; Mon92].

The basic idea in SPH is to calculate a quantity $A(\vec{x})$ at position \vec{x} by integrating $A(\vec{x}')$, multiplied with a Dirac-Delta function, over the hole volume V

$$A(\vec{x}) = \int_V A(\vec{x}') \delta(|\vec{x} - \vec{x}'|) d\vec{x}'. \quad (4.1)$$

\vec{x}' is the position of any point in the volume V . The Dirac-Delta function is defined to be unity for $\vec{x}' = \vec{x}$ and zero otherwise. For practical reasons [Vio12], the Dirac-Delta function is approximated by a weighting function or kernel function $W(h, |\vec{x} - \vec{x}'|)$. h is the so-called smoothing length that defines the support volume with, in our case, a constant value of $h = 2.05L_0$, and L_0 as the initial particle spacing. In all simulations we use an initial regular Cartesian order of the particles. We replace the Dirac-Delta function by the kernel function in Eq. 4.1 and get

$$A(\vec{x}) = \int_V A(\vec{x}') W(h, |\vec{x} - \vec{x}'|) d\vec{x}'. \quad (4.2)$$

This is called kernel approximation where the kernel function is any function that fulfills the following conditions [Liu10]:

1. Unity condition: The kernel function should be normalized so that it ensures the 0th order consistency

$$\int_V W(h, |\vec{x} - \vec{x}'|) d\vec{x}' = 1. \quad (4.3)$$

2. Delta function property: The limit of the kernel function for $h \rightarrow 0$ should be

the Dirac-Delta function

$$\lim_{h \rightarrow 0} W(h, |\vec{x} - \vec{x}'|) = \delta(|\vec{x} - \vec{x}'|). \quad (4.4)$$

3. Compact condition: The support of the kernel function should be finite. Therefore the kernel function is zero elsewhere

$$W(h, |\vec{x} - \vec{x}'|) = 0 \quad \text{for } |\vec{x} - \vec{x}'| > r_c. \quad (4.5)$$

Here $r_c = \kappa_h h$ specifies the support domain of the particles [Liu10] with the constant κ_h .

4. Positivity condition: The kernel function should be non-negative inside the support domain to be physically meaningful [Liu10]. This condition is mathematically not necessary for convergence

$$W(h, |\vec{x} - \vec{x}'|) \geq 0 \quad \text{for any } |\vec{x} - \vec{x}'|. \quad (4.6)$$

5. Decay condition: The kernel function value should be monotonically decreasing so that particles with a larger relative distance to each other influence themselves less than nearer particles.
6. Symmetric property condition: The kernel function should be symmetric so that the value of the kernel function only depends on the distance between two particles and not on the position.
7. Smoothness condition: The kernel function should be smooth enough to provide a good approximation. That is important especially for disordered particle configurations.

In addition, the kernel function should be of high enough order so that it can be differentiated at least one time for the first derivative.

Kernel functions usually used in literature are B-spline functions of different order [Mon85; Vio12] or Wendland kernels [Wen95]. In this work we use a Wendland C2

kernel function of order 4 with $r_c = 2h$.

$$W(h, |\vec{x} - \vec{x}'|) = \frac{f_w}{h^d} \begin{cases} (1 - \frac{q}{2})^4 (1 + 2q) & \text{for } 0 \leq q \leq 2 \\ 0 & \text{for } 2 < q \end{cases} \quad (4.7)$$

d is the dimension and f_w is a normalization constant with $f_w = \frac{3}{4}, \frac{7}{4\pi}, \frac{21}{16\pi}$ for $d = 1, d = 2,$ and $d = 3$. $q = \frac{|\vec{x} - \vec{x}'|}{h}$ is the non-dimensional smoothing length [Vio12]. The first derivative of the kernel function is

$$\frac{\partial W(h, |\vec{x} - \vec{x}'|)}{\partial x} = \frac{f_w}{h^{d+1}} \begin{cases} -5q (1 - \frac{q}{2})^3 & \text{for } 0 \leq q \leq 2 \\ 0 & \text{for } 2 < q \end{cases} \quad (4.8)$$

Next, we approximate the integral in Eq. 4.2 by a summation over discrete interpolation points in the vicinity of \vec{x}

$$A(\vec{x})_a = \sum_b \frac{m_b}{\rho_b} A(\vec{x}_b) W(h, |\vec{x}_a - \vec{x}_b|) \quad (4.9)$$

This is called the particle approximation. All of these interpolation points are called particles. The indexes a and b represent the particle of interest and the particles in the vicinity of a (see Fig. 4.1). b particles are called neighbor particles. m_b and ρ_b are the mass and density of particle b . In the following $r_{ab} = |\vec{x}_a - \vec{x}_b|$ is the distance between particle a and b . In the following we abbreviate the kernel function $W(h, |\vec{x}_a - \vec{x}_b|) = W_{ab}$.

An example, using Eq. 4.9 with $A = \rho$, is the calculation of the density of particle a [Mon92]

$$\rho_a = \sum_b m_b W_{ab}. \quad (4.10)$$

Note that particle a should also be considered in the vicinity because $W_{aa} \neq 0$. Due to the particle approximation, the 0th moment (unity condition of the kernel function) is not guaranteed [Liu10]. To guarantee it we may use a renormalization function, the shepard kernel, to ensure the unity condition [Bon99; Gre09]. This is very important if the support domain is truncated e.g. at free surfaces or when surface tension has to be calculated as we will see later. For bulk flow the error is

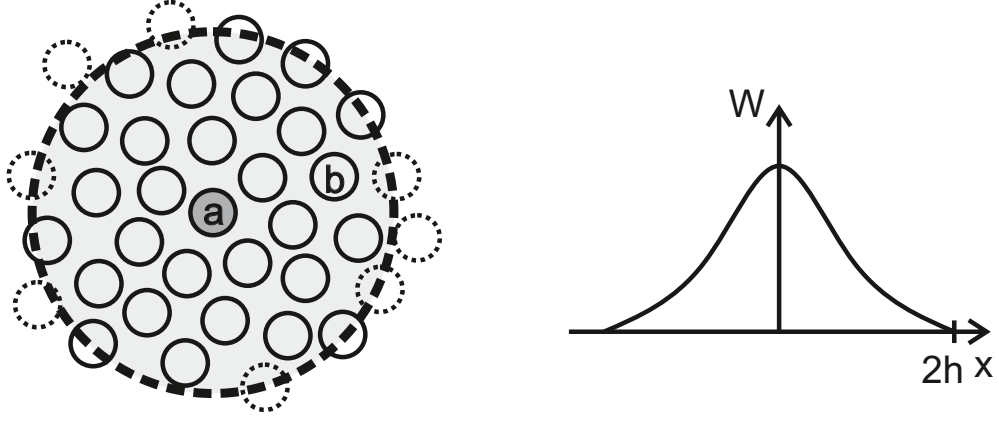


Figure 4.1: (Left) Scheme of discrete particle distribution around a particle of interest, particle a , and its particles in the vicinity b within the support of the kernel function. Dashed particles are outside the support domain. (Right) Schematic representation of a kernel function W with a support domain of $2h$.

normally in the range of a few percent. We discuss this point in Sec. 4.5.1.

One strong advantage of the SPH method is that the gradient of a quantity $A(\vec{x})$ can be derived from the gradient of the kernel function [Gin77]

$$\nabla A(\vec{x})_a = \sum_b \frac{m_b}{\rho_b} A(\vec{x}_b) \nabla W(h, r_{ab}) \quad (4.11)$$

where the gradient of the kernel function

$$\nabla W(h, r_{ab}) = \frac{\vec{r}_{ab}}{r_{ab}} \frac{\partial W}{\partial x} \quad (4.12)$$

is analytically known from Eq. 4.8. However Eq. 4.11 is never used in practical applications because conservation of linear momentum is not guaranteed. There are alternative formulations of first order derivatives in SPH. One can formulate the first derivative using [Mon92]

$$\nabla A(\vec{x})_a = \sum_b \frac{m_b}{\rho_b} (A_b - A_a) \nabla W(h, r_{ab}) \quad (4.13)$$

or [Col03]

$$\left(\frac{1}{\rho}\nabla A(\vec{x})\right)_a = \sum_b m_b \frac{A_b + A_a}{\rho_a \cdot \rho_b} \nabla W(h, r_{ab}). \quad (4.14)$$

Eq. 4.13 guarantees that the gradient of a constant field is exactly zero even if numerical errors are present. Linear momentum is only conserved if the 1th moment of the kernel function is exactly zero [Liu10]. Eq. 4.14 conserves linear momentum exactly as long as the kernel function is symmetric but the gradient of a constant field is only zero if the 1th moment of the kernel function is exactly zero. In literature Eq. 4.13 is often used for the divergence of a velocity field, where the gradient of a constant field is very important, and Eq. 4.14 is often used for the pressure gradient because linear momentum is more important in this case.

In principle we may calculate the second derivative of a quantity as the derivative of Eq. 4.11. However, for particle disorder it tends to diverge [Mon05]. Therefore Brookshaw [Bro85] introduced a hybrid formulation for the second derivative using the first order derivative of the kernel function in combination with a finite difference approximation

$$\left(\nabla \cdot \alpha \nabla \vec{A}(\vec{x})\right)_a = \sum_b \frac{m_b}{\rho_b} (\alpha_a + \alpha_b) \frac{\vec{r}_{ab}}{r_{ab}^2} \nabla_a W_{ab} \cdot (\vec{A}_a - \vec{A}_b). \quad (4.15)$$

α is a variable that does not depend explicit on position but e.g. may depend on other properties of a fluid. \vec{r}_{ab} is the distance vector between particle a and b pointing from particle a to b . r_{ab} is the length of the distance vector. We abbreviate the gradient with respect to particle a as $\nabla_a W_{ab} = \nabla_a W(h, r_{ab})$. In contrast to other formulations of the second derivative [Fat11] this formulation proved to be less sensitive to particle disorder.

4.3 Discrete balance equations

In this section we present the discrete balance equations using the operators from Sec. 4.2. We close this section reviewing the projection method to calculate the pressure.

4.3.1 Continuity equation

In SPH exist two different ways [Mon92] to formulate the discrete continuity equation. One way is to directly use the discrete continuity equation [Mor96; Sze12] using Eq. 4.13

$$\frac{D\rho_a}{Dt} = \rho_a \sum_b \frac{m_b}{\rho_b} (\vec{u}_b - \vec{u}_a) \cdot \nabla_a W_{ab}. \quad (4.16)$$

A disadvantage of this equation is the error of conservation due to integration errors. Another formulation of the discrete continuity equation is [Hu06]

$$\rho_a = m_a \sum_b W_{ab} \quad (4.17)$$

where the density is directly calculated using the mass and volume of particle a . Note that the summation of the kernel function represents the reciprocal volume $1/V_a$. Advantages of this formulation is its applicability to multi-phase systems with density differences between the phases and the conservation property. We use Eq. 4.17 throughout this thesis.

4.3.2 Component balance

We formulate the discrete component balance including the gradient energy term (Eq. 3.16) in SPH. It is a fourth-order partial differential equation. There are different possibilities for the discrete form of a fourth-order partial differential equation. One way, if the kernel function is of high enough order (at least 5th order polynom), is to use a fourth derivative of the kernel function. Due to the sensitivity of the higher-order derivatives of the kernel function to particle disorder it is not possible to perform stable simulations using the fourth-order derivative of the kernel function. Another way is to use a biharmonic formulation analog to Watkins et al. [Wat96] who published a similar idea for the second-order derivative. This simplification is valid as long as the mobility only depends on local information e.g. local composition and not on spatial derivatives. The biharmonic formulation of a fourth-order operator for a quantity $A(\vec{x})$ is

$$\nabla^4 A = \nabla^2 (\nabla^2 A) = \nabla^2 (A''). \quad (4.18)$$

We split up the fourth-order derivative into two consecutive parts of second-order and use Eq. 4.15 for the inner part A''_a of particle a

$$A''_a = \alpha \nabla^2 A_a = (\nabla \cdot \alpha \nabla A)_a = \sum_b \frac{m_b}{\rho_b} (\alpha_a + \alpha_b) \frac{\vec{r}_{ab}}{r_{ab}^2} \nabla_a W_{ab} \cdot (A_a - A_b) \quad (4.19)$$

with the parameter α . The outer part of Eq. 4.18 is

$$\nabla^4 A_a = (\nabla \cdot \beta \nabla A'')_a = \sum_b \frac{m_b}{\rho_b} (\beta_a + \beta_b) \frac{\vec{r}_{ab}}{r_{ab}^2} \nabla_a W_{ab} \cdot (A''_a - A''_b) \quad (4.20)$$

with the parameter β . It becomes apparent that this formulation is robust and accurate due to particle disorder similar to the second-order derivative [Fat11]. Therefore we use it for the Cahn-Hilliard equation. The error resulting from the discretization is in the same magnitude as for the second-order derivative [Hir14]. We find the discrete component balance (Eq. 3.26) with $\alpha = \kappa'$, $\beta = M$, $A = \omega$ and $A'' = \mu$ for a binary mixture (with mass fraction $\omega_i = \omega$)

$$\frac{D\omega_a}{Dt} = \sum_b \frac{m_b}{\rho_b} (M_a + M_b) \frac{\vec{r}_{ab}}{r_{ab}^2} \nabla_a W_{ab} \cdot (\mu_a - \mu_b) \quad (4.21)$$

with

$$\mu_a = \mu_a^0 - \kappa'_a \nabla^2 \omega_a \quad (4.22)$$

and

$$\kappa' \nabla^2 \omega_a = \sum_b \frac{m_b}{\rho_b} (\kappa'_a + \kappa'_b) \frac{\vec{r}_{ab}}{r_{ab}^2} \nabla_a W_{ab} \cdot (\omega_a - \omega_b). \quad (4.23)$$

In these equations we omit the index of the components because only one component is considered in a binary mixture and the second component follows from the closing condition

$$\omega_2 = 1 - \omega_1. \quad (4.24)$$

Note that the chemical potential μ_a is dimensionless ($\mu/(RT)$) and also is κ'_a ($\kappa'/(RT)$), see Eq. 3.7). Eqs. 4.21, 4.22, 4.23 together with Eq. 3.7 are the discrete component

balance.

4.3.3 Momentum balance

In the momentum balance (Eq. 3.23) we need first-order derivatives for the pressure term, for the color to calculate the normals, for the normals to calculate the curvature and for the surface tension to calculate the Marangoni force. In addition we need a second-order derivative for the divergence of the viscous stress tensor.

We use the positive formulation of the gradient (Eq. 4.14) for the pressure force

$$\left(\frac{\nabla p}{\rho}\right)_a = \sum_b \frac{m_b}{\rho_a \cdot \rho_b} (p_b + p_a) \nabla_a W_{ab} \quad (4.25)$$

with the pressure p_a and p_b of particle a and b . It is common in literature to use the positive formulation of the gradient especially for the pressure force to ensure linear momentum conservation. For a constant pressure field the gradient of the pressure is only zero for a constant pressure $p = 0$. Since we have only pressure gradients in the Navier-Stokes equations we define the reference pressure $p = 0$.

The discrete formulation of the viscous term using the second-order derivative (Eq. 4.15) is

$$\left(\frac{\eta}{\rho} \nabla^2 \vec{u}\right)_a = \sum_b \frac{m_b}{\rho_a \rho_b} (\eta_a + \eta_b) \frac{\vec{r}_{ab}}{r_{ab}^2} \nabla_a W_{ab} \cdot (\vec{u}_a - \vec{u}_b) \quad (4.26)$$

with the distance vector \vec{r}_{ab} between particle a and b pointing from particle a to b and its magnitude r_{ab} .

The gravitational force is straight forward since it only depends on particle a . The last two terms in Eq. 3.23 account for interface forces. To formulate surface tension at a sharp interface, Brackbill et al. [Bra92] and later, in the context of SPH, Morris [Mor00] introduced the so-called Continuum Surface Force (CSF) approach. In the CSF approach the surface force, that is a force per area, is reformulated as a force per volume. Therefore, the surface tension is numerically smoothed out around the sharp interface. We need the normal vector \vec{n} at the interface between phases to calculate the magnitude and direction of the interface forces. The normal vector at an interface is calculated from a color field where a unique color is assigned to particles of every phase. We use the negative formulation of the gradient (Eq. 4.13)

to calculate the gradient of the color field because it is important that the gradient vanishes if the color is constant. Otherwise we get surface tension due to numerical artifacts in the bulk.

$$\vec{n}_a = \left(\frac{\nabla C}{[C]} \right)_a = \sum_b \frac{m_b}{\rho_b} \frac{(C_b - C_a)}{[C]} \nabla_a W_{ab} \quad (4.27)$$

with the color C and its jump across the interface $[C]$. Whether the color is a smooth or a sharp function across the interface, the jump of the color function represents the absolute difference between the maximum and minimum of the color function. The normalized normal vector is

$$\vec{\hat{n}} = \frac{\vec{n}}{|\vec{n}|} \quad (4.28)$$

with the magnitude of the normal vector $|\vec{n}|$. The curvature is

$$\kappa_a = - \left(\nabla \cdot \vec{\hat{n}} \right)_a = - \sum_b \frac{m_b}{\rho_b} \left(\vec{\hat{n}}_b - \vec{\hat{n}}_a \right) \nabla_a W_{ab}. \quad (4.29)$$

We again use the negative formulation because it is important that the curvature is zero for equal normal vectors. Note that we truncate the field of normals to avoid numerical artifacts and only consider normals with magnitude larger than ε/h with $\varepsilon = 0.01$.

The last term in Eq. 3.23 accounts for gradients of the surface tension tangential to the interface. We use a projection of the gradient of the surface tension into the tangential direction of the interface

$$(\nabla_S \sigma)_a = \left(\nabla \sigma - \left(\nabla \sigma \cdot \vec{\hat{n}} \right) \vec{\hat{n}} \right)_a \quad (4.30)$$

with the gradient of the surface tension coefficient σ

$$(\nabla \sigma)_a = \sum_b \frac{m_b}{\rho_b} (\sigma_b - \sigma_a) \nabla_a W_{ab}. \quad (4.31)$$

The delta function in Eq. 3.23 is unity at the interface. In the discrete formulation we smooth out the delta function

$$\delta_a = |\vec{n}_a|. \quad (4.32)$$

This leads to a distribution of the surface force in a volume that in the limit is equal to that of a delta function.

Finally the discrete momentum balance in SPH used in this thesis is

$$\begin{aligned} \frac{D\vec{u}_a}{Dt} = & - \sum_b \frac{m_b}{\rho_a \rho_b} (p_b + p_a) \nabla W_{ab} + \sum_b \frac{m_b}{\rho_a \rho_b} (\eta_a + \eta_b) \frac{\vec{r}_{ab}}{r_{ab}^2} \nabla_a W_{ab} \cdot (\vec{u}_a - \vec{u}_b) \\ & + \vec{g}_a + \frac{|\vec{n}_a|}{\rho_a} \left(\sigma_a \kappa_a \vec{n}_a + (\nabla_S \sigma)_a \right). \end{aligned} \quad (4.33)$$

4.3.4 Stochastic terms

In Eq. 3.27 we postulated the stochastic term in the component balance as a linear relationship between the amplitude and the increment of a Wiener process. As shown by Espanol et al. [Esp03a] the amplitude of the stochastic term is directly connected to the irreversible part of the balance equations. A way to consistently formulate the stochastic term is to use the "noise route to dissipation". It means that we postulate a form of the stochastic term, e.g. the amplitude, and then check if the postulated form fits into a thermodynamic consistent framework. Such a framework is the so-called GENERIC formalism (General Equation for Non-Equilibrium Reversible-Irreversible Coupling) proposed by Grmela and Öttinger [Grm97b]. It combines all known laws, e.g. conservation of a quantity, and is expressed in one general equation for the state of a system. For the amplitude of the component, a consistent form was proposed by Thieulot et al. [Thi05]. The amplitude $A_w (M_i)_a$ of the stochastic term of particle a for component i of the mixture is

$$A_w (M_i)_a = \frac{1}{m_a} \sum_b \sqrt{-2k_B T \frac{m_a m_b}{\rho_b} (M_a + M_b) \frac{1}{r_{ab}} \frac{\partial W_{ab}}{\partial r_{ab}}}. \quad (4.34)$$

k_B is the Boltzmann constant. The increment of the Wiener process is

$$d\tilde{W}_{ab} = J_{ab} \sqrt{dt} \quad (4.35)$$

with a Gaussian random number J_{ab} for each particle pair $a - b$ and the time step dt . The discrete stochastic term of the component equation (Eq. 3.15) in terms of the mass fraction ω_a of particle a is

$$d\tilde{\omega}_a = \frac{1}{m_a} \sum_b \sqrt{-2k_B T \frac{m_a m_b}{\rho_b} (M_a + M_b) \frac{1}{r_{ab}} \frac{\partial W_{ab}}{\partial r_{ab}}} J_{ab} \sqrt{dt}. \quad (4.36)$$

4.3.5 Estimation of pressure

The pressure in the momentum balance is still unknown. For incompressible fluids there are two ways to calculate the pressure. One way is to use an equation of state for a so-called weakly compressible fluid and is known as weakly-compressible SPH (WCSPH). It is a stiff equation that relates a small density variation to a pressure variation. One example is the Tait equation [Tai88]. This equation is commonly used in SPH to simulate the pressure of water [Col03; Mon92].

An alternative way to determine the pressure for a truly incompressible fluid is to use a projection method. We can apply the Helmholtz-Hodge decomposition [Hel58] on the momentum balance. The momentum balance is divided into a curl-free and divergence-free part. In a predictor step we first calculate an intermediate solution of velocity and density using the curl-free part. The curl-free part of the momentum balance (Eq. 4.33) consists of all terms except the pressure term. In a second step we solve a Pressure Poisson Equation to calculate the pressure and then correct the intermediate velocity using the pressure term to get the final velocity of the time step. In SPH this projection method was introduced by Cummins and Rudman [Cum99] and is usually called incompressible SPH (ISPH). The details of the projection method are discussed in literature [Gre09; Hu07; Sha03; Sze12] and we only review the discrete equations used in this thesis.

The curl-free part of the momentum balance is

$$\vec{a}_{a,*} = \sum_b \frac{m_b}{\rho_a \rho_b} (\eta_a + \eta_b) \frac{\vec{r}_{ab}}{r_{ab}^2} \nabla_a W_{ab} \cdot (\vec{u}_a - \vec{u}_b) + \vec{g}_a + \frac{|\vec{n}_a|}{\rho_a} \left(\sigma_a \kappa_a \vec{n}_a + (\nabla_S \sigma)_a \right). \quad (4.37)$$

We calculate the intermediate velocity using an explicit Euler scheme

$$\vec{u}_{a,*} = \vec{u}_a^t + \vec{a}_{a,*} \Delta t. \quad (4.38)$$

Then we determine the new particle position

$$\vec{x}_{a,*} = \vec{x}_a^t + \vec{u}_{a,*} \Delta t \quad (4.39)$$

also using an explicit Euler step and the time step Δt . The intermediate particle position is only necessary because we calculate the intermediate density using Eq. 4.17 instead of the continuity equation (Eq. 4.16). The subscript $*$ indicates the intermediate step. When the intermediate density is calculated we put the particles back to the old particle position \vec{x}_a^t and calculate the pressure using the Pressure Poisson Equation

$$\nabla \cdot \left(\frac{\nabla p}{\rho_*} \right) = \frac{\nabla \cdot \vec{u}_*}{\Delta t}. \quad (4.40)$$

We use the divergence of the velocity as a condition for incompressibility. The discrete Laplace of the pressure using Eq. 4.15 is (for $\alpha = 1$)

$$\nabla \cdot \left(\frac{\nabla p}{\rho_{a,*}} \right)_a = \sum_b 2 \frac{m_b}{\rho_b \rho_a} \cdot (p_a - p_b) \frac{\vec{r}_{ab}}{r_{ab}^2} \nabla_a W_{ab} \quad (4.41)$$

and the right hand side is

$$\frac{\nabla \cdot \vec{u}_{a,*}}{\Delta t} = \frac{1}{\Delta t} \sum_b \frac{m_b}{\rho_b} (\vec{u}_{b,*} - \vec{u}_{a,*}) \nabla_a W_{ab}. \quad (4.42)$$

The Pressure Poisson Equation requires the solution of a linear equation system. We use a stabilized version of the biConjugate Gradient (biCGStab) method from the PETSc library [Bal16] with a boomerAMG preconditioner from the HYPRE library [Fal16].

Then, with the acceleration using the pressure term

$$\vec{a}_{a,**} = - \sum_b \frac{m_b}{\rho_a \cdot \rho_b} (p_b + p_a) \nabla_a W_{ab}, \quad (4.43)$$

we determine the final velocity with an Euler step

$$\vec{u}_a^{t+1} = \vec{u}_{a,*} + \vec{a}_{a,**} \Delta t. \quad (4.44)$$

The final position of particle a is

$$\vec{x}_a^{t+1} = \vec{x}_a^t + \frac{\vec{u}_a^t + \vec{u}_a^{t+1}}{2} \Delta t. \quad (4.45)$$

Here a semi-implicit step with the velocities at time t and $t + 1$ is used. More details on the projection method in SPH is found in Keller [Kel15].

4.4 Boundary conditions

In most applications in engineering, the computational domain of interest is bounded. Therefore suitable boundary conditions should be applied. We will present the three kinds of boundary conditions used in this thesis in the following. These are periodic boundary conditions, solid wall boundary conditions and open boundary conditions.

4.4.1 Periodic boundary conditions

The most simple boundary conditions are the periodic boundary conditions. It means that all information that leaves the domain at a periodic boundary is continued at another boundary, normally on the other side of the domain. An example is shown in Fig. 4.2. Periodic boundary conditions are often used in molecular simulations if a portion of a fluid in a bulk is modeled. Periodic boundary conditions are typically used for astrophysical systems. In engineering problems periodic boundary conditions are used if a domain is a representative sample of a larger domain. This is the case if freely homogeneous nucleation in a fluid mixture is considered. Periodic

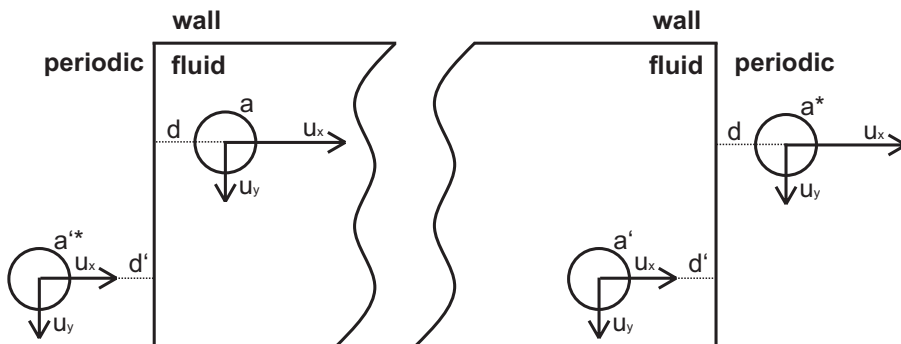


Figure 4.2: Scheme of periodic boundary conditions on the left and right side of the domain. Particles leaving the domain on the right side enter the domain on the left side and the other way around.

boundary conditions are also important to compare academic validation examples with analytic solutions of the problem where no boundary effects are considered. Last but not least, in SPH periodic boundary conditions were used for a long time to simulate tube or channel flow because there were no discrete formulations for open boundary conditions available in the 90s.

Technically periodic boundary conditions are applied by copying fluid information near one boundary to the corresponding boundary. This is shown in Fig. 4.2. Every particle near a periodic boundary has a corresponding particle, indicated with an asterisk * in Fig. 4.2, on the other side of the domain. The information of the corresponding particle is updated in every step when the information of the root particle changes. This can be very expensive if multiple consecutive gradients are calculated and the information of the corresponding particle needs to be updated every time as it is the case for surface forces.

4.4.2 Solid wall boundary conditions

For bounded domains we classify boundary conditions into penetrable and impenetrable wall boundary conditions. We call the first ones open boundary conditions (presented in the next section). Impenetrable boundary conditions are often referred to as solid wall boundary conditions.

Due to the integral character of SPH the wall partially needs to be discretized up to a certain distance from the fluid domain. In SPH there exist different approaches to model solid wall boundary conditions. In the last 30 years a few approaches became widely accepted. At the beginning, solid walls are modeled by repulsive forces [Mon92] that are artificially tuned to represent impenetrable walls. Nowadays this approach is very unpopular because it leads to nonphysical results.

One very popular approach to model solid wall boundary conditions was introduced by Morris in 1997 [Mor97] (We review this approach for completeness but will not use it in the present model). Morris used spatially fixed and regularly ordered solid wall particles to discretize the wall. This approach is sketched in Fig. 4.3. We get the information of a wall particle, e.g. velocity, from a projection of the information of the interacting fluid particle considering the boundary condition. Dirichlet and Neumann boundary conditions are applied by considering a fixed value or a fixed gradient at the boundary. In this way a no-slip boundary condition for the velocity is applied by projecting the wall particle with reversed normal and tangential

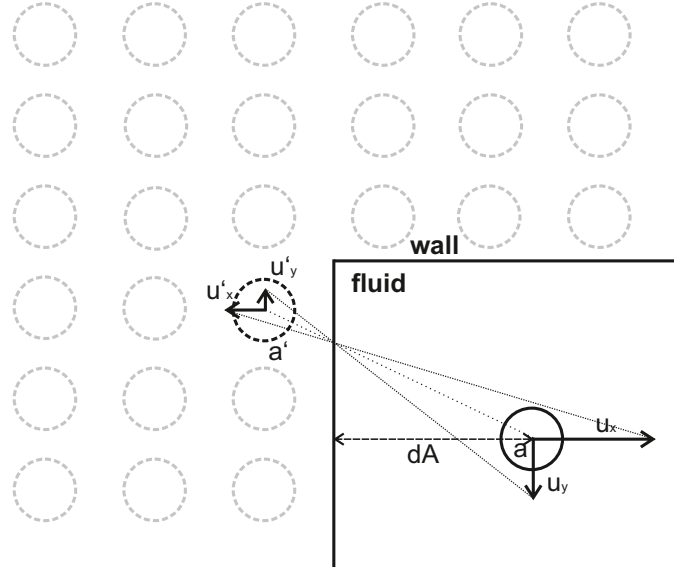


Figure 4.3: Scheme of Morris boundary conditions. The dotted particles are regularly ordered wall particles, e.g. particle a' . dA is the distance between particle a and the wall boundary. The properties of a wall particle a' is projected from the interacting fluid particle considering the boundary condition of each property (here no-slip boundary condition for velocity, e.g. for the tangential and normal velocity at the wall $\vec{u}^t = 0$ and $\vec{u}^n = 0$).

velocity. For a slip boundary condition only the normal component of the velocity is inverted.

For the projection we need the distance from the fluid particle to the imaginary boundary that is $L_0/2$ away from the nearest wall particle. The distance from a particle to the boundary is approximated by SPH interpolation considering only the wall particles next to the boundary

$$\vec{dA} = \left(\frac{\sum_j^{Nb \in \partial} \vec{x}_j W_{ij}}{\sum_j^{Nb \in \partial} W_{ij}} - \vec{x}_i \right) - \frac{L_0}{2} \hat{n}. \quad (4.46)$$

Here \vec{dA} and \hat{n} are the distance vector and the unit normal vector to the wall. $Nb \in \partial$ indicates a summation over all wall neighbor particles.

This approach is normally used for irregular solid wall boundary conditions inside a fluid domain. In the present work we do not have interior solid walls and therefore do not use the approach of Morris.

Another approach for solid wall boundary conditions was introduced by Cummins and Rudman [Cum99]. Instead of using spatially fixed solid particles and project their properties from fluid particles we mirror the fluid particles across the boundary in every time step or interaction between a fluid particle. In this way an image of the fluid particles represent the wall particles. This is sketched in Fig. 4.4.

The properties of the wall particles are manipulated to incorporate Dirichlet and Neumann boundary conditions. The boundary condition for the properties $\Psi \in [\vec{u}, p, T, \omega_i, \mu_i]$ at the wall is considered in the property of an image particle. The property of an image particle is

$$\vec{\Psi}'_a = 2\vec{\Psi}_w - \delta_w \vec{\Psi}_a \quad (4.47)$$

with the value of the wall $\vec{\Psi}_w$ and the sign

$$\delta_w = \begin{cases} +1 & \text{for Dirichlet boundary conditions} \\ -1 & \text{for Neumann boundary conditions with } \vec{\Psi}_w = 0 \end{cases} \quad (4.48)$$

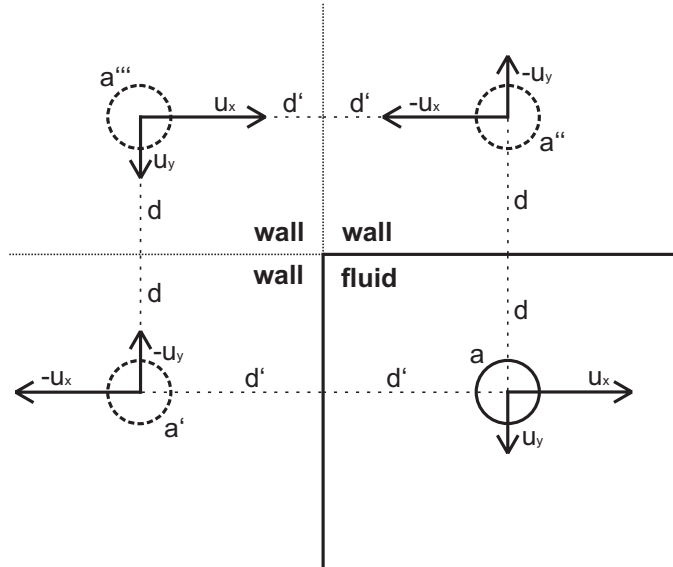


Figure 4.4: Scheme of mirror boundary conditions. The fluid particles are mirrored across the boundary and the images represent the wall particles (dotted particles). Their properties are manipulated to incorporate Dirichlet and Neumann boundary conditions. Here no-slip boundary conditions of an impenetrable wall is shown.

More details can be found in [Hir16a; Sze12]. This technique works well on straight walls but leads to errors on curved boundaries. In the current model for polymer membranes we only need straight walls.

In addition to the approaches presented here, other models exist in the literature, for example the boundary tangent method introduced by Yildiz et al. [Yil09] or the unified semi-analytical boundary conditions introduced by Ferrand et al. [Fer13]. A more detailed overview of boundary conditions is found in [Kho16; Mon05; Sze12] and the reference therein. In this thesis we only use wall boundary conditions from Cummins and Rudman (mirror particles) at straight walls.

4.4.3 Open boundary conditions

Open boundary conditions represent penetrable boundary conditions. They get important if the fluid shrinks or an external pressure gradient is applied to the system and particles enter and leave the computational domain. An example is the flow of a fluid through a tube. Open boundary conditions are relatively new in SPH since their application is nontrivial due to the integral character of SPH. Most of the approaches mentioned in literature are applied to weakly compressible SPH (WCSPH) only. We give a short overview of them here.

Lastiwka et al. [Las09] introduced non-reflecting boundary conditions for free surface flow using a theoretical relation between pressure, density and velocity. Discrete formulations of open boundaries are modeled using a buffer zone that contains in- or outflow particles only.

Federico et al. [Fed12] introduced open boundary conditions for WCSPH using buffer zones at the in- and outlet as well. Particles inside that zones are considered as in- or outflow particles with fixed and specified velocities. This approach is similar to the model proposed by Vacondio et al. [Vac12] for the Shallow Water Equation. All these models used first order consistent SPH kernel and gradients to account for particle deficit.

Recently, Werdelmann et al. [Wer14] introduced an approach to model open boundaries with WCSPH. It is based on the buffer zone approach at the in- and outlet but with increasing and decreasing particle sizes to account for particle deficit when a particle reaches the boundary. They used a specified mass flux assuming laminar tube flow to model growth and shrinkage of the particles before they are set into the domain or released from it. Particles in the buffer zone are generated using exact

mirroring of particles at the open boundary.

Kassiotis et al. [Kas13] introduced open boundary conditions for the unified semi-analytical boundary condition approach for SPH. In this approach, the boundary is divided into several linear segments on which the particle deficit at the boundary can be calculated analytically. The boundary condition is imposed on the segment. For open boundary conditions new particles grow or shrink on the boundary segment until they are released to the fluid. For growth or shrinkage an in- or outflow flux is directly introduced as a source or sink in the boundary condition of the solid wall segment.

In contrast to WCSPH one can use the property of ISPH that pressure and density can be calculated independently from each other. The only model available for open boundary conditions for ISPH was introduced by Hosseini et al. [Hos11]. They applied the buffer zone approach for in- or outflow particles, based on the model of Lastiwka et al [Las09]. At the inlet an unidirectional velocity profile and at the outlet zero pressure and zero stress is applied. In contrast to the presented estimation of the pressure in Subsec. 4.3.5, they use a rotational projection scheme. In this scheme the pressure term of the last integration step is considered in the predictor step. In the corrector step (where the PPE is solved) only the difference to the last pressure is estimated and Neumann boundary conditions are used on all boundaries. They demonstrate that these boundary conditions can lead to correct solutions for Poiseuille flow and flow around obstacles. They mention that homogeneous Neumann pressure boundary conditions at in- or outflow boundaries are intrinsic in the projection method referencing [Cum99]. Therefore, they copy the pressure and velocity specified on the boundary to boundary particles to approximate Dirichlet boundary conditions for pressure.

In this thesis we use the ISPH method. Since the model of Hossini et al. has the drawback that the integration scheme is changed, two new approaches were proposed during the preparation of this thesis [Hir16a; Kun16]. Both approaches are based on the mirror boundary conditions presented earlier. As done for impenetrable boundaries we also mirror fluid particles at the penetrable boundary to create image particles that represent the wall. In contrast to an impermeable boundary the velocity normal to the boundary is not reversed if the pressure is specified. This equals a Neumann boundary condition for the velocity normal to the boundary. The tangential velocity is reversed.

When a particle moves away from the boundary and there is space for a new particle it is set perpendicularly behind the nearest fluid particle. If a particle leaves the computational domain it is removed from the simulation. The difference between the approach of Hirschler et al. and Kunz et al. is the location of the mirror axis. In [Hir16a] the boundary is divided into boundary segments of the size of a particle and every boundary segment is moved with a particle at the open boundary. If the boundary segment is moved far enough into the domain that a new particle is created behind this particle so that the new particle is inside the original domain. The boundary segment is shifted back behind this new particle.

The disadvantages is that the system is only approximately incompressible and large errors at low resolution appear. But the advantage is that the approach can be applied without corrections for consistent SPH kernels. The approach of Kunz et al. [Kun16] is similar but the boundaries of the domain are fixed at any time to the original computational domain. As a consequence corrections for the consistency of SPH are needed because of the large void space at the open boundary. This is in general more computationally expensive. But if surface forces are considered in a multi-phase system, corrections for kernel consistency are present anyway. Therefore the computational overhead is low. A big advantage is that the approach of Kunz et al. is very robust and accurate and in combination with the integration scheme of Hu & Adams [Hu07] (see Sec. 4.5.2) total volume is also conserved.

Very recently Khorasanizade and Sousa [Kho16] proposed an innovative open boundary approach. This approach is similar to the two approaches described previously but differs in the main aspect that the pressure at the open boundary is only approximated with the mean pressure around the boundary and not exactly specified. We use the approach of Hirschler et al. and Kunz et al. during this thesis. If corrected SPH is used, then the model of Kunz et al. is applied because of its robustness and accuracy. In any other cases we use the approach of Hirschler et al.

4.5 Numerical stability

In Sec. 4.2 we mentioned that the unity condition for the SPH kernel function is not guaranteed for random particle distributions. One way to guarantee the unity condition of the kernel function was proposed by Bonet & Lok [Bon99]. It is called the corrected SPH approach. We review this approach in Sec. 4.5.1.

In practical applications we observe that a corrected SPH approach is not enough to guarantee stable and accurate simulations. The reason is that in SPH we must satisfy two conditions. The first condition is the already mentioned consistency of the kernel function. The second condition is the consistency of the particle distribution [Liu10]. If the spacing between particles is larger than the interaction radius then the particles become disconnected and even corrected SPH approaches can't prevent that.

In a proper ISPH approach particles, initially on a regular Cartesian grid, may move on the same trajectory. In front of a stagnation point parts of the particles move in different directions and get disconnected when their distance is larger than the cut-off radius. As a result a large void space is formed between them. Therefore we need a numerical correction that rearranges the particles if necessary without influencing the balance equations.

In literature there exist two approaches to improve the particle consistency in ISPH. The first approach was introduced by Hu & Adams [Hu07]. It is the so-called combined density-invariant and divergence-free approach (DIDF). The other approach was introduced by Xu et al. [Xu09] and modified by Lind et al. [Lin12]. It is called the particle shifting technique. Using these approaches improve the particle consistency and also the 0th and 1th moment of the kernel function and the gradient of the kernel function. We review both approaches in Sec. 4.5.2 and 4.5.3.

4.5.1 Corrected kernel function and corrected gradient of kernel function

In this section we review the corrected SPH approach introduced by Bonet & Lok [Bon99]. Further details about the implementation and accuracy are found in [Kel15]. We are using the mixed kernel and gradient correction of Bonet & Lok. The idea of the corrected SPH approach of Bonet & Lok is to renormalize the kernel function and the gradient of the kernel function to guarantee that Eq. 4.3 for the kernel and the 1th moment

$$\sum_b \frac{m_b}{\rho_b} \nabla_a W_{ab} = 0 \quad (4.49)$$

for the gradient of the kernel are fulfilled. The renormalized kernel function is

$$\tilde{W}_{ab} = \frac{W_{ab}}{\sum_b \frac{m_b}{\rho_b} W_{ab}} \quad (4.50)$$

with the Shepard kernel S_a [She68]

$$S_a = \sum_b \frac{m_b}{\rho_b} W_{ab} \quad (4.51)$$

and the uncorrected kernel function W_{ab} . In the nominator the interaction between all particles including the interaction of particle a with itself need to be considered. In most of the terms in the balance equations we need the gradient of the kernel function. In the mixed kernel and gradient correction of Bonet & Lok, the corrected gradient of the corrected kernel is

$$\tilde{\nabla}_a \tilde{W}_{ab} = \mathbf{L}_a \nabla_a \tilde{W}_{ab} \quad (4.52)$$

with the correction matrix, that ensures symmetric vector direction,

$$\mathbf{L}_a = \left(\sum_b \frac{m_b}{\rho_b} \nabla_a \tilde{W}_{ab} \otimes \vec{r}_{ab} \right)^{-1} \quad (4.53)$$

and the corrected gradient of the kernel, that ensures equal magnitude of the vector,

$$\nabla_a \tilde{W}_{ab} = \frac{\nabla_a W_{ab} - \gamma}{\sum_b \frac{m_b}{\rho_b} W_{ab}} \quad (4.54)$$

with

$$\gamma = \frac{\sum_b \frac{m_b}{\rho_b} \nabla_a W_{ab}}{\sum_b \frac{m_b}{\rho_b} W_{ab}}. \quad (4.55)$$

The nominators in Eqs. 4.54 and 4.55 are the same as in Eq. 4.50.

An advantage of the corrected SPH approach is that a constant pressure field has zero gradient because of Eq. 4.49. In all previous discrete formulations in Sec. 4.3 we may replace the kernel or gradient of the kernel function by Eqs. 4.50 or 4.52,

respectively, if the corrected SPH approach is used.

In addition we may use the corrected SPH approach if we only consider a subset of the particles in the domain. For the curvature and the gradient of the surface tension we use only particles with normal vectors of magnitude larger than a threshold $\varepsilon/h > 0.01$ (see Sec. 4.3.3). In all other cases we use all particles in the vicinity, including mirrored particle at the boundary.

4.5.2 Density-invariant divergence-free approach

Hu & Adams [Hu07] introduced an approach to improve particle consistency of the ISPH method for bulk flow problems. The idea is to split up the time integration of velocity and position into two parts in the corrector step of the projection method in ISPH. In a first integration step the left side of the continuity equation

$$\frac{1}{\rho} \frac{D\rho}{Dt} = \nabla \cdot \vec{u} \quad (4.56)$$

is used as criterion for incompressibility in the Pressure Poisson equation

$$\frac{\tau^2}{2} \nabla \cdot \left(\frac{\nabla p}{\rho_*} \right)_a = \frac{\rho_a^0 - \rho_a^{*,t+1}}{\rho_a^0}. \quad (4.57)$$

τ is the time step and ρ_a^0 is the initial density of particle a . In this first step we calculate a pressure to correct the position of the particles on the half time step using an explicit Euler step. The intermediate velocity is

$$\vec{u}_{a,*} = \vec{u}_a^t + 0.5 \cdot a_{a,*}^{\vec{}} \Delta t \quad (4.58)$$

and the intermediate position is

$$\vec{x}_{a,*} = \vec{a}_{a,*} \Delta t. \quad (4.59)$$

In a second integration step the divergence of the velocity is used as criterion for incompressibility in the Pressure Poisson Equation

$$\tau \nabla \cdot \left(\frac{\nabla p}{\rho_*} \right)_a = \nabla_a \cdot \vec{u}_*^{t+1}. \quad (4.60)$$

In this second step a pressure to correct the velocity of the particles is calculated. The final velocity is

$$\vec{u}_a^{t+1} = \vec{u}_{a,*} + \vec{a}_{a,**} \Delta t \quad (4.61)$$

with the acceleration of the corrector step indicated by ** and the position is

$$\vec{x}_a^{t+1} = \vec{u}_a^t + \vec{u}_a^{t+1} \Delta t + 0.5 \cdot \vec{a}_{a,**} \cdot (\Delta t)^2. \quad (4.62)$$

In the DIDF approach we need to solve the Pressure Poisson equation two times per time step. Therefore the numerical effort increases drastically because the solution step of the LES takes approx. 70 % of the hole computation time. Furthermore the approach is not applicable to free surface flows [Hu15]. On the other hand the DIDF approach improves the conservation of volume because both particle position and velocity are considered as criterion for incompressibility.

We use this approach in some simulations where volume conservation is of major importance especially in the presence of stagnation points. In all other cases we allow small errors in the conservation of volume to reduce computational effort. In the following we call this approach DIDF to indicate the density invariant and divergence free nature.

Nevertheless particles still remain on their trajectory and split up at stagnation points. Therefore another approach to regularize the particles is necessary.

4.5.3 Particle Shifting

Particles in SPH move on their streamline due to their Lagrangian nature. Therefore particles split near a stagnation point leaving a void space between two streamlines. This leads to large errors in the particle consistency of SPH. Xu et al. [Xu09] introduced the particle shifting technique to geometrically shift particles slightly away from its streamlines into a void space. As a result the particles are more regularly distributed in the domain. We introduce the shifting algorithm in the following.

The idea is to shift particles slightly into a void space after every time step. The

total shifting vector $\vec{r}_{a,s}$ is

$$\vec{r}_{a,s} = C\alpha\vec{R}_a \quad (4.63)$$

with the arbitrary constant $C = 0.04$, the shifting magnitude $\alpha = |\vec{u}_{max}|dt$, the magnitude of the maximum particle velocity $|\vec{u}_{max}|$, the time step dt , and the shifting vector

$$\vec{R}_a = \sum_b^{Nb} \frac{\bar{r}_a^2}{r_{ab}^2} \hat{r}_{ab}. \quad (4.64)$$

\hat{r}_{ab} , r_{ab} and \bar{r}_a are the unit distance vector between particle a and b , the distance between both particles and the average particle spacing in the neighborhood defined as

$$\bar{r}_a = \frac{1}{Nb} \sum_b^{Nb} r_{ab}. \quad (4.65)$$

In this approach we assume that all particles represent the same volume. Therefore a geometrically uniform distribution is the best particle distribution.

Some properties of the fluid are connected to the particles and their position. If we shift the particles we need to correct the hydrodynamic variables Ψ to be consistent and not influence the balance equations. According to Xu et al. a Taylor series of the hydrodynamic variable

$$\Psi_{a'} = \Psi_a + \delta\vec{r}_{aa'} \cdot (\nabla\Psi)_a + \dots \quad (4.66)$$

is used to approximate the property of a particle at the new position a' after shifting. We use a linear interpolation and neglect quadratic and higher terms. Hydrodynamic variables used in this thesis are the velocity, concentration and temperature. The density is not a hydrodynamic variable in this context because we calculate the density by summation of masses in the neighborhood instead of calculating the continuity equation directly. Therefore we are able to calculate the density at any point.

The particle shifting technique is independent of the time integration and does not

affect the balance equations because we shift the particles only at the very end of a time step and correct the particle properties accordingly.

Originally the shifting technique by Xu et al. assumes that every particle is an identical interpolation point in the domain. In a multi-phase system this is not valid any more because of the presence of an interface. In SPH the interface between two phases is defined by the type (color) of the particles. Therefore the interface is implicitly moved when particles change their position. If we shift the particles then we implicitly shift the interface between phases as well. To overcome this shortcoming we modify Eq. 4.63 near an interface between two phases and apply shifting only in the tangential direction to the interface. This can be done by only consider the tangential part of Eq. 4.63. A similar extension was proposed by Lind. et al. [Lin12]. They modified the shifting technique for free surface flows based on a Fickian approach.

In the last part of this section we compare the 3 previously introduced approaches for numerical stability and combinations of them. One common test case in literature is a two-dimensional Taylor-Green vortex. In this test case all boundaries are periodic and initially a divergence-free velocity profile

$$u_x = \sin(2\pi x)\cos(2\pi y) \quad (4.67)$$

$$u_y = -\cos(2\pi x)\sin(2\pi y) \quad (4.68)$$

is imposed. The vortex decays due to viscous dissipation of the fluid. Details about this test case are found in [Lin12; Xu09]. We consider a case with Reynolds number $Re = 1000$.

The magnitude of velocity and the particle distribution are shown in Fig. 4.5 at time $t = 0.24s$ for different combinations of the previous approaches. Fig. 4.5a shows the results without any numerical stability. We see that particles are aligned on their streamline and large void spaces are formed between the streamlines. The other 3 cases in the top line (Fig. 4.5b-d) are cases where the corrected SPH and DIDF approach without particle shifting is used. Except for some small deviations we get the same particle distribution as in Fig. 4.5a. We note that the velocity distribution

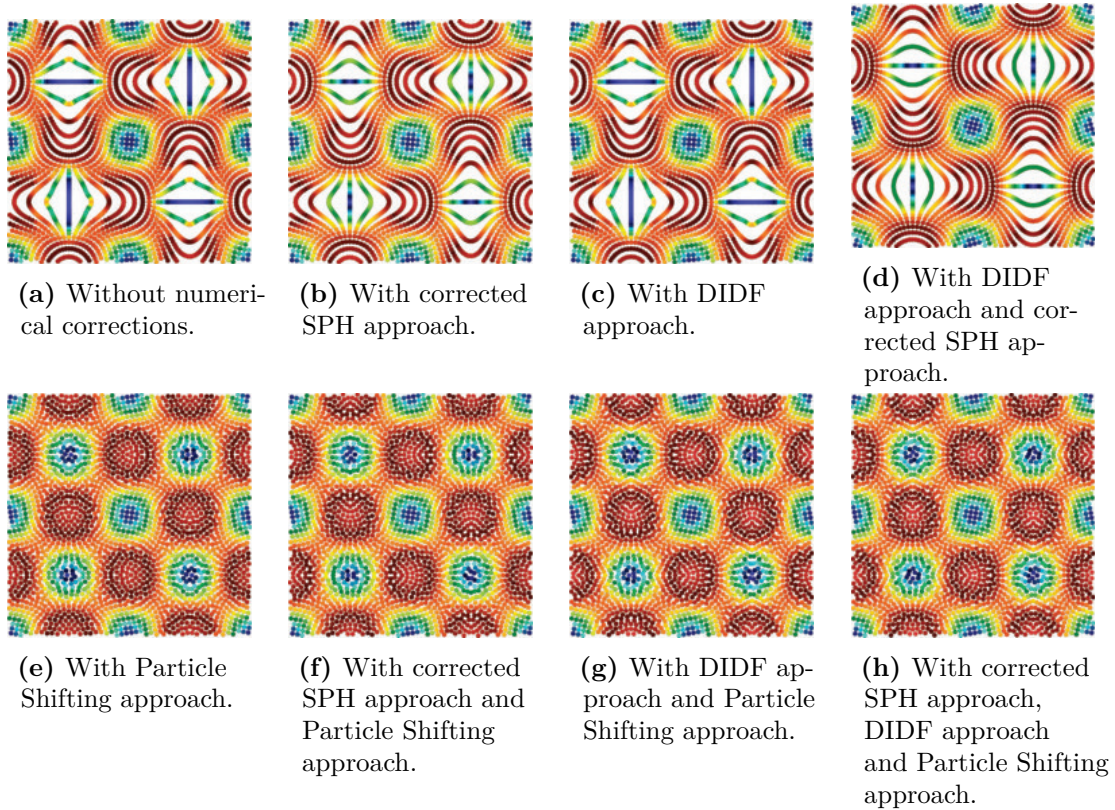


Figure 4.5: Taylor-Green vortex simulation with different numerical stability approaches. Particle distribution shown at time $t = 0.24s$. The Reynolds number is $Re = 1000$. Color indicates the magnitude of the velocity of the particles. Red indicates $|u| = 1m/s$ and blue $|u| = 0m/s$. Colors are distributed by an unsaturated rainbow color scheme.

is good but the simulation tend to diverge. If we apply the particle shifting approach alone or in addition with any of the other stability approaches (Fig. 4.5e-h) the particle distribution as well as the velocity distribution is very smooth. As shown by Xu et al. the accuracy is largely improved.

In this thesis we use the corrected SPH and particle shifting approach where particle movement or surface tension is involved. The DIDF approach is only used in simulations where volume conservation is crucial since this is the main advantage of the approach.

4.6 Time integration

In this thesis we use two different time integration schemes. We use a predictor-corrector scheme to solve the momentum balance and an explicit Euler scheme to integrate the component balance.

The predictor-corrector scheme, based on the decomposition of Chorin [Cho68], was introduced by Cummins and Rudman [Cum99] to SPH. In a predictor step the curl-free part of the Navier-Stokes equations are solved using an explicit Euler time step. In the corrector step the divergence-free part, that is the pressure term, is integrated where the pressure is calculated using the Pressure Poisson Equation (PPE). The velocity is integrated explicitly while the position of particles is calculated semi-implicit. Details are mentioned in Sec. 4.3.5 and Sec. 4.5.2. A detailed overview is found in [Kel15].

We use an explicit Euler integration scheme [Eul68] to integrate the component balance. The mass fraction is updated between the calculation of the forces in the predictor step of the momentum balance and the integration step of the predictor. Therefore the mass fraction is sequentially coupled to the velocity.

For an explicit integration scheme there exist criteria for the maximum time step because the algorithm is not unconditionally stable. Therefore the following time step criteria are used throughout the thesis.

The time step criterion due to convective transport (Courant-Friedrichs-Lewy (CFL) criterion) is

$$\Delta t_{CFL} = \alpha_{CFL} \frac{L_0}{u_{max}} \quad (4.69)$$

with $\alpha_{CFL} = 0.05$ and the magnitude of the maximum velocity u_{max} . The time step criterion for viscous and mass diffusion is

$$\Delta t_{visc} = \alpha_{diff} \frac{L_0^2}{\nu_{max}} \quad (4.70)$$

and

$$\Delta t_{mass} = \alpha_{diff} \frac{L_0^2}{D_{max}}. \quad (4.71)$$

with $\alpha_{visc} = 0.0625$. ν_{max} and D_{max} are the maximum kinematic viscosity and maximum diffusion coefficient or mobility, respectively.

4.7 Validation of implementation

We do not present a validation of the implementation here. For completeness a comprehensive validation of the discrete component and momentum balance is found in the Appendices C, D and G.

4.8 Delimitation from Smoothed Dissipative Particle Dynamics

The SDPD method was introduced by Revenga and Espanol [Esp03a] as an thermodynamic consistent extension of the SPH method for very small scales where thermal fluctuations are relevant. For example, when modeling flow in very thin tubes thermal fluctuations may be important. The SDPD method is a mesoscopic simulation method and describes a coarse-grained molecular system. Therefore, the scale of application is very similar to the DPD method but the formulation of the balance equations is different. While the balance equations are formulated using a conservative, dissipative and random force in DPD, the macroscopic balance equations are extended by thermal fluctuations in SDPD. Therefore it is better accessible for engineers because the known quantities, e.g. viscosity, are input parameters to the balance equations (in contrast to DPD where e.g. friction coefficients need to be calibrated). SDPD combines the accessibility from a top-down view of a fluid on the mesoscale with the consistent features for the so-called fluctuation dissipation theorem in DPD. The fluctuation dissipation theorem states that the amplitude of the fluctuation is proportional to the dissipative term. For example, the amplitude of the stochastic term in the component balance is proportional to the diffusive term in the component balance. As a result fluctuations of the average quantities such as partial mass density, momentum and energy scale correct with the particle size [Váz09], e.g. in smaller systems the fluctuations are larger than in large systems. In this thesis we only include fluctuations of partial mass density in the component balance. For a consistent SDPD model, fluctuations of the momentum should be considered as well. This is not possible in the ISPH approach because of the smoothing property of the projection method. Besides we do not apply an exact projection because it is numerically unstable [Cum99]. On the other hand we do not use a

WCSPH approach (with an equation of state for the pressure) because the pressure field is very noisy, but very accurate in ISPH. Therefore the numerical method used in this thesis is a modified SPH approach or an inconsistent SDPD approach.

Very recently an extended WCSPH model with smooth pressure fields is available [Ada13] and we suggest to use it in the future if momentum transport is important in the formation of polymer membranes. If momentum transport is not important the current SPH model is satisfactory and represents a consistent SDPD approach when transport of momentum is neglected.

4.9 Compact discrete model equations

In this section we summarize the discrete equations of the model that we use in the remainder of this thesis. The boundary conditions differ from case to case. Therefore we introduce them separately for each case later.

The discrete continuity equation is

$$\rho_a = m_a \sum_b W_{ab}. \quad (4.72)$$

The discrete component balance is

$$\begin{aligned} \frac{D\omega_a}{Dt} = & \sum_b \frac{m_b}{\rho_b} (M_a + M_b) \frac{\vec{r}_{ab}}{r_{ab}^2} \nabla_a W_{ab} \cdot (\mu_a - \mu_b) \\ & + \frac{1}{m_a} \sum_b \sqrt{-2k_B T \frac{m_a m_b}{\rho_b} (M_a + M_b) \frac{1}{r_{ab}} \frac{\partial W_{ab}}{\partial r_{ab}}} J_{ab} \sqrt{dt} \end{aligned} \quad (4.73)$$

with

$$\mu_a = \mu_a^0 - \kappa'_a \nabla^2 \omega_a, \quad (4.74)$$

$$\kappa'_a \nabla^2 \omega_a = \sum_b \frac{m_b}{\rho_b} (\kappa'_a + \kappa'_b) \frac{\vec{r}_{ab}}{r_{ab}^2} \nabla_a W_{ab} \cdot (\omega_a - \omega_b). \quad (4.75)$$

and

$$\omega_2 = 1 - \omega_1. \quad (4.76)$$

The discrete momentum balance is

$$\begin{aligned} \frac{D\vec{u}_a}{Dt} = & - \sum_b \frac{m_b}{\rho_a \rho_b} (p_b + p_a) \nabla W_{ab} + \sum_b \frac{m_b}{\rho_a \rho_b} (\eta_a + \eta_b) \frac{\vec{r}_{ab}}{r_{ab}^2} \nabla_a W_{ab} \cdot (\vec{u}_a - \vec{u}_b) \\ & + \vec{g}_a + \frac{|\vec{n}_a|}{\rho_a} \left(\sigma_a \kappa_a \vec{n}_a + (\nabla_S \sigma)_a \right). \end{aligned} \quad (4.77)$$

The pressure is calculated using the discrete PPE

$$\sum_b 2 \frac{m_b}{\rho_b \rho_a} \cdot (p_a - p_b) \frac{\vec{r}_{ab}}{r_{ab}^2} \nabla_a W_{ab} = \frac{1}{\Delta t} \sum_b \frac{m_b}{\rho_b} (\vec{u}_{b,*} - \vec{u}_{a,*}) \nabla_a W_{ab}. \quad (4.78)$$

CHAPTER 5

Viscous fingering

In Sec. 2.3 we have seen evidences that the motion of the precipitation front (interface between stable and unstable polymer solution) is similar to the displacement of viscous fingers, at least in the first moment of contact of polymer solution and coagulation bath. Therefore we study viscous fingering in this chapter. Viscous fingering may only be relevant in the preparation of flat sheet membranes [Ren04] but a model for polymer membrane formation should reproduce these experiments as well. Here, we pursue two goals. In the first part we demonstrate that the proposed model captures the motion of viscous fingers. In the second part we analyze the experiments of Sec. 2.3 with a focus on viscous fingering.

Viscous fingering is a hydrodynamic instability (or sometimes also called morphological instability) that is observed on different length scales. It arises when a less viscous fluid displaces a more viscous fluid. The phenomena is observed in miscible as well as in immiscible systems. The main driving force in these systems is the force with which the less viscous fluid is pushed into the more viscous one. Its origin can be a body force, e.g. gravity, an external pressure gradient or capillary forces in three phase systems. Its counter part is dispersion and surface tension in miscible and immiscible systems, respectively. In both cases viscous fingering is studied in Hele-Shaw cells [Hel98].

In literature viscous fingering is typically discussed in these two extreme cases. Immiscible viscous fingering is studied in the limit of very small diffusive mass transport between two distinguishable phases. In this case a sharp interface is assumed. As a result only surface tension between two immiscible phases is considered and diffusive

mass transfer across the interface is neglected. This case is sometimes also referred as immiscible displacement where the viscosity in each bulk is different.

Miscible viscous fingering is studied in the limit of very small surface tension¹ between two miscible fluids where the viscosity depends on the concentration. Here, a wide diffusive interface between the fluids is assumed. Surface tension is neglected and diffusive mass transport across the interface dominates. Both cases are limiting cases of the more general case where surface tension and diffusive mass transport may be present. In the present model we consider diffusive mass transport and capillary stress and therefore cover the general case (and also the extreme cases). In principle miscible as well as immiscible viscous fingering may occur during precipitation of polymer membranes depending on the preparation conditions. Therefore we study miscible and immiscible viscous fingering in a Hele-Shaw cell and investigate if the model predicts the dynamics found in the experiments in Sec. 2.3.5.

5.1 Current state on modeling of viscous fingering in literature

Immiscible viscous fingering was first analyzed in the 50s by Hill [Hil52], Saffman & Taylor [Saf58] and Chuoke et al. [Chu59]. Since then further investigations followed [Ben86; Cas00; Cou00; Hom87; Tan00b]. A review of the main results of immiscible viscous fingering for interfacial pattern formation is found in [Cas04]. Viscous fingering was studied by engineers, especially in secondary oil recovery in porous rocks, by physicists and by mathematicians. The seminal work was done by Saffman and Taylor in 1958 when they rigorously studied viscous fingering. Therefore the phenomena is often named Saffman-Taylor instability. In the 80s full understanding and numerical solution was achieved by studying Stokes flow and displacement in Hele-Shaw cells. Mathematical discussions of linear stability analysis are carried out characterizing the growth rate of the fingers and its width.

There is a wide range of systems where viscous fingering is present. Prominent examples for viscous fingering are secondary oil recovery or systems with chemical reactions where the viscosity changes with the composition of the mixture [Hej10].

¹ In Eq. 3.19 we find that the capillary stress depends on a gradient of the partial mass density. This gradient may be present in miscible systems during mixing of components. In general its effect is very small because the gradient of the partial mass density and the energy parameter tends to vanish when components mix.

Also in two-phase flow in porous media so-called capillary fingering is observed that shows the same dynamic behavior as viscous fingering. A comprehensive overview is found in [Cue14; Kue88]. In the context of polymer systems related to membrane formation, Ren et al. [Ren04] first discussed viscous fingering as mechanism for macrovoids in flat membranes due to small gravitational effects.

Modeling of viscous fingering was pioneered by Tryggvason & Aref [Try83] who studied Hele-Shaw cells using vortex-sheet calculations in the 80s. Up to date Hele-Shaw cells are studied using a variety of simulation methods, e.g. finite-volume or phase-field methods [Cue14; Deg86; Mei88; Par84]. In the context of SPH viscous fingering was not yet discussed.

Similar instabilities are the Rayleigh-Taylor instability (RTI) and Kelvin-Helmholtz instability (KHI) even though the mechanisms are different. In RTI the instability is driven by density differences under gravity and in KHI the instability arises due to viscosity differences in shear flow. The RTI [Cum99; Gre09; Sha12a; Sze12; Tar05] and the KHI [Fat14; Pri08; Sha11] were discussed in several articles in the context of SPH. Therein it was found that the dynamics of the RTI and KHI are well captured in SPH but there are some deviations in the prediction of the limit of stability.

5.2 Hele-Shaw cell

A Hele-Shaw cell [Hel98] is a setup where we observe Hele-Shaw flow (after Henry Hele-Shaw). The characteristics of Hele-Shaw flow is Stokes flow between two parallel plates with a small gap. The length (direction of main flow) and the width of the cell are much larger than the height or gap between the plates and therefore the resistance of flow is dominated by the height of the cell. A schematic example is shown in Fig. 5.1.

We assume a developed flow pattern between the plates, e.g. Poiseuille flow of a Newtonian fluid. In simulations of Hele-Shaw cells we may reduce the 3D cell to a 2D problem by partial integration of the friction due to the gap. A detailed derivation is found in Appendix I. The effective friction, assuming a parabolic velocity profile in the direction of the gap, is [Lan87]

$$\vec{F} = \nabla p = -\frac{12\eta}{b^2}\vec{u}. \quad (5.1)$$

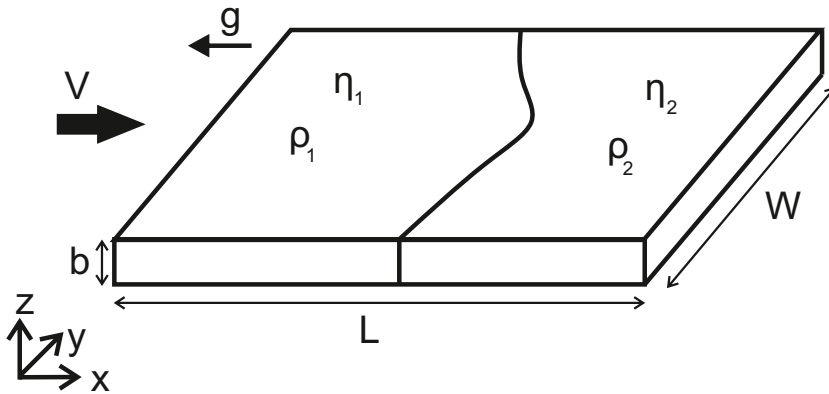


Figure 5.1: Sketch up of a Hele-Shaw cell.

This term is a body force $[N/m^3]$ in the momentum balance in all simulations of viscous fingering.

It may be seen in Eq. 5.1 that the resistance scales linear with the velocity and the viscosity of a fluid. It also scales quadratic with the gap size b between the plates. Therefore in the presence of a difference in the viscosity or different velocities the resistance differs. The velocity in a Hele-Shaw cell obeys Darcy's law because the velocity is proportional to the gradient of the pressure [Cas04; Saf58]

$$\vec{u} \propto \nabla p. \quad (5.2)$$

This is why its principles are valid in flow in porous media and a Hele-Shaw cell may be used to effectively describe Darcy flow in a porous media.

We will first investigate immiscible and miscible viscous fingering in the context of SPH. Afterwards we investigate the more general case with the proposed model including the Cahn-Hilliard equation and capillary stress.

5.3 Immiscible viscous fingering

We observe immiscible viscous fingering in systems with at least two immiscible fluids that represent two distinguishable phases with different viscosity. Assume that the fluids are in a Hele-Shaw cell. When the less viscous fluid displaces the more viscous fluid then viscous fingering may be observed (here we assume that gravity is negligible). Two quantities are involved to control the dynamics of the displacement. The first quantity is the velocity of displacement. It is the velocity with which the

less viscous fluid is pushed into the more viscous one. The second quantity is the surface tension. It acts against the displacement because of the curvature of the interface between the phases. Due to the displacement the curvature increases and therefore the capillary stress increases and tends to reduce the curvature.

A stability analysis of the displacement in immiscible viscous fingering was presented by Chuoke et al. [Chu59]. We skip a review of the derivation of the limit of stability for immiscible viscous fingering here and refer to Appendix H, and only briefly summarize the results of the linear stability analysis and characteristics.

We consider flow in a Hele-Shaw cell. According to Hill [Hil52], Saffman and Taylor [Saf58], Chuoke et al. [Chu59] and [Mah85], we find an instability of displacing when a fluid 1 displaces a fluid 2 and if

$$(\rho_2 - \rho_1)g + \left[\frac{12(\eta_2 - \eta_1)}{b^2} \right] V \geq 0 \quad (5.3)$$

is fulfilled, where g and V are the gravity in the reverse x-direction (cf. Fig. 5.1) and the magnitude of velocity in the x-direction perpendicular to a gap with size b . In the absence of gravity the first term on the left hand side vanishes. Eq. 5.3 represents a balance of forces of the system. From linear stability analysis Chuoke et al. [Chu59] found that an instability at the interface between two fluids in an immiscible system grows for wavelengths of the initial disturbance of an interface greater than

$$\lambda_c = 2\pi \sqrt{\frac{\sigma}{\frac{b^2}{12}(\eta_1 - \eta_2)(V - V_c)}}. \quad (5.4)$$

The wavelength corresponds to the tip to tip distance between the fingers. The fastest growing wavelength is

$$\lambda_m = \sqrt{3}\lambda_c. \quad (5.5)$$

V_c is the critical velocity of displacement. It represents the magnitude of velocity V that is necessary before viscous fingers are initiated. If the velocity V is lower than V_c the interface between the two fluids is stable and each perturbation of the interface decays. V_c results from Eq. 5.3 for the case that the left hand side is exactly

zero. In the case that the gravity is zero, V_c is also zero. In a Hele-Shaw cell this means that a finger is unstable for $\lambda > \lambda_c$ and the growth rate is largest for $\lambda = \lambda_m$. According to [Try83] the characteristic velocity U^* and the dimensionless surface tension B are [Mah85]

$$U^* = \left| \frac{(\eta_1 - \eta_2) V}{\eta_1 + \eta_2} \right| \quad (5.6)$$

and

$$B = \frac{\sigma b^2}{6U^*W^2(\eta_2 + \eta_1)}. \quad (5.7)$$

The characteristic length is the width of the Hele-Shaw cell W [Pra15]. With these characteristics the dimensionless time and length are

$$t^* = \frac{U^* \cdot t}{WB^{1/2}} \quad (5.8)$$

and

$$\vartheta^* = \frac{\vartheta}{WB^{1/2}} \quad (5.9)$$

for immiscible systems where surface tension is present. $B^{1/2}$ was included by [Try83] to scale surface tension. For miscible systems or in the limit of zero surface tension B vanishes and therefore can be excluded from Eqs. 5.8 and 5.9. Remaining characteristics are the Capillary number Ca with respect to the more viscous phase (in our case phase 2) and the dimensionless viscosity ratio A

$$Ca = \frac{V\eta_2}{\sigma} \quad (5.10)$$

and

$$A = \frac{\eta_2 - \eta_1}{\eta_2 + \eta_1}. \quad (5.11)$$

It was found in experiments and numerical studies (see [Mah85] and references therein) that the dimensionless distance between the longest fingers ϑ^* follows the

power law

$$\vartheta^* \sim (t^*)^{1.6} \quad (5.12)$$

with a deviation of the exponent of $+/- 0.4$. The power law holds after some initialization time and is independent of the ratio of viscosity and the dimensionless surface tension B . This power law may be used to identify fingering dynamics and to validate the numerical model.

In the next sections we analyze the effect of surface tension on the fingering dynamics. The influence of numerical resolution is found in Appendix J. The simulation domain is a Hele-Shaw cell (2D) as discussed in the previous section with a gap size b and a cell width W . The computational setup of the Hele-Shaw cell is shown in Fig. 5.2. We neglect diffusive mass transfer for immiscible fluids and therefore do not solve the component equation. We only consider the continuity and momentum equation (see Subsec. 3.4.3). The parameters of the simulation domain and the properties of the fluids are summarized in Table 5.1. We apply open pressure boundary conditions in x direction and periodic boundary conditions in y direction. We arbitrarily choose a velocity of displacement $V = 2.35\text{mm/s}$. The corresponding pressure gradient in x direction is $dp/dx = 430.1\text{Pa/m}$. We estimated this value from steady-state Stokes flow using the more viscous fluid in the Hele-Shaw cell. If not explicitly stated we use a resolution of 180×30 particles that corresponds to $L_0 = 5.167\text{mm}$, the corrected SPH and particle shifting approach. The normals at the interface are calculated with a sharp color function (see Appendix G.3 for a detailed discussion of

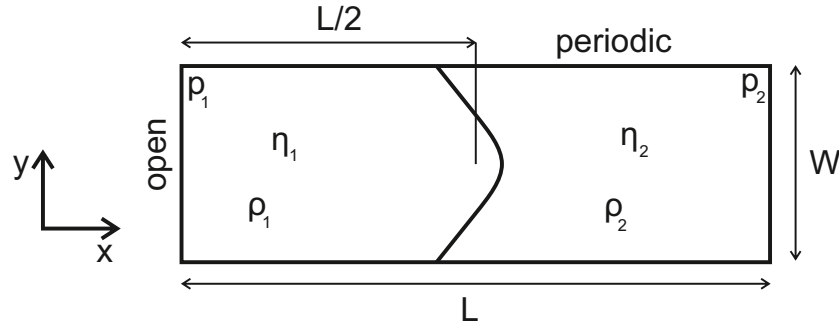


Figure 5.2: Schematic setup of computational domain for viscous fingering.

Table 5.1: Summary of properties of the fluids and parameters of Hele-Shaw cell for an immiscible system.

Parameter	Units	Value
b	[mm]	1.0
W	[mm]	155.0
L	[mm]	930.0
L_0	[mm]	5.167
$\rho_1 = \rho_2$	[kgm^{-3}]	100
V	[$mm s^{-1}$]	2.35
dp/dx	[$Pa m^{-1}$]	430.1
A	[$-$]	1/3
η_1	[$mPas$]	10.0
σ	[Nm^{-1}]	see text

the color function). Initially we apply a co-sinusoidal perturbation to the type of phase of the particles (color function C of each particle)

$$C = \begin{cases} 0 & x < L_x/2 - 4 \cdot \cos(\pi/(L_y/2)y) \\ 1 & else. \end{cases} \quad (5.13)$$

Both fluids move through the computational domain but we are only interested in the relative motion of the fluids. Since the computational domain is limited we shift all particles back with the average velocity of the system after each time step. In other words we simulate the motion of the fluids relative to the average velocity of the fluid in the domain.

5.3.1 Limit of stability of displacement

First we investigate if the numerical model predicts the limit of stability of viscous fingering. We simulate a Hele-Shaw cell with initial perturbation around the theoretical critical wave length λ_c . We keep all simulation parameters except the surface tension constant to alter λ . The critical surface tension σ_c is defined as the surface tension at $\lambda = \lambda_c$.

In Fig. 5.3 we show results of the simulations with different surface tension at $t^* = 20$ (except for $\sigma = 0.01\% \sigma_c$ because the scaling proposed by Tryggvason & Aref [Try83] is not valid in this case). From left to right the surface tension increases. On the left side of each plot the particle distribution and on the right side the computed

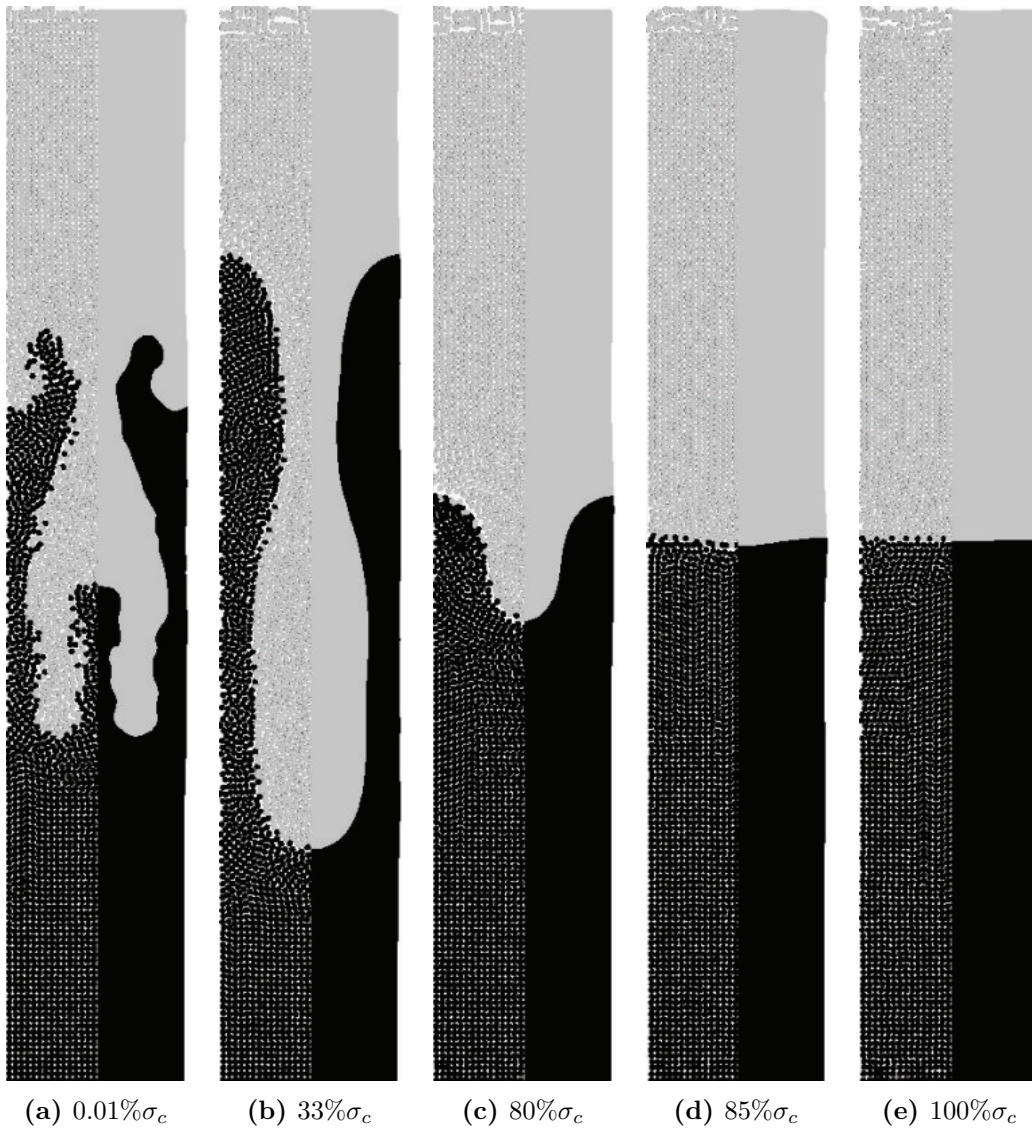


Figure 5.3: Stability of immiscible viscous fingering with different wavelength of the perturbation at $t^* = 20$. The limit of stability is between $\sigma = 80\%\sigma_c$ and $\sigma = 85\%\sigma_c$. The density ratio is unity and the viscosity ratio is $A = 1/3$. The time for $\sigma = 0.01\%\sigma_c$ is $t^* = 200$ because the scaling is not valid in the zero surface tension limit. On the left side the particle distribution and on the right side the contour plot of the two phases are shown.

distribution of the phases are shown. On both sides the color indicates the phases. We start on the right side of Fig. 5.3. In Fig. 5.3e we see exactly the case of $\lambda = \lambda_c$. The interface between the fluids remain stable. This is what we expect from theory. Then we reduce the surface tension by 15%. We still get a stable interface between the fluids at steady-state. If we again reduce the surface tension by 5% the interface between the fluids is unstable and a finger grows. Therefore the limit of stability is between $\sigma = 80\%\sigma_c$ and $\sigma = 85\%\sigma_c$. This corresponds to a deviation from the critical wave length λ_c of 8 to 10 %. Compared to the deviation of the limit of stability of a Rayleigh-Taylor instability of 10 to 15 % [Sha12b] our results are reasonable.

We further reduce the surface tension to $\sigma = 33\%\sigma_c$. This case corresponds to the maximum growth rate $\lambda = \lambda_m$. At $t^* = 20$ we get a bottle-like shape of the finger. In addition we see that the finger grows faster than in the previous cases. The reason is the dependence of the wave number on the grow rate [Tan88].

In the limit of negligible surface tension, as shown in Fig. 5.3a, the critical wave length is below the resolution ($\lambda_c = 4.9mm < L_0 = 5.167mm$). Therefore the interface is very rough because every instability may grow. In this case the dimensionless time is scaled by a factor of 10 because the scaling law including surface tension is not valid any more in the limit of zero surface tension. One effect seen in Fig. 5.3a is the splitting of fingers. From the initial single perturbation two intermediate stable fingers are formed that grow simultaneously. The splitting of the finger is not a numerical artifact because the splitting of fingers is observed in literature for similar cases as well.

5.3.2 Analysis of the dynamics of displacement

Next we analyze the dynamics of displacement for a single finger in a Hele-Shaw cell at the maximum growth rate $\lambda = \lambda_m = W$. This case is equal to the case in Fig. 5.3b. The simulation parameters and the resolution are the same as before. The surface tension is $\sigma = 57.21mNm^{-1}$.

The particle distribution and contour plot at times $t^* = 3, 6, 10, 15$ and 20 are shown in Fig. 5.4. The time series demonstrates the evolution of the single finger. We see that first a cylindrical finger grows. Then a contraction arises that leads to a bottle-like shape of the finger. At late times the bottle-like finger elongates but the shape remains.

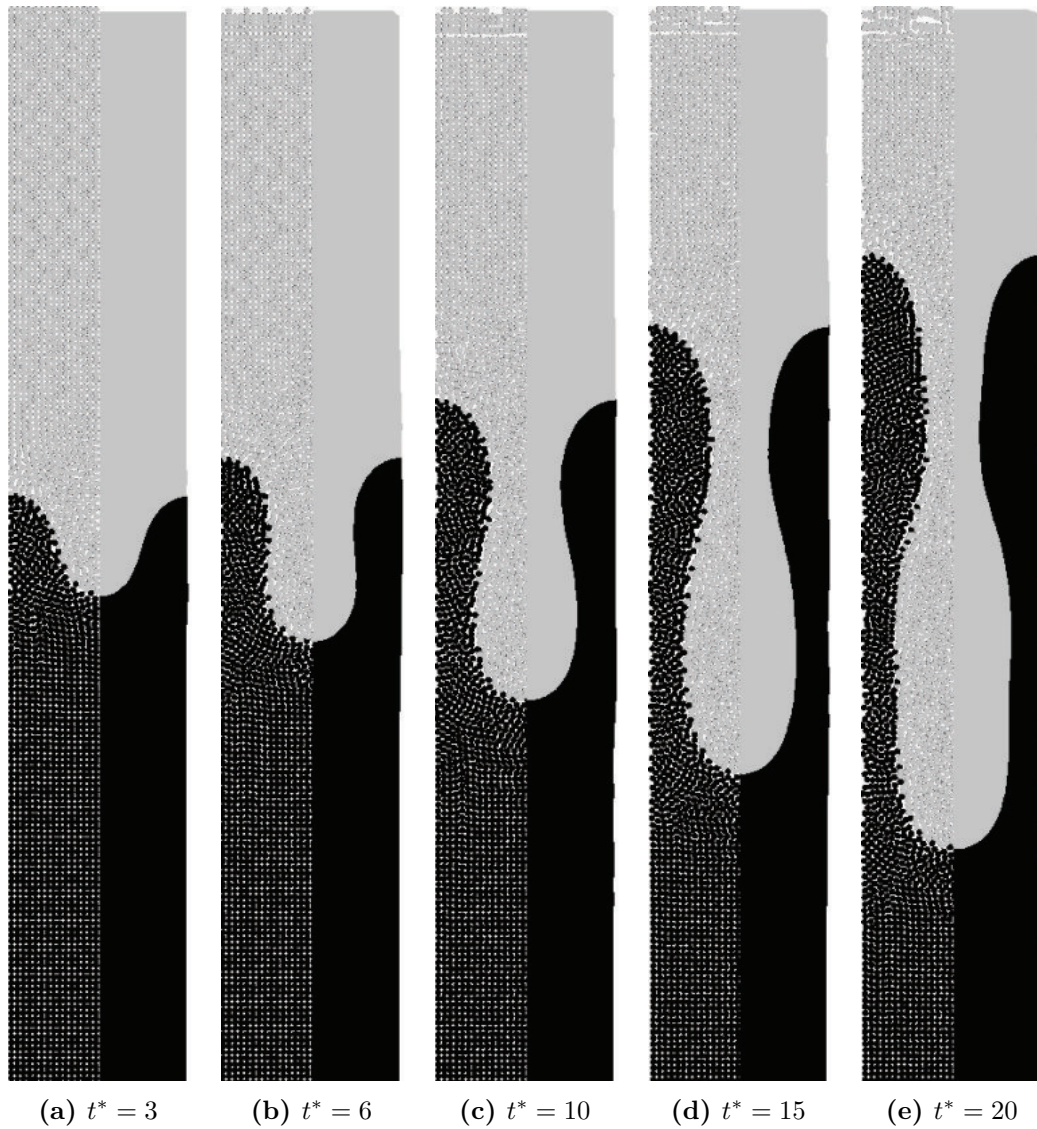


Figure 5.4: Time evolution of immiscible viscous fingering with the maximum growth rate with wavelength of the perturbation $\lambda = \lambda_m$. The density ratio is unity and the viscosity ratio is $A = 1/3$. On the left side the particle distribution and on the right side the contour plot of the two phases are shown.

There are two reasons for the bottle-like shape. The first reason is that the viscosity ratio A is larger than a critical value $A = 0.2$. It was found in [Try83] that bottle-like shapes are formed for higher viscosity ratios. Another reason may be the bounded domain.

Before we analyze the velocity of displacement we have a closer look on the pressure and velocity field in Fig. 5.5. On the left side of each plot in Fig. 5.5 the pressure contour is shown. On the right side of each plot the magnitude of the velocity is shown. Each plot corresponds to the same sequential time as in Fig. 5.4.

The pressure field is almost identical in all time steps. It is linear along the flow direction indicating Stokes flow. In contrast to that the velocity increases from left to right. At early time the peak of the velocity is at the tip of the initial perturbation. At $t^* = 10$ when the finger starts to form a bottle-like shape there are two different peaks of velocity. One peak is still located at the tip of the finger but a second peak of similar magnitude is located at the contraction of the finger. This may indicate that the contraction influences the dynamics of the growth of the finger too. With increasing time these two peaks remain but their distance increases along the finger. Next we compare the growth of the finger with the power law found in experiments (Eq. 5.12). We estimate the size of the finger by measuring the distance between the tip of the finger and its counter part, e.g. the maximum distance between the interface of the phases in flow direction. We subtract the initial distance to account for the initial perturbation of the interface and calculate the dimensionless distance using Eqs. 5.8 and 5.9.

In Fig. 5.6 the dimensionless distance is plotted over the dimensionless time. We compare the finger length taken from the simulation with different power laws. The first power law is $\vartheta \sim (t^*)^{1.6}$ (Eq. 5.12). The second power law in Fig. 5.6 is the linear dependence of the dimensionless finger length on the dimensionless time representing flow in a channel.

We identify 2 different regimes in Fig. 5.6. At small times ($t^* < 7$) we found good agreement with the super-linear power law for immiscible viscous fingering. This indicates that the growth of a cylindrical finger fits very well to the dynamics found in experiments. For later times ($t^* > 7$) we find agreement between the growth of the finger in simulation with the linear power law. This indicates that the growth of the finger is dominated by the flow in the contraction and the finger is elongated by a laminar flow pattern. In the contraction, Stokes flow in a channel can be

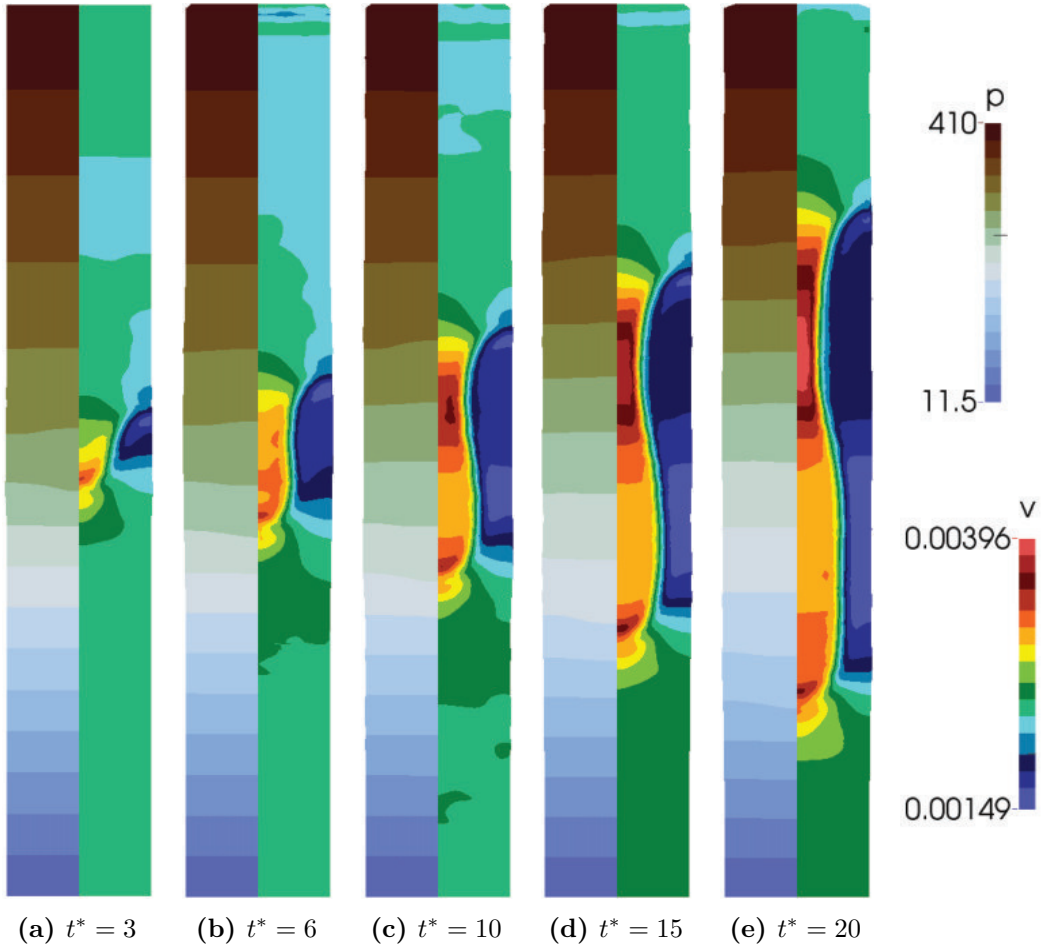


Figure 5.5: Time evolution of immiscible viscous fingering with the maximum growth rate with wavelength of the perturbation $\lambda = \lambda_m$. The density ratio is unity and the viscosity ratio is $A = 1/3$. On the left side the contour of the pressure and on the right side the contour of the velocity are shown. The legends are found on the right side. The units of pressure p and velocity $|v|$ are Pa and m/s .

found because of the small gap b . The dominating resistance in the momentum balance is the viscous resistance due to the reduction of dimensions (Eq. 5.1) and the dominating force is the pressure force. Therefore, assuming a constant velocity in the contraction, the evolution of the fluid linearly depends on the pressure force

$$dx = \frac{b^2}{12\eta} \nabla p \cdot dt. \quad (5.14)$$

The growth rate of the finger is dominated by a linear time relationship.

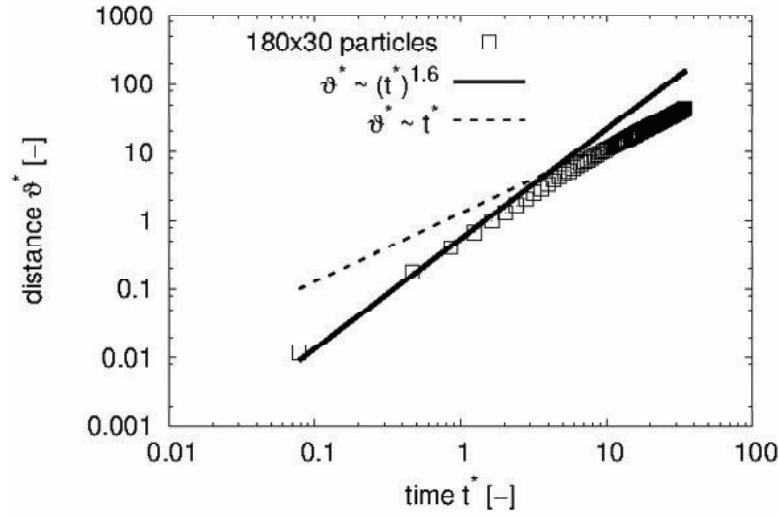


Figure 5.6: Comparison of finger growth over time with power law for viscous fingering and flow in a channel for $\lambda = \lambda_m$.

5.3.3 Influence of diffuse interface on immiscible fingering

Until now we assumed that the interface between two immiscible fluids is sharp and therefore calculated the surface tension using a sharp color function. In this section we investigate the influence of a diffuse interface. We consider surface tension and diffusive mass transfer across the interface. Due to the small errors shown in Chap. G in Fig. G.12 we expect a small deviations in the finger shape. We investigate the deviation by considering the case of maximum growth rate.

The simulation parameters are the same as before except that additionally the Cahn-Hilliard equation is solved to propagate the color field. We neglect fluctuations here because their magnitude is very small. We assume a binary mixture in an unstable state with initial concentration $\omega = 0.1$ and $\omega = 0.5$ corresponding to η_1 and η_2 . Note that we consider a binary mixture where phase 1 corresponds to a mass fraction $\omega < 0.5$ and phase 2 corresponds to a mass fraction $\omega \geq 0.5$. We consider a linear relationship of the viscosity on the mass fraction. The diffusion coefficient in the Cahn-Hilliard equation is set to $D = 9.7829 \cdot 10^{-7} m/s$ to keep the interface as thin as possible without losing smoothness. The chemical potential is calculated using Eq. 4.22 with an interaction parameter $\chi_{12} = 3$. We consider the case for maximum growth rate with $\lambda = \lambda_m$ for immiscible viscous fingering.

The time series of the contour compared to the results for immiscible fingering (Fig.

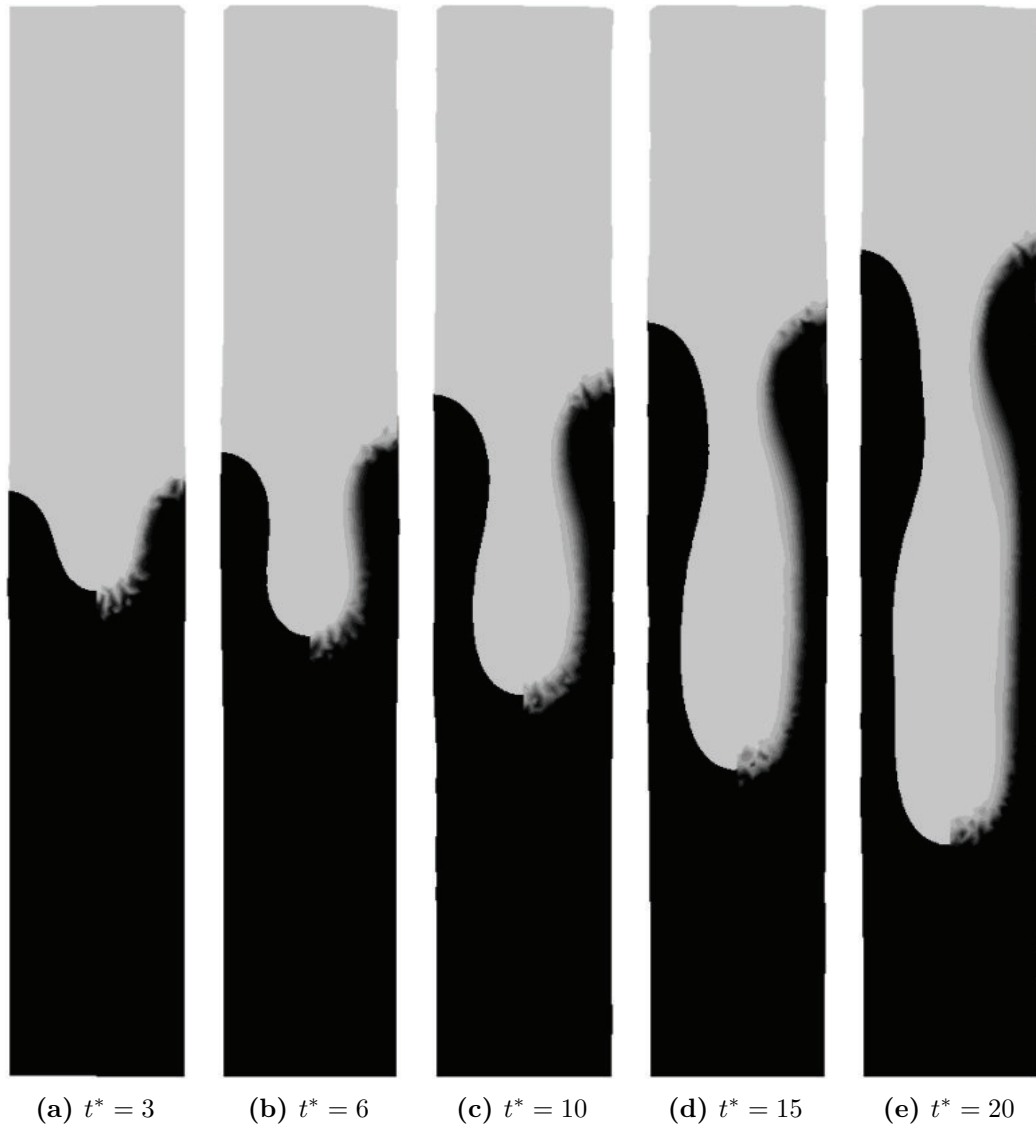


Figure 5.7: Time evolution of immiscible viscous fingering without (left) and with (right) the Cahn-Hilliard equation with the maximum growth rate and $\lambda = \lambda_m$. The density ratio is unity and the viscosity ratio is $A = 1/3$. The contour of the two phases is shown with the grey scale fitted to $\omega \in [0.1, 0.5]$ in 10 steps. Lower and larger concentrations are clipped.

5.4) is shown in Fig. 5.7. On the left side we see the previous results and on the right side we see the results with a diffuse interface. The color indicates the concentration $\omega \in [0.1, 0.5]$ in 10 steps. The viscosity ratio is still $A = 1/3$. Higher and lower concentrations are clipped to enable direct comparison.

We see that the interface between the fluids is diffuse but the growth of the finger tip is similar. Therefore we conclude that the dynamics of immiscible fingering is almost unchanged by the diffuse interface. At later times we see small deviation at the bottle neck of the finger. The length of the bottle neck is shorter in the diffuse case. Reasons for that are the dispersion effect in radial direction and an increase of the viscosity in the dark phase because the system tends to phase separate. Therefore the mass fraction increases near the interface in the dark phase. Similar effects are observed in the experiments in Chap. 2 for different viscosity ratios.

5.3.4 Influence of different diffusion coefficients on the shape of fingers

Next we investigate the influence of different diffusion coefficients on the shape of the finger. The fluid properties and the simulation parameters are summarized in Tab. 5.2. The simulation domain is the same as in the previous sections using $L \cdot W = 180 \times 30$ particles. We assume that the more viscous phase 2 is unstable and consider a binary mixture where phase 1 corresponds to a mass fraction $\omega < 0.5$ and phase 2 corresponds to a mass fraction $\omega \geq 0.5$. We alter the diffusion coefficient between $D = 10^{-7} m^2/s$ and $D = 10^{-5} m^2/s$.

The shapes of the viscous finger for 3 different diffusion coefficients are shown in Fig. 5.8. All shapes are shown at the same time step $t = 150s$. The grey scale indicates the composition where a dark area represents a polymer rich region. With increasing diffusion coefficient we see that the polymer rich phase is darker indicating that phase separation is present. The color of the polymer lean phase is almost identical. At the tip of the fingers we observe very different behavior. For small diffusion coefficients we see that the influence of diffusion is very small. The interface between the phases is scattered and we don't have a smooth diffuse interface. Numerically such a system is not appropriately resolved because the diffuse interface evolves too slow compared to the motion of the fluid. Fig. 5.8c is shown here for completeness. For a medium diffusion coefficient (Fig. 5.8b) the interface between the phases is smooth and a single finger is observed. We identify an increase of the polymer content at the interface aligned parallel to the interface because phase 2 starts to

Table 5.2: Summary of properties of the fluids and parameters of Hele-Shaw cell for an immiscible system.

Parameter	Units	Value
b	[mm]	1.0
W	[mm]	155.0
L	[mm]	930.0
L_0	[mm]	5.167
$\rho_1 = \rho_2$	[kgm^{-3}]	100
ω_1	[$-$]	0.1
ω_2	[$-$]	0.5
V	[$mm s^{-1}$]	2.35
dp/dx	[Pam^{-1}]	430.1
A	[$-$]	1/3
η_1	[$mPas$]	10.0
σ	[mNm^{-1}]	34.68
Pe	[$-$]	$3.64 \cdot 10^6$
Re	[$-$]	1.82
D	[m^2s^{-1}]	see text

phase separate forming a dense layer. In this case the displacement is of the same magnitude as the dispersion.

For a high diffusion coefficient we find faster smoothing of the mass fraction than convective motion of the finger. We observe phase separation in front of the tip of the finger. We also observe stable alternating lamella followed by a bubble in front of the tip. We don't see finger pores. The morphology is very similar to the observed Liesegang patterns in Chap. 2. To highlight this similarity, we investigate the morphology in more detail. In Fig. 5.9 a time series of the simulation using $D = 10^{-5}m^2/s$ is shown. From top to bottom the time increases. We observe a viscous finger and an evolving alternating lamella-like structure. The alternating lamella-like structure indicates a diffusion front in the front of the finger. It can be seen that the diffusion front evolves faster than the viscous finger. Beside, the viscous finger evolves not only by convective transport but also by coalescence of the finger tip with a lamella.

Next we investigate the speed of the diffusion front. This is done by estimating the distance between the initial position of the finger tip and the position of the leading lamella over time (see Fig. 5.10). The simulation data is shown as symbols and

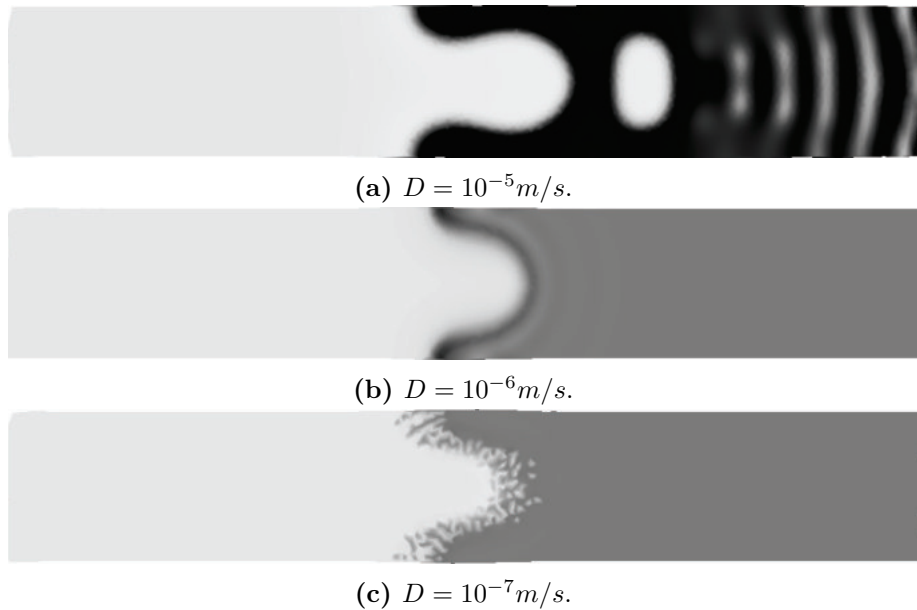


Figure 5.8: Shape of viscous finger at time $t = 150s$. Influence of different magnitude of diffusion coefficient during viscous fingering. From top to bottom we decreased the diffusion coefficient by a factor of 10. The grey scale indicates the composition where black represents pure polymer in the polymer rich phase.

the solid line represents a power law fit. The simulation data is not smooth because we identify the diffusion front using a threshold for the composition $\omega > 0.5$ on the alternating lamella. The slope of the fitted power law is approximately 0.7. For pure diffusion we would expect a slope of 0.5 as shown for the experiments in Fig. 2.7. Nevertheless, it is much smaller than the slope for viscous fingering.

We conclude that immiscible viscous fingering is modeled accurately with the proposed model. In the next section we investigate miscible viscous fingering because it is the other extreme case with negligible surface tension.

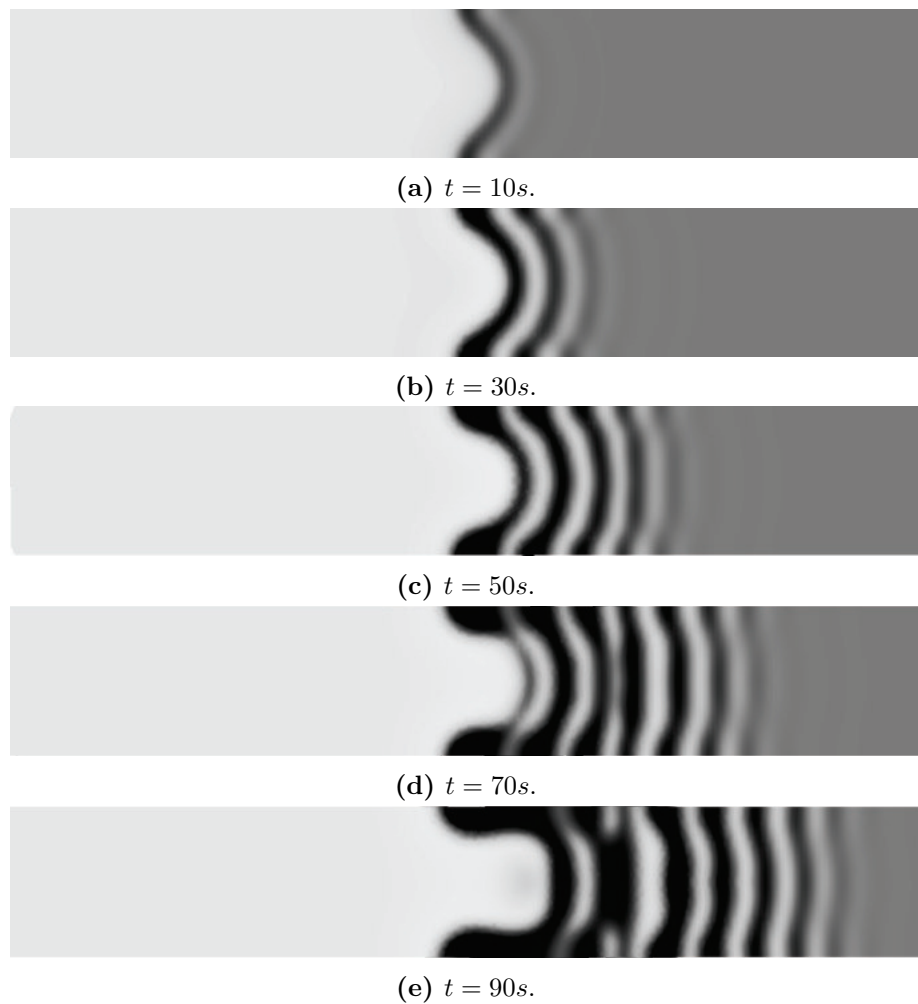


Figure 5.9: Time series of the shape of a viscous finger with $D = 10^{-5}m^2/s$. Increasing time from top to bottom. The grey scale indicates the composition where black represents pure polymer in the polymer rich phase.

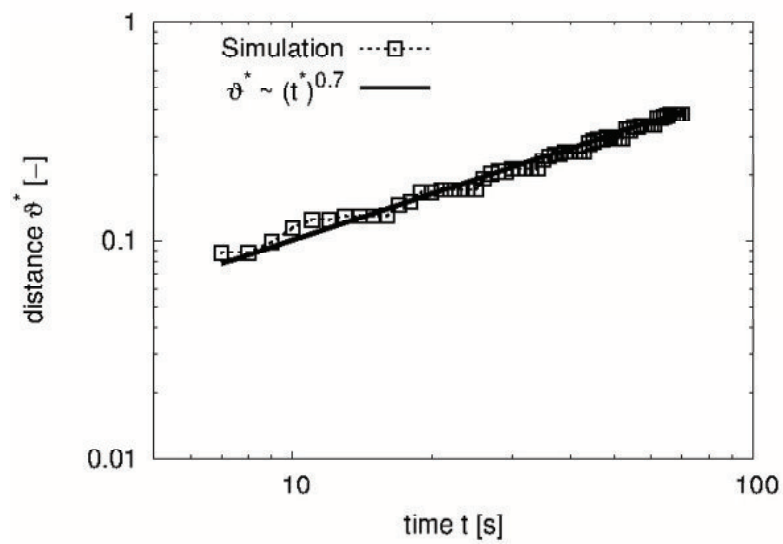


Figure 5.10: Evolution of diffusion front over time for the case $D = 10^{-5} m^2/s$. The power law is a fit of the simulation data.

5.4 Miscible Fingering

Miscible viscous fingering is typically discussed in the context of porous media or reactive miscible systems [Hej10; Hom87]. In contrast to immiscible viscous fingering the viscosity depends on concentration and the interface between the fluids is very smooth due to dispersion. Here we only highlight the differences between immiscible and miscible viscous fingering and refer to detailed discussions in literature [Hom87]. The mathematical analysis is more difficult for miscible system. Theoretical analysis of the limit of stability are only available for the case of a jump in viscosity at the interface (but still consider dispersion). The first analysis is found in [Chu59] and reviewed by Homsy [Hom87]. Here we summarize the main results.

The critical wavelength of an initial perturbation (initial tip to tip distance of the fingers) between two regions of different concentration is

$$\lambda_c = \frac{4}{A Pe}. \quad (5.15)$$

Here A and Pe are the dimensionless viscosity ratio and the Peclet number

$$Pe = \frac{UW}{D} \quad (5.16)$$

with the diffusion coefficient D . The characteristic velocity $U = V$ is the velocity of displacement. In the simulations in this section we choose the characteristic velocity as the mean velocity of displacement. The viscosity η_2 depends on composition as

$$\mu_2 = (1 + \beta\omega) \mu_1. \quad (5.17)$$

β is a constant. The corresponding wavelength of maximum growth rate is

$$\lambda_m = (2\sqrt{5} - 4) \lambda_c. \quad (5.18)$$

We define the dimensionless time and length of miscible viscous fingering as

$$t^* = \frac{U \cdot t}{W} \quad (5.19)$$

and

$$\vartheta^* = \frac{\vartheta}{W}. \quad (5.20)$$

Note that dispersion is not scaled. An attempt to find a characteristic law of miscible fingering is shown in Pramanik et al. [Pra15]. They found that the width of the mixing area of the interface scales linearly with the square root of the time

$$\vartheta^* \sim \sqrt{t^*} \quad (5.21)$$

where the mixing area ϑ^* is defined as the region between 0.001% to 0.999 % of the maximum concentration. They justified this relation because they found that the mixing area scales linearly with the square root of the Peclet number. They also found that this relation holds only for the beginning of miscible viscous fingering as long as the dispersion perpendicular to the initial interface between the fluids is dominant and fingers grow unidirectional. For later times

$$\vartheta^* \sim (t^*)^{0.5+a} \quad (5.22)$$

with a as a positive constant. We will show later that $a = 0.3$ and therefore

$$\vartheta^* \sim \sqrt{(t^*)^{1.6}} \quad (5.23)$$

is similar to immiscible viscous fingering except for the square root.

In this section we demonstrate that the proposed model predicts the dynamics of miscible viscous fingering. Therefore we consider the component and momentum balance but neglect surface tension and fluctuations of the mass fraction. We consider binary diffusion of a tracer. We also neglect the gradient term of the partial mass density in the Cahn-Hilliard equation because its effect is very small due to the low gradient in partial mass. We assume that it is possible to exchange the chemical potential in the driving force by the concentration. Then, the component balance simplifies to Fickian diffusion equation. In addition, we assume that the viscosity depends on the tracer concentration. The simulation parameters are summarized in Tab. 5.3. We vary the diffusion coefficient to alter the wavelength of the initial perturbation. The setup is the same as for immiscible viscous fingering

Table 5.3: Summary of fluid properties and parameters of the Hele-Shaw cell for a miscible system.

Parameter	Units	Value
b	$[mm]$	1.0
W	$[mm]$	155.0
L	$[mm]$	930.0
$\rho_1 = \rho_2$	$[kgm^{-3}]$	100
ω_1	$[-]$	0.0
ω_2	$[-]$	0.5
β	$[-]$	2
V	$[mms^{-1}]$	2.35
dp/dx	$[Pam^{-1}]$	430.1
A	$[-]$	1/3
η_1	$[mPas]$	10.0
D	$[m^2s^{-1}]$	see text
D_c	$[m^2s^{-1}]$	$4.705 \cdot 10^{-6}$

including the initial perturbation shown in Eq. 5.13. The pressure gradient is $dp/dx = 430.1 Pam^{-1}$ and we use a resolution of 180×30 particles for the Hele-Shaw cell. The value of the constant β in Eq. 5.17 is 2 assuming that the maximum concentration in the system is $\omega_{max} = 0.5$. The initial concentrations are $\omega_1 = 0$ and $\omega_2 = 0.5$

We investigate the limit of stability, compare it to the theoretical value and analyze the dynamics of displacement. We skip a study of convergence because we expect analog behavior as for immiscible viscous fingering.

5.4.1 Limit of stability of displacement

We start with the analysis of the limit of stability of miscible displacement. We keep all simulation parameters (Tab. 5.3) except the diffusion coefficient constant. Therefore the wavelength of the initial perturbation increases linearly with the diffusion coefficient.

The distribution of mass fraction for 5 different diffusion coefficients are shown in Fig. 5.11 at time $t^* = 8$. On the left side we see the particle distribution and on the right side we see a smooth contour plot. The grey scale indicates the concentration in the range $\omega \in [0, 0.5]$. Instead of a critical wavelength we consider a critical diffusion coefficient D_c .

First we consider the case $D = D_c$ (Fig. 5.11e). Similar to immiscible viscous fingering the displacement is stable for the critical value $D = D_c$. When we decrease the diffusion coefficient to $D = 85\%D_c$ we still don't find a propagation of a finger. Quantitatively we confirm this observation by analyzing ϑ^* over time and find exactly $\vartheta^* \sim \sqrt{t^*}$. This indicates that dispersion is the dominant mechanism.

Then we further decrease the diffusion coefficient to $D = 47\%D_c$. This is the case of the maximum growth rate according to the theory. We see that a finger evolves slowly but as we will see later only by dispersion. Therefore the limit of stability is around $D = 47\%D_c$.

When we further decrease the diffusion coefficient we observe fingering (Fig. 5.11b). For the limit of a very low diffusion coefficient where the wavelength of stability is below the numerical resolution we observe stochastic-like mixing of the phases. This case is added for completeness, but clearly, we don't observe fingers because of numerical errors.

We found that the limit of stability is around $D = 47\%D_c$. This is clearly lower than predicted by the theory. A reason may be that the critical wavelength was derived by assuming a sharp interface but enable dispersion over the interface. In the simulations we find a very diffuse interface between the fluids. This is a clear contrast. A diffuse interface increases the size of the initial perturbation due to dispersion. Therefore the wavelength is changed to a larger value. To compensate this, the wavelength of the initial perturbation needs to be smaller than the critical value from theory.

5.4.2 Analysis of the dynamics of displacement

Next we analyze the dynamics of displacement for miscible viscous fingering. We consider the case with maximum growth rate $\lambda = \lambda_m$. The particle distribution and the contour of the mass fraction at $t^* = 1.5, 3, 4.5, 6$ and 8 are shown in Fig. 5.12. The grey scale is divided in 10 steps so that iso-lines are visible.

We observe that the finger evolves and the mixing area between the fluids increases with time. We also observe that the shape of the initial perturbation remains as may be seen from the iso-lines. This indicates that dispersion in the direction of the flow dominates and viscous fingering dynamics may be small. We demonstrate this in Fig. 5.13a.

The size of the mixing area ϑ^* versus time t^* for $D = 10\%D_c$, $D = 21\%D_c$ and

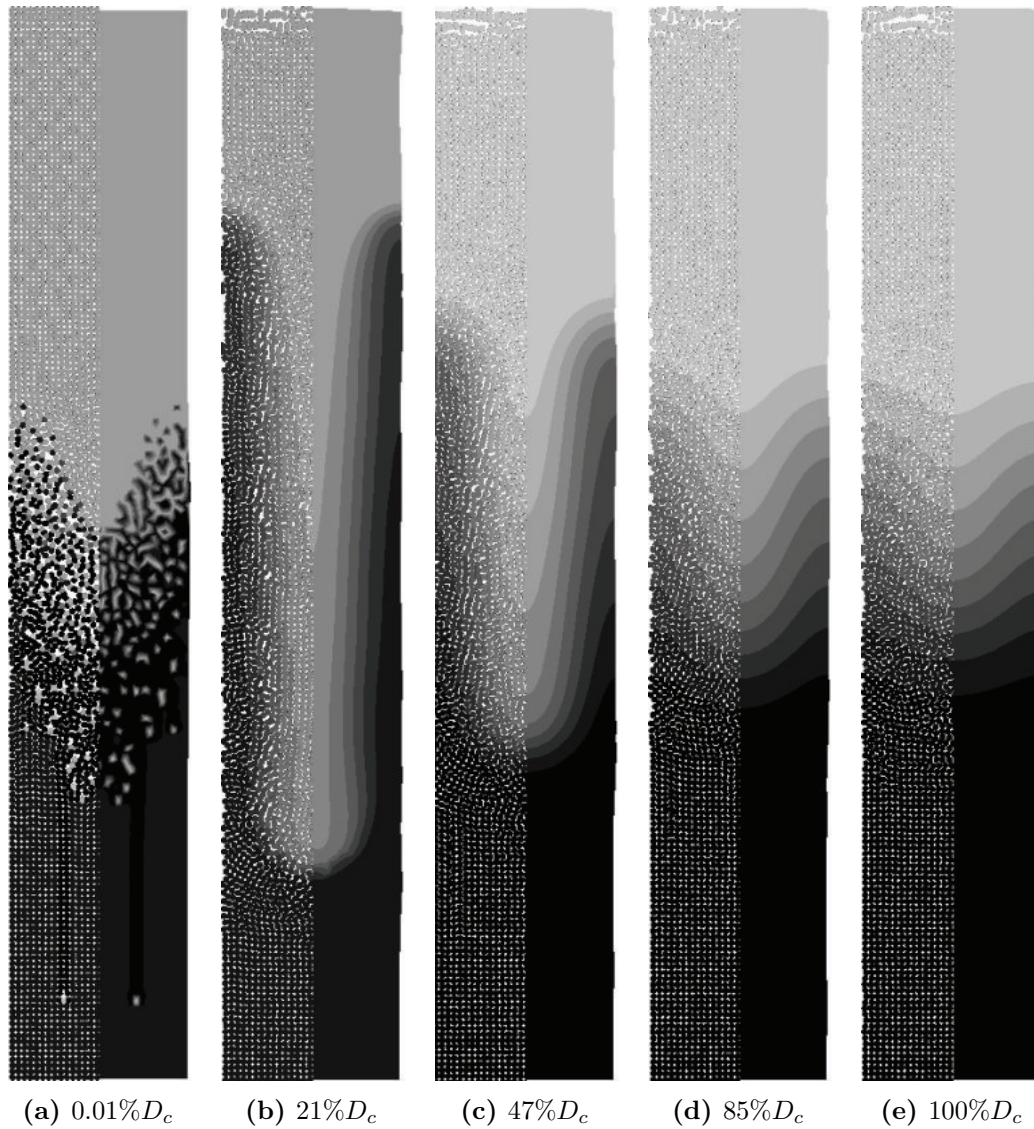


Figure 5.11: Stability of miscible viscous fingering with different wavelength of the perturbation at $t^* = 8$. The limit of stability is between $D = 21\%D_c$ and $D = 47\%D_c$. The density ratio is unity and the viscosity ratio is $A = 1/3$. On the left side the particle distribution and on the right side the contour plot of the two phases are shown. For $D = 0.01\%D_c$ the time is $t^* = 1.6$.

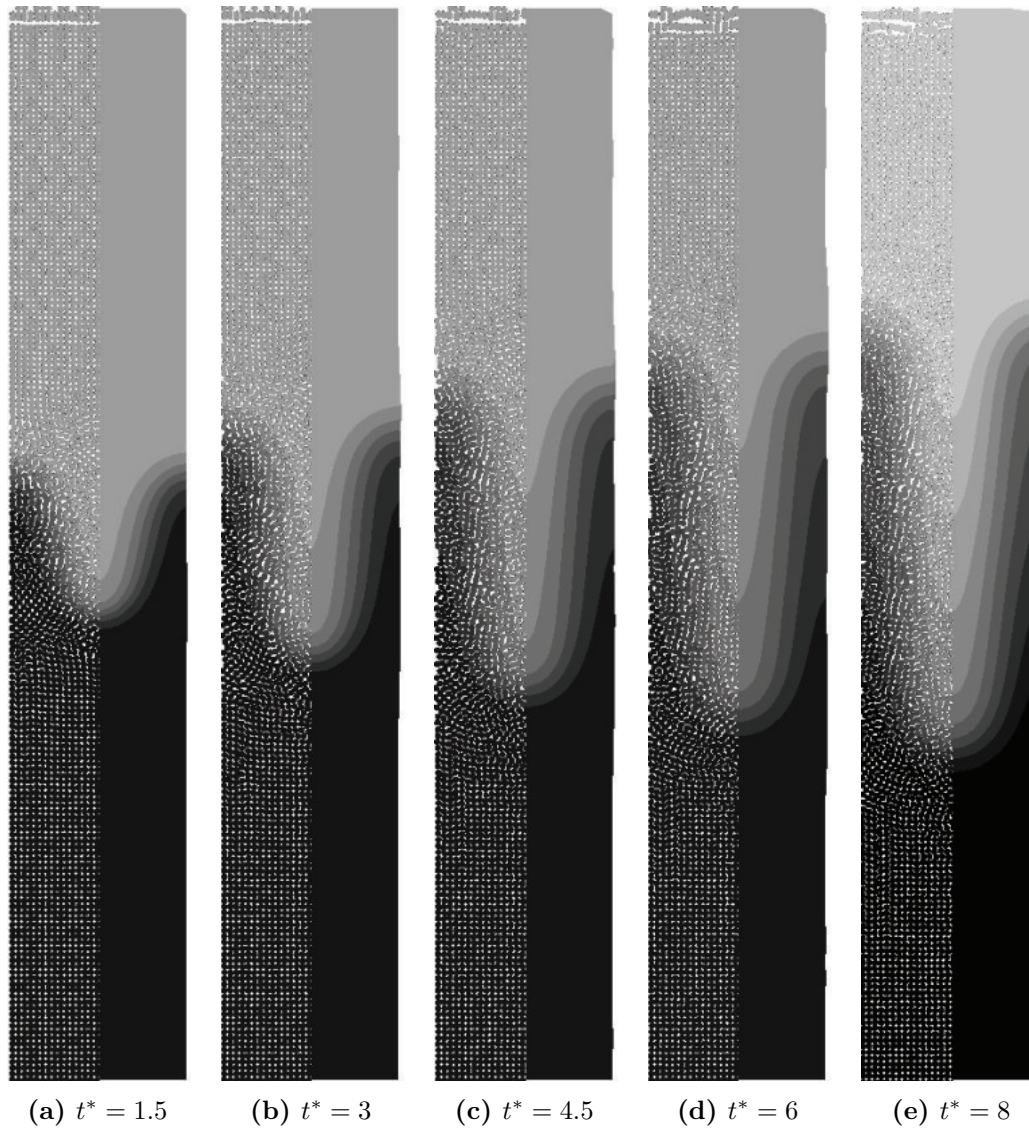
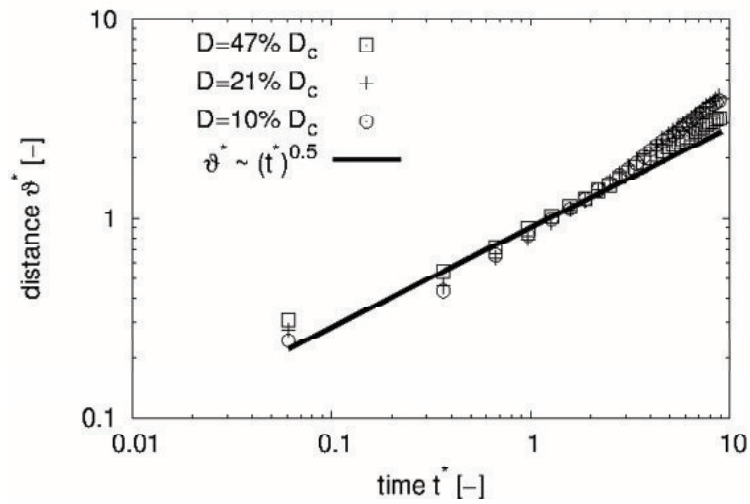
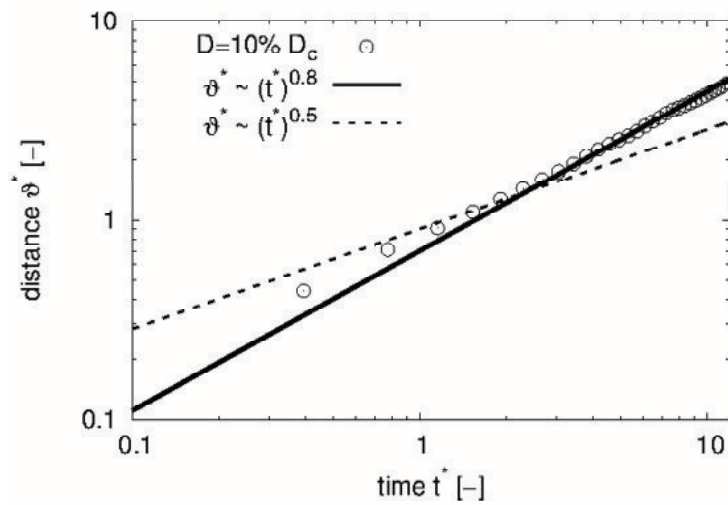


Figure 5.12: Time evolution of miscible viscous fingering with the maximum growth rate with wavelength of the perturbation $\lambda = \lambda_m$. The density ratio is unity and the viscosity ratio is $A = 1/3$. On the left side the particle distribution and on the right side the contour plot of the two phases are shown.



(a) Comparison of growth of mixing area for systems.



(b) Comparison of growth of mixing area to different power laws.

Figure 5.13: Top: Comparison of finger growth over time with theory of Pramanik et al. [Pra15] for different wavelengths. Bottom: Comparison of one wavelength ($D = 10\% D_c$) with power law for diffusive transport $\sim \sqrt{t^*}$ and power law similar to immiscible viscous fingering $\sim (t^*)^{0.8}$.

$D = 47\%D_c$ are shown in Fig. 5.13a. As a reference we plot Eq. 5.21 too. We see that $D = 47\%D_c$ follows the scaling law for dispersion $\vartheta \sim \sqrt{t^*}$ (Eq. 5.21). Only at larger times the growth of the mixing area is larger and slowly changes to miscible fingering dynamics. The transition to fingering dynamics is faster for lower diffusion coefficients as shown in Fig. 5.13a for $D = 21\%D_c$ and $D = 10\%D_c$.

There remains the question about the scaling law for miscible viscous fingering when the dynamics is dominated by the instability instead of dispersion. The dynamics of fingering instability may be similar in miscible and immiscible systems. For immiscible systems we found that $\vartheta^* \sim (t^*)^{1.6}$ and for later times, when only flow through a channel is dominant, $\vartheta^* \sim t^*$. For miscible systems we may expect a similar behavior with a transition from the dynamics of dispersion, viscous fingering and flow through a channel.

We demonstrate the scaling law for $D = 10\%D_c$ in Fig. 5.13b. We found that $\vartheta^* \sim \sqrt{t^*}$ at the beginning when dispersion is dominant. For later times we observe a transition to $\vartheta^* \sim \sqrt{(t^*)^{1.6}}$. We haven't observed a third transition in the simulations. The reason is that the finger never formed a bottle-like shape.

5.5 Comparison of fingering dynamics to experiments

As a result of the last two sections, we conclude that the growth of finger pores are similar to immiscible viscous fingering. Therefore we only consider immiscible viscous fingering in the remainder of the thesis. In this section we use the criterion of instability for immiscible viscous fingering (Eq. 5.3) to identify experiments presented in Chap. 2 that show the dynamics of viscous fingering.

We calculate the critical wave length using Eq. 5.4. In addition we estimate the velocity of displacement using the Washburn equation [Was21] to determine the characteristic velocity in the experiments. In a Hele-Shaw cell the stationary average velocity neglecting inertial and gravitational effects is

$$|\vec{U}| = \frac{b^2 \Delta p}{12\eta W}. \quad (5.24)$$

W , b and η are the characteristic length of the channel, the width of the gap and the viscosity of the coagulation bath, e.g. water. With the capillary pressure

$$\Delta p = \frac{2\sigma \cos\alpha}{b} \quad (5.25)$$

the characteristic velocity is

$$|\vec{U}| = \frac{b\sigma \cos\alpha}{6\eta W}. \quad (5.26)$$

We assume that the characteristic length in the Hele-Shaw cell is $W = 10\text{mm}$ because it represents a characteristic width of the morphology found in the experiments. In the experiments the height of the cell is $b = 50\mu\text{m}$. The contact angle between pure water and glass is approximately $\alpha = 51^\circ$ and the surface tension of water-air is $\sigma = 72.8\text{mN/m}$. The characteristic length in flow direction in the Hele-Shaw cell is approximately $L = 30\text{mm}$. This is the length that the non-solvent mixture is accelerated until contact with the polymer solution. For the first moments of displacement this represents the characteristic velocity of displacement. The viscosity of the non-solvent is used in the Washburn equation (Eq. 5.26) because it is the counterpart to the capillary force that accelerates the coagulation bath due to wetting of coagulation bath on the glass slides in the experiment. We calculate the critical wavelength of perturbation λ_c using the surface tension of PSf-water $\sigma = 70.5\text{mN/m}$.

In Tab. 5.4 we present the characteristic velocity $|\vec{U}|$ and the wave length of critical perturbation. If no critical wavelength is given the displacement should be stable. We see that the velocity decreases with increasing viscosity of the non-solvent mixture. The critical wave length increases with decreasing velocity. The critical wave length also decreases with increasing viscosity of the polymer solution when the viscosity of the coagulation bath is constant.

We analyze the critical wavelength to identify a critical wavelength below which finger pores grow as viscous fingers. For a polymer solution of 15/85 wt% PSf/NMP and a coagulation bath of 99.9/0.01 wt% H₂O/Agar no critical wavelength exist because the interface is stable. We found sponge pores in this case. Finger pores are found for a polymer solution of 15/85% PSf/NMP and a coagulation bath of 100 wt% H₂O. The calculated critical wavelength is $\lambda_c = 7.63\mu\text{m}$. We expect that

Table 5.4: Analysis of stability of displacement λ_c and velocity of displacement $|\vec{U}|$. FP, SP and LP represents finger pores, sponge pores and Liesegang patterns.

#	FP/SP/LP	λ_c [μm]	$ \vec{U} $ [mm/s]	Composition polymer solution [wt %]					Composition coagulation bath [wt %]				
				PSf	PVP	PEG	Agar	NMP	PVP	PEG	Agar	H ₂ O	
1	FP	7.63	12.7	15	-	-	-	85	-	-	-	100	
2	FP	14.8	3.38	15	-	-	-	85	1	-	-	99	
3	FP	24.3	1.27	15	-	-	-	85	2	-	-	98	
4	FP	30.5	0.81	15	-	-	-	85	3	-	-	97	
5	FP	58.5	0.23	15	-	-	-	85	6	-	-	94	
6	FP	8.36	10.6	15	-	-	-	85	-	1	-	99	
7	LP	10.8	6.36	15	-	-	-	85	-	2	-	98	
8	FP/SP	11.8	5.30	15	-	-	-	85	-	3	-	97	
9	FP/SP	12.8	4.55	15	-	-	-	85	-	6	-	94	
10	FP	31.8	0.75	15	-	-	-	85	-	-	0.01	99.99	
11	FP	54.7	0.26	15	-	-	-	85	-	-	0.025	99.975	
12	FP	146	0.051	15	-	-	-	85	-	-	0.05	99.95	
13	FP/SP	-	0.014	15	-	-	-	85	-	-	0.1	99.9	
14	FP/SP	8.96	12.7	15	1	-	-	84	-	-	-	100	
15	FP/SP	4.62	12.7	15	2	-	-	83	-	-	-	100	
16	SP	3.80	12.7	15	3	-	-	82	-	-	-	100	
17	FP/SP	1.94	12.7	15	6	-	-	79	-	-	-	100	
18	FP	7.27	12.7	15	-	1	-	84	-	-	-	100	
19	FP	6.56	12.7	15	-	2	-	83	-	-	-	100	
20	FP/SP	4.36	12.7	15	-	3	-	82	-	-	-	100	
21	SP	5.32	12.7	15	-	6	-	79	-	-	-	100	
22	FP/SP	7.40	12.7	15	-	-	0.01	84.99	-	-	-	100	
23	FP/SP	6.95	12.7	15	-	-	0.025	84.975	-	-	-	100	
24	FP/SP	7.99	12.7	15	-	-	0.05	84.95	-	-	-	100	
25	FP/LP/SP	7.23	12.7	15	-	-	0.1	84.9	-	-	-	100	

systems with the same velocity of displacement $|\vec{U}|$ but lower critical wavelength also lead to finger pores. As seen in Tab. 5.4, e.g. for a polymer solution of 15/3/82 wt% PSf/PVP/NMP and a coagulation bath of 100 wt% H₂O ($\lambda_c = 3.80\mu m$), this is not the case. This is more obvious if we plot the number of experiment over the critical wavelength λ_c (Fig. 5.14). There is no correlation between morphology and critical wavelength because for small critical wavelength all kind of morphology is present. A characterization of pores using only the critical wavelength may not be possible. Since only the difference in the viscosity between polymer solution and coagulation bath is considered in the critical wavelength, an additional parameter characterizing the ratio between diffusive and convective transport (e.g. phase separation and viscous displacement) may be necessary. This may be studied in detail in further work on viscous fingering in flat sheet membranes.

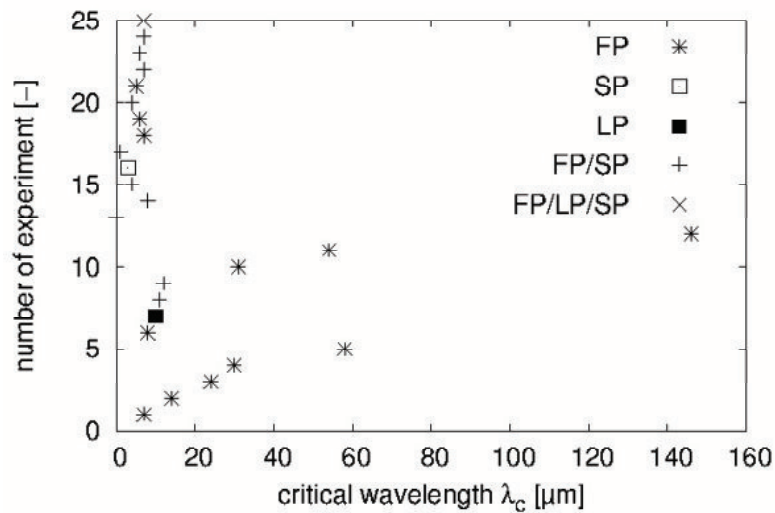


Figure 5.14: Number of experiment plotted over critical wavelength λ_c .

5.6 Conclusion

In this chapter we demonstrated that our model predicts immiscible viscous fingering within a reasonable accuracy compared to studies on Rayleigh-Taylor instability (RTI). RTI is very similar to viscous fingering but the mechanism is different. We investigated immiscible and miscible viscous fingering separately. In theory there exists a critical wave length of a perturbation at the interface that leads to viscous fingering. We found that within a deviation of 15-20% the model matches the stability criterion. An analysis of the growth of a single finger shows that the finger grows with the super-linear power law until a contraction of the finger is formed for immiscible fluids. The same behavior was found in the previous experiments. This indicates that the dynamics involved in the experiments and immiscible viscous fingering may be similar. After contraction, the finger grows with a linear power law indicating that viscous flow in a channel dominates. We also demonstrated that a diffuse interface between the fluids leads to similar results than a sharp interface. For a diffuse interface we need to specify a diffusion coefficient in the component balance. We varied the diffusion coefficient and demonstrated that for large diffusion coefficients lamella-like structures are visible. Fingers grow mainly by coalescence of lamella with the finger tip. Analyzing the evolution of the diffusion front, we found that it propagates similar than in the experiments. Conclusively, the lamella-like structures are not a result of convective but of diffusive mass transport.

In the second part of the chapter we demonstrated the influence of diffusion by investigating miscible viscous fingering for a binary system. We found that the theoretical critical wave length that leads to finger growth is not matched. The reason is that in theory a sharp interface is assumed but in the simulation the interface is very diffuse. An analysis of the dynamics of the finger growth shows that the regimes of growth are reversed and altered compared to immiscible viscous fingering. First diffusion in a channel and then fingering instability is present. The power law is proportional to the square root of the time instead of the time itself. We conclude that immiscible viscous fingering may be present in the experiments. Finally we compared the stability criterion of a Hele-Shaw cell to the experiments of Sec. 2.3. We were not able to characterize the formation of finger pores using the stability criterion. There is no relation between critical wavelength of a perturbation at the interface between polymer solution and coagulation bath, and the morphology

of the membrane. As seen in the analysis in Sec. 2.3.5, viscous fingering is only present in the first moments after contact of polymer solution and coagulation bath. Later another effect dominates the evolution of the morphology. This effect may be the propagation of a diffusion front as we have seen in the study of immiscible viscous fingering. Therefore, since viscous fingering is only present in the first moments of evolution of morphology, there exist doubts about the relevance of viscous fingering on morphology because the experimental setup (fluids in a small gap between two solids) is a Hele-Shaw cell. For example, if one glass slide would be omitted in the experiment, viscous fingering is not present but finger pores may evolve.

We investigate the propagation of a diffusion front in the next chapter because the velocity of a diffusion front may be very relevant to the morphology in polymer membranes.

CHAPTER 6

Liesegang pattern

In Chap. 2 we found lamella-like structures in the experiments and analyzed that the propagation velocity of the morphology corresponds to a pure diffusive mass transport. In the last chapter we observed lamella in front of a viscous finger. These lamella are found in so-called Liesegang patterns. In this chapter we investigate Liesegang patterns formation during the formation of pores in porous membranes. Liesegang patterns were very recently postulated as mechanism for membrane formation by Foard & Wagner [Foa12b]. We extend the work of Foard & Wagner to highlight characteristics of polymer membranes that are found in Liesegang patterns. In 1896, Liesegang [Lie96] observed periodic pattern of alternating structures, so-called Liesegang patterns. An example are chemical reaction systems where an electrolyte E_1 with low viscosity diffuses into another electrolyte E_2 or gel with a higher viscosity. At the mixing front a chemical reaction takes place. Liesegang patterns evolve with the moving reaction front and form alternating bands or rings [Ant99]. A review of Liesegang patterns is found e.g. in [Ste54].

Liesegang patterns are also observed in phase separating systems [Foa12b]. The characteristics of a chemical reaction system are very similar to an immersion precipitation system when a non-solvent diffuses into a more viscous polymer solution and the precipitation front moves towards the polymer solution. Here we observe alternating pattern of precipitate behind a moving phase separation front. This was previously investigated by Ball [Bal90], Hantz and Biro [Han06], Köpf et al. [Köp10] and Foard [Foa12a; Foa09; Foa12b].

Foard and Wagner [Foa09] first proposed Liesegang patterns to explain the mor-

phology of polymer membranes and showed that finger and sponge pores may be found in Liesegang patterns in 2D [Foa12b] and 3D (in the appendix of [Foa12a]). They concluded that a lot more investigations on Liesegang patterns are necessary to analyze the influences of various process conditions on the morphology of polymer membranes.

The proposed model in Chap. 3 is already able to predict Liesegang patterns. But, as described in Sec. 3.4.2, it is difficult to use a real ternary system of polymer, solvent and non-solvent because the gradients of the chemical potential are large and need to be resolved in the diffuse interface for accurate results. Therefore, in the first part of this chapter, we simplify the ternary system to a binary system with simple thermodynamics. Then characteristics of thermodynamics and kinetics, as two major phenomena that explain different type of pore shapes, and the computational setup are introduced. We demonstrate that the proposed SPH model predicts similar morphology than observed in the experiments in Chap. 2. From application point of view, the transition from sponge pores to macrovoids are of major importance. We investigate the transition from sponge pores to macrovoids and the transition from lamella-like structures to macrovoids and highlight its relation to the preparation process of immersion precipitation membranes.

In an outlook, Foard concluded that thermal fluctuations may be important to simulate realistic pore structures. In the second part of this chapter we investigate the influence of thermal fluctuations on the pore shape. Finally we include hydrodynamics and investigate their influence on the morphology.

6.1 Simplification of ternary to binary system

6.1.1 Recap of realistic ternary system

Before we simplify our model, we first recap the realistic system of a polymer solution (polymer + solvent) and a coagulation bath (non-solvent). A ternary phase diagram is shown in Fig. 6.1. There are 4 points indicated as A , B , C and D that are important for the following discussion. Points A and D represent the composition of the homogeneous bulk phases of the polymer solution and the coagulation bath. B and C indicate corresponding equilibrium compositions on the binodal.

Next, we analyze the profiles of mass fractions when polymer solution and coagulation bath are in contact. In Fig. 6.2 the mass fractions are plotted orthogonal to the

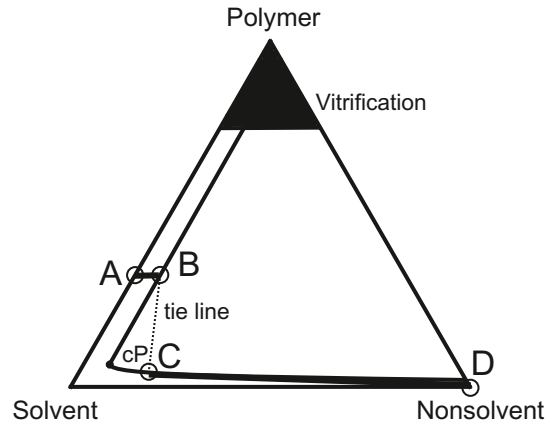
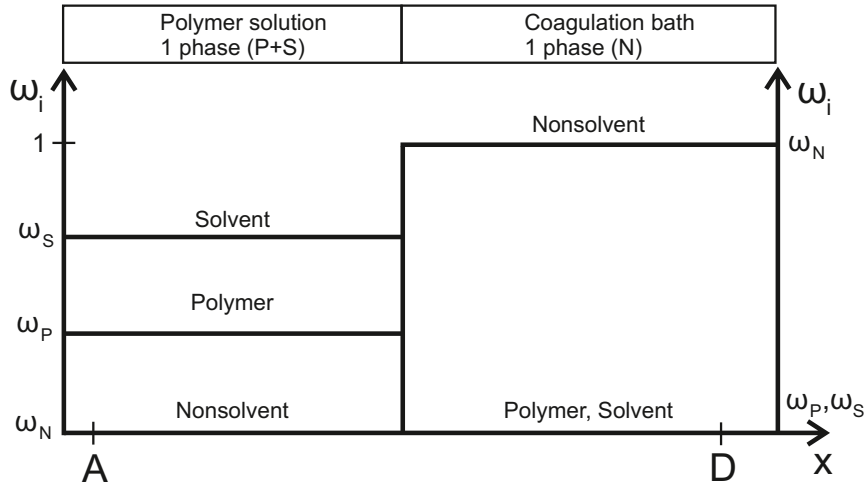


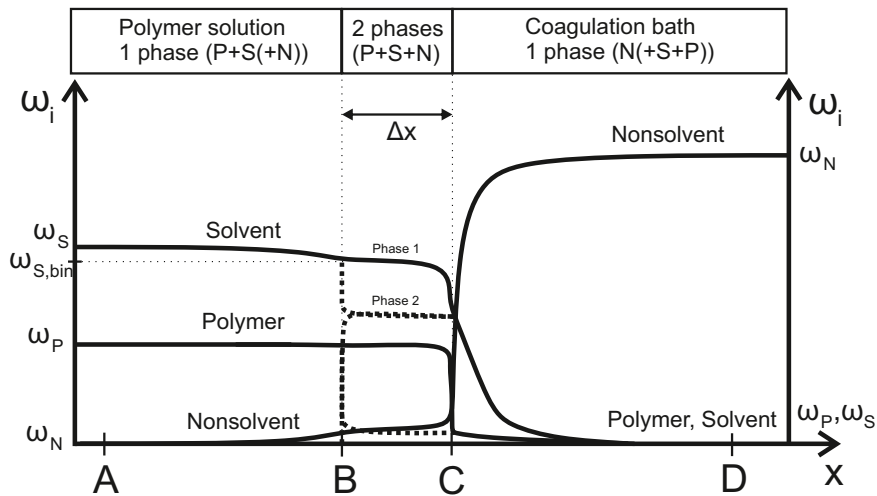
Figure 6.1: Schematic plot of a ternary phase diagram of polymer, solvent and non-solvent with a miscibility gap between polymer and non-solvent. The spinodal is not shown. *A* indicates an initial composition of the polymer solution. *B* indicates the composition on the binodal. *C* indicates the composition in the polymer lean phase at phase equilibrium. *D* indicates the initial composition of the coagulation bath.

interface between polymer solution and coagulation bath. At time $t = 0^-$ (Fig. 6.2a) the transition between polymer solution and coagulation bath is sharp. The polymer solution only consists of polymer and solvent and the coagulation bath only consists of non-solvent. The composition of these two phases corresponds to points *A* and *D* in Fig. 6.1.

For $t > 0$ the sharp transition between the polymer solution (left) and the coagulation bath (right) smooths out because small amount of polymer, solvent and non-solvent diffuses into the other phase. Within the smooth transition between the polymer solution and coagulation bath, at equilibrium, a composition exists that corresponds to *B* and *C* in Fig. 6.1. An example is the mass fraction of solvent on the binodal $\omega_{s,bin}$ at point *B*, as indicated in Fig. 6.2b. Between these points the mixture is unstable and phase separates into *B* and *C*. This is indicated in Fig. 6.2 by solid and dashed lines, named as Phase 1 and Phase 2, and is the region where morphology evolves. The size of this region is Δx and depends on the change of composition in the polymer solution and coagulation bath over time. In other words, it depends on the kinetics of the system. We link the term phase separation front velocity u_{ps} with the change of Δx in time.



(a) Schematic plot of mass fractions of polymer, solvent and non-solvent at time $t = 0^-$.



(b) Mass fraction normal to the interface between polymer solution (left) and coagulation bath (right) at time $t > 0$. Between the homogeneous, stable phases a two phase region exists where morphology evolves. In the two phase region solid and dashed lines indicate the corresponding phase equilibrium (Point B (Phase 1) and C (Phase 2)). The extension of the two phase region is Δx . $\omega_{s,bin}$ indicates the mass fraction of solvent on the binodal (point B). P, S and N represent polymer, solvent and non-solvent.

Figure 6.2: Profiles of composition over space orthogonal to the phase separation front for two different times. Top: $t = 0^-$. Bottom: $t > 0$

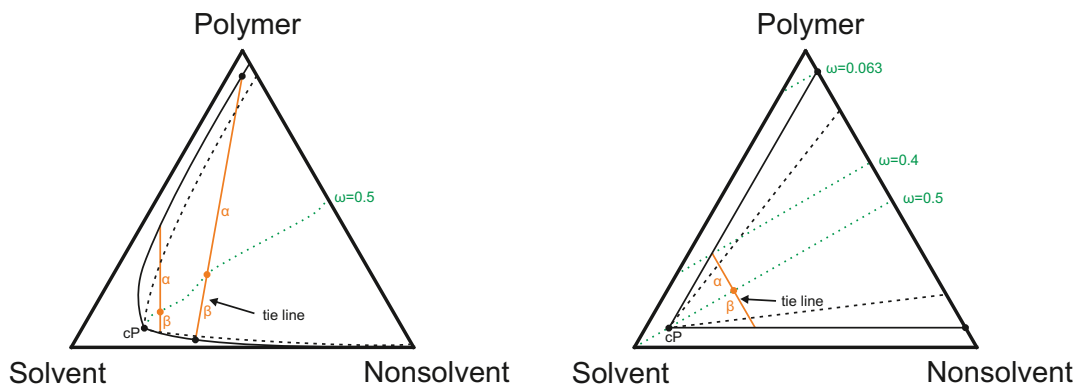
6.1.2 Simplified binary model

In the following we simplify the realistic ternary system to a reduced binary system in 3 steps. First we define auxiliary quantities and then we reduce the mass transport in the polymer solution outside and inside of the miscibility gap. The mass transport outside of the miscibility gap is approximated by the front velocity and the initial, binary composition. Inside of the miscibility gap we solve a component balance for a reduced composition. Finally, we approximate the ternary thermodynamics for a reduced binary mixture.

Definition of auxiliary quantities

The tie line connects corresponding compositions in phase equilibrium. The characteristics of the free energy along each tie line is similar. It shows two minimum at the phase equilibrium and a maximum in between. As shown in Fig. 6.3, we divide the tie line into two parts from the maximum of the free energy (orange dot) to each minimum on the binodal. The parts are labeled α and β . The fraction of each part is $\alpha/(\alpha + \beta)$ and $\beta/(\alpha + \beta)$ and indicates the fraction of polymer rich and polymer lean phase. The sum of the fractions is unity.

In Fig. 6.3a the phase diagram of a realistic ternary mixture is shown. α and β vary



(a) Phase diagram of realistic ternary system.

(b) Phase diagram of simplified system.

Figure 6.3: Schematic plot of phase diagrams of realistic (left) and simplified (right) ternary systems. Black solid and dashed lines indicate the binodal and spinodal. cP is the critical point. Definition of auxiliary quantities ω (green), and α and β (orange). The orange dot indicates the maximum of the free energy along each tie line.

for each tie line. The ternary phase diagram of the fluid mixture in the simplified model is shown in Fig. 6.3b. We assume that the miscibility gap and the free energy along each tie line are symmetric. Therefore, $\alpha = \beta$ and $\alpha/(\alpha + \beta) = \beta/(\alpha + \beta) = 0.5$. Next, we define the auxiliary quantity ω

$$\omega = \omega_N + \frac{\beta}{\alpha + \beta} \omega_S \quad (6.1)$$

and

$$1 - \omega = \omega_P + \frac{\alpha}{\alpha + \beta} \omega_S, \quad (6.2)$$

respectively. In the ternary phase diagrams in Fig. 6.3, $\omega = \text{const.}$ represents an contour line. In the realistic ternary system, the shape of the contour line may vary depending on the ratio between α and β while in the simplified system each contour line is a straight line perpendicular to the binary polymer/non-solvent axis because of the symmetry of the free energy in the miscibility gap. Using Eqs. 6.1 and 6.2 and $\alpha = \beta$, we get

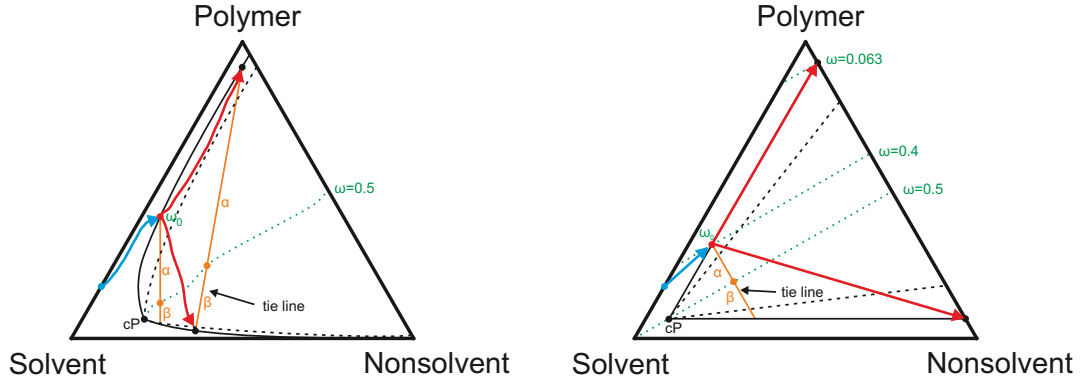
$$\omega_N = 2\omega - 1 + \omega_P \quad (6.3)$$

in the binary system.

Mass transport in the polymer solution outside of the miscibility gap

Next, we simplify mass transport in the polymer solution outside of the miscibility gap. This region is shown in Fig. 6.2b on the left side. The composition path of the initial polymer solution to the composition on the binodal where a mixture enters the miscibility gap is shown as blue line in Fig. 6.4. There arise the following questions: What is the direction of the composition path? How long does it take to reach the composition on the binodal? To answer these questions, we consider the mass balance in the homogeneous polymer solution

$$\frac{dm(t)}{dt} = \dot{m}^+ - \dot{m}^- \quad (6.4)$$



(a) Phase diagram of realistic ternary system.

(b) Phase diagram of simplified system.

Figure 6.4: Schematic plot of phase diagrams of realistic (left) and simplified (right) ternary systems. Composition path in homogeneous polymer solution (blue) and heterogeneous polymer solution (red).

with the time dependent mass $m(t)$ and the mass flux \dot{m}^+ into and \dot{m}^- out of the homogeneous polymer solution. In integral form the mass balance is

$$\frac{dm(t)}{dt} = \oint_{\Omega} \sum_j (\vec{j}_j \cdot \vec{n}) d\Omega \quad (6.5)$$

with the mass flux \vec{j}_j of component j across the surface Ω and the normal \vec{n} pointing out of the polymer solution. We assume that the density of the polymer solution is constant and therefore

$$m(t) = \rho V(t). \quad (6.6)$$

Assuming that mass transport of polymer is negligible (mass flux of polymer $\vec{j}_{Polymer}$ is very small), solvent diffuses out and non-solvent diffuses into the polymer solution, and with

$$\oint_{\Omega} d\Omega = \Omega, \quad (6.7)$$

the mass balance is

$$\rho \frac{dV(t)}{dt} = \Omega (\vec{j}_N - \vec{j}_S). \quad (6.8)$$

It indicates that if the mass flux of solvent out of the polymer solution is larger than the mass flux into the polymer solution, then the polymer solution shrinks. Assuming that the mass flux into and out of the polymer solution is uni-directional in x-direction

$$\frac{dV(t)}{dt} = \Omega \frac{dx(t)}{dt}, \quad (6.9)$$

we get

$$\frac{dx(t)}{dt} = \frac{1}{\rho} (\vec{j}_N - \vec{j}_S) = -u_{ps} \quad (6.10)$$

We define the change of the volume as the negative velocity u_{ps} .

Eq. 6.10 indicates that the composition path in the polymer solution outside of the miscibility gap (blue path in Fig. 6.4) is controlled by the ratio of the mass flux of solvent and non-solvent that may be time-dependent. The time to reach the binodal depends on the difference between the mass fluxes and is related to the shrinkage of the polymer solution and, therefore, to u_{ps} . If u_{ps} is large, the time to reach the binodal is short.

In the realistic ternary system, we need to solve the component balance for each component and, as a result, get u_{ps} . If the position of the binodal is known, then an initial composition of the polymer solution is directly related to the composition at the binodal where we enter the miscibility gap.

In the simplified model, we do not solve the component balance in the homogeneous polymer solution. Therefore we are not able to connect an initial composition of the polymer solution with the composition on the binodal. But since we are only interested in the evolution of morphology, and therefore only in the transport inside the miscibility gap, it is only necessary to know the composition on the binodal to quantify morphology. Therefore, we use the composition on the binodal, ω_0 , where we enter the miscibility gap as an input parameter in the simplified model. To account for the shrinkage of the polymer solution, we consider u_{ps} as a boundary condition between homogeneous and heterogeneous (unstable) polymer solution.

Mass transport inside of the miscibility gap

Finally, we simplify mass transport inside the miscibility gap. The composition on the binodal ω_0 , where we enter the miscibility gap, is given. The red composition path in the phase diagram in Fig. 6.4 indicates the direction from ω_0 to the final phase equilibrium where the polymer matrix solidifies. The following questions arise: What is the direction of the path? How long does it take until the final composition is reached? To answer these questions, we consider the mass balance and the component balance of the heterogeneous (unstable) region. This region is the 2 phase region in the middle in Fig. 6.2.

The formulation of the mass balance is similar to Eq. 6.10 but the fluxes are reversed. Thus, the unstable region expands with the velocity u_{ps} when the mass flux of non-solvent is lower than the mass flux of solvent.

Assuming that convective transport is zero and there are no sources, the component balances of non-solvent, solvent and polymer are

$$\rho \frac{d\omega_N}{dt} = -\nabla \cdot \vec{j}_N, \quad (6.11)$$

$$\rho \frac{d\omega_S}{dt} = -\nabla \cdot \vec{j}_S \quad (6.12)$$

and

$$\rho \frac{d\omega_P}{dt} = -\nabla \cdot \vec{j}_P. \quad (6.13)$$

Next, we add Eq. 6.11 and partially, weighted by the volume ratio, Eq. 6.12 to get

$$\rho \frac{d\omega_N}{dt} + \frac{\beta}{\alpha + \beta} \cdot \rho \frac{d\omega_S}{dt} = -\nabla \cdot \vec{j}_N - \frac{\beta}{\alpha + \beta} \cdot \nabla \cdot \vec{j}_S. \quad (6.14)$$

Then, using $\omega = \omega_N + \beta/(\alpha + \beta)\omega_S$

$$\rho \frac{d\omega}{dt} = -\nabla \cdot \left(\vec{j}_N + \frac{\beta}{\alpha + \beta} \vec{j}_S \right). \quad (6.15)$$

Analog by swapping non-solvent with polymer, we get

$$\rho \frac{d(1-\omega)}{dt} = -\nabla \cdot \left(\vec{j}_P + \frac{\alpha}{\alpha + \beta} \vec{j}_S \right). \quad (6.16)$$

Now, we introduce an ansatz for the mass flux of each component j , e.g.

$$\vec{j}_j = -D_j \nabla \mu_j, \quad (6.17)$$

solve Eqs. 6.15, 6.16 and the mass balance, and get the direction of the composition path (red path in Fig. 6.4) and the final equilibrium composition. In Eq. 6.17, D_j is an effective diffusion coefficient of component j in the ternary polymer, solvent and non-solvent mixture.

In the remaining part of this section, we only consider the simplified model and Eq. 6.15. In the simplified model, the total mass flux in Eq. 6.15 is

$$\vec{j}_\omega = \vec{j}_N + \frac{1}{2} \vec{j}_S. \quad (6.18)$$

The mass flux of non-solvent and solvent are

$$\vec{j}_N = -D_N \nabla \mu_N = -D_N \nabla (\mu_N^{local} + \kappa' \nabla^2 \omega_N) \quad (6.19)$$

and

$$\vec{j}_S = -D_S \nabla \mu_S = -D_S \nabla (\mu_S^{local} + \kappa' \nabla^2 \omega_S). \quad (6.20)$$

μ_S^{local} is the total local chemical potential. Therefore, Eq. 6.15 reduces to

$$\rho \frac{d\omega}{dt} = -\nabla \cdot \left(-D_N \nabla \mu_N - \frac{1}{2} D_S \nabla \mu_S \right). \quad (6.21)$$

We assume that the diffusion coefficients of solvent and non-solvent are equal and constant inside the miscibility gap, $D_N = D_S = D$, and get

$$\rho \frac{d\omega}{dt} = D \nabla^2 \left(\mu_N + \frac{1}{2} \mu_S \right) \quad (6.22)$$

or

$$\rho \frac{d\omega}{dt} = D\nabla^2 \left(\mu_N^{local} + \frac{1}{2}\mu_S^{local} + \kappa' \nabla^2 \left(\omega_N + \frac{1}{2}\omega_S \right) \right), \quad (6.23)$$

respectively, and with $\omega = \omega_N + \frac{1}{2}\omega_S$

$$\rho \frac{d\omega}{dt} = D\nabla^2 \left(\mu_N^{local} + \frac{1}{2}\mu_S^{local} + \kappa' \nabla^2 \omega \right). \quad (6.24)$$

The last step in the formulation of the simplified model is the reduction of the chemical potential in the ternary system to a chemical potential of an approximate binary system. We start with the chemical potentials μ_j^{local} based on the Flory-Huggins equation of state. We use the equations presented by Zhou in the appendix of [Zho06c]

$$\mu_N^{local} = \omega_S^2 \chi_{NS} + \omega_P^2 \chi_{NP} + \omega_P (\omega_S (\chi_{NS} + \chi_{NP} - \chi_{SP})) + \ln(\omega_N) \quad (6.25)$$

and

$$\begin{aligned} \mu_S^{local} = & (\omega_S - 1)^2 \chi_{NS} + \omega_P^2 \chi_{NP} \\ & + \omega_P ((\omega_S - 1) (\chi_{NS} + \chi_{NP}) + \chi_{SP} - \omega_S \chi_{SP}) + \ln(\omega_S). \end{aligned} \quad (6.26)$$

Plugging in $\omega_N = \omega - \frac{1}{2}\omega_S$ and $\omega_P = 1 - \omega - \frac{1}{2}\omega_S$ leads to

$$\begin{aligned} \mu_N^{local} = & \omega_S^2 \chi_{NS} + \left(1 - \omega - \frac{1}{2}\omega_S\right)^2 \chi_{NP} \\ & + \left(1 - \omega - \frac{1}{2}\omega_S\right) (\omega_S (\chi_{NS} + \chi_{NP} - \chi_{SP})) + \ln\left(\omega - \frac{1}{2}\omega_S\right) \end{aligned} \quad (6.27)$$

and

$$\begin{aligned} \mu_S^{local} = & (\omega_S - 1)^2 \chi_{NS} + \left(1 - \omega - \frac{1}{2}\omega_S\right)^2 \chi_{NP} \\ & + \left(1 - \omega - \frac{1}{2}\omega_S\right) ((\omega_S - 1) (\chi_{NS} + \chi_{NP}) + \chi_{SP} - \omega_S \chi_{SP}) + \ln(\omega_S). \end{aligned} \quad (6.28)$$

Because of the symmetry of the binodal to $\omega = 0.5$, we can assume that $\chi_{PS} = \chi_{NS} = \chi_\omega$ and get

$$\begin{aligned} \mu_N^{local} = \omega_S^2 \chi_\omega + \left(1 - \omega - \frac{1}{2}\omega_S\right)^2 \chi_{NP} \\ + \left(1 - \omega - \frac{1}{2}\omega_S\right) \omega_S \chi_{NP} + \ln\left(\omega - \frac{1}{2}\omega_S\right) \end{aligned} \quad (6.29)$$

and

$$\begin{aligned} \mu_S^{local} = (\omega_S - 1)^2 \chi_\omega + \left(1 - \omega - \frac{1}{2}\omega_S\right)^2 \chi_{NP} \\ + \left(1 - \omega - \frac{1}{2}\omega_S\right) ((\omega_S - 1)(\chi_{NP} + \chi_\omega) + \chi_\omega - \omega_S \chi_\omega) + \ln(\omega_S). \end{aligned} \quad (6.30)$$

Next, to further simplify the chemical potential of ω , we need to specify the equilibrium composition on the binodal after infinite time. In the real system this is the point of vitrification where mass transfer almost stops. We choose $\omega_S \approx 0$ because we neglect glass transition in our model. This leads to the chemical potential of non-solvent as

$$\mu_N^{local} = (1 - \omega)^2 \chi_{NP} + \ln(\omega). \quad (6.31)$$

Because of $\ln(\omega_S) = \ln(0) = -\infty$, we approximate this term as

$$\ln(\omega_S) \approx -2 \ln(1 - \omega) \quad (6.32)$$

Finally, we find the chemical potential of solvent μ_S^{local}

$$\mu_S^{local} = \chi_\omega + (1 - \omega)^2 \chi_{NP} - (1 - \omega) \chi_{NP} - 2 \ln(1 - \omega). \quad (6.33)$$

Now, we added Eqs. 6.31 and 6.33

$$\mu^{local} = \mu_N^{local} + \frac{1}{2} \mu_S^{local} \quad (6.34)$$

and get

$$\mu^{local} = \left(1 - 2\omega + \frac{3}{2}\omega^2\right) \chi_{NP} + \ln(\omega) + \frac{1}{2}\chi_{\omega} - \ln(1 - \omega). \quad (6.35)$$

In this equation we can modify the shape of the chemical potential using the interaction parameter χ_{ω} and χ_{NP} . In the remainder of this thesis we choose $\chi_{\omega} = 2$. $\chi_{NP} = \chi_{12}$ remains for the moment. We assume that the quadratic term ω^2 is negligible and get

$$\mu^{local} = \ln(\omega) - \ln(1 - \omega) + (1 - 2\omega) \chi_{12} + 1. \quad (6.36)$$

This equation is identical to the binary chemical potential in Eq. 3.7.

Compact balance equations of simplified model

In the simplified model we only consider the heterogeneous region (inside the miscibility gap) where morphology evolves. The compact balance equation of the simplified model is the component balance

$$\rho \frac{d\omega}{dt} = D \nabla^2 \mu \quad (6.37)$$

with the chemical potential

$$\mu = \mu^{local} + \kappa' \nabla^2 \omega \quad (6.38)$$

and

$$\mu^{local} = \ln(\omega) - \ln(1 - \omega) + \chi_{12}(1 - 2\omega) + 1. \quad (6.39)$$

We can skip the balance for $1 - \omega$ because of the unity condition. The heterogeneous region expands continuously with velocity u_{ps} . The composition on the binodal ω_0 when we enter the miscibility gap is considered as boundary condition in the direction of the expansion of the domain.

To convert the numerical parameters to physical composition we can use

$$\omega_N = 0.063 \quad (6.40)$$

for $\omega \geq 0.5$ and

$$\omega_P = 0.063 \quad (6.41)$$

for $\omega \leq 0.5$ because the position of the binodal is known. With Eq. 6.1 the mass fraction of solvent is

$$\omega_S = 2(\omega - \omega_N) \quad (6.42)$$

or, using Eq. 6.2, the mass fraction of solvent is

$$\omega_S = 2(1 - \omega - \omega_P) \quad (6.43)$$

respectively, in the polymer rich and polymer lean phase. For example, if $\omega_0 = 0.4$ then $\omega_N = 0.063$, $\omega_S = 0.674$ and $\omega_P = 0.263$.

6.2 Characteristics of the system

In this section we introduce a thermodynamic and a kinetic characteristics of the system. We summarize the derivation in the following. A detailed derivation is shown in Appendix K.

Lets start with the kinetic characteristics. We balance the components j at the interface (PGF) between stable (polymer solution) and unstable region. A sketch up is shown in Fig. 6.5. We assume that

- only solvent (S) diffuses across the interface,
- the interface between the stable polymer solution and unstable region is infinitesimal small, e.g. in the sharp interface limit,
- the driving force μ_j is continuous at the interface,
- there is no source at the interface,
- there is a jump in ρ_j at the interface,
- there is only unidirectional diffusive transport across the interface.

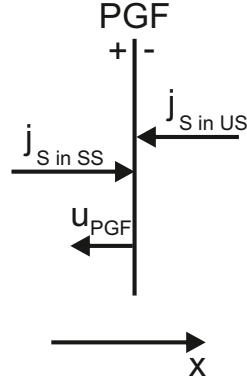


Figure 6.5: Sketch up at the transition between stable and unstable system (PGF). The subscripts *S in SS* and *S in US* indicate solvent at the interface in the homogeneous (stable) and heterogeneous (unstable) polymer solution.

Using these assumptions, the component balance of component j in terms of the partial density ρ_j and the mass flux \vec{j}_j is

$$0 = [\vec{j}_j^+ - \vec{j}_j^- - (\rho_j^+ - \rho_j^-) \vec{u}_{PGF}] \cdot \vec{n} \quad (6.44)$$

with the normal to the interface \vec{n} . For a unidirectional balance in the direction of the space variable x and with a linear relationship for the driving force of the diffusive fluxes \vec{j}_j we get

$$u_{PGF} = \frac{D_j^- \frac{\partial \mu_j^-}{\partial x}}{\rho_j^+ - \rho_j^-} \left(1 - \frac{D_j^+}{D_j^-} \right). \quad (6.45)$$

We introduce the quantities shown in Fig. 6.5 and for $j = S$, Eq. 6.45 is

$$u_{PGF} = \frac{D_{(S \text{ in } SS)} \frac{\partial \mu_{(S \text{ in } SS)}}{\partial x}}{\rho_{(S \text{ in } SS)}^+ - \rho_{(S \text{ in } US)}^-} \left(\frac{D_{(S \text{ in } US)}}{D_{(S \text{ in } SS)}} + 1 \right) \quad (6.46)$$

with the effective diffusion coefficients $D_{(S \text{ in } SS)}$ and $D_{(S \text{ in } US)}$ of solvent in the homogeneous (stable) and heterogeneous (unstable) polymer solution. The subscript $(S \text{ in } SS)$ and $(S \text{ in } US)$ indicate the property of solvent, e.g. partial density, in the stable solution (*SS*) and in the unstable solution (*US*) at the interface. We define

the latter ratio in Eq. 6.46 as the dimensionless number Hi

$$\frac{D_{(S \text{ in } US)}}{D_{(S \text{ in } SS)}} = Hi \quad (6.47)$$

and abbreviate the former ratio as

$$\Phi = \frac{D_{PS(S \text{ in } SS)} \frac{\partial \mu_{(S \text{ in } SS)}}{\partial x}}{\rho_{(S \text{ in } SS)}^+ - \rho_{(S \text{ in } US)}^-}. \quad (6.48)$$

The final equation for the phase separation front velocity u_{ps} is

$$u_{ps} = u_{PGF} = \Phi (Hi + 1). \quad (6.49)$$

We check plausibility considering known cases of Hi . In the case of $Hi \rightarrow \infty$ the phase separation front velocity limits to $u_{ps} = \Phi \cdot Hi \sim D_{(S \text{ in } US)}$. This means that the phase separation front velocity may move very fast into the polymer solution. In the case of $Hi \rightarrow 0$ we get $u_{ps} = \Phi \sim D_{(S \text{ in } SS)}$. This means that the front moves very slow into the polymer solution. Since Hi cannot be negative the phase separation front always moves into the polymer solution.

We may also express Hi in terms of the velocity of the interface

$$Hi = \frac{u_{ps}}{\Phi} - 1 = \frac{u_{ps} \cdot l}{D_{(S \text{ in } SS)}} - 1 \quad (6.50)$$

where l represents a characteristic length and Φ (Eq. 6.48) is a characteristic velocity. Φ is proportional to $D_{(S \text{ in } SS)}$ and therefore

$$Hi = \frac{u_{ps} \cdot \Phi^*}{D_{(S \text{ in } SS)}} - 1 \quad (6.51)$$

with

$$\Phi^* = \frac{\rho_{(S \text{ in } SS)}^+ - \rho_{(S \text{ in } US)}^-}{\frac{\partial \mu_{(S \text{ in } SS)}}{\partial x}}. \quad (6.52)$$

In principle Φ^* or $\frac{\partial \mu_{(S \text{ in } SS)}}{\partial x}$, respectively, may be time and position dependent. We will use Hi as a function of the phase separation front velocity u_{ps} (Eq. 6.51) in the

discussion of results in the remaining of this chapter.

Next, we define the thermodynamic characteristics A as position on the binodal where we enter the miscibility gap, ω_0 , with respect to ω at the critical point $\omega_{cP} = 0.5$

$$A = \omega_{cP} - \omega_0. \quad (6.53)$$

Therefore, $A = 0$ when we enter the miscibility gap at the critical point. The present definition of A is different from Foard & Wagner [Foa12b]. Because of the symmetry of the miscibility gap we only need to investigate half of the range of ω_0 and therefore only $A \geq 0$.

6.3 Computational setup

The computational setup is shown in Fig. 6.6. We consider mass transport relative to the phase separation front velocity. Therefore the phase separation front is spatially fixed in the simulations and we move particles relative to the front. Since we previously assumed that the phase separation front velocity is constant along the interface between homogeneous (stable) and heterogeneous (unstable) polymer solution, all particles are equally moved and the relative configuration of particles remains.

If not stated otherwise the transition of the homogeneous (stable) to heterogeneous (unstable) region is at $x = 0.25 \cdot L_x$. We consider a rectangular domain of size $L_x \cdot L_y$. The boundary conditions are periodic in y-direction. In x-direction we apply open boundary conditions because the particles move (due to the chosen reference

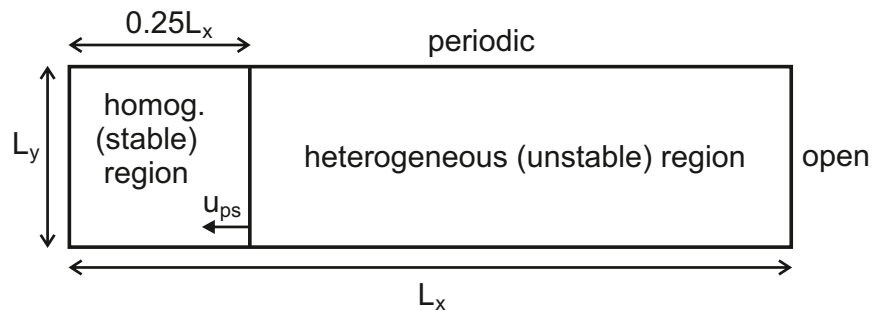


Figure 6.6: Computational domain for Liesegang patterns.

frame which is the velocity of the phase separation front), therefore leave and enter the domain, and apply Neumann boundary conditions for the chemical potential and the gradient energy term. As shown in Appendix D the influence of Neumann boundary conditions on phase separation is minor. If a Dirichlet boundary condition would be applied then the effect of the boundary condition on the pore structure is only negligible if the phase separation front velocity is much larger than the phase separation dynamics, e.g. lower diffusion coefficient or gradient of the chemical potential. In general this is not the case.

The simulation parameters are summarized in Tab. 6.1. The size of the simulation domain is $L_x = 2\mu m$ in x-direction and $L_y = 1\mu m$ in y-direction. We use 32,768 particles with initial regular Cartesian particle spacing $L_0 = 7.8125nm$. We choose the diffusion coefficient in the heterogeneous (unstable) region as a function of the mass fraction of polymer in the binary polymer/non-solvent system

$$D = D_0 \cdot (1 - \omega) \omega \quad (6.54)$$

with $D_0 = 10^{-10} \frac{m^2}{s}$ to guarantee positive values of ω . This is important if thermal fluctuations are present because the amplitude of the stochastic term scales with the magnitude of the diffusion coefficient. In the homogeneous (stable) region the diffusion coefficient is set to zero because this region only acts as boundary condition and transport in the homogeneous region is not important here.

The parameter χ_{12} in the equation of state (Eq. 6.39) is $\chi_{12} = 1.0$ in the homogeneous (stable) and $\chi_{12} = 3.0$ in the heterogeneous (unstable) region in the pseudo-binary system. Throughout this chapter we investigate $\omega_0 \in [0.25, 0.5]$. Remember that in the simulation an initial value $\omega_0 = 0.5$ represents $A = 0$.

If not stated otherwise we only use fluctuations to initialize the system. A detailed investigation of the effect of thermal fluctuations during the evolution of morphology is shown in Sec. 6.6.

The velocity of the phase separation front u_{ps} is an input parameter of the simulation. Finally, we need to specify Φ^* in Eq. 6.51, defined as Eq. 6.52. The spatial gradient of the chemical potential varies over time and the difference between the partial density of solvent in the homogeneous and heterogeneous region is very small. For simplicity, we assume that Φ^* in Eq. 6.51 is constant. In detail, we assume that the spatial gradient of the chemical potential is in the order of 1 and the difference of

Table 6.1: Summary of properties of the fluids and parameters for Liesegang patterns.

Parameter	Units	Value
L_x	$[\mu m]$	2.0
L_y	$[\mu m]$	1.0
L_0	$[nm]$	7.8125
$\#N_{particles}$	$[-]$	32,768
ρ	$[kgm^{-3}]$	1000
D	$[m^2s^{-1}]$	see text
ω_0	$[-]$	see text

the partial densities is in the order of 10^{-6} . Therefore, we choose $\Phi^* = 10^{-6}$ as a constant parameter throughout the simulation. The diffusion coefficient $D_{(S\ in\ SS)}$ is replaced by the maximum value of the diffusion coefficient $D = 2.5 \cdot 10^{-11} \frac{m^2}{s}$ as defined above. Therefore, Hi is determined by u_{ps} only.

6.3.1 Example of evolution of morphology behind moving front

In this section we demonstrate the formation of morphology behind a phase separation front in detail and discuss the physical phenomena that lead to morphology. The model parameters are the same as described in the last section. The characteristics are $A = 0.1$ and $Hi = 159$. Therefore $\omega_0 = 0.4$ ($\omega_N = 0.063$, $\omega_S = 0.674$, $\omega_P = 0.263$) and $u_{ps} = 0.004m/s$.

First we start with a general overview of the simulation results. In Fig. 6.7, representative snapshots of the simulation are shown. The grey scale indicates the value of $\omega \in [0.39975, 0.40025]$ and the color is constant outside of this region. Black and white represent ω (pores) and $1 - \omega$ (polymer matrix).

Initially (Fig. 6.7a), the heterogeneous (unstable) region is perturbed by a small random fluctuation of ω with an amplitude of $d\omega = 0.0005$. After a short time, e.g. $t = 0.01ms$ (Fig. 6.7b), the system starts to phase separate in the unstable region and non-directional pores are formed. In this stage, phase separation is independent of the motion of the phase separation front because nuclei that rise in the very right region are not influenced by the phase separation front. At later times (Fig. 6.7c), the pores grow and form its characteristic shapes. In the present case the characteristic shapes are sponge pores (spherical pores). Now, new nuclei, originated at the phase separation front, are influenced by the motion of the phase separation front. Finally, after very long time, a steady-state of the pore shapes are found (Fig.

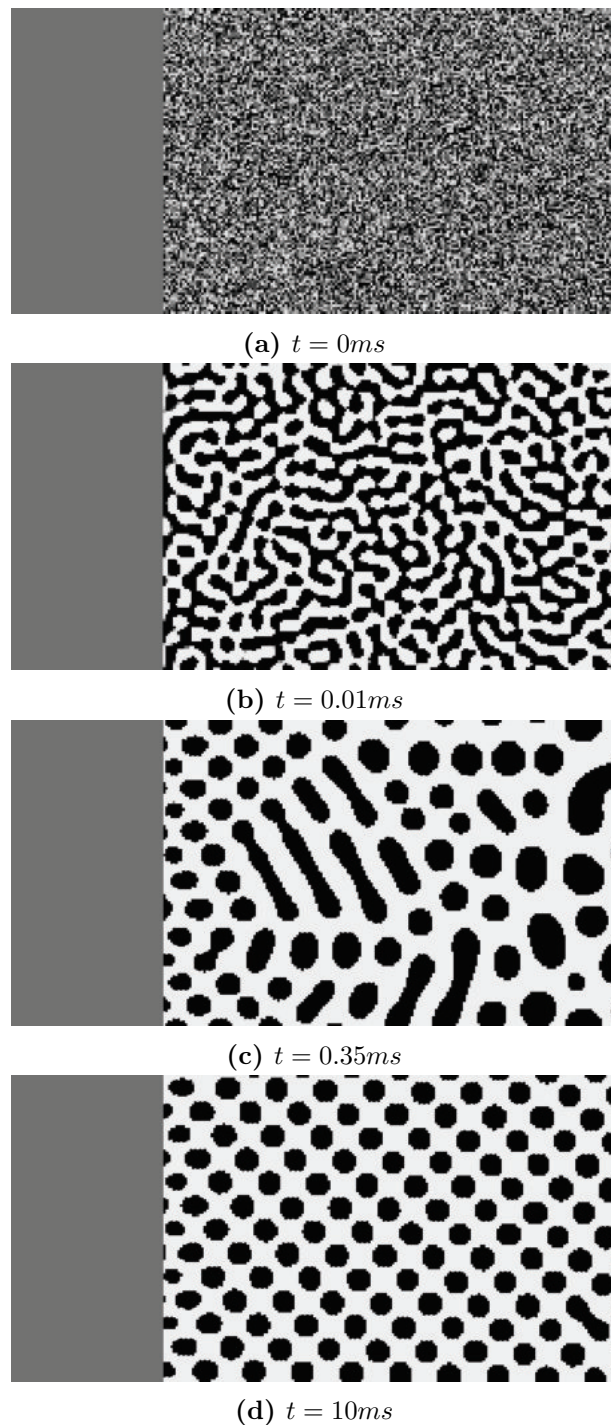


Figure 6.7: Time evolution of morphology at constant $Hi = 159$ and $A = 0.1$. Black and white represent ω (pores) and $1 - \omega$ (membrane matrix). The scale is $0.39975 < \omega < 0.40025$ and the color is constant outside of this range. Therefore the diffuse interface is not visible at later times.

6.7d). These pore shapes represent the characteristic pore shapes for a given A and Hi .

Next we analyze the formation of pores at the phase separation front in detail. In Fig. 6.8, 4 consecutive close-ups of the previous simulation are shown. Herein we observe the complete formation of a pore at the phase separation front. First a nuclei exists at the phase separation front (small black pore on the left side in Fig. 6.8a) because of initial fluctuations in the system or local differences between of the composition in the stable and unstable region between two neighboring points. When the phase separation front moves to the left, the nuclei grows because new nuclei that originate at the phase separation front are influenced by the existing nuclei and coalesce with the existing nuclei (red arrow in Fig. 6.8). In addition, the existing nuclei grows because of mass transport between nuclei and polymer rich phase (blue arrow in Fig. 6.8). As a result a small pore grows (Fig. 6.8b).

The shape of the small pore depends on the different surface tension between homogeneous polymer solution and both phases in the heterogeneous region along the phase separation front, the relaxation along the phase separation front, the kinetics of phase separation, the velocity of the phase separation front and the volume ratio between polymer rich and polymer lean phase. This complex interplay of diffusive

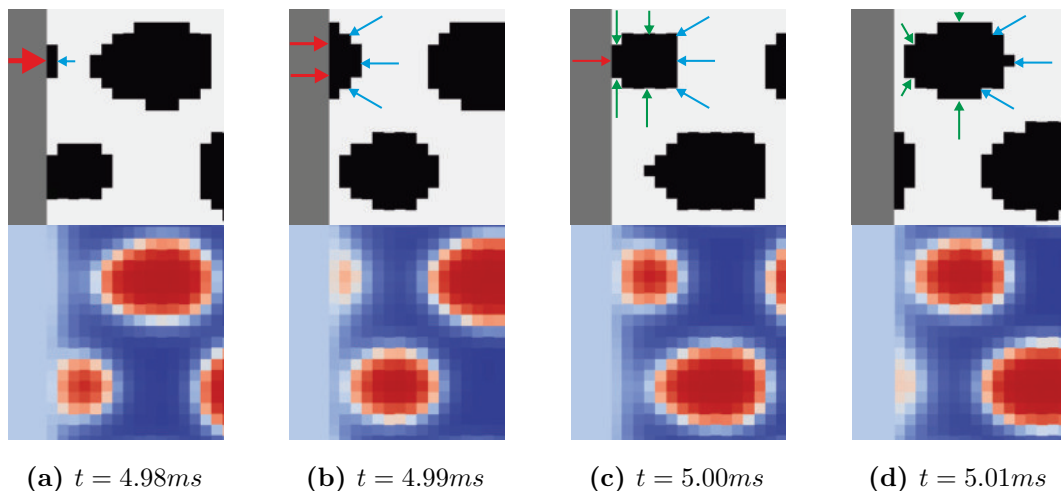


Figure 6.8: Detailed evolution of morphology at constant $Hi = 159$ and $A = 0.1$. Top: Black and white represent ω (pores) and $1 - \omega$ (membrane matrix). The scale is $0.39975 < \omega < 0.40025$ and the color is constant outside of this range. Therefore the diffuse interface is not visible. Bottom: continuous color scale indicates ω in polymer rich (blue) and polymer lean (red) phase.

mass transport is responsible for different morphology.

In the present model we only alter the velocity of the phase separation front and the volume ratio between polymer rich and polymer lean phase. For simplicity, the interactions between homogeneous region and both phases in the heterogeneous region are the same. The relaxation along the phase separation front and the kinetics of phase separation are identical because of the isotropic diffusion coefficient in the component balance.

In the present case (Fig. 6.8), the velocity of the phase separation front is larger than the relaxation along the phase separation front (green arrows in Fig. 6.8c). As a result we observe a contraction of the pore at the phase separation front (Fig. 6.8c). After contraction, the pore detaches from the phase separation front (Fig. 6.8d). Finally a new pore is formed and now grows independent of the phase separation front.

6.4 Influence of Hi and A on pore shape

In this section we first reproduce the results of Foard & Wagner [Foa12b]. They proposed a morphology diagram. In this diagram the shape of the pores are shown depending on the initial composition and the phase separation front velocity. Here we choose a similar diagram using the characteristics A and Hi .

We use the setup presented in the previous section. We consider different, constant A and Hi (thus altering ω_0 and u_{ps}) and evaluate the morphology at steady-state. Fig. 6.9 shows the morphology phase diagram. We show representative images of the phase distribution of different regimes in the phase diagram. In these images black represents ω and white represents $1 - \omega$. This corresponds to the pores (black) and the polymer matrix (white).

We identify 4 characteristic regimes. The first regime is called unstructured sponge pores. It is found for low Hi and large A . Characteristic morphology in this regime shows large unstructured pores. A membrane in this regime may be mechanically unstable because defects may be present. This regime represents polymer solutions with high polymer concentration and high mobility of solvent in the polymer solution. In the second regime we find macrovoids for low Hi and low A . In this regime finger pores or macrovoids are found. We identify two characteristics in this regime. The first characteristic is that with higher Hi the finger pores or macrovoids get thinner.

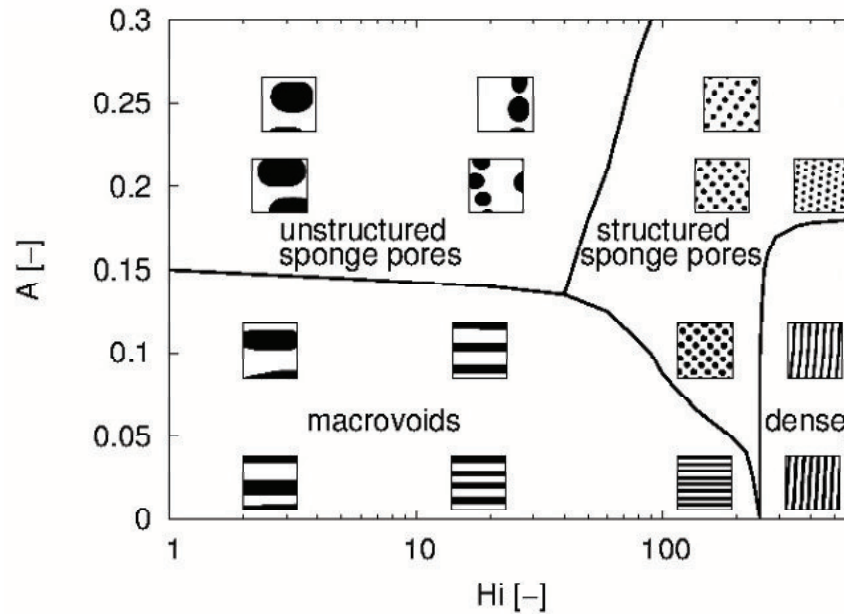


Figure 6.9: Morphology phase diagram of model fluid mixture from 2D simulations using the characteristics A (Eq. 6.53) vs. Hi (Eq. 6.51). The results are at steady-state. Black and white indicate ω (pores) and $1 - \omega$ (polymer matrix).

At the limit of very thin macrovoids we find a transition to the dense regime. This regime represents low polymer concentration. The second characteristic is found at the phase separation front. For higher A bottle-like macrovoids are found. The limiting case is a detachment of the macrovoid from the phase separation front. The angle of the neck of the bottle-like macrovoid is believed to depend on the contact angle between the polymer lean, polymer rich and stable polymer solution phases [Foa12a].

The third regime is called structured sponge pores. It is found for large Hi and large A . In this regime sponge pores of different size are found. We also found two characteristics in this regime. For larger Hi and constant A the sponge pores get smaller and the pore density is higher. The second characteristic is that for constant Hi and larger A the sponge pores get smaller but remain at the same pore density. This regime may represent a polymer solution with an additional pore builder. This is in accordance with Boom et al. who proposed that macrovoids are suppressed using a pore builder [Boo92]. With pore builder added to the polymer solution, the transport resistance at the interface between stable polymer solution and unstable polymer solution increases and, therefore, the time for non-solvent to diffuse into the

stable polymer solution increases. As a result, the non-solvent in the stable polymer solution disperses and the composition of the binodal is reached at the same time in a large region in the polymer solution. Finally, we would observe a very fast velocity of the phase separation front because this large region gets unstable at almost the same time and therefore $Hi \gg 0$.

The last regime is the dense regime when the macrovoid structure change to a lamella-like structure for large Hi and low A . We interpret these structures as dense layers. A characteristic of this regime is that for higher A the stripes are smaller but, as for the sponge pores, remain their density.

From application point of view the question arises: why is there a transition from sponge pores to macrovoids? We may answer this question using Fig. 6.9. In realistic immersion precipitation processes the phase separation front velocity (and therefore Hi) decreases because the resistance for solvent, that diffuses out of the polymer solution, increases when the membrane grows. For $A \approx 0.1$ a transition from dense structure into sponge pores and into macrovoids are found for different Hi . Such a transition is found in many experiments, e.g. [Che99; Git70; Wit96], and also in the experiments in Chap. 2. The mass fraction of polymer in the polymer solution for $A = 0.1$ is $\omega_P = 0.263$. In the experiments we found a transition from finger pores to sponge pores at $\omega_P = 0.25$ which is very similar to the present results. Another transition from sponge pores to finger pores are found for $Hi \approx 150$ and different A . In the next section we focus on these two transitions because they were typically observed in the preparation process.

6.5 Transition of pore shapes

In Fig. 6.9 we identify 5 different transitions between the 4 regimes. The most interesting ones are the transitions from sponge pores to finger pores and from dense layer to finger pores. In this section we focus on these two transitions and their physical significance.

6.5.1 Transition from sponge pores to finger pores

We investigate the transition from sponge pores to finger pores by variation of A from initially $A = 0.25$ to $A = 0$ ($\omega_P = 0.563$ to $\omega_P = 0.063$). We keep Hi constant at $Hi = 159$. This case corresponds to a change of the composition in the polymer

solution over time. It may be caused by heterogeneity of the polymer solution or variation of the polymer solution in the preparation process. In other cases, A increases, e.g. by adding PVP, because of a shift of the critical point and different shape of the free energy in the miscibility gap. In this discussion we assume that the diffusion coefficients remain the same for $A > 0$.

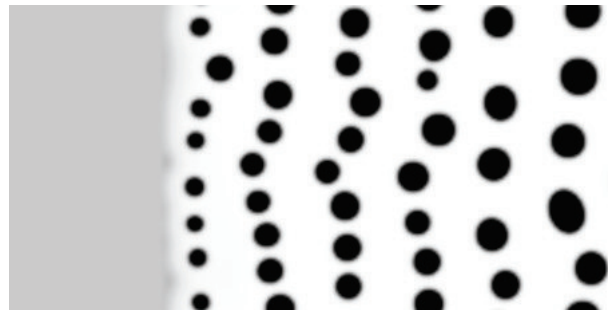
We perform a simulation with the same numerical setup as before. First we keep $A = 0.25$ ($\omega_P = 0.563$) constant for $1ms$. Then we linearly decrease A for $3ms$ until we reach $A = 0$ ($\omega_P = 0.063$). Afterwards we keep $A = 0$. Remember that $A = 0$ and $A = 0.25$ correspond to $\omega_0 = 0.5$ and $\omega_0 = 0.25$.

The morphology is shown for 4 different times in Fig. 6.10. The grey scale from black to white indicates the composition where a black region represents the polymer lean phase and the white region represents the polymer matrix. At each time in Fig. 6.10 we see the stable polymer solution on the left side of the figure. From top to bottom the grey color gets darker which indicates that the initial composition changes from $A = 0.25$ to $A = 0$ ($\omega_P = 0.563$ to $\omega_P = 0.063$). On the right side of each figure we get the morphology behind the phase separation front. In this region the polymer solution is unstable. The phase separation front is located at the interface between the homogeneous and heterogeneous region.

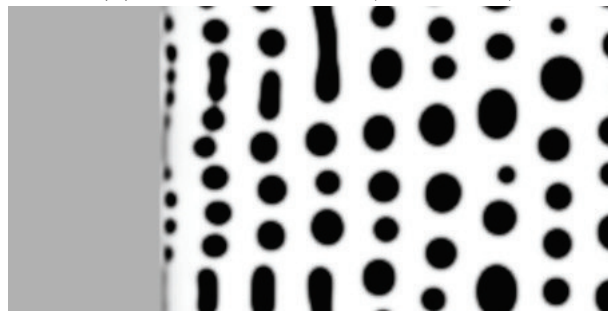
Fig. 6.10a shows the morphology at $A = 0.25$ ($\omega_P = 0.563$) at time $t = 1ms$. We observe sponge pores with different pore size. In Fig. 6.10b the initial composition is reduced to $A = 0.1515$ ($\omega_P = 0.366$) at time $t = 2ms$. We still observe sponge pores but they are larger than in Fig. 6.10a. We also observe that some small pores coalesce forming a lamella. Until $t = 3.3614ms$ sponge pores with equal size are formed. In Fig. 6.10c we reach a critical initial composition $A = 0.0427$ ($\omega_P = 0.1484$). We observe tear-drop-like structures formed at the phase separation front. This leads to a transition to finger pores as shown in Fig. 6.10d for $A = 0$ ($\omega_P = 0.063$) and $t = 4ms$.

In this simulation we only changed ω_0 in the stable region over time. From application point of view that may happen due to heterogeneous solutions or altering process conditions during the preparation of polymer membranes. It also demonstrates that when we enter the miscibility gap close to the critical point it is more likely to find finger pores.

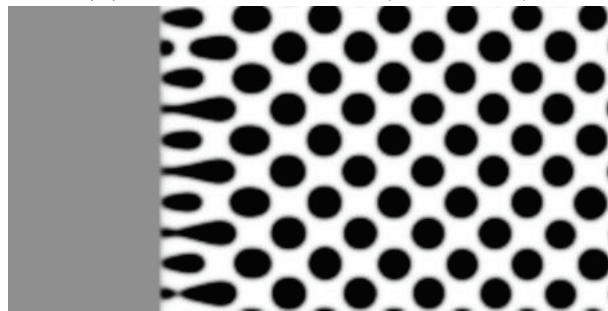
The reason for the transition from sponge to finger pores is highlighted in Fig. 6.11 in detail. For sponge pores, the pores detach from the phase separation front because



(a) $t = 1ms$, $A = 0.25$ ($\omega_P = 0.563$).



(b) $t = 2ms$, $A = 0.1515$ ($\omega_P = 0.366$).



(c) $t = 3.3614ms$, $A = 0.0427$ ($\omega_P = 0.1484$).



(d) $t = 4ms$, $A = 0$ ($\omega_P = 0.063$).

Figure 6.10: Time evolution of morphology at constant $Hi = 159$ and variable A from $A = 0.25$ to $A = 0$ ($\omega_P = 0.563$ to $\omega_P = 0.063$).

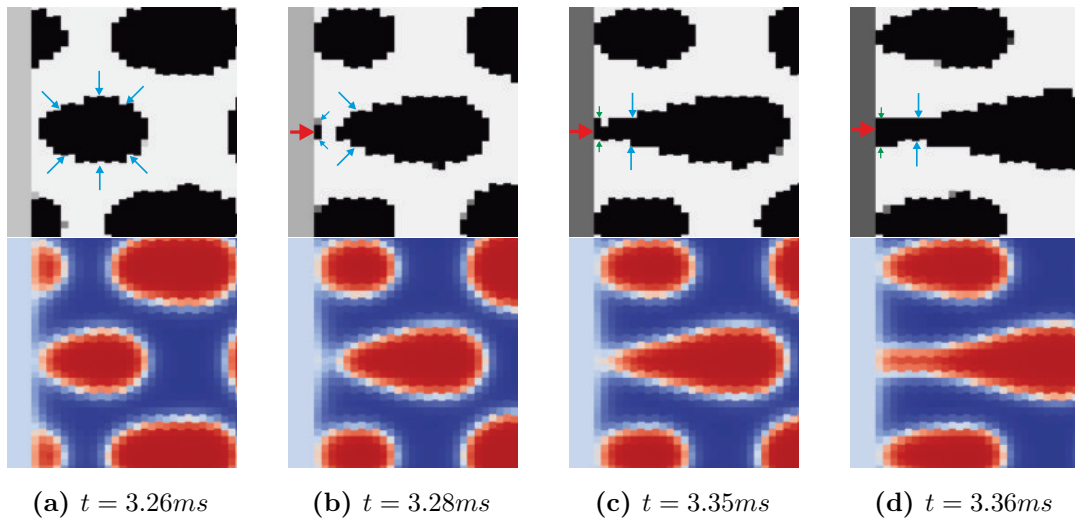
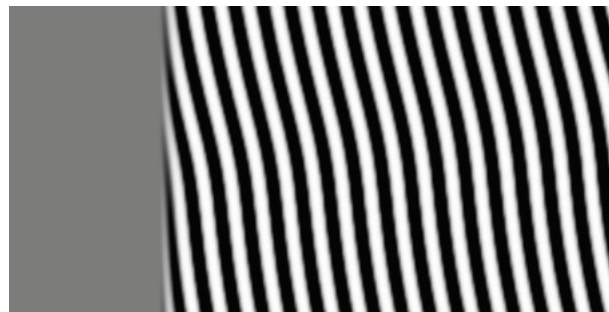


Figure 6.11: Detailed evolution of morphology at constant $Hi = 159$ and variable A . Top: Black and white represent ω (pores) and $1 - \omega$ (membrane matrix). The scale is $0.435 < \omega < 0.455$ and the color is constant outside of this range. Therefore the diffuse interface is not visible. Bottom: continuous color scale indicates ω in polymer rich (blue) and polymer lean (red) phase.

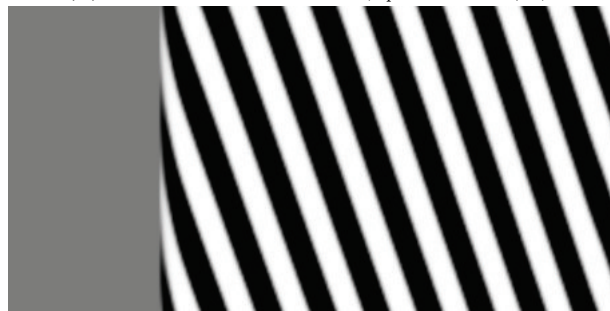
the relaxation along the interface between stable and unstable region is too slow. At the transition from sponge pores to finger pores, the relaxation along the interface (green arrows in Fig. 6.11) is similar to the velocity of the phase separation front and therefore the pore doesn't detach any more perpendicular to the phase separation front. We first get elongated structures and finally finger pores. A similar explanation is found in Foard [Foa12a] who argued that the distance between two pores formed behind the phase separation front decreases with increasing initial concentration (in our case $A \rightarrow 0$). Then the time to detach from the phase separation front is larger than the time to create a new pore and coalesce with the previous pore.

6.5.2 Transition from lamella layer to finger pores

Next we investigate the transition from dense or lamella structures to finger pores. This transition may be very common after initial contact of the polymer solution and coagulation bath. Because of fast diffusion of non-solvent into the polymer solution (large u_{ps}), the phase separation front evolves very fast in the first moments and a dense layer of the polymer rich phase is formed. After that, the velocity of the phase separation front drastically decreases because further diffusion of non-solvent from



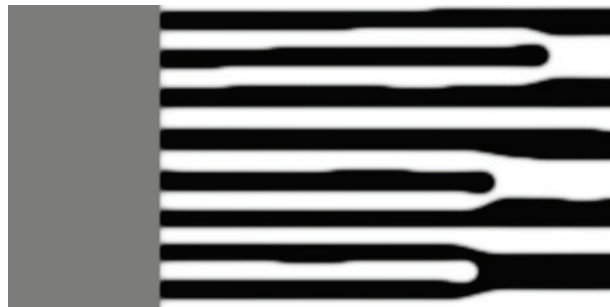
(a) $t = 0.5ms$, $Hi = 399$ ($u_{ps} = 0.01m/s$).



(b) $t = 4ms$, $Hi = 130$.



(c) $t = 5.8ms$, $Hi = 72.6$.



(d) $t = 7ms$, $Hi = 49.3$.

Figure 6.12: Time evolution of morphology at constant $A = 0$ ($\omega_P = 0.063$) and variable Hi from $Hi = 399$ to $Hi = 49.3$ from top to bottom. The grey scale indicates the composition of polymer where black is polymer rich.

the coagulation bath into the polymer solution is inhibited by the large diffusive resistance in the polymer rich layer. This means that Hi is large in the first moments and then drastically decreases.

We investigate decreasing Hi from initially $Hi = 399$ ($u_{ps} = 0.01m/s$) to $Hi = 1.6$ ($u_{ps} = 0.065mm/s$). $A = 0$ ($\omega_P = 0.063$) and is constant throughout the simulation. At the beginning we keep Hi constant for $t = 0.5ms$ and then reduce it exponentially. In the simulation we decrease the velocity of the phase separation front

$$\vec{u}_{ps} = a \cdot e^{b(t-t_0)} \quad (6.55)$$

with $a = 0.01$, $b = -322.0$ and $t_0 = 0.0005s$. For $t > 0.4s$ we keep Hi constant at $Hi = 1.6$. We consider the same numerical setup as in the last section. As shown in Fig. 6.9 we expect a transition from lamella structures to finger pores.

The morphology is shown in a time series in Fig. 6.12. At the beginning (Fig. 6.12a) we find lamella structures for high Hi numbers. The distance between the lamella and the thickness of the lamella are small. Then, Hi decreases and the distance between the lamella increases. At a critical Hi number, where the morphology changes, the lamella tend to flip in the normal direction to the interface of the stable and unstable region (Fig. 6.12c). For all later times finger structures are formed when Hi is further decreased.

The details of the transition between lamella structures and finger pores are highlighted in Fig. 6.13. When the velocity of the phase separation front reduces, the lamella doesn't detach any more because the velocity of mass transport between polymer rich (red) and polymer lean (blue) phase is similar to the phase separation front velocity. Then nuclei of the polymer lean phase can grow (Fig. 6.13) and the lamella is disrupted. Because of the slow relaxation along the interface between homogeneous and heterogeneous region the pore remains and finger pores are formed. Finally we compare the critical Hi number of the transition from lamella to finger structures of the present simulation with the steady-state results of Fig. 6.9. We find that in the present simulation it is lower ($Hi = 60$) than in Fig. 6.9 ($Hi = 160$). It indicates that there is a difference between morphology at steady-state and during a dynamic simulation and maybe multiple stationary states. This may be a subject for further analysis of morphology evolution. Nevertheless the order of Hi is similar. The reason for this difference is that new structures that are formed close to the

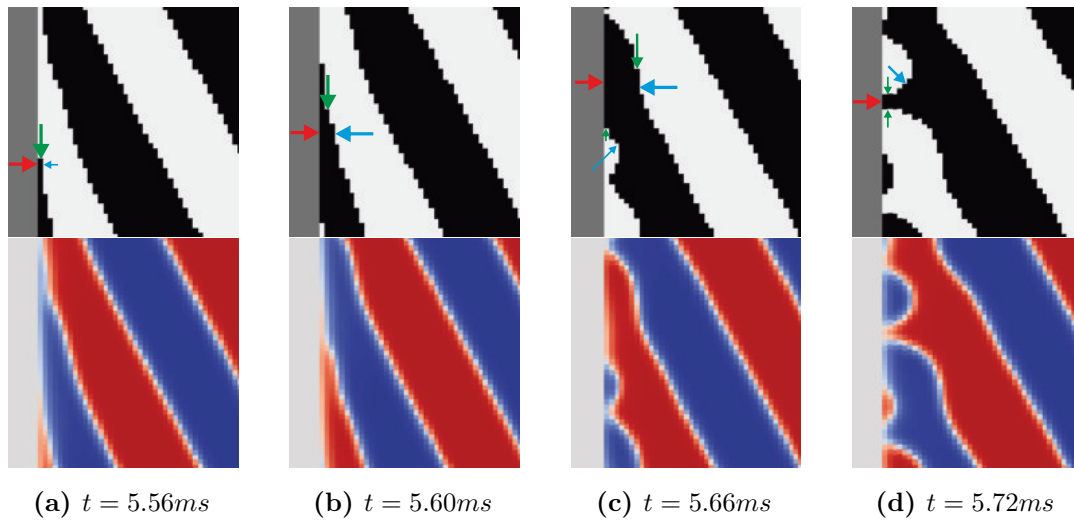


Figure 6.13: Detailed evolution of morphology at constant $A = 0$ and variable $Hi = 159$. Top: Black and white represent ω (pores) and $1 - \omega$ (membrane matrix). The scale is $0.50025 < \omega < 0.49975$ and the color is constant outside of this range. Therefore the diffuse interface is not visible. Bottom: continuous color scale indicates ω in polymer rich (blue) and polymer lean (red) phase.

phase separation front are influenced by the previously further evolving morphology. In the previous case of constant A and Hi (steady-state, see Fig. 6.9) an equilibrium morphology evolves because each newly formed structure tend to form the same morphology. As a result, the influence of previously evolving morphology on new structures is minor. In the current case of variable A or Hi , the equilibrium morphology changes with time and previously evolving morphology influences newly formed structures (similar to a boundary condition as discussed in Appendix D). Conclusively, by continuous reduction of Hi we observe a shift of the transition between lamella structures and finger pores.

6.6 Influence of fluctuations in composition on pore shape

In Appendix D we discuss the influence of consistent thermal fluctuations of the concentration on phase separation. We concluded that only the initial decomposition and late stage phase separation are influenced by thermal fluctuations. In other stages the phase separation dynamics is controlled by deterministic effects only. In Liesegang patterns we expect the same behavior. Fluctuations of the concentration are necessary for a consistent model but may be of negligible magnitude in the

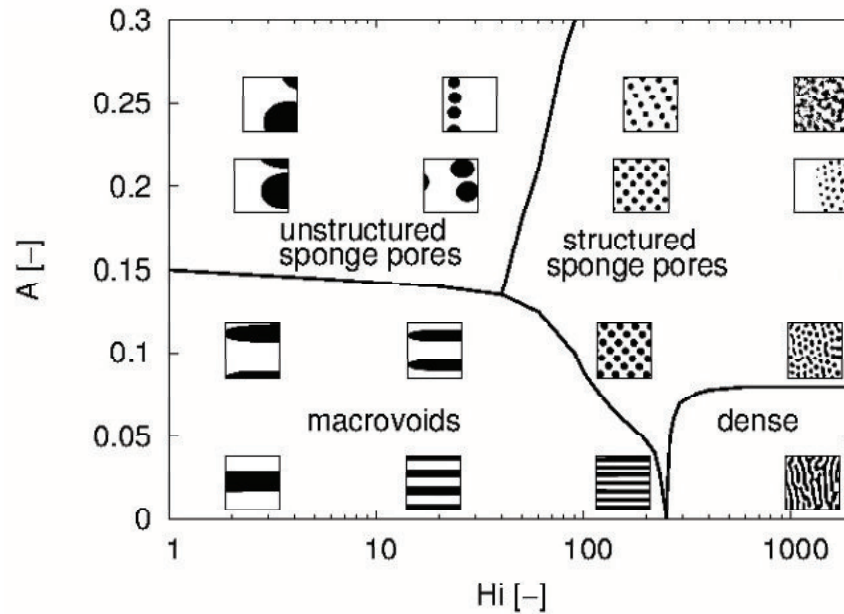


Figure 6.14: Morphology phase diagram of model fluid mixture from 2D simulations using the characteristics A (Eq. 6.53) vs. Hi (Eq. 6.51) with thermal fluctuations. The results are at steady-state. Black and white indicate ω (pores) and $1 - \omega$ (polymer matrix).

present case. Therefore we investigate the influence of fluctuations of ω on the pore shape.

We consider the previous model as described in Sec. 6.3. In addition we consider fluctuations of ω as described in Sec. 4.3.4 and D.1.5. We redo the simulations of Sec. 6.4 at $T = 298K$ and plot the results in the morphology diagram.

The results are shown in Fig. 6.14. There are only small differences compared to Fig. 6.9. We observe the same characteristic pore shapes in the same region but two small differences. First, small artificial structures especially for low Hi vanish. Second, we observe a smaller region of dense layers limited to $A \approx 0.08$ ($\omega_P = 0.223$).

In addition we investigated the influence of up to 100 times larger fluctuations and ended up with the same morphology. We conclude that fluctuations are only necessary for consistency and may lead to more realistic structures. Otherwise one may neglect them in the present model.

6.7 Influence of hydrodynamics on pore shape

In this section we investigate the influence of hydrodynamics on the pore shape. So far, we haven't considered the momentum balance in the simplified model in Sec. 6.1.2. If we derive the momentum balance for the simplified model, we end up with the same equation as in Sec. 3.4.3 in Eq. 3.32, assuming a sharp interface in the momentum balance. In the component balance we use the chemical potential but in the momentum balance we use the CSF approach, where the surface tension depends directly on the surface tension coefficient σ . In principle, we could calculate the surface tension coefficient using Eq. 3.2. But this implies a realistic value of κ' . Otherwise the magnitude of the surface tension would be in an unrealistic range. Therefore, we decouple the surface tension and the chemical potential and use different values in the component balance, by defining κ' , and the momentum balance, by choosing σ . This gives us a degree of freedom and we may vary the surface tension in the momentum balance independently from the chemical potential in the component balance.

In this section, we first demonstrate the influence of the hydrodynamics by investigating different ratios between the diffusive mass transport (based on the gradient of the chemical potential) and the surface force in the momentum balance. Then, we investigate the influence of gradients of the surface tension in the momentum balance because this may be a relevant mechanism of finger pore formation in the theory of e.g. Matz [Mat72].

6.7.1 Influence of surface tension

We consider the setup used in the previous sections but now consider the component balance for ω and the momentum balance without thermal fluctuations. The parameters are summarized in Tab. 6.2. This time the length of the domain is $L_x = 2mm$ and the height is $L_y = 1mm$. To avoid numerical artifacts caused by errors in the numerical calculation of surface tension we enable surface tension after $t = 0.159ms$ when first pores are present. The parameters are $D = 10^{-4}m^2/s$, $\eta = 10mPas$, $\rho = 1000kg/m^3$, $Hi = 166$, $A = 0.1$ and $\Psi^* = 0.004$. We vary the surface tension from $\sigma = 0mN/m$ to $\sigma = 70.5mN/m$ and investigate the effect of the surface tension on the pore shape. We assume that the surface tension between the homogeneous phase, the polymer rich and polymer lean phase are the same.

Table 6.2: Summary of properties of the fluids and parameters for Liesegang patterns including surface tension in the momentum balance.

Parameter	Units	Value
L_x	$[\mu m]$	2.0
L_y	$[\mu m]$	1.0
L_0	$[nm]$	7.8125
$\#N_{particles}$	$[-]$	32,768
ρ	$[kgm^{-3}]$	1000
η	$[mPas]$	10
D	$[m^2s^{-1}]$	10^{-4}
A	$[-]$	0.1
Hi	$[-]$	166
Ψ^*	$[-]$	0.004
σ	$[mNm^{-1}]$	see text

Here we neglect gradients of the surface tension.

In Fig. 6.15 we show the morphology for 4 different surface tensions at time $t = 3ms$.

The first image (Fig. 6.15a) shows the morphology without surface tension as a reference. From top to bottom the surface tension increases by 4 orders. We find only small deviations between Fig. 6.15a and b. When we further increase the surface tension by two orders (Fig. 6.15c) we observe small influence of the surface tension. First we see a contraction of the pores that touch the interface between stable and unstable region because the contact angle between the polymer lean and homogeneous phase is 60° because the surface tension between the 3 phases is identical. Second we see ripening of the pores by surface tension. This gets more obvious when we increase the surface tension by another order (Fig. 6.15d). After formation of the pores at the interface between stable and unstable region ripening dominates the pore formation. In this case diffusive phase separation is smaller than viscous phase separation where the surface tension in the momentum balance dominates. This leads to larger pores.

In the real system of PSf-NMP-H₂O and additives the surface tension is in the same order as in Fig. 6.15d. But this does not mean that ripening due to surface tension dominates in the polymer system because the viscosity of the polymer solution is at least 3 orders larger than in the present simulation. In the simulation we assumed lower viscosity due to time step restrictions that would lead to very large computation times. Another difference of the simulation to the real physical system

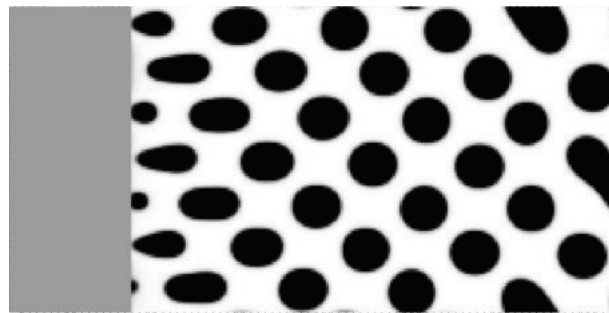
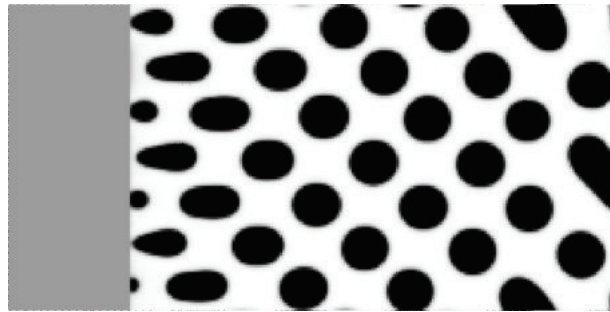
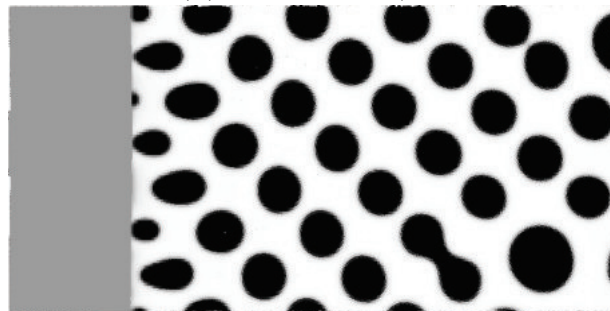
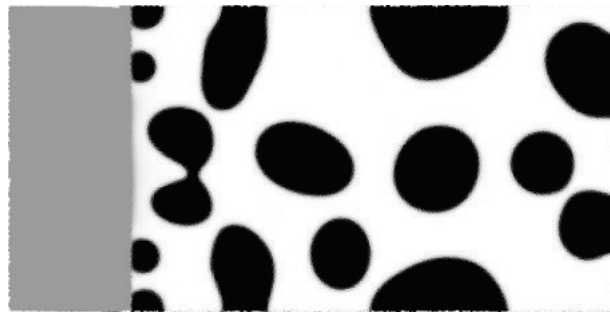
(a) $\sigma = 0mN/m$.(b) $\sigma = 0.0705mN/m$.(c) $\sigma = 7.05mN/m$.(d) $\sigma = 70.5mN/m$.

Figure 6.15: Morphology for 4 different surface tensions at time $t = 3ms$. (a) $\sigma = 0mN/m$, (b) $\sigma = 0.0705mN/m$, (c) $\sigma = 7.05mN/m$, (d) $\sigma = 70.5mN/m$. The grey scale indicates the phases with its diffuse interface in between. White and black correspond to polymer matrix ($1 - \omega$) and pores (ω).

is the gradient of the chemical potential. We expect that the gradient of the chemical potential is much larger than in the simulation. This leads to larger diffusive mass transport. Together with the higher viscosity, we expect that surface tension effects are in the order of Fig. 6.15c, where only diffusive coarsening is present.

6.7.2 Influence of gradient in the surface tension

In this parameter study we extend the previous simulation by surface tension gradients. As in the last section, we use the CSF approach to model surface tension in the momentum balance and the chemical potential in the component balance. Therefore we can choose different surface tension in the momentum balance than in the chemical potential in the component equation. As a result, we are able to vary the surface tension coefficient and its gradient in the momentum balance.

We consider the same setup and parameters as before with a surface tension $\sigma_0 = 70.5mN/m$. We assume a linear gradient perpendicular to the phase separation front between stable polymer solution and unstable polymer solution. The surface tension coefficient is

$$\sigma = \sigma_0 + \sigma_T \frac{x}{L_x} \quad (6.56)$$

where the surface tension depends on the relative position of a particle in the domain varying from 0 to 1. The slope of the surface tension coefficient σ_T is varied from $-0.5mN/m$ to $-50mN/m$. Note that the surface tension decreases from left to right. Therefore the fluid in the pores (represented by ω) suffers a force driving it into the stable polymer solution while the fluid in the continuous phase ($1 - \omega$) is driven into the coagulation bath. This represents the physical case that the surface tension decreases from coagulation bath to polymer solution because there is a transition from an immiscible to miscible system where the local surface tension is lower because of the larger interface width or the lower gradient in partial mass density, respectively.

In Fig. 6.16 we see the morphology and the velocity distribution during precipitation for different slopes of the surface tension coefficient σ_T at time $t = 1.95ms$. From top to the bottom the magnitude of the slope increases. The grey scale in the background indicates the phase distribution where white color represents the polymer matrix ($1 - \omega$). The arrows in front indicate the direction of the velocity and the color of

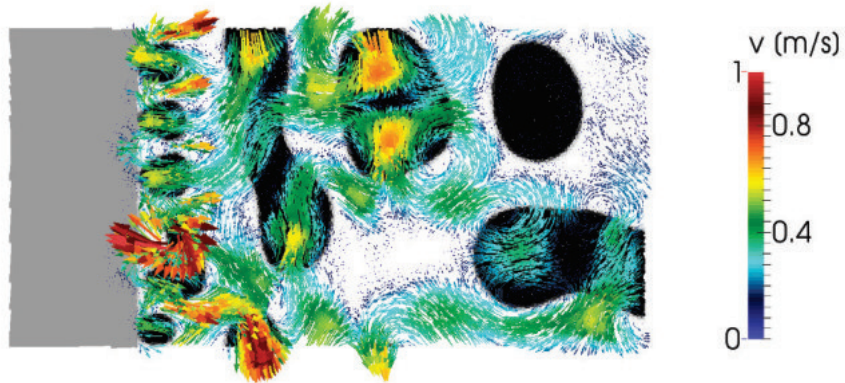
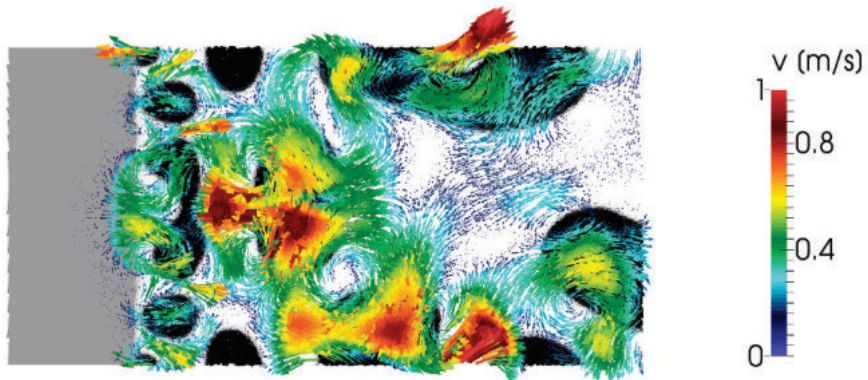
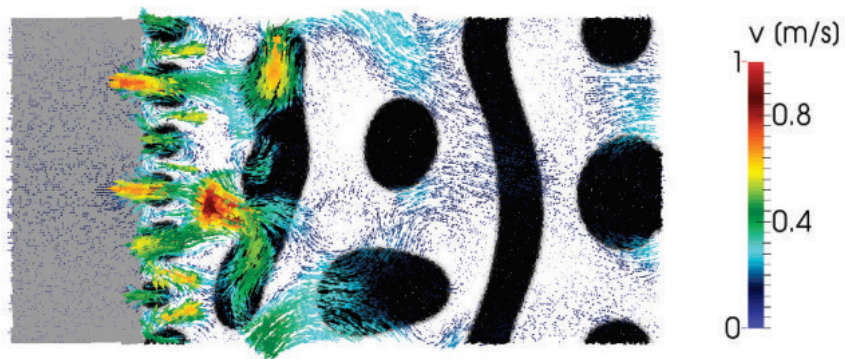
(a) $\sigma_T = -0.5mN/m$.(b) $\sigma_T = -5mN/m$.(c) $\sigma_T = -50mN/m$.

Figure 6.16: Morphology for 3 different surface tensions gradients at time $t = 1.95ms$. The surface tension is $\sigma_0 = 70.5mN/m$. (a) $\sigma_T = -0.5mN/m$, (b) $\sigma_T = -5mN/m$, (c) $\sigma_T = -50mN/m$. The grey scale indicates the phases with its diffuse interface in between. The arrows show the direction of velocity and the color indicates its magnitude. Only 20% of the arrows are shown.

the arrows indicate the magnitude of the velocity. We only show arrows for $\approx 20\%$ of the particles.

First we compare the magnitude of the velocity in all cases in Fig. 6.16 with the velocity of the phase separation front. The magnitude of the velocity of the phase separation front is $u_{ps} = 1m/s$. It is in the same magnitude as the peak velocity in all cases.

If gradients in the surface tension would be the main driving force for finger pores, we would expect that the magnitude of the velocity increases with increasing σ_T . This is not the case here and therefore the influence of a gradient in the surface tension may be minor (as concluded in the last section because of large viscosity). Even if the influence of a gradient in the surface tension is minor we see convection cells near the phase separation front. The convection is well visible in Fig. 6.16c. The phase that represents the polymer matrix (white) is driven to the right (and therefore into the coagulation bath somewhere outside the simulation domain) while the fluid in the pores (black) is driven into the stable polymer solution (to the left side).

In the phase distribution (grey scale in the background) we only see small influences of the convection cells. Inside the stable polymer solution on the left side we observe increasing velocity with increasing slope σ_T . The magnitude is very low and negligible compared to the velocity of the phase separation front.

Based on the present results, the theory of convection cells as mechanism for macrovoids or finger pores [Fro73; Mat72] is very unlikely. Convection cells may be only important in systems with low viscosity (or moderate Reynolds numbers).

6.8 Conclusion

In this chapter we introduced Liesegang patterns as the mechanism to explain the formation of porous structures in polymer membranes. In the context of membrane formation, Liesegang patterns are alternating structures evolving behind a precipitation front. The mechanism depends on diffusive transport.

First we introduced the simplified model that predicts Liesegang patterns with ω as a reduced composition. This model only considers the component balance equation and a characteristic kinetic during phase separation. This enables us to reduce the ternary system to a binary system where the velocity of phase separation front is an

input parameter.

We defined two characteristic parameters for the system. These numbers are the difference between the reduced mass fraction ω on the binodal, where we enter the miscibility gap, and ω_{cP} at the critical point, A , and the ratio between the diffusion coefficient of solvent in the coagulation bath and in the polymer solution, Hi . Hi is directly related to the phase separation front velocity.

We found that the morphology can be classified depending on A and Hi . For example, for low A and low Hi we find finger pores and for higher A and large Hi we find sponge pores. In addition, the transition between different kind of pores is similar to structures found in experiments. Therefore we conclude that Liesegang patterns may be the main mechanism responsible for pore formation during phase inversion process in porous polymer membranes.

In the second part of the chapter we investigated the influence of thermal fluctuations and hydrodynamics on the pore shape. We found that thermal fluctuations have minor influence on the type of pore. The influence of hydrodynamics, especially surface tension, is only relevant for polymer systems with low viscosity. For typical polymer solutions the influence of hydrodynamics is minor. If hydrodynamics influence the pore shape then gradients of the surface tension are only relevant if they are large.

We conclude that a model based on the component balance predicts the formation of morphology during the beginning of the phase inversion process. In the current model we have not considered late time effects like shrinkage and mechanical stress. Furthermore the most simplified model helps to understand the formation of pores but, in the present form, is limited to qualitative results.

CHAPTER 7

Conclusion and Outlook

7.1 Conclusion

In this thesis a model to predict morphology in porous polymer membranes is proposed. The isotherm model is based on the component and momentum balance. The important feature of the proposed model is diffusive mass transport where the gradient of the chemical potential is the driving force. Herein it is important to include the presence of a continuous interface between two phases. This interface needs to be resolved for direct simulation of the morphology.

First we investigated viscous fingering because we observed the propagation of viscous fingering in experiments. The proposed model predicts the propagation of a viscous finger well but we found doubts that viscous fingering may only be relevant in confined geometries. In addition, because of the large viscosity of the polymer solution, viscous fingering may only be relevant in the first moments of contact between polymer solution and coagulation bath.

Using the same model in a boundless geometry (where convective transport is negligible) we investigated the diffusive propagation of a phase separation front between stable polymer solution and coagulation bath. The mechanism are Liesegang patterns. With a simplified variant of the model we are able to predict all morphology that we previously observed in the experiments. Therefore we conclude that Liesegang patterns are responsible for the formation of pores in porous polymer membranes. Finally, we also investigated the effect of gradients of the surface tension during the evolution of Liesegang patterns but found that their effect is minor and may not be

relevant in the polymer system.

So far, we are able to falsify some of the theories on the formation mechanism of pores in membranes. Gradients of the surface tension (Theory of Matz [Mat72] and Frommer and Messalam [Fro73]) and viscous fingering (Theory of Ren et al. [Ren04]) are not relevant and do not explain the formation of finger pores. Delayed and spontaneous demixing (Theory of Reuvers and Smolders [Reu87b; Smo92] is, in principle, very similar to the mechanism of Liesegang patterns because the velocity of the phase separation front is a result of different diffusion transport properties. Contrary to delayed and spontaneous demixing, Liesegang patterns explain that the velocity of the phase separation front is responsible for the formation of pores and therefore provides a kinetic parameter to characterize morphology.

Lastly, the proposed model is unable to investigate shrinkage or cracks of the polymer. Therefore we are unable to falsify the theory of Strathmann et al. [Str75]. We may argue that shrinkage is a late time effect and may be slower than diffusive mass transport.

7.2 Outlook

The present pseudo-binary model is the most simplified model that predict morphology. In its present form it is limited to qualitative results only because the model-fluid is very simple (simple thermodynamics), the surface tension in the component and momentum balance is not coupled (state-of-the-art formulation), and only a ternary system is considered. For direct comparison of numerical results to experiments and a fully predictive model for pore structures, additional work is necessary. These works are summarized in the following.

Ternary system

A next step to extend this work is to use the ternary system and investigate mass transport of polymer, solvent and non-solvent inside and outside of the miscibility gap including the transition from stable to unstable polymer solution. In this case, thermal fluctuations are a key element to initiate phase separation. A comparison of the results of the ternary system to the present results may give further information about the velocity of the phase separation front and the limits of the reduced binary system.

Realistic thermodynamics

Currently we use a model-fluid to study the morphology behind a precipitation front in general. For a quantitative result we need realistic thermodynamics. This implies that also gradients in the diffuse interface, with its physical length-scale, need to be resolved. The physical diffuse interface is very thin and in the order of a few nanometers. Therefore the numerical effort is too large for the simulation of a large part of the membrane. For a very small part of the membrane, e.g. a small layer, it may be possible to extend the current model to a multi-component system and quantitatively predict the pore structure.

Alternatively one may coarse grain the thermodynamics to a practical scale determined by the typical scale of the pore size. Then a numerical free energy function including the correctly scaled surface energy may be constructed. On the coarse grain level we only have to account for the ratio of the transport coefficients and physical properties to enable quantitative results.

Another way to include realistic thermodynamics may be an adaptive numerical resolution to resolve large gradients. Near an interface we use larger resolution and reduce the resolution in the bulk phase.

Investigation of 3D structures

In 3D, additional types of structures are possible than in 2D. This was demonstrated by Foard [Foa12a] in the appendix of the PhD thesis. We may find dislocations, tubes, spheres and planes. Our model is not limited to 2D and may be extended to 3D straight forward. A next task may be an investigation of Liesegang patterns in 3D.

Current drawbacks are related to computational effort of the SPH method. Therefore more efficient implementations of the SPH algorithms are needed to reduce computational effort. Additionally, adaptive strategies like coupling of SPH to Finite Volume method or adaptive resolution may enhance the performance and reduce computation time. Alternatively, one may use another numerical method, e.g. a phase-field method based on finite-volumes, because the Cahn-Hilliard equation is also used in phase-field approaches and efficient solution methods exist.

Additional experiments

Direct observation or identification of the mechanism of pore formation in experiments is not possible yet. The reason is that we need to resolve space on nanoscale and time on microscale. This is not possible for liquid mixtures today. Therefore new experimental techniques to resolve these scales are necessary for direct observations. Beside direct observation some effects may be investigated by state-of-the-art setups. For example the effect of shrinkage of the polymer matrix can be observed using a defined and bounded geometry during phase inversion. Volume can be measured before and after phase inversion and if a difference is found, one gets a measure for the effect of shrinkage. Similar experiments are reported in literature indicating that shrinkage up to 20% of the initial volume are common for polysulfone membranes. It may be interesting if a fluctuation of the volume is seen during phase separation. It may also be possible to experimentally approximate the diffusion coefficients during phase separation. For example, if we assume that the proposed model is valid, we can measure the velocity of the phase separation front in experiments and then recursively fit the transport coefficients.

Other preparation processes

A straight forward extension of the presented work for wet-casting of phase inversion membranes is its application to dry-casting process and thermal-induced phase separation (TIPS) process. Dry-casting process is very relevant because an industrial spinning process always starts with a dry-casting unit. During dry-casting the solvent evaporates into the surrounding gas phase. Therefore a gas-liquid interface at the precipitation front arises instead of a liquid-liquid interface. In addition it may be sufficient to consider a binary mixture in the polymer solution and neglect the adsorbed gas in numerical discretization. This may reduce the computational complexity.

The TIPS process is already included in the proposed model because of the coupling of heat transport (demonstrated in the Appendix in Chap. G). A detailed investigation and comparison to experiments is needed to show that Liesegang patterns are present too. Besides, TIPS in a binary system may be used to develop a model that predicts shrinkage during the formation of pores.

Bibliography

- [Ada10a] ADAMI, S., X. Y. HU, and N. A. ADAMS: ‘A conservative SPH method for surfactant dynamics’. *Journal of Computational Physics* (2010), vol. 229: pp. 1909–1926 (cit. on p. 262).
- [Ada10b] ADAMI, S., X. Y. HU, and N. A. ADAMS: ‘A new surface-tension formulation for multi-phase SPH using a reproducing divergence approximation’. *Journal of Computational Physics* (2010), vol. 229: pp. 2011–5021 (cit. on pp. 57, 241, 255, 257, 259–261).
- [Ada13] ADAMI, S., X.Y. HU, and N.A. ADAMS: ‘A transport-velocity formulation for smoothed particle hydrodynamics’. *Journal of Computational Physics* (2013), vol. 241: pp. 292–307 (cit. on p. 86).
- [Ahm95] AHMAD, B., N. AHMAD, A. SAEED, and N.-U. ISLAM: ‘Rheology of Poly(Vinyl Pyrrolidone) in Aqueous and Organic Media’. *Journal of Chemical Society Pakistan* (1995), vol. 17: pp. 7–10 (cit. on p. 17).
- [Akt05] AKTHAKUL, ARIYA, CHRISTOPHER E. SCOTT, ANNE M. MAYES, and ALEXANDER J. WAGNER: ‘Lattice Boltzmann simulation of asymmetric membrane formation by immersion precipitation’. *Journal of Membrane Science* (2005), vol. 249(1–2): pp. 213–226 (cit. on pp. 4, 49, 55).
- [Amb95] AMBROSONE, LUIGI, GERARDINO D ERRICO, ROBERTO SARTORIO, and VINCENZO VITAGLIANO: ‘Analysis of Velocity Cross-correlation and Preferential Solvation for the System N-Methylpyrrolidone-Water at 20 °C’. *J. Chem. Soc. Faraday Trans.* (1995), vol. 91(9): pp. 1339–1344 (cit. on p. 19).

- [And96] ANDERSON, D. M. and G. B. MCFADDEN: ‘A diffuse-interface description of fluid systems’. *NIST Int. Rep. 5887, National Institute of Standards and Technology, Gaithersburg, MD* (1996), vol. (cit. on p. 210).
- [And98] ANDERSON, D. M., G. B. MCFADDEN, and A. A. WHEELER: ‘Diffuse-interface methods in fluid mechanics’. *Annu. Rev. Fluid Mech.* (1998), vol. 30: pp. 130–165 (cit. on pp. 45, 207).
- [Ant99] ANTAL, T., M. DROZ, J. MAGNIN, and Z. RÁCZ: ‘Formation of Liesegang Patterns: A Spinodal Decomposition Scenario’. *Phys. Rev. Lett.* (15 1999), vol. 83: pp. 2880–2883 (cit. on pp. 15, 50, 123).
- [Bal01] BALASHOVA, IDA M., RONALD P. DANNER, PUSHPINDER S. PURI, and J. LARRY DUDA: ‘Solubility and Diffusivity of Solvents and Nonsolvents in Polysulfone and Polyetherimide’. *Ind. Eng. Chem. Res.* (2001), vol. 40: pp. 3058–3064 (cit. on p. 19).
- [Bal87] BALASUBRAMANIAM, R. and AN-TI CHAI: ‘Thermocapillary migration of droplets: An exact solution for small marangoni numbers’. *Journal of Colloid and Interface Science* (1987), vol. 119(2): pp. 531–538 (cit. on p. 264).
- [Bal96] BALASUBRAMANIAM, R. and R.S. SUBRAMANIAM: ‘Thermocapillary bubble migration—thermal boundary layers for large Marangoni numbers’. *International Journal of Multiphase Flow* (1996), vol. 22(3): pp. 593–612 (cit. on p. 264).
- [Bal16] BALAY, SATISH et al.: *PETSc Web page*. <http://www.mcs.anl.gov/petsc>. Version 3.3. 2016 (cit. on p. 69).
- [Bal90] BALL, R C and R L H ESSERY: ‘Spinodal decomposition and pattern formation near surfaces’. *Journal of Physics: Condensed Matter* (1990), vol. 2(51): p. 10303 (cit. on p. 123).
- [Bas09] BASA, MIHAI, NATHAN J. QUINLAN, and MARTIN LASTIWKA: ‘Robustness and accuracy of SPH formulations for viscous flow’. *International Journal for Numerical Methods in Fluids* (2009), vol. 60(10): pp. 1127–1148 (cit. on p. 249).

- [Ben86] BENSIMON, DAVID, LEO P. KADANOFF, SHOUDAN LIANG, BORIS I. SHRAIMAN, and CHAO TANG: ‘Viscous flows in two dimensions’. *Rev. Mod. Phys.* (4 Oct. 1986), vol. 58: pp. 977–999 (cit. on p. 90).
- [Bir07] BIRD, R. B., W. E. STEWART, and E. N. LIGHTFOOT: *Transport Phenomena, revised second ed.* Wiley, New York, 2007: pp. 532–538 (cit. on p. 43).
- [Bon99] BONET, J. and T.-S. L. LOK: ‘Variational and momentum preservation aspects of Smooth Particle Hydrodynamic formulations’. *Comput. Method. Appl. M.* (1999), vol. 180: pp. 97–115 (cit. on pp. 60, 76, 77).
- [Boo92] BOOM, MARCEL REMKO: ‘Membrane formation by immersion precipitation: The role of a polymeric additive’. PhD thesis. University of Enschede, 1992 (cit. on pp. 3, 10, 13, 40, 145).
- [Bou97] BOUSSINESQ, J.: *Theorie de l’écoulement tourbillonnant et tumultueux des liquides dans les lits rectilignes a grande section.* Vol. 1. Gauthier-Villars et Fils, 1897 (cit. on p. 250).
- [Bra92] BRACKBILL, J. U., D. B. KOTHE, and C. ZEMACH: ‘A Continuum Method for Modeling Surface Tension’. *J. Comp. Phys.* (1992), vol. 100: pp. 335–354 (cit. on pp. 65, 255).
- [Bra94] BRAY, A.J.: ‘Theory of phase-ordering kinetics’. *Advances in Physics* (1994), vol. 43(3): pp. 357–459 (cit. on p. 50).
- [Bro80] BROENS, L., F. W. ALTENA, and C. A. SMOLDERS: ‘Asymmetric membrane structures as a result of phase separation phenomena’. *Desalination* (1980), vol. 32: pp. 33–45 (cit. on p. 14).
- [Bro85] BROOKSHAW, L.: ‘A Method of Calculating Radiative Heat Diffusion in Particle Simulations’. *Proc. ASA* (1985), vol. 6(2): pp. 207–210 (cit. on p. 62).
- [Bur66] BURGGRAF, O.: ‘Analytical and numerical studies of the structure of steady separated flows’. *J. Fluid Mech.* (1966), vol. 24: pp. 113–151 (cit. on p. 246).

- [Cah58] CAHN, J. W. and J. E. HILLIARD: ‘Free Energy of a Nonuniform System. I. Interfacial Free Energy’. *Journal of Chemical Physics* (1958), vol. 28 (2): pp. 258–267 (cit. on pp. 36, 38, 215).
- [Can85] CANEBA, G. T. and D. S. SOONG: ‘Polymer Membrane Formation through the Thermal-Inversion Process. 2. Mathematical Modeling of Membrane Structure Formation’. *Macromolecules* (1985), vol. 18: pp. 2545–2555 (cit. on p. 2).
- [Can86] CANNY, J.: ‘A computational Approach to Edge Detection’. *IEEE Transactions on Pattern Analysis and Machine Intelligence* (1986), vol. 8(6): pp. 679–698 (cit. on p. 218).
- [Cas00] CASADEMUNT, J. and F.X. MAGDALENO: ‘Dynamics and selection of fingering patterns. Recent developments in the Saffman–Taylor problem’. *Physics Reports* (2000), vol. 337(1–2): pp. 1–35 (cit. on p. 90).
- [Cas04] CASADEMUNT, JAUME: ‘Viscous fingering as a paradigm of interfacial pattern formation: Recent results and new challenges’. *Chaos* (2004), vol. 14(3): pp. 809–824 (cit. on pp. 90, 92).
- [Che98] CHEN, SHIYI and GARY D. DOOLEN: ‘LATTICE BOLTZMANN METHOD FOR FLUID FLOWS’. *Annual Review of Fluid Mechanics* (1998), vol. 30(1): pp. 329–364 (cit. on p. 55).
- [Che99] CHENG, LIAO-PING, DAR-JONG LIN, CHIEN-HSIEH SHIH, AN-HWA DWAN, and CARL C. GRYTE: ‘PVDF membrane formation by diffusion-induced phase separation-morphology prediction based on phase behavior and mass transfer modeling’. *Journal of Polymer Science Part B: Polymer Physics* (1999), vol. 37(16): pp. 2079–2092 (cit. on pp. 48, 146).
- [Cho68] CHORIN, A. J.: ‘Numerical solution of the Navier-Stokes equations’. *Math. Comp.* (1968), vol. 22: pp. 745–762 (cit. on p. 84).
- [Chu59] CHUOKE, R. L., P. van MEURS, and C. van der POEL: ‘The Instability of Slow, Immiscible, Viscous Liquid–Liquid Displacements in Permeable Media’. *Trans. AIME* (1959), vol. 216: pp. 233–268 (cit. on pp. 90, 93, 109, 271, 273).

- [Cle99] CLEARY, P. W. and J. J. MONAGHAN: ‘Conduction Modelling Using Smoothed Particle Hydrodynamics’. *Journal of Computational Physics* (1999), vol. 148: pp. 227–264 (cit. on p. 241).
- [Coh79] COHEN, C., G. B. TANNY, and S. PRAGER: ‘Diffusion-controlled formation of porous structures in ternary polymer systems’. *Journal of Polymer Science Part B: Polymer Physics* (1979), vol. 17: pp. 477–489 (cit. on p. 48).
- [Col03] COLAGROSSI, A. and M. LANDRINI: ‘Numerical simulation of interfacial flows by smoothed particle hydrodynamics’. *J. Comp. Phys.* (2003), vol. 191: pp. 448–475 (cit. on pp. 57, 62, 68).
- [Cou00] COUDER, Y.: *Perspectives in Fluid Dynamics*. Ed. by BATCHELOR, G. K. and M. WORSTER. Cambridge University Press, 2000 (cit. on p. 90).
- [Cra75] CRANK, J.: *The mathematics of diffusion*. 2nd. Oxford University Press, 1975 (cit. on p. 241).
- [Cue14] CUETO-FELGUEROSO, LUIS and RUBEN JUANES: ‘A phase-field model of two-phase Hele-Shaw flow’. *Journal of Fluid Mechanics* (2014), vol. 758: pp. 522–552 (cit. on p. 91).
- [Cum99] CUMMINS, S. J. and M. RUDMAN: ‘An SPH Projection Method’. *J. Comp. Phys.* (1999), vol. 152: pp. 584–607 (cit. on pp. 57, 68, 73, 75, 84, 85, 91).
- [Deg86] DEGREGORIA, A. J. and L. W. SCHWARTZ: ‘A boundary-integral method for two-phase displacement in Hele-Shaw cells’. *Journal of Fluid Mechanics* (1986), vol. 164: pp. 383–400 (cit. on p. 91).
- [Don14] DONEV, A., A. NONAKA, Y. SUN, T. G. FAI, A. L. GARCIA, and J. B. BELL: ‘Low mach number fluctuating hydrodynamics of diffusively mixing fluids’. *Comm. App. Math. and Comp. Sci.* (2014), vol. 9: pp. 47–105 (cit. on p. 47).
- [Esp03a] ESPANOL, P. and M. REVENGA: ‘Smoothed dissipative particle dynamics’. *Physical Review E* (2003), vol. 67: p. 026705 (cit. on pp. 46, 47, 67, 85).

- [Esp03b] ESPANOL, PEP and CEDRIC THIEULOT: ‘Microscopic derivation of hydrodynamic equations for phase-separating fluid mixtures’. *The Journal of Chemical Physics* (2003), vol. 118(20) (cit. on pp. 42, 44).
- [Eul68] EULER, L.: *Institutiones calculi integralis*. Petersburg: Acad. Imp. Reprinted in OO, 1768 (cit. on p. 84).
- [Fal16] FALGOUT, ROBERT, ANDY CLEARY, JIM JONES, EDMOND CHOW, VAN HENSON, CHUCK BALDWIN, PETER BROWN, PANAYOT VASSILEVSKI, and ULRIKE MEIER YANG: *Hypre Web page*. <http://acts.nerisc.gov/hypre>. 2016 (cit. on p. 69).
- [Fat11] FATEHI, R. and M. T. MANZARI: ‘Error estimation in smoothed particle hydrodynamics and a new scheme for second derivatives’. *Computers and Mathematics with Applications* (2011), vol. 61: pp. 482–498 (cit. on pp. 62, 64, 225).
- [Fat14] FATEHI, ROUHOLLAH, MOSTAFA SAFDARI SHADLOO, and MEHRDAD T MANZARI: ‘Numerical investigation of two-phase secondary Kelvin–Helmholtz instability’. *Proceedings of the Institution of Mechanical Engineers, Part C: Journal of Mechanical Engineering Science* (2014), vol. 228(11): pp. 1913–1924 (cit. on p. 91).
- [Fat15] FATH, ANJA and DIETER BOTHE: ‘Direct numerical simulations of thermocapillary migration of a droplet attached to a solid wall’. *International Journal of Multiphase Flow* (2015), vol. 77: pp. 209–221 (cit. on p. 264).
- [Fed12] FEDERICO, I., S. MARRONE, A. COLAGROSSI, F. ARISTODEMO, and M. ANTUONO: ‘Simulating 2D open-channel flows through an SPH model’. *Eur. J. Mech. B-Fluid* (2012), vol. 34: pp. 35–46 (cit. on p. 74).
- [Fed13] FEDOSOV, A.: ‘Thermocapillary motion’. *arXiv preprint* (2013), vol.: arXiv:1303.0243 (cit. on pp. 264, 269).
- [Fer13] FERRAND, M., D. R. LAURENCE, B. D. ROGERS, D. VIOLEAU, and C. KASSIOTIS: ‘Unified semi-analytical wall boundary conditions for inviscid laminar or turbulent flows in the meshless SPH method’. *Int. J. Numer. Meth. Fluids* (2013), vol. 71: pp. 446–472 (cit. on p. 74).

- [Fer96] FERZIGER, J. M. and M. PERIC: *Computational Methods for Fluid Dynamics*. Springer, 1996 (cit. on p. 56).
- [Fif00] FIFE, P. C.: ‘Models for phase separation and their mathematics’. *Electronic Journal of Differential Equations* (2000), vol. 48: pp. 1–26 (cit. on p. 38).
- [Flo42] FLORY, PAUL J.: ‘Thermodynamics of High Polymer Solutions’. *J. Chem. Phys.* (1942), vol. 10: pp. 51–61 (cit. on p. 40).
- [Foa12a] FOARD, E. M.: ‘A numerical and analytical analysis of the physics of phase-separation fronts’. PhD thesis. North Dakota State University, Fargo, USA, 2012 (cit. on pp. 123, 124, 145, 149, 163).
- [Foa09] FOARD, E. M. and A. J. WAGNER: ‘Enslaved phase-separation fronts in one-dimensional binary mixtures’. *Physical Review E* (2009), vol. 79: p. 056710 (cit. on pp. 15, 49, 123).
- [Foa12b] FOARD, E. M. and A. J. WAGNER: ‘Survey of morphologies formed in the wake of an enslaved phase-separation front in two dimensions’. *Physical Review E* (2012), vol. 85: p. 011501 (cit. on pp. 6, 15, 28, 50, 55, 123, 124, 139, 144).
- [Fro73] FROMMER, MOSHE A. and RAMI M. MESSALEM: ‘Mechanism of Membrane Formation. VI. Convective Flows and Large Void Formation during Membrane Precipitation’. *Ind. Eng. Chem. Prod. Res. Dev.* (1973), vol. 12(4): pp. 328–333 (cit. on pp. 9, 11, 159, 162).
- [Ghi82] GHIA, U., K. N. GHIA, and C. T. SHIN: ‘High-Re Solutions for Incompressible Flow Using three Navier–Stokes Equations and a Multigrid Method’. *J. Comp. Phys.* (1982), vol. 48: pp. 387–411 (cit. on pp. 245, 246, 249).
- [Gin77] GINGOLD, R. A. and J. J. MONAGHAN: ‘Smoothed Particle Hydrodynamics: theory and application to non-spherical stars’. *Mon. Not. R. astr. Soc* (1977), vol. 181: pp. 375–389 (cit. on pp. 57, 58, 61).

- [Git70] GITTENS, G. J., P. A. HITCHCOCK, D. C. SAMMON, and G. E. WAKLEY: ‘The structure of cellulose acetate membranes for reverse osmosis. Part I. membranes prepared from a dioxane based dope’. *Desalination* (1970), vol. 8: p. 369 (cit. on p. 146).
- [Gre09] GRENIER, N., M. ANTUONO, A. COLAGROSSI, D. LE TOUZÉ, and B. ALESSANDRINI: ‘An Hamiltonian interface SPH formulation for multi-fluid and free surface flows’. *Journal of Computational Physics* (2009), vol. 228: pp. 8380–8393 (cit. on pp. 57, 60, 68, 91, 255).
- [Grm97a] GRMELA, MIROSLAV and HANS CHRISTIAN ÖTTINGER: ‘Dynamics and thermodynamics of complex fluids. I. Development of a general formalism’. *Phys. Rev. E* (6 1997), vol. 56: pp. 6620–6632 (cit. on p. 3).
- [Grm97b] GRMELA, MIROSLAV and HANS CHRISTIAN ÖTTINGER: ‘Dynamics and thermodynamics of complex fluids. I. Development of a general formalism’. *Phys. Rev. E* (6 1997), vol. 56: pp. 6620–6632 (cit. on p. 67).
- [Gro01] GROSS, JOACHIM and GABRIELE SADOWSKI: ‘Perturbed-Chain SAFT: An Equation of State Based on a Perturbation Theory for Chain Molecules’. *Ind. Eng. Chem. Res.* (2001), vol. 40: pp. 1244–1260 (cit. on p. 41).
- [Had99] HADLAND, H. P., R. BALASUBRAMANIAM, G. WOZNIAK, and S. R. SUBRAMANIAN: ‘Thermocapillary migration of bubbles and drops at moderate to large Marangoni number and moderate Reynolds number in reduced gravity’. *Experiments in Fluids* (1999), vol. 26(3): pp. 240–248 (cit. on p. 264).
- [Haj14] HAJRA, BODHISATTA: ‘A Review of Some Recent Studies on Buoyancy Driven Flows in an Urban Environment’. *International Journal of Atmospheric Sciences* (2014), vol. 2014: 15, Article ID 362182 (cit. on p. 245).
- [Han67] HANSEN, CHARLES M.: ‘The Three Dimensional Solubility Parameter and Solvent Diffusion Coefficient, Their Importance in Surface Coating Formulation’. PhD thesis. Danish Technical Press, Copenhagen, 1967 (cit. on p. 8).

- [Han06] HANTZ, PÉTER and ISTVÁN BIRÓ: ‘Phase Separation in the Wake of Moving Fronts’. *Phys. Rev. Lett.* (8 2006), vol. 96: p. 088305 (cit. on pp. 50, 123).
- [He11] HE, YAN-DONG, YUAN-HUI TANG, and XIAO-LIN WANG: ‘Dissipative particle dynamics simulation on the membrane formation of polymer–diluent system via thermally induced phase separation’. *Journal of Membrane Science* (2011), vol. 368: pp. 78–85 (cit. on pp. 4, 56).
- [Hej10] HEJAZI, S. H., P. M. J. TREVELYAN, J. AZAIEZ, and A. de WIT: ‘Viscous fingering of a miscible reactive $A + B \rightarrow C$ interface: a linear stability analysis’. *Journal of Fluid Mechanics* (2010), vol. 652: pp. 501–528 (cit. on pp. 90, 109).
- [Hel98] HELE–SHAW, H. S.: ‘The flow of water’. *Nature* (1898), vol. 58: pp. 33–36 (cit. on pp. 89, 91).
- [Hel58] HELMHOLTZ, H.: ‘Über Integrale der hydrodynamischen Gleichungen, welcher der Wirbelbewegungen entsprechen’. *Journal für die reine und angewandte Mathematik* (1858), vol. 55: pp. 25–55 (cit. on p. 68).
- [Heß10] HESS, STEFFEN and VOLKER SPRINGEL: ‘Particle hydrodynamics with tessellation techniques’. *Monthly Notices of the Royal Astronomical Society* (2010), vol. 406(4): pp. 2289–2311 (cit. on p. 257).
- [Hil52] HILL, S. and F.INST. P: ‘Channeling in packed columns’. *Chemical Engineering Science* (1952), vol. 1(6): pp. 247–253 (cit. on pp. 90, 93).
- [Hir14] HIRSCHLER, MANUEL, MANUEL HUBER, WINFRIED SÄCKEL, PHILIP KUNZ, and ULRICH NIEKEN: ‘An Application of the Cahn-Hilliard Approach to Smoothed Particle Hydrodynamics’. *Mathematical Problems in Engineering* (2014), vol. 2014: p. 694894 (cit. on pp. 64, 215, 218, 228, 230).
- [Hir16a] HIRSCHLER, MANUEL, PHILIP KUNZ, MANUEL HUBER, FRIEDEMANN HAHN, and ULRICH NIEKEN: ‘Open boundary conditions for ISPH and their application to micro-flow’. *Journal of Computational Physics* (2016), vol. 307: pp. 614–633 (cit. on pp. 74–76).

- [Hir16b] HIRSCHLER, MANUEL, WINFRIED SÄCKEL, and ULRICH NIEKEN: ‘On Maxwell-Stefan diffusion in Smoothed Particle Hydrodynamics’. *International Journal of Heat and Mass Transfer* (2016), vol. 103: pp. 548–554 (cit. on p. 240).
- [Hom87] HOMSY, G. M.: ‘Viscous Fingering in Porous Media’. *Annual Review of Fluid Mechanics* (1987), vol. 19(1): pp. 271–311 (cit. on pp. 90, 109).
- [Hos11] HOSSEINI, S. M. and J. FENG: ‘Pressure boundary conditions for computing incompressible flows with SPH’. *J. Comput. Phys.* (2011), vol. 230: pp. 7473–7487 (cit. on p. 75).
- [Hu15] HU, X.: *personal communication*. SPHERIC 2015, Parma. May 2015 (cit. on p. 80).
- [Hu09] HU, X. Y. and N. A. ADAMS: ‘A constant-density approach for incompressible multi-phase SPH’. *Journal of Computational Physics* (2009), vol. 228: pp. 2082–2091 (cit. on p. 57).
- [Hu06] HU, X. Y. and N. A. ADAMS: ‘A multi-phase SPH method for macroscopic and mesoscopic flows’. *Journal of Computational Physics* (2006), vol. 213: pp. 844–861 (cit. on pp. 57, 63, 255, 259, 260).
- [Hu07] HU, X. Y. and N. A. ADAMS: ‘An incompressible multi-phase SPH method’. *J. Comp. Phys.* (2007), vol. 227: pp. 264–278 (cit. on pp. 68, 76, 77, 79).
- [Hub16] HUBER, M., F. KELLER, W. SÄCKEL, M. HIRSCHLER, P. KUNZ, S.M. HASSANIZADEH, and U. NIEKEN: ‘On the physically based modeling of surface tension and moving contact lines with dynamic contact angles on the continuum scale’. *Journal of Computational Physics* (2016), vol. 310: pp. 459–477 (cit. on p. 255).
- [Hug42] HUGGINS, MAURICE L.: ‘Some Properties of Solutions of Long-Chain compounds’. *J. Phys. Chem.* (1942), vol. 46: pp. 151–158 (cit. on p. 40).
- [Jac99] JACQMIN, D.: ‘Calculation of Two-Phase Navier-Stokes Flows Using Phase-Field Modeling’. *Journal of Computational Physics* (1999), vol. 155: pp. 96–127 (cit. on p. 44).

- [Jam08] JAMET, D. and C. MISBAH: ‘Thermodynamically consistent picture of the phase-field model of vesicles: Elimination of the surface tension’. *Phys. Rev. E* (4 2008), vol. 78: p. 041903 (cit. on pp. 37, 45).
- [Jam02] JAMET, DIDIER, DAVID TORRES, and J.U. BRACKBILL: ‘On the Theory and Computation of Surface Tension: The Elimination of Parasitic Currents through Energy Conservation in the Second-Gradient Method’. *Journal of Computational Physics* (2002), vol. 182(1): pp. 262–276 (cit. on p. 36).
- [Kah00] KAHL, HEIKE and SABINE ENDERS: ‘Calculation of surface properties of pure fluids using density gradient theory and SAFT–EOS’. *Fluid Phase Equilibria* (2000), vol. 172: pp. 27–42 (cit. on p. 38).
- [Kan08] KANG, Q., H. L. CUI, L. HU, and L. DUAN: ‘On-board Experimental Study of Bubble Thermocapillary Migration in a Recoverable Satellite’. *Microgravity Science and Technology* (2008), vol. 20(2): pp. 67–71 (cit. on p. 264).
- [Kan06] KANG, Q., L. HU, C. HUANG, H.L. CUI, L. DUAN, and W.R. HU: ‘Experimental investigations on interaction of two drops by thermocapillary-buoyancy migration’. *International Journal of Heat and Mass Transfer* (2006), vol. 49(15–16): pp. 2636–2641 (cit. on p. 264).
- [Kas13] KASSIOTIS, C., D. VIOLEAU, and M. FERRAND: ‘Semi–Analytical Conditions for Open Boundaries in Smoothed PArticle Hydrodynamics’. *Proceedings to the 8th international SPHERIC workshop*. 2013 (cit. on p. 75).
- [Kel15] KELLER, FRANZ: ‘Simulation of the Morphogenesis of Open-porous Materials’. PhD thesis. University of Stuttgart, 2015 (cit. on pp. 70, 77, 84).
- [Kho16] KHORASANIZADE, SH. and J. M. M. SOUSA: ‘An innovative open boundary treatment for incompressible SPH’. *International Journal for Numerical Methods in Fluids* (2016), vol. 80(3): pp. 161–180 (cit. on pp. 74, 76).

- [Kho14] KHORASANIZADE, SHAHAB and JOAO M. M. SOUSA: ‘A detailed study of lid-driven cavity flow at moderate Reynolds numbers using Incompressible SPH’. *International Journal for Numerical Methods in Fluids* (2014), vol. 76(10): pp. 653–668 (cit. on p. 249).
- [Kim05] KIM, J.: ‘A continuous surface tension force formulation for diffuse-interface models’. *Journal of Computational Physics* (2005), vol. 204: pp. 784–804 (cit. on pp. 224, 225).
- [Kim12] KIM, J.: ‘Phase-Field Models for Multi-Component Fluid Flows’. *Commun. Comput. Phys.* (2012), vol. 12:3: pp. 613–661 (cit. on p. 224).
- [Kim90] KIMMERLE, K. and H. STRATHMANN: ‘Analysis of the structure-determining process of phase inversion membranes’. *Desalination* (1990), vol. 78: p. 283 (cit. on p. 10).
- [Koe77] KOENHEN, D. M., M. H. V. MULDER, and C. A. SMOLDERS: ‘Phase separation phenomena during the formation of asymmetric membranes’. *Journal of Applied Polymer Science* (1977), vol. 21(1): pp. 199–215 (cit. on p. 10).
- [Koo98] KOOLS, W. F. C.: ‘Membrane Formation by Phase Inversion in Multicomponent Polymer Systems’. Habilitation. Universität Twente, 1998 (cit. on pp. 19, 41, 52).
- [Köp10] KÖPF, MICHAEL H., SVETLANA V. GUREVICH, RUDOLF FRIEDRICH, and LIFENG CHI: ‘Pattern Formation in Monolayer Transfer Systems with Substrate-Mediated Condensation’. *Langmuir* (2010), vol. 26(13): pp. 10444–10447 (cit. on p. 123).
- [Kor14] KORDILLA, JANNES, WENXIAO PAN, and ALEXANDRE TARTAKOVSKY: ‘Smoothed particle hydrodynamics model for Landau–Lifshitz–Navier–Stokes and advection–diffusion equations’. *Journal of Chemical Physics* (2014), vol. 141: p. 224112 (cit. on p. 227).
- [Kor01] KORTEWEG, D. J.: ‘Sur la forme que prennent les equations du mouvement des fluides si l on tient compte des forces capillaires par des variations de densite’. *Archives Neerlandaises des Sciences Exactes et Naturelles* (1901), vol. 6: pp. 1–24 (cit. on p. 45).

- [Kro14] KRONE, MICHAEL, MARKUS HUBER, KATRIN SCHARNOWSKI, MANUEL HIRSCHLER, DANIEL KAUKER, GUIDO REINA, ULRICH NIEKEN, DANIEL WEISKOPF, and THOMAS ERTL: ‘Evaluation of Visualizations for Interface Analysis of SPH’. *Euro Vis 2014 Short Papers 3* (2014), vol. 2014 (cit. on p. 215).
- [Kue88] KUEPER, BERNARD H. and EMIL O. FRIND: ‘An overview of immiscible fingering in porous media’. *Journal of Contaminant Hydrology* (1988), vol. 2(2): pp. 95–110 (cit. on p. 91).
- [Kun16] KUNZ, P., M. HIRSCHLER, M. HUBER, and U. NIEKEN: ‘Inflow/outflow with Dirichlet boundary conditions for pressure in ISPH’. *Journal of Computational Physics* (2016), vol. 326: pp. 171–187 (cit. on pp. 75, 76).
- [Lan87] LANDAU, L. D. and E. M. LIFSHITZ: *Course of Theoretical Physics: Fluid Dynamics*. Ed. by SYKES, J. B. and W. H. REID. 2nd. Vol. 6. Elsevier Ltd., Butterwoth Heinemann, 1987 (cit. on pp. 43, 44, 91, 250, 251, 281).
- [Lan80] LANDAU, L. D. and E. M. LIFSHITZ: *Course of Theoretical Physics: Statistical Physics Part 1*. Ed. by SYKES, J. B. and M. J. KEARSLEY. 3rd. Vol. 5. Elsevier Ltd., Butterwoth Heinemann, 1980 (cit. on p. 213).
- [Las09] LASTIWKA, M., M. BASA, and N. J. QUINLAN: ‘Permeable and non-reflecting boundary conditions in SPH’. *Int. J. Numer. Meth. Fluids* (2009), vol. 61: pp. 709–724 (cit. on pp. 74, 75).
- [Le 08] LE TOUZÉ, D., G. OGER, and B. ALESSANDRINI: ‘Smoothed Particle Hydrodynamics simulation of fast ship flows’. *Proc. 27th Symposium on Naval Hydrodynamics*. 2008 (cit. on p. 57).
- [Lee08] LEE, E.-S., C. MOULINEC, R. XU, D. VIOLEAU, D. LAURENCE, and P. STANSBY: ‘Comparisons of weakly compressible and truly incompressible algorithms for the SPH mesh free particle method’. *Journal of Computational Physics* (2008), vol. 227: pp. 8417–8436 (cit. on pp. 246, 249).

- [Lee06] LEE, H., S. R. CHAUDHURI, W. B. KRANTZ, and S. HWANG: ‘A model for evaporative casting of polymeric membranes incorporating convection due to density changes’. *Journal of Membrane Science* (2006), vol. 284: pp. 161–172 (cit. on p. 48).
- [Lee10] LEE, H., W. B. KRANTZ, and S. HWANG: ‘A model for wet-casting polymeric membranes incorporating nonequilibrium interfacial dynamics vitrification and convection’. *Journal of Membrane Science* (2010), vol. 354: pp. 74–85 (cit. on pp. 3, 48).
- [LeQ81] LEQUERE, O., J. A. C. HUMPHERY, and F. S. SHERMAN: ‘Numerical calculation of thermally driven 2D unsteady laminar flow in cavities of rectangular cross section’. *Numer. Heat Transfer* (1981), vol. 4: pp. 249–283 (cit. on p. 245).
- [Ler15] LEROY, A., D. VIOLEAU, M. FERRAND, and A. JOLY: ‘Buoyancy modelling with incompressible SPH for laminar and turbulent flows’. *International Journal for Numerical Methods in Fluids* (2015), vol. 78(8): pp. 455–474 (cit. on pp. 250, 253, 254).
- [Lie96] LIESEGANG, R. E.: ‘Über einige Eigenschaften von Gallerten’. *Naturwissenschaftliche Wochenschrift* (1896), vol. 11(30): pp. 353–362 (cit. on pp. 15, 123).
- [Lif61] LIFTSHITZ, I. M. and V. V. SLYOZOV: ‘The Kinetics of Precipitation from Supersaturated Solid Solutions’. *J. Phys. Chem. Solids* (1961), vol. 19: pp. 35–50 (cit. on p. 215).
- [Lin12] LIND, S. J., R. XU, P. K. STANSBY, and B. D. ROGERS: ‘Incompressible Smoothed Particle Hydrodynamics for free-surface flows: A generalised diffusion-based algorithm for stability and validations for impulsive flows and propagating waves’. *J. Comp. Phys.* (2012), vol. 231: pp. 1499–1523 (cit. on pp. 77, 82).
- [Liu03] LIU, G. R. and M. B. LIU: *Smoothed Particle Hydrodynamics. A mesh-free particle method*. World Scientific Publishing Co. Pte. Ltd. Singapore, 2003 (cit. on p. 58).

- [Liu10] LIU, M. B. and G. R. LIU: ‘Smoothed Particle Hydrodynamics (SPH): an Overview and Recent Developments’. *Arch. Comput. Method. Eng.* (2010), vol. 17: pp. 25–76 (cit. on pp. 58–60, 62, 77).
- [Loe63] LOEB, SIDNEY and SRINIVASA SOURIRAJAN: ‘Sea Water Demineralization by Means of an Osmotic Membrane’. *Saline Water Conversion—II*. Vol. 38. 1963. Chap. 9: pp. 117–132 (cit. on pp. 2, 9).
- [Low98] LOWENGRUB, J. and L. TRUSKINOVSKY: ‘Quasi-incompressible Cahn-Hilliard fluids and topological transitions’. *Proc. R. Soc. Lond. A* (1998), vol. 454: pp. 2617–2654 (cit. on p. 44).
- [Luc77] LUCY, L. B.: ‘A numerical approach to the testing of the fission hypothesis’. *The Astronomical Journal* (1977), vol. 82: pp. 1013–1024 (cit. on p. 57).
- [Ma11] MA, CHEN and DIETER BOTHE: ‘Direct numerical simulation of thermocapillary flow based on the Volume of Fluid method’. *International Journal of Multiphase Flow* (2011), vol. 37(9): pp. 1045–1058 (cit. on pp. 246, 264, 266–268).
- [Mah85] MAHER, J. V.: ‘Development of Viscous Fingering Patterns’. *Phys. Rev. Lett.* (14 1985), vol. 54: pp. 1498–1501 (cit. on pp. 29, 93, 94).
- [Mat72] MATZ, R.: ‘The structure of cellulose acetate membranes II. The physical and transport characteristics of the porous layer of anisotropic membranes’. *Desalination* (1972), vol. 11(2): pp. 207–215 (cit. on pp. 11, 16, 154, 159, 162).
- [Mei88] MEIBURG, E. and G. M. HOMS Y: ‘Nonlinear unstable viscous fingers in Hele-Shaw flows. II. Numerical simulation’. *Physics of Fluids* (1988), vol. 31(3): pp. 429–439 (cit. on p. 91).
- [Mez12] MEZGER, THOMAS G.: *Das Rheologie Handbuch*. 4th ed. Vincentz Network, 2012 (cit. on p. 17).
- [Min15] MINO, YASUSHI, TORU ISHIGAMI, YUSUKE KAGAWA, and HIDETO MATSUYAMA: ‘Three-dimensional phase-field simulations of membrane porous structure formation by thermally induced phase separation in polymer

- solutions'. *Journal of Membrane Science* (2015), vol. 483: pp. 104–111 (cit. on pp. 50, 56).
- [Mon85] MONAGHAN, J. J.: 'Particle Methods for Hydrodynamics'. *Computer Physics Reports* (1985), vol. 3(2):71-124: pp. 9, 14, 16, 26 (cit. on p. 59).
- [Mon94] MONAGHAN, J. J.: 'Simulating Free Surface Flows with SPH'. *Journal of Computational Physics* (1994), vol. 110: pp. 399–406 (cit. on p. 57).
- [Mon92] MONAGHAN, J. J.: 'SMOOTHED PARTICLE HYDRODYNAMICS'. *Annu. Rev. Stron. Astrphys.* (1992), vol. 30: pp. 543–574 (cit. on pp. 58, 60, 61, 63, 68, 71).
- [Mon05] MONAGHAN, J. J.: 'SMOOTHED PARTICLE HYDRODYNAMICS'. *Reports on Progress in Physics* (2005), vol. 68, Issue 8: pp. 1703–1759 (cit. on pp. 57, 58, 62, 74).
- [Mon12] MONAGHAN, J. J.: 'Smoothed Particle Hydrodynamics and Its Diverse Applications'. *Annu. Rev. Fluid Mech.* (2012), vol. 44: pp. 323–346 (cit. on pp. 58, 255).
- [Mor00] MORRIS, J. P.: 'Simulating surface tension with Smoothed Particle Hydrodynamics'. *Int. J. Numer. Meth. Fluids* (2000), vol. 33: pp. 333–353 (cit. on pp. 65, 255, 257, 259, 260).
- [Mor97] MORRIS, J. P., P. J. FOX, and Y. ZHU: 'Modeling Low Reynolds Number Incompressible Flows Using SPH'. *J. Comp. Phys.* (1997), vol. 136: pp. 214–226 (cit. on pp. 57, 71).
- [Mor96] MORRIS, JP.: 'Analysis of smoothed particle hydrodynamics with applications'. PhD thesis. Department of Mathematics, Monash University, 1996 (cit. on p. 63).
- [Mou11] MOUSAZADEH, M. H. and E. FARAMARZI: 'Calculation of surface tension of metals using density gradient theory and PC-SAFT equation of state'. *fluid Phase Equilibria* (2011), vol. 301: pp. 13–17 (cit. on p. 224).
- [Nas03] NAS, S. and G. TRYGGVASON: 'Thermocapillary interaction of two bubbles or drops'. *Int. J. Multi. Flow* (2003), vol. 29: pp. 1117–1135 (cit. on pp. 246, 264).

- [Oku97] OKUZONO, T.: ‘Smoothed-particle method for phase separation in polymer mixtures’. *Physical Review E* (1997), vol. 56 (4): p. 4416 (cit. on pp. 57, 215).
- [15] *OpenFOAM Documentation*. 2.4.0. The OpenFOAM Foundation. Mar. 2015 (cit. on pp. 246, 247, 252).
- [Ött05] ÖTTINGER, HANS CHRISTIAN: *Beyond equilibrium thermodynamics*. John Wiley & Sons, 2005: p. 656 (cit. on pp. 3, 46, 47).
- [Par84] PARK, C.-W. and G. M. HOMSY: ‘Two-phase displacement in Hele Shaw cells: theory’. *Journal of Fluid Mechanics* (1984), vol. 139: pp. 291–308 (cit. on p. 91).
- [Pat80] PATANKAR, SUHAS V.: *Numerical Heat Transfer and Fluid Flow*. McGraw-Hill, 1980 (cit. on p. 56).
- [Pen82] PENOT, F.: ‘Numerical calculation of 2D natural convection in isothermal open cavities’. *Numer. Heat Transfer* (1982), vol. 5: pp. 421–437 (cit. on p. 245).
- [Pes09] PESSO, T. and S. PIVA: ‘Laminar natural convection in a square cavity: low Prandtl numbers and large density differences’. *Int. J. Heat Mass Transfer* (2009), vol. 52: pp. 1036–1043 (cit. on p. 252).
- [Pla13] PLANKOVÁ, BARBORA, JAN HRUBÝ, and VÁCLAV VINS: ‘Prediction of the homogeneous droplet nucleation by the density gradient theory and PC-SAFT equation of state’. *AIP Conf. Proc.* (2013), vol. 1527: pp. 101–104 (cit. on p. 38).
- [Poz02] POZORSKI, JACEK and ARKADIUSZ WAWREŃCZUK: ‘SPH computation of incompressible viscous flows’. *Journal of Theoretical and Applied Mechanics* (2002), vol. 40(2)(4): pp. 917–937 (cit. on p. 246).
- [Pra15] PRAMANIK, SATYAJIT and MANORANJAN MISHRA: ‘Effect of Péclet number on miscible rectilinear displacement in a Hele-Shaw cell’. *Phys. Rev. E* (3 Mar. 2015), vol. 91: p. 033006 (cit. on pp. 94, 110, 115).
- [Pri08] PRICE, D. J.: ‘Modelling discontinuities and Kelvin-Helmholtz instabilities in SPH’. *Journal of Computational Physics* (2008), vol. 227: pp. 10040–10057 (cit. on p. 91).

- [Pro10] PROVATAS, NIKOLAS and KEN ELDER: *Phase-Field Methods in Material Science and Engineering*. Wiley-VCH, 2010 (cit. on p. 56).
- [Raf08] RAFIEE, ASHKAN: ‘MODELLING OF GENERALIZED NEWTONIAN LID-DRIVEN CAVITY FLOW USING AN SPH METHOD’. *The ANZIAM Journal* (03 2008), vol. 49: pp. 411–422 (cit. on p. 246).
- [Ray85] RAY, R. J., W. B. KRANTZ, and R. L. SANI: ‘Linear stability theory model for finger formation in asymmetric membranes’. *Journal of Membrane Science* (1985), vol. 23: pp. 155–182 (cit. on p. 11).
- [Ray79] RAYLEIGH, L.: ‘On the capillary phenomena of jets’. *Proceedings of the Royal Society of London* (1879), vol. 29: pp. 71–97 (cit. on p. 259).
- [Ray92] RAYLEIGH, LORD: ‘On the theory of surface forces - II. Compressible fluids’. *Phil. Mag.* (1892), vol. 33: pp. 209–220 (cit. on p. 45).
- [Ren04] REN, JIZHONG, ZHANSHENG LI, and FOOK-SIN WONG: ‘Membrane structure control of BTDA-TDI/MDI (P84) co-polyimide asymmetric membranes by wet-phase inversion process’. *Journal of Membrane Science* (2004), vol. 241: pp. 305–314 (cit. on pp. 5, 13, 16, 89, 91, 162).
- [Reu87a] REUVERS, A. J., J. W. A. van den BERG, and C. A. SMOLDERS: ‘Formation of Membranes by means of Immersion Precipitation. Part I. A model to describe mass transfer during immersion precipitation’. *Journal of Membrane Science* (1987), vol. 34: pp. 45–65 (cit. on p. 48).
- [Reu87b] REUVERS, A. J. and C. A. SMOLDERS: ‘Formation of Membranes by means of Immersion Precipitation. Part II. The mechanism of formation of membranes prepared from the system cellulose acetate-acetone-water’. *Journal of Membrane Science* (1987), vol. 34: pp. 67–86 (cit. on pp. 12, 162).
- [Roo09] ROOSWOG, S.: ‘Astrophysical smooth particle hydrodynamics’. *New Astronomy Reviews* (2009), vol. 53(4-6): pp. 78–104 (cit. on p. 58).
- [Saf58] SAFFMAN, P. G. and G. TAYLOR: ‘The Penetration of a Fluid into a Porous Medium or Hele-Shaw Cell Containing a More Viscous Liquid’. *Proceedings of the Royal Society of London A: Mathematical, Physical*

- and Engineering Sciences* (1958), vol. 245(1242): pp. 312–329 (cit. on pp. 90, 92, 93).
- [Sch13] SCHÄFER, ELISABETH, CHRISTINA VOGELPOHL, GABRIELE SADOWSKI, and SABINE ENDERS: ‘Simultane Modellierung von Phasengleichgewichten und Grenzflächeneigenschaften mithilfe des PCP-SAFT-Modells’. *Chemie Ingenieur Technik* (2013), vol. 85(10): pp. 1512–1522 (cit. on p. 38).
- [Sch83] SCHREIBER, R. and H.B KELLER: ‘Driven cavity flows by efficient numerical techniques’. *J. Comput. Phys.* (1983), vol. 49(2): pp. 310–333 (cit. on pp. 245, 246).
- [Sha11] SHADLOO, M. S. and M. YILDIZ: ‘Numerical modeling of Kelvin–Helmholtz instability using smoothed particle hydrodynamics’. *International Journal for Numerical Methods in Engineering* (2011), vol. 87(10): pp. 988–1006 (cit. on p. 91).
- [Sha12a] SHADLOO, M. S., A. ZAINALI, and M. YILDIZ: ‘Simulation of single mode Rayleigh–Taylor instability by SPH method’. *Computational Mechanics* (2012), vol. 51(5): pp. 699–715 (cit. on pp. 91, 256).
- [Sha12b] SHADLOO, M. S., A. ZAINALI, M. YILDIZ, and A. SULEMAN: ‘A robust weakly compressible SPH method and its comparison with an incompressible SPH’. *International Journal for Numerical methods in Engineering* (2012), vol. 89: pp. 939–956 (cit. on p. 98).
- [Sha15] SHADLOO, MOSTAFA. personal communication. Nov. 2015 (cit. on p. 223).
- [Sha16] SHADLOO, M.S., G. OGER, and D. LE TOUZÉ: ‘Smoothed Particle Hydrodynamics method for fluid flows, towards industrial applications: Motivations, current state, and challenges’. *Computers & Fluids* (2016), vol. 136: pp. 11–34 (cit. on p. 58).
- [Sha03] SHAO, S. and E. Y. M. LO: ‘Incompressible SPH method for simulating Newtonian and non-Newtonian flows with a free surface’. *Advances in Water Resources* (2003), vol. 26: pp. 787–800 (cit. on pp. 57, 68).
- [She68] SHEPARD, D.: ‘A two dimensional function for irregular space data’. *Proceedings of ACM national conference* (1968), vol.: pp. 517–524 (cit. on p. 78).

- [Smo92] SMOLDERS, C. A., A. J. REUVERS, R. M. BOOM, and I. M. WIENK: ‘Microstructures in phase-inversion membranes. Part 1. Formation of macrovoids’. *Journal of Membrane Science* (1992), vol. 73: pp. 259–275 (cit. on pp. 9, 10, 12, 14, 16, 28, 162).
- [Ste54] STERN, KURT H.: ‘The Liesegang Phenomenon’. *Chemical Reviews* (1954), vol. 54(1): pp. 79–99 (cit. on p. 123).
- [Ste59] STERNLING, C. V. and L. E. SCRIVEN: ‘Interfacial turbulence: Hydrodynamic instability and the marangoni effect’. *AIChE Journal* (1959), vol. 5(4): pp. 514–523 (cit. on p. 11).
- [Str77] STRATHMANN, H. and K. KOCK: ‘The formation mechanism of phase inversion membranes’. *Desalination* (1977), vol. 21: pp. 241–255 (cit. on p. 11).
- [Str75] STRATHMANN, H., K. KOCK, and P. AMAR: ‘The formation mechanism of asymmetric membranes’. *Desalination* (1975), vol. 16: pp. 179–203 (cit. on pp. 2, 5, 9–11, 13, 16, 18, 21, 22, 28, 29, 162).
- [Str11] STRATHMANN, HEINRICH: *Introduction to Membrane Science and Technology*. 1st ed. Wiley-VCH, 2011: p. 524 (cit. on pp. 1, 2).
- [Sub01] SUBRAMANIAN, R. S. and R. BALASUBRAMANIAM: *The Motion of Bubbles and Drops in Reduced Gravity*. Cambridge University Press, 2001 (cit. on p. 264).
- [Sze12] SZEWC, K., J. POZORSKI, and J.-P. MINIER: ‘Analysis of the incompressibility constraint in the smoothed particle hydrodynamics method’. *Int. J. Numer. Meth. Eng.* (2012), vol. 92: pp. 343–369 (cit. on pp. 63, 68, 74, 91).
- [Sze13] SZEWC, K., J. POZORSKI, and J.-P. MINIER: ‘Simulations of single bubbles rising through viscous liquids using Smoothed Particle Hydrodynamics’. *International Journal of MultiphaseFlow* (2013), vol. 50: pp. 98–105 (cit. on p. 255).
- [Sze15] SZEWC, K., J. POZORSKI, and J.-P. MINIER: ‘Spurious interface fragmentation in multiphase SPH’. *Int. J. Numer. Meth. Engng* (2015), vol. 103(9): pp. 625–649 (cit. on pp. 255, 257, 259).

- [Sze11] SZEWC, K., J. POZORSKI, and A. TANIÈRE: ‘Modeling of natural convection with Smoothed Particle Hydrodynamics: Non-Boussinesq formulation’. *International Journal of Heat and Mass Transfer* (2011), vol. 54(23–24): pp. 4807–4816 (cit. on pp. 250, 252–254).
- [Tai88] TAIT, P. G.: ‘Report on some of the physical properties of fresh water and sea water’. *Rept. Sci. Results Voy., H.M.S. Challenger, Phys. Chem.* (1888), vol. 2: pp. 1–76 (cit. on p. 68).
- [Tan88] TAN, C. T. and G. M. HOMSY: ‘Simulation of nonlinear viscous fingering in miscible displacement’. *Physics of Fluids* (1988), vol. 31(6): pp. 1330–1338 (cit. on p. 98).
- [Tan00a] TANAKA, H.: ‘Viscoelastic phase separation’. *J. Phys.: Condens. Matter* (2000), vol. 12: R207–R264 (cit. on p. 37).
- [Tan12] TANG, YUAN-HUI, YAN-DONG HE, and XIAO-LIN WANG: ‘Effect of adding a second diluent on the membrane formation of polymer/diluent system via thermally induced phase separation: Dissipative particle dynamics simulation and its experimental verification’. *Journal of Membrane Science* (2012), vol. 409–410: pp. 164–172 (cit. on pp. 4, 56).
- [Tan15] TANG, YUAN-HUI, YAN-DONG HE, and XIAO-LIN WANG: ‘Investigation on the membrane formation process of polymer–diluent system via thermally induced phase separation accompanied with mass transfer across the interface: Dissipative particle dynamics simulation and its experimental verification’. *Journal of Membrane Science* (2015), vol. 474: pp. 196–206 (cit. on pp. 4, 56).
- [Tan13] TANG, YUAN-HUI, YAN-DONG HE, and XIAO-LIN WANG: ‘Three-dimensional analysis of membrane formation via thermally induced phase separation by dissipative particle dynamics simulation’. *Journal of Membrane Science* (2013), vol. 437: pp. 40–48 (cit. on pp. 4, 56).
- [Tan00b] TANVEER, S.: ‘Surprises in viscous fingering’. *Journal of Fluid Mechanics* (2000), vol. 409: pp. 273–308 (cit. on p. 90).

- [Tar05] TARTAKOVSKY, A. M. and P. MEAKIN: ‘A smoothed particle hydrodynamics model for miscible flow in three-dimensional fractures and the two-dimensional Rayleigh-Taylor instability’. *Journal of Computational Physics* (2005), vol. 207: pp. 610–624 (cit. on p. 91).
- [Tay93] TAYLOR, R. and R. KRISHNA: *Multicomponent mass transfer*. Wiley, New York, 1993 (cit. on pp. 233, 234, 236).
- [Thi05] THIEULOT, C. and L. P. B. M. JANSSEN: ‘Smoothed particle hydrodynamics model for phase separating fluid mixtures. I. General equations’. *Physical Review E* (2005), vol. 72: p. 016713 (cit. on pp. 57, 67).
- [Tho80] THOMPSON, R.L., K.J. DE WITT, and T.L. LABUS: ‘MARANGONI BUBBLE MOTION PHENOMENON IN ZERO GRAVITY’. *Chemical Engineering Communications* (1980), vol. 5(5-6): pp. 299–314 (cit. on p. 264).
- [Ton14] TONG, M. and D. BROWNE: ‘An incompressible multi-phase smoothed particle hydrodynamics (SPH) method for modelling thermocapillary flow’. *Int. J. Heat Mass Trans.* (2014), vol. 73: pp. 284–292 (cit. on pp. 246, 262–264, 266, 267).
- [Try83] TRYGGVASON, GRETAR and HASSAN AREF: ‘Numerical experiments on Hele Shaw flow with a sharp interface’. *Journal of Fluid Mechanics* (1983), vol. 136: pp. 1–30 (cit. on pp. 22, 24, 91, 94, 96, 100).
- [Tsa90] TSAY, C. S. and A. J. MCHUGH: ‘Mass Transfer Modeling of Asymmetric Membrane Formation by Phase Inversion’. *Journal of Polymer Science: Part B: Polymer Physics* (1990), vol. 28: pp. 1327–1365 (cit. on p. 48).
- [V13] V., A. GHASEMI, B. FIROOZABADI, and M. MAHDINIA: ‘2D numerical simulation of density currents using the {SPH} projection method’. *European Journal of Mechanics - B/Fluids* (2013), vol. 38: pp. 38–46 (cit. on pp. 250, 253).
- [Vac12] VACONDIO, R., B. D. ROGERS, P. K. STANSBY, and P. MIGNOSA: ‘SPH Modeling of Shallow Flow with Open Boundaries for Practical Flood Simulation’. *JJ. Hydraul. Eng.* (2012), vol. 138: pp. 530–541 (cit. on p. 74).

- [Váz09] VÁZQUEZ-QUESADA, ADOLFO, MARCO ELLERO, and PEP ESPAÑOL: ‘Consistent scaling of thermal fluctuations in smoothed dissipative particle dynamics’. *The Journal of Chemical Physics* (2009), vol. 130(3), 034901 (cit. on p. 85).
- [Vin14] VINS, V., B. PLANKOVA, J. HRUBY, and DAVID CELNY: ‘Density gradient theory combined with the PC-SAFT equation of state used for modeling the surface tension of associating systems’. *EPJ Web of Conferences* (2014), vol. 67: p. 02129 (cit. on pp. 38, 41).
- [Vio12] VIOLEAU, DAMIEN: *Fluid Mechanics and the SPH Method*. Oxford University Press, 2012 (cit. on pp. 58–60).
- [Waa93] WAALS, J. D. van der: ‘The thermodynamic theory of capillarity under the hypothesis of a continuous density variation’. *J. Stat. Phys.* (1893), vol. 20: pp. 197–244 (cit. on pp. 36, 45).
- [Wan11] WANG, L. K., J. P. CHEN, Y-T. HUNG, and N. K. SHAMMAS: *Membrane and Desalination Technologies*. 1st ed. Humana Press, 2011: p. 716 (cit. on pp. 1, 2).
- [Wan08] WANG, XIAO-LIN, HU-JUN QIAN, LI-JUN CHEN, ZHONG-YUAN LU, and ZE-SHENG LI: ‘Dissipative particle dynamics simulation on the polymer membrane formation by immersion precipitation’. *Journal of Membrane Science* (2008), vol. 311(1–2): pp. 251–258 (cit. on pp. 4, 56).
- [Was21] WASHBURN, EDWARD W.: ‘The Dynamics of Capillary Flow’. *Phys. Rev.* (3 1921), vol. 17: pp. 273–283 (cit. on p. 116).
- [Wat96] WATKINS, S. J., A. S. BHATTAL, N. FRANCIS, J. A. TURNER, and A. P. WHITWORTH: ‘A new prescription for viscosity in Smoothed Particle Hydrodynamics’. *Astron. Astrophys. Suppl. Ser.* (1996), vol. 119: pp. 177–187 (cit. on p. 63).
- [Wen95] WENDLAND, H.: ‘Piecewise polynomial, positive definite and compactly supported radial functions of minimal degree’. *Adv. Comput. Math.* (1995), vol. 4: pp. 389–396 (cit. on p. 59).

- [Wer14] WERDELMANN, B., W. KREBS, E. PORTILLO-BILBAO, R. KOCH, and H.-J. BAUER: ‘Open Boundary Conditions Using the Mirror Ghost Particle Approach in OpenFOAM SPH’. *Proceedings to the 9th international SPHERIC workshop*. 2014 (cit. on p. 74).
- [Wit96] WITTE, P. van de, P. J. DIJKSTRA, J. W. A. van den BERG, and J. FEIJEN: ‘Phase separation processes in polymer solutions in relation to membrane formation’. *Journal of Membrane Science* (1996), vol. 117: pp. 1–31 (cit. on pp. 3, 10, 146).
- [Woz01] WOZNIAK, G., R. BALASUBRAMANIAM, H. P. HADLAND, and S. R. SUBRAMANIAN: ‘Temperature fields in a liquid due to the thermocapillary motion of bubbles and drops’. *Experiments in Fluids* (2001), vol. 31(1): pp. 84–89 (cit. on p. 264).
- [Xie05] XIE, JING-CHANG, HAI LIN, PU ZHANG, FANG LIU, and WEN-RUI HU: ‘Experimental investigation on thermocapillary drop migration at large Marangoni number in reduced gravity’. *Journal of Colloid and Interface Science* (2005), vol. 285(2): pp. 737–743 (cit. on p. 264).
- [Xu09] XU, R., P. STANSBY, and D. LAURENCE: ‘Accuracy and stability in incompressible SPH (ISPH) based on the projection method and a new approach’. *J. Comp. Phys.* (2009), vol. 228: pp. 6703–6725 (cit. on pp. 77, 80, 82, 226, 246, 249).
- [Yil09] YILDIZ, M., R. A. ROOK, and A. SULEMAN: ‘SPH with the multiple boundary tangent method’. *International Journal for Numerical Methods in Engineering* (2009), vol. 77(10): pp. 1416–1438 (cit. on pp. 74, 249).
- [You59] YOUNG, N., J. GOLDSTEIN, and M. BLOCK: ‘The motion of bubbles in a vertical temperature gradient’. *J. Fluid Mech.* (1959), vol. 6: pp. 350–356 (cit. on pp. 256, 264, 268, 269).
- [Yu14] YU, LEI, FENG YANG, and MING XIANG: ‘Phase separation in a PS-f/DMF/water system: a proposed mechanism for macrovoid formation’. *RSC Adv.* (80 2014), vol. 4: pp. 42391–42402 (cit. on pp. 2, 6, 9, 10, 14, 24, 28).

- [Zha10] ZHAO, JIAN-FU, ZHEN-DONG LI, HUI-XIONG LI, and JING LI: ‘Thermocapillary Migration of Deformable Bubbles at Moderate to Large Marangoni Number in Microgravity’. *Microgravity Science and Technology* (2010), vol. 22(3): pp. 295–303 (cit. on p. 264).
- [Zho06a] ZHOU, B.: ‘Simulations of Polymeric Membrane Formation in 2D and 3D’. PhD thesis. Massachusetts Institute of Technology, 2006 (cit. on pp. 38, 40, 41).
- [Zho06b] ZHOU, B. and A. C. POWELL: ‘Phase field simulations of early stage structure formation during immersion precipitation of polymeric membranes in 2D and 3D’. *Journal of Membrane Science* (2006), vol. 268: pp. 150–164 (cit. on pp. 4, 50, 55).
- [Zho06c] ZHOU, D., P. ZHANG, and W. E: ‘Modified models of polymer phase separation’. *Physical Review E* (2006), vol. 73: p. 061801 (cit. on p. 133).
- [Zhu01] ZHU, Y. and P. J. FOX: ‘Smoothed Particle Hydrodynamics Model for Diffusion through Porous Media’. *Transport in Porous Media* (2001), vol. 43: pp. 441–471 (cit. on p. 241).

APPENDIX A

Measurements of viscosity

Here we present the detailed results of measurements of viscosity. The viscosity is determined using the rotational rheometer RheoStress 600 from HAAKE with a titanium cone and a diameter of 35mm with an angle of 1° at constant temperature $T = 293.15\text{K}$. The shear stress τ is measured at constant rate $\dot{\gamma}$ for different rates. The dynamic viscosity η is calculated in the software RheoWin from HAAKE. Each measurement is repeated 3 times. The plots show the arithmetic average of shear stress over shear rate and dynamic viscosity over shear rate for each mixture indicated in Tab. 2.2. The error bars indicate the maximum and minimum values. The data is ordered in 5 sections. First the data for the reference solution is given. Then data for the Agar, PVP and PEG as an thicker is shown. Finally the dependence of the viscosity of the polymer solution and water on the mass fraction of thicker is summarized.

The shear rate $\dot{\gamma}$ is varied in a range of 0.001 to 200 $[1/s]$. In some mixtures the large errors occur at low shear rates. Therefore, we only use the measurements at $\dot{\gamma} = 10 [1/s]$ in the discussion in Chap. 2.

Reference solution

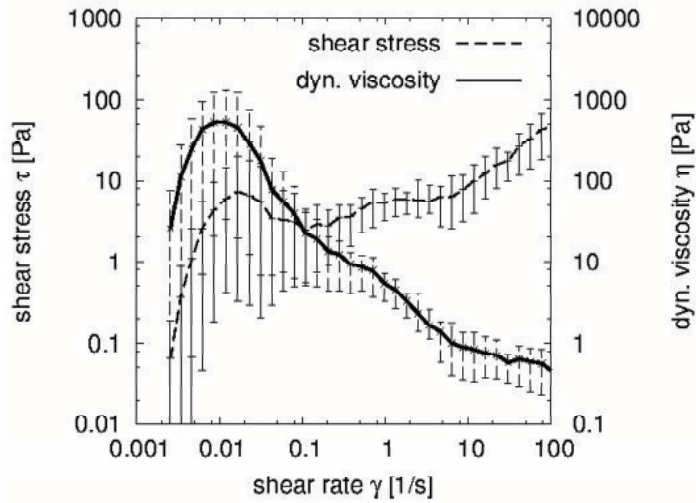


Figure A.1: Shear stress and viscosity for different shear rates. 15 % PSf - 85 % NMP.

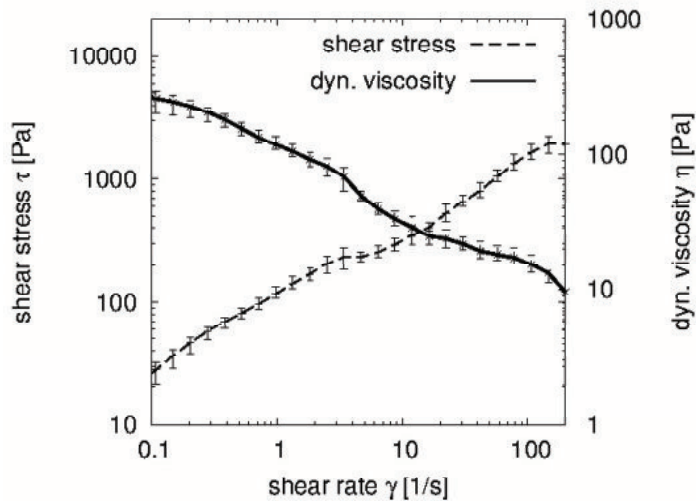


Figure A.2: Shear stress and viscosity for different shear rates. 25 % PSf - 79 % NMP - 6% PVP.

Agar

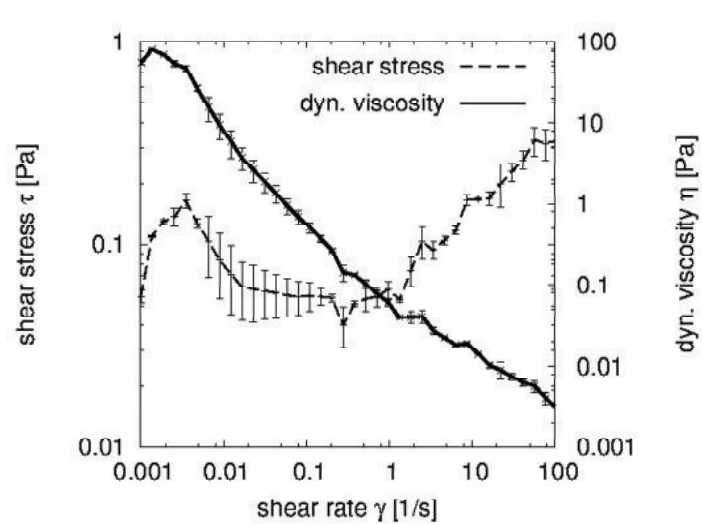


Figure A.3: Shear stress and viscosity for different shear rates. 99.99 % H₂O - 0.01 % Agar.

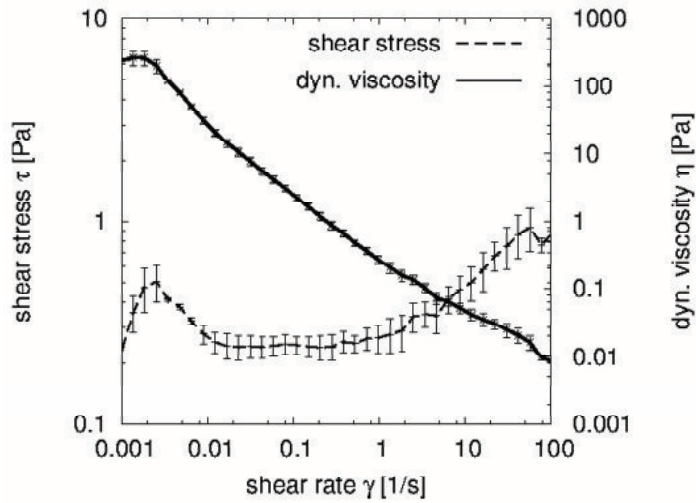


Figure A.4: Shear stress and viscosity for different shear rates. 99.975 % H₂O - 0.025 % Agar.

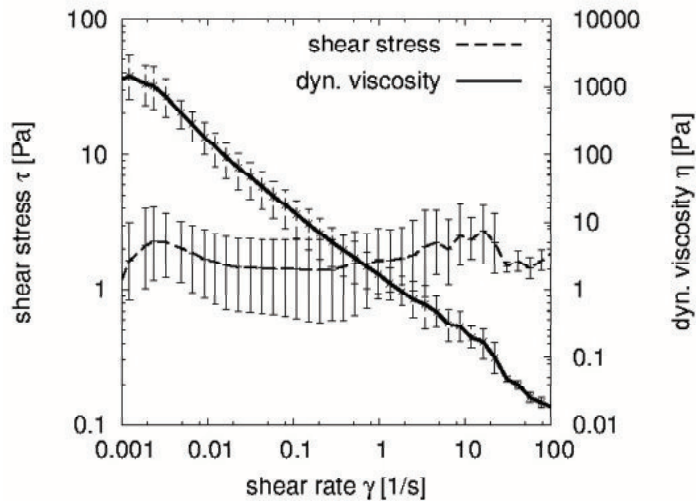


Figure A.5: Shear stress and viscosity for different shear rates. 99.95 % H₂O - 0.05 % Agar.

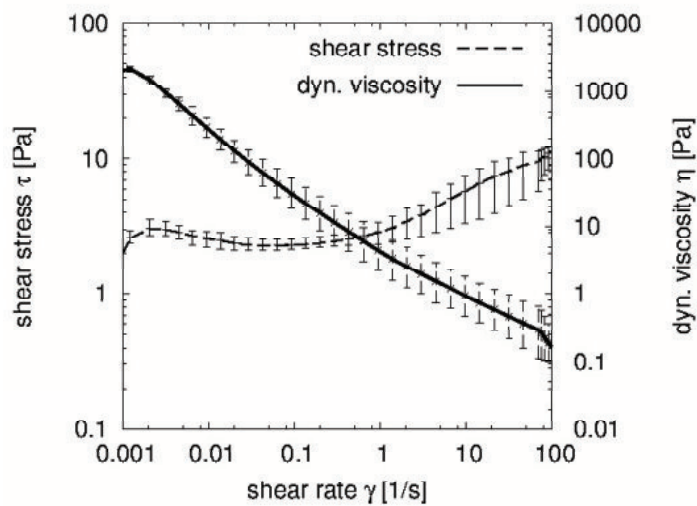


Figure A.6: Shear stress and viscosity for different shear rates. 99.9 % H₂O - 0.1 % Agar.

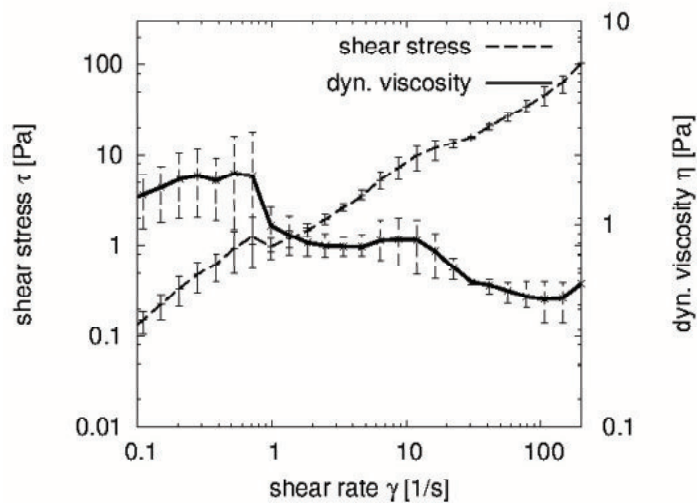


Figure A.7: Shear stress and viscosity for different shear rates. 15 % PSf - 84.99 % NMP - 0.01 % Agar.

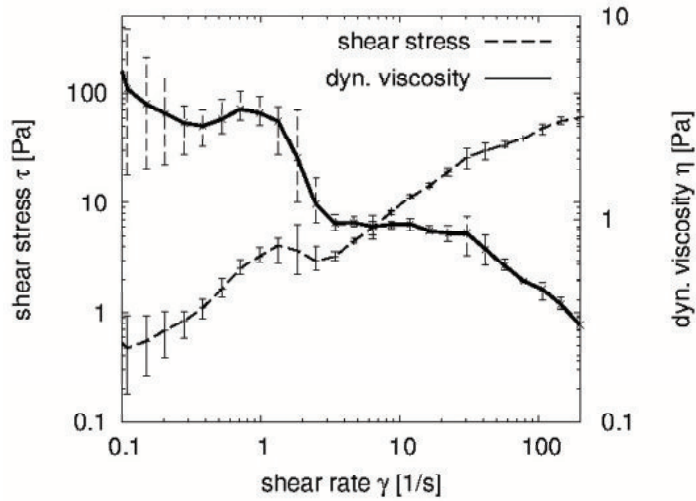


Figure A.8: Shear stress and viscosity for different shear rates. 15 % PSf - 84.975 NMP - 0.025 % Agar.

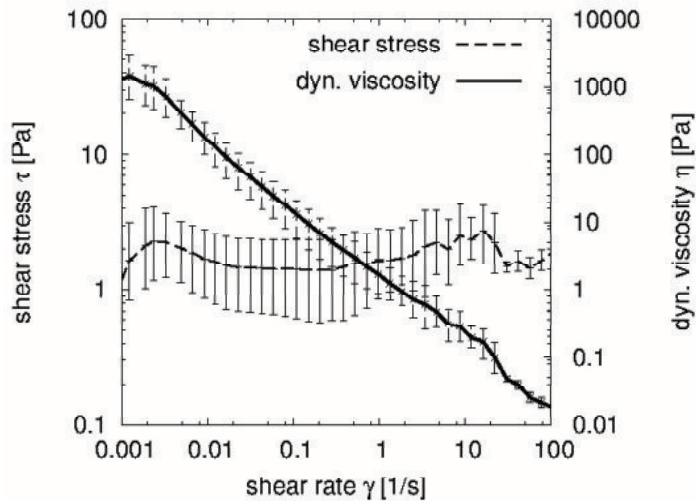


Figure A.9: Shear stress and viscosity for different shear rates. 15 % PSf - 84.95 NMP - 0.05 % Agar.

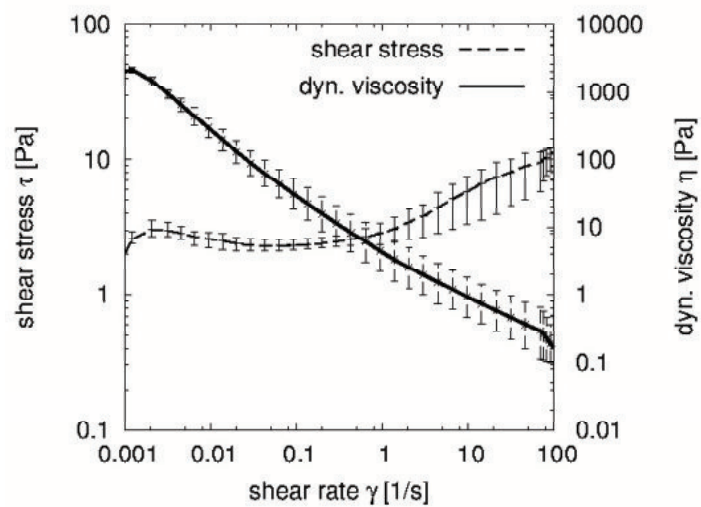


Figure A.10: Shear stress and viscosity for different shear rates. 15 % PSf - 84.9 NMP - 0.1 % Agar.

PVP

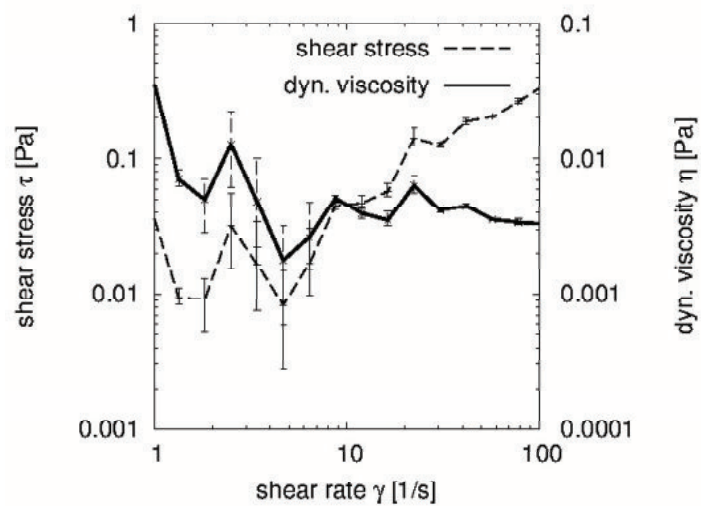


Figure A.11: Shear stress and viscosity for different shear rates. 99 % H₂O - 1 % PVP.

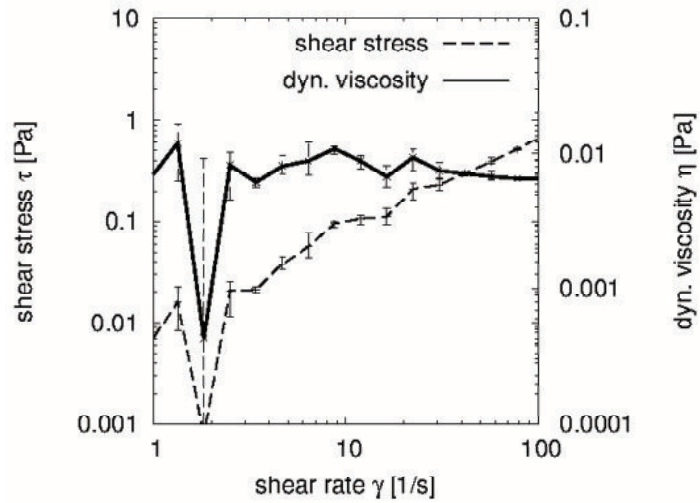


Figure A.12: Shear stress and viscosity for different shear rates. 98 % H₂O - 2 % PVP.

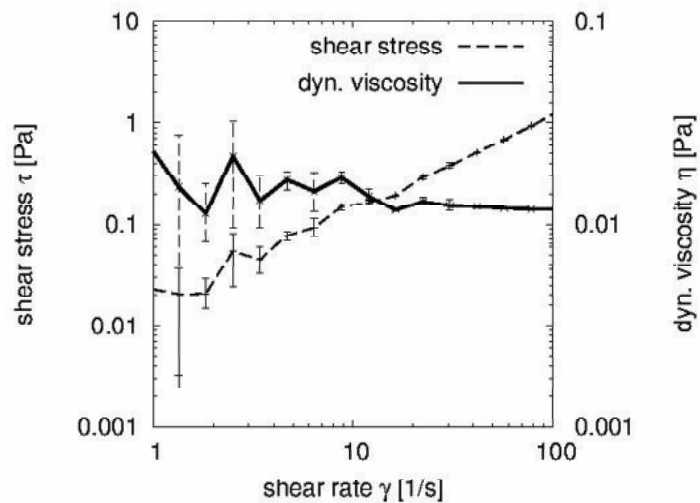


Figure A.13: Shear stress and viscosity for different shear rates. 97 % H₂O - 3 % PVP.

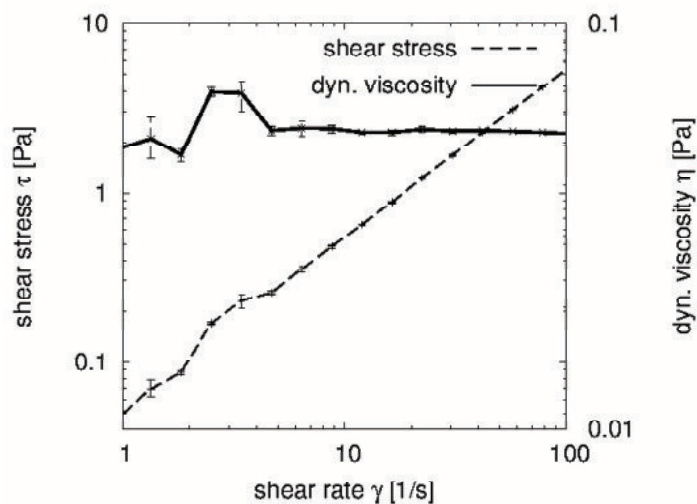


Figure A.14: Shear stress and viscosity for different shear rates. 94 % H₂O - 6 % PVP.

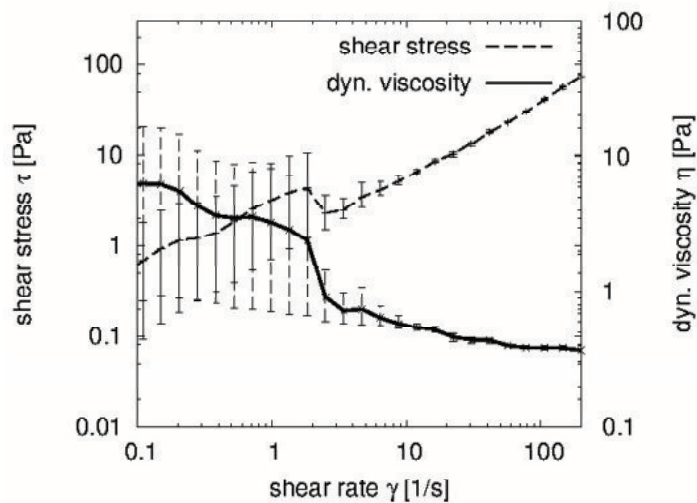


Figure A.15: Shear stress and viscosity for different shear rates. 15 % PSf - 84 % NMP - 1 % PVP.

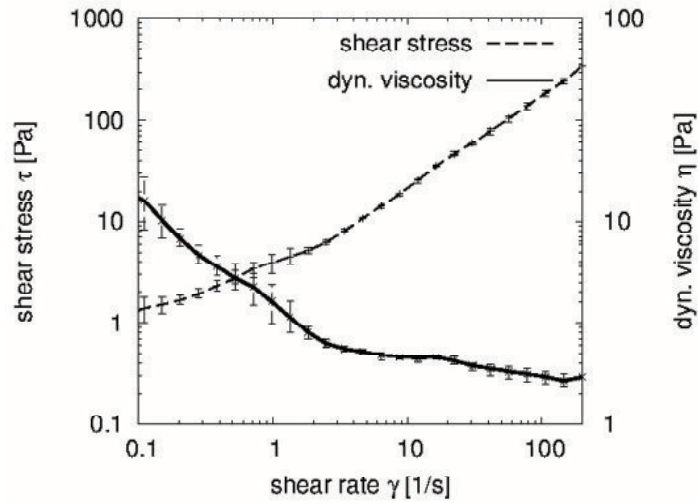


Figure A.16: Shear stress and viscosity for different shear rates. 15 % PSf - 83 % NMP - 2 % PVP.

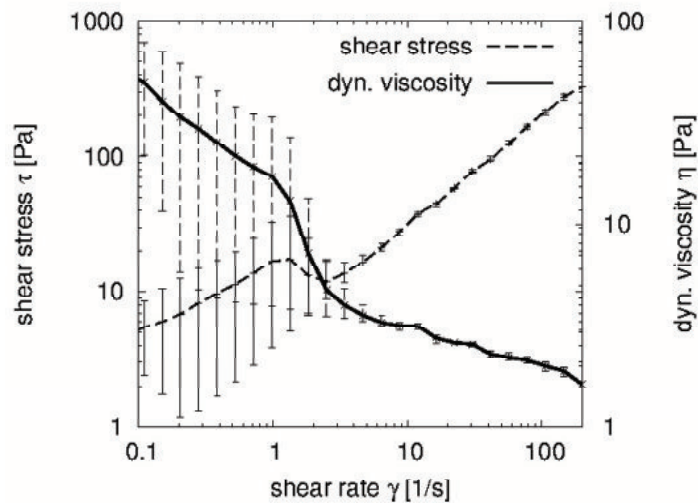


Figure A.17: Shear stress and viscosity for different shear rates. 15 % PSf - 82 % NMP - 3 % PVP.

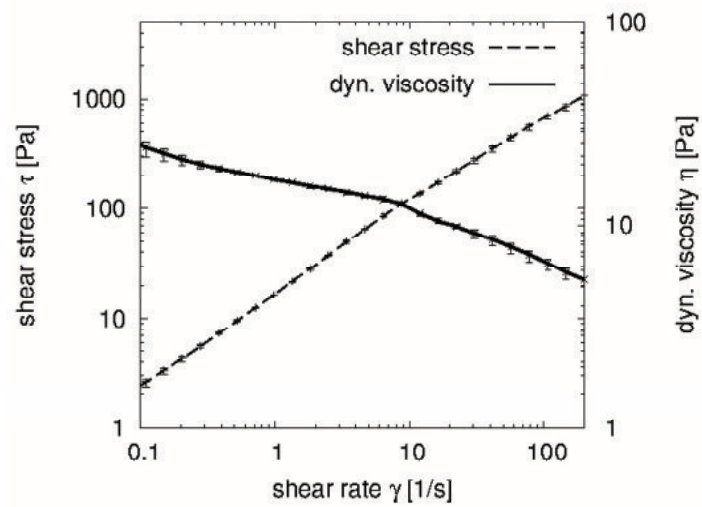


Figure A.18: Shear stress and viscosity for different shear rates. 15 % PSf - 79 % NMP - 6 % PVP.

PEG

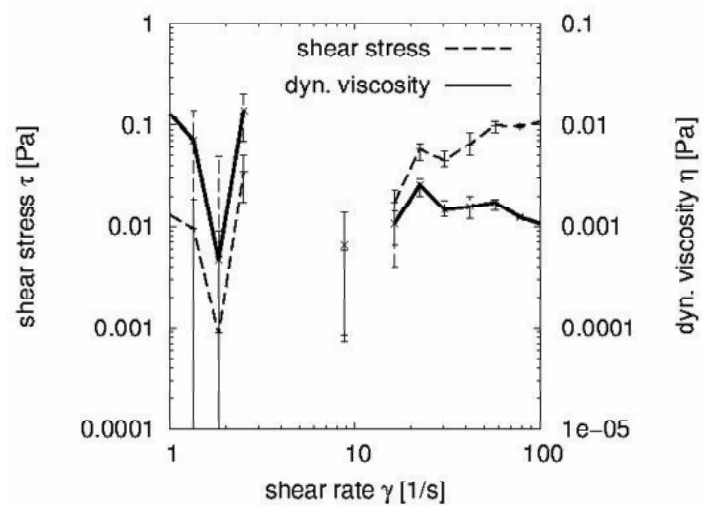


Figure A.19: Shear stress and viscosity for different shear rates. 99 % H₂O - 1 % PEG.

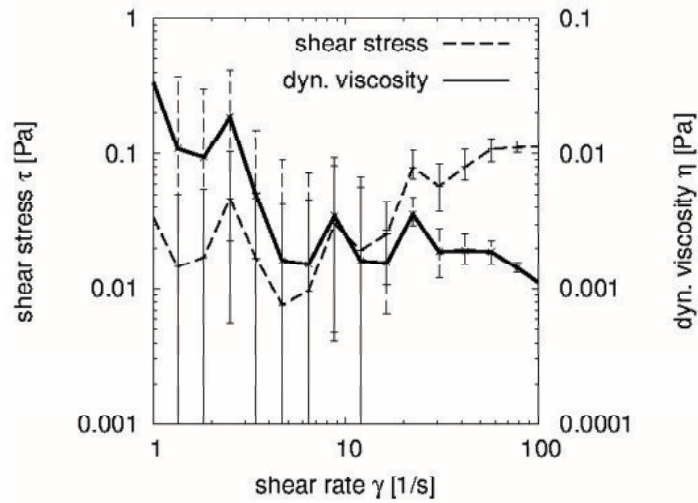


Figure A.20: Shear stress and viscosity for different shear rates. 98 % H₂O - 2 % PEG.

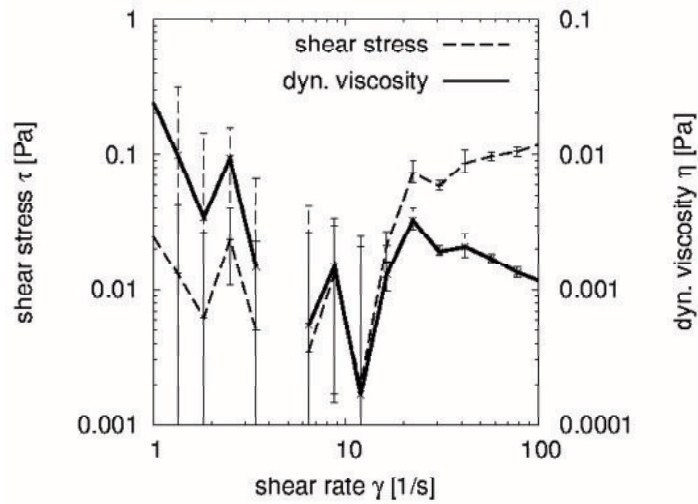


Figure A.21: Shear stress and viscosity for different shear rates. 97 % H₂O - 3 % PEG.

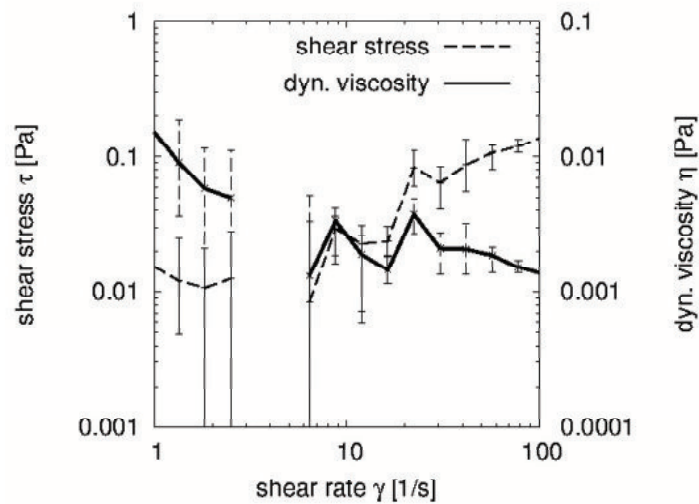


Figure A.22: Shear stress and viscosity for different shear rates. 94 % H₂O - 6 % PEG.

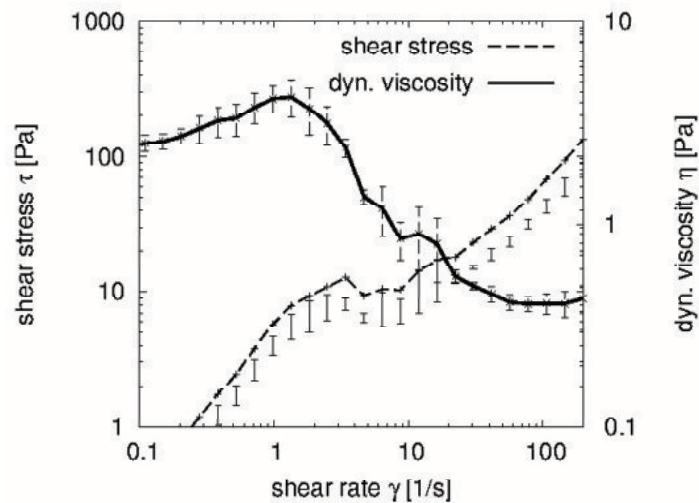


Figure A.23: Shear stress and viscosity for different shear rates. 15 % PSf - 84 % NMP - 1 % PEG.

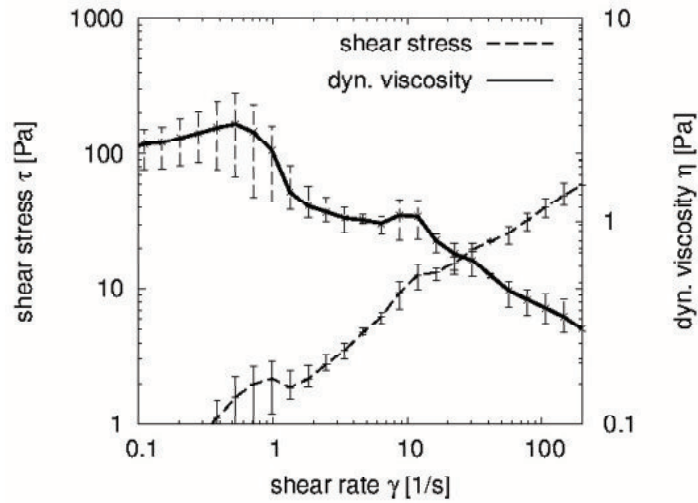


Figure A.24: Shear stress and viscosity for different shear rates. 15 % PSf - 83 % NMP - 2 % PEG.

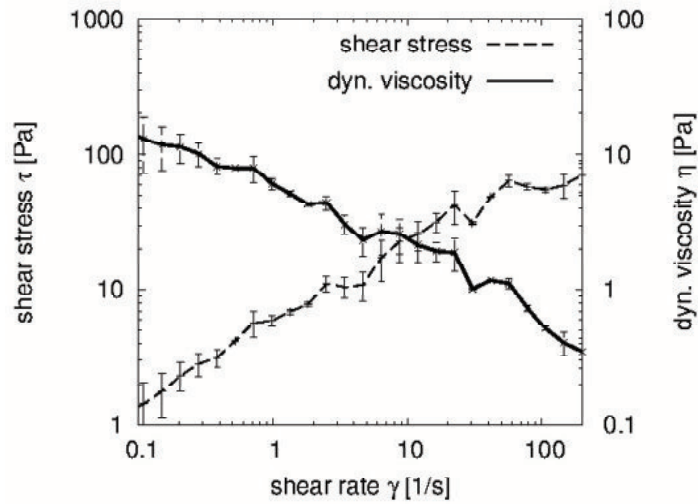


Figure A.25: Shear stress and viscosity for different shear rates. 15 % PSf - 82 % NMP - 3 % PEG.

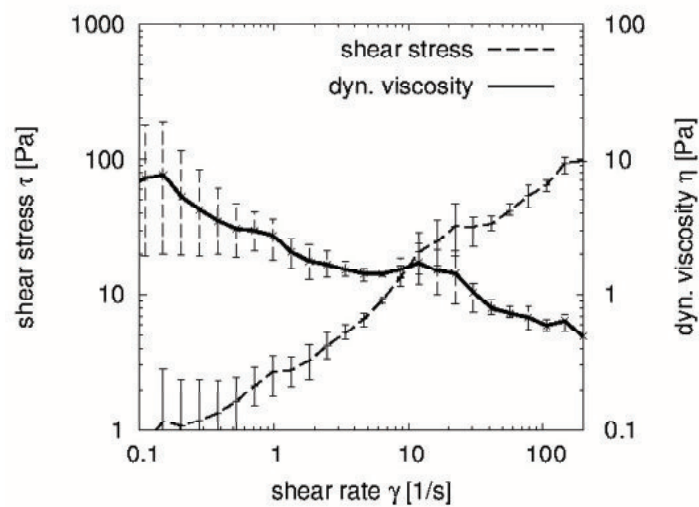


Figure A.26: Shear stress and viscosity for different shear rates. 15 % PSf - 79 % NMP - 6 % PEG.

Dependence of viscosity from mass fraction

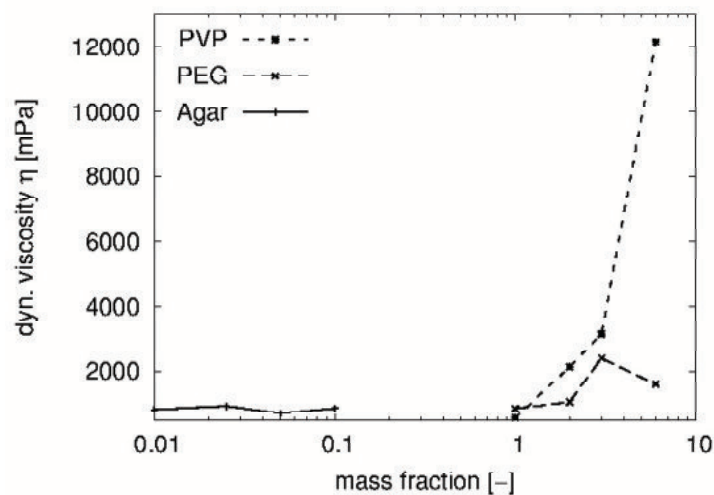


Figure A.27: Dependence of viscosity of the polymer solution from different additives and different mass fractions. The concentration of PSf is fixed at 15 %. NMP is reduced when additives are added.

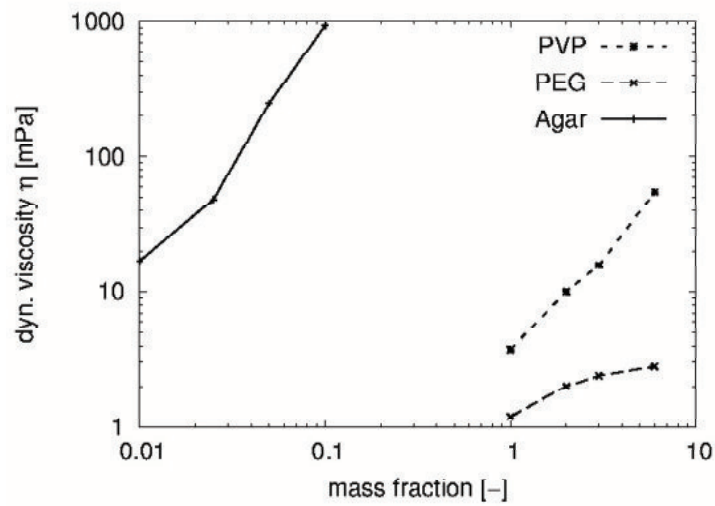


Figure A.28: Dependence of viscosity of the coagulation bath from different additives and different mass fractions. Mixture of water and additive.

APPENDIX B

Review of proof of sharp interface limit from diffuse interface

The derivation of the sharp interface limit from a diffuse interface formulation was presented in [And98]. Here we review the derivation for completeness.

Start with the momentum balance with a diffuse interface

$$\frac{D\rho\vec{u}}{Dt} = \nabla \cdot \mathbf{m} \quad (\text{B.1})$$

with

$$\mathbf{m} = -p\mathbf{I} + \mathbf{T} + \tau \quad (\text{B.2})$$

and

$$\mathbf{T} = \left[\kappa' \rho \nabla^2 \rho + \frac{\kappa'}{2} |\nabla \rho|^2 \right] \mathbf{I} - \kappa' \nabla \rho \otimes \nabla \rho \quad (\text{B.3})$$

τ and \mathbf{T} include viscous stress and the stress due to the interface. ε is the width of the interface and we define a reduced energy parameter κ'_E as

$$\kappa'_E = \varepsilon^2 \kappa' \quad (\text{B.4})$$

with the gradient energy parameter κ' . Consider a pillbox (cylinder element) with radial coordinate r and height 2δ . The interface width is

$$\varepsilon \ll \delta \ll L \quad (\text{B.5})$$

with L as the length scale of the system, e.g. the diameter of the pillbox.

First rewriting the momentum balance

$$\frac{D\rho\vec{u}}{Dt} - \nabla \cdot \mathbf{m} = \frac{\partial(\rho\vec{u})}{\partial t} + \nabla \cdot (\rho\vec{u} \otimes \vec{u}) - \nabla \cdot \mathbf{m} = 0 \quad (\text{B.6})$$

Then we integrate over the volume V_p

$$\int_{V_p} \left(\frac{\partial(\rho\vec{u})}{\partial t} + \nabla \cdot (\rho\vec{u} \otimes \vec{u}) - \nabla \cdot \mathbf{m} \right) dV = 0 \quad (\text{B.7})$$

$$\int_{V_p} \left(\frac{\partial(\rho\vec{u})}{\partial t} \right) dV + \int_{V_p} (\nabla \cdot (\rho\vec{u} \otimes \vec{u})) dV + \int_{V_p} (-\nabla \cdot \mathbf{m}) dV = 0. \quad (\text{B.8})$$

Using the divergence theorem for the first term, we may change the first term

$$- \int_{S_p} (\rho\vec{u}) \vec{u}_I \cdot \vec{\hat{n}}_s dS + \int_{V_p} (\nabla \cdot (\rho\vec{u} \otimes \vec{u})) dV + \int_{V_p} (-\nabla \cdot \mathbf{m}) dV = 0. \quad (\text{B.9})$$

Now, we transform the system into a moving coordination system with an arbitrary velocity \vec{u}_I using the product rule for the last term

$$\frac{D\rho\vec{u}}{Dt} = \frac{D\rho\vec{u}}{Dt'} - \vec{u}_I \cdot \nabla (\rho\vec{u}) \quad (\text{B.10})$$

$$= \frac{D\rho\vec{u}}{Dt'} - \nabla \cdot (\rho\vec{u}_I \otimes \vec{u}) + \rho\vec{u} \nabla \cdot \vec{u}_I \quad (\text{B.11})$$

The first and the third term on the right hand side do not contribute in the limit of zero volume of the pillbox. Therefore,

$$\int_{S_p} \left(\frac{D\rho\vec{u}}{Dt'} + \rho\vec{u} \nabla \cdot \vec{u}_I \right) \cdot \vec{\hat{n}}_s dS = 0. \quad (\text{B.12})$$

Putting Eqs. B.9, B.11 and B.12 together and using the divergence theorem leads to

$$0 = - \int_{S_p} (\rho\vec{u}) \vec{u}_I \cdot \vec{\hat{n}}_s dS + \int_{S_p} (\rho\vec{u}\vec{u}) \cdot \vec{\hat{n}}_s dS - \int_{S_p} \mathbf{m} \cdot \vec{\hat{n}}_s dS \quad (\text{B.13})$$

$$= \int_{S_p} \left[\rho\vec{u} (\vec{u} - \vec{u}_I) \cdot \vec{\hat{n}}_s - \vec{\hat{n}}_s \cdot \mathbf{m} \right] dS \quad (\text{B.14})$$

Now we assume that the velocity of the fluid is bounded. This means that the velocity terms do not contribute to the side integral of the box and only contributes to the integral on top and bottom. In addition we assume that the non-classical terms have no magnitude to the upper and lower area because $\varepsilon \ll \delta$. With these assumption

$$\mathbf{m} = \left[-p + \kappa' \rho \nabla^2 \rho + \frac{\kappa'}{2} |\nabla \rho|^2 \right] \mathbf{I} - \kappa' \nabla \rho \otimes \nabla \rho + \tau \quad (\text{B.15})$$

With A_p as the fraction of the surface S_p on the inner side it follows

$$0 = \int_{A_p} \left[\rho \vec{u} (\vec{u} - \vec{u}_I) \cdot \vec{\hat{n}}_S - \vec{\hat{n}}_S \cdot (-p \mathbf{I} + \tau) \right] dA - \int_{side} \vec{\hat{m}} \cdot \mathbf{T} dS \quad (\text{B.16})$$

The first term accounts for the plane on top and bottom while the last term accounts for the surrounding side. $\vec{\hat{m}}$ is the normalized vector on the side that is perpendicular to $\vec{\hat{n}}_S$.

Locally at the interface as leading dimension

$$\nabla \rho \sim \rho_r \cdot \vec{\hat{n}} = \frac{\partial \rho}{\partial r} \vec{\hat{n}} \quad (\text{B.17})$$

with ρ_r as the gradient of the density at r and $\vec{\hat{n}}$ as the normalized normal to the surface. Analog

$$\nabla^2 \rho \sim \rho_{rr} = \frac{\partial^2 \rho}{\partial r^2}. \quad (\text{B.18})$$

Reformulating the normal contribution of the capillary tensor $\vec{\hat{m}} \cdot \mathbf{T} = \mathbf{T} \vec{\hat{m}}$ and multiplying from right with $\vec{\hat{m}} \cdot \vec{\hat{m}} = \vec{\hat{m}}^T \vec{\hat{m}} = 1$ leads to

$$\vec{\hat{m}} \cdot \mathbf{T} = \left(\vec{\hat{m}} \cdot \mathbf{T} \cdot \vec{\hat{m}} \right) \vec{\hat{m}}. \quad (\text{B.19})$$

Inserting this equation in Eq. B.16, we get

$$0 = \int_{A_p} \left[\rho \vec{u} (\vec{u} - \vec{u}_I) \cdot \vec{\hat{n}}_S - \vec{\hat{n}}_S \cdot (-p \mathbf{I} + \tau) \right] dA - \oint_C \int_{-\infty}^{+\infty} \left(\vec{\hat{m}} \cdot \mathbf{T} \cdot \vec{\hat{m}} \right) \vec{\hat{m}} dr dl \quad (\text{B.20})$$

where C is the contour as the intersection between S_p and the surface of the box, dr is the increment of the height of the box and dl is the increment in azimuth direction along C . This equation, especially the last term, derives from the splitting of the cylinder element dS in $drdl$.

We now define

$$\gamma = \int_{-\infty}^{+\infty} (\vec{m} \cdot \mathbf{T} \cdot \vec{m}) dr \quad (\text{B.21})$$

that in fact is the Kramer's potential that is the surface energy as shown by Anderson & McFadden [And96]. Now we focus on the last term of Eq. B.20 that is

$$- \oint_C \gamma \vec{m} dl \quad (\text{B.22})$$

Applying the divergence theorem

$$- \oint_C \gamma \vec{m} dl = \int_{A_p} [\gamma \nabla \cdot \vec{m} + \vec{m} \cdot \nabla \gamma] dA \quad (\text{B.23})$$

with

$$\vec{m} \cdot \nabla \gamma = \nabla_S \gamma \quad (\text{B.24})$$

and

$$\gamma \nabla \cdot \vec{m} = -\gamma (\nabla_S \cdot \vec{n}) \vec{n} \quad (\text{B.25})$$

leads to

$$- \oint_C \gamma \vec{m} dl = - \int_{A_p} [\nabla_S \gamma - \gamma (\nabla_S \cdot \vec{n}) \vec{n}] dA \quad (\text{B.26})$$

Herein A_p is the interface area, ∇_S is the surface gradient tangential to the interface and $\nabla_S \cdot \vec{n} = \kappa$ is the curvature of the interface.

Putting all together the momentum balance (Eq. B.20) is

$$0 = \int_{A_p} \left\{ \left[\rho \vec{u} (\vec{u} - \vec{u}_I) \cdot \vec{n}_S - \vec{n}_S \cdot (-p \mathbf{I} + \tau) \right] - \left[\nabla_S \gamma - \gamma \kappa \vec{n} \right] \right\} dA \quad (\text{B.27})$$

This equation is similar to the familiar sharp interface balance in continua. The left hand side, the accumulation, is zero as mostly assumed for infinitesimal small interfaces. The first term on the right hand side are the flux into and out of the balance element and the last term is the source term at the interface. The source term accounts for variation of surface energy in tangential and normal direction to the interface (first and second term). The integration area is arbitrary and therefore we can write

$$\left[\rho \vec{u} (\vec{u} - \vec{u}_I) \cdot \vec{n}_S - \vec{n}_S \cdot (-p\mathbf{I} + \tau) \right] = \nabla_S \gamma - \gamma \kappa \vec{n} \quad (\text{B.28})$$

that is the classical balance at the interface.

APPENDIX C

Validation of thermodynamic consistent fluctuations of concentration

In Chap. 4 and 6 we considered thermodynamic consistent fluctuations of the composition. In this section we demonstrate that the implementation of the fluctuations reproduces the Gaussian equilibrium distribution with the mean square fluctuation of the composition [Lan80]

$$\langle(\Delta\omega)^2\rangle = \frac{k_B T}{m \frac{\partial\mu}{\partial\omega}}. \quad (\text{C.1})$$

k_B , T and m are the Boltzmann constant, absolute temperature and the mass of a fluid element. The implementation of the fluctuations of the composition is valid if we reproduce the distribution for different sizes of fluid elements. The distribution should be wider for small system sizes and limit to a Dirac-delta function for very large systems. The latter case is the macroscopic continuum limit where fluctuations are negligible.

We consider only diffusive mass transport. We use a 2D square periodic domain with $L \cdot L = 30 \cdot 30$ particles in regular Cartesian order and a binary system with an initial composition $\omega = 0.5$. We assume that the system is miscible and

$$\frac{\partial\mu}{\partial\omega} = 1. \quad (\text{C.2})$$

The temperature and density are $T = 298.15K$ and $\rho = 1kg/m^3$. The diffusion coefficient is $D = 10^{-6}m^2/s$. A variation of the size of the system leads to a variation

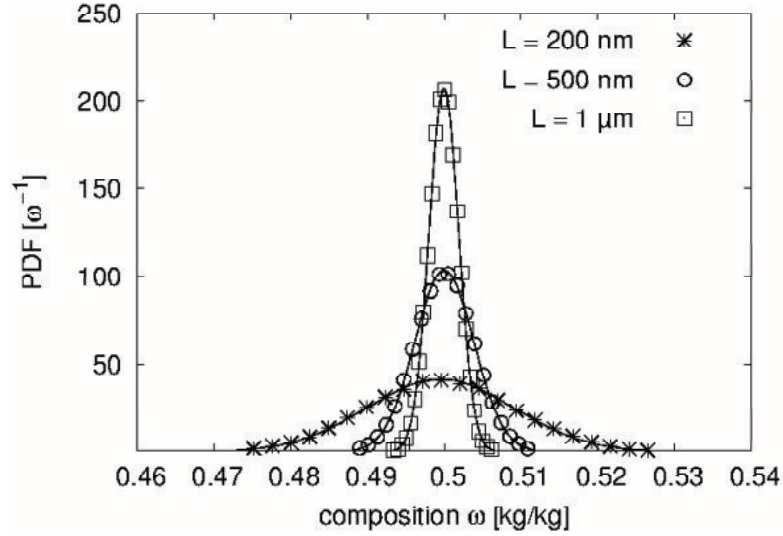


Figure C.1: Distribution of the probability density function (PDF) versus mass fraction. The mean mass fraction is $\omega = 0.5$. Three different sizes of the system with $L = 200\text{nm}$, $L = 500\text{nm}$ and $L = 1\mu\text{m}$ lead to different variances. The variance of the distribution increases with decreasing system size. For large system size we limit to a Dirac-Delta function.

of the mass of a fluid element. We investigate 3 different sizes with $L = 200\text{nm}$, $L = 500\text{nm}$ and $L = 1\mu\text{m}$ corresponding to $m = 1.78 \cdot 10^{-12}\text{kg}$, $m = 1.11 \cdot 10^{-15}\text{kg}$ and $m = 4.44 \cdot 10^{-17}\text{kg}$ with a time step according to the diffusive time step criteria. The kernel function is a Wendland kernel with a smoothing length $h = 2.05L_0$.

The distribution of the composition results from sampling of a single particles over several time steps. We use a particle in the center of the domain and sample for 500,000 time steps, starting at the beginning of the simulation.

Fig. C.1 shows the distribution of the composition. The symbols and the solid lines indicate the results of the simulation and the theoretical value. We find good agreement of the simulations for all sizes of the system with the theoretical value and conclude that we reproduce thermal fluctuations of the composition correctly.

APPENDIX D

Phase separation

In this appendix we validate the discretized component balance (Cahn-Hilliard equation) for a binary fluid mixture and investigate the influence of thermal fluctuations and boundary conditions.

D.1 Validation of binary phase separation model

One common example [Cah58; Oku97] to validate the Cahn-Hilliard equation is a liquid patch of a binary mixture with periodic boundary conditions. Initially the system is in an unstable state and small random perturbations of the composition are imposed. Then the mixture immediately starts to separate. The dynamics of the coarsening in the diffusion-limited case is captured by the power law of Lifshitz and Slyozov [Lif61]. The power law

$$\Omega \propto t^{-1/3} \tag{D.1}$$

states that the surface area Ω increases proportional to the time to the power of $-1/3$. This means that the surface area decreases monotonically with increasing time t . We use this relation to validate the present SPH model for phase separation. Note that the power law is only valid for free phase separation where droplets are formed but holds for 2D and 3D as demonstrated in [Hir14; Kro14].

Before we investigate the influence of different model parameters we present a reference. The reference is a binary isotherm mixture. We consider the early stage of separation where the transport is limited by diffusion. It is therefore valid to only

consider the Cahn-Hilliard equation and neglect momentum transport. In a binary mixture it is only necessary to calculate the change of one component due to the closing condition. We assume that the mass fractions, volume fractions and molar fractions are equal in the mixture. Using the mass fraction of component 1 ($\omega_1 = \omega$) the Cahn-Hilliard equation is

$$\frac{D\omega}{Dt} = \nabla \cdot (M\nabla\mu). \quad (\text{D.2})$$

As mentioned in chapter 3 the real physical equation of state may not be useful because the physical length scale needs to be resolved. We use a model-fluid with the chemical potential as shown in Eq. 4.22. We discuss the choice of κ' in Sec. D.1.3.

We consider a two dimensional quadratic domain with physical size $1\mu m^2$. The domain is discretized with 50×50 particles. Therefore the initial particle spacing is $L_0 = 0.02\mu m$. We use periodic boundary conditions. The mobility M represents the transport resistance. Here we use it as if it is a diffusion coefficient (Eq. 3.13). Further parameters are $M = 10^{-10} \frac{m^2}{s}$ in the reference simulation and $\rho = 1000 \frac{kg}{m^3}$. We use a Wendland C2 kernel with a smoothing length $h = 2.05L_0$ and we neglect the stochastic term in Eq. 3.26 for the moment.

We consider a system in an unstable state. Initially a small, uniformly and artificial random perturbation $\Delta\omega_0 = 5 \cdot 10^{-4}$ is imposed to the mass fraction. The size of this random perturbation can in principle be infinitesimal small since the system is in an unconditionally unstable state. We investigated the size of the perturbation and it indeed turned out that the dynamics of phase separation is independent of the amplitude of the initial perturbation. Therefore the value of $\Delta\omega_0$ is justified.

We start with two extreme cases that correspond to critical and off-critical phase decomposition. By critical phase decomposition we refer to an initial composition of the system at the maximum of the free energy inside the miscibility gap, as shown in Fig. D.1. In our case, for a critical initial composition, the volume fraction of both components in the binary mixture are identical. Correspondingly, off-critical phase decomposition refers to any other initial composition of the system inside the miscibility gap and the volume fractions of both components differ. For the chosen chemical potential we identify the critical point at $\omega_0 = 0.5$ and we expect critical phase decomposition at this initial mean concentration. The other case $\omega_0 = 0.25$ is

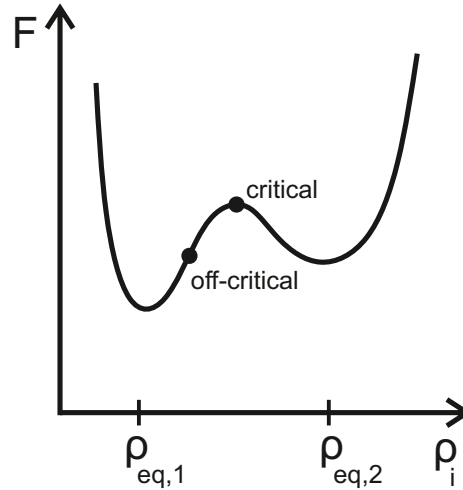


Figure D.1: Schematic plot of free energy over partial density. *critical* and *off-critical* indicate initial composition of the system. *critical* refers to the maximum of the free energy inside the miscibility gap.

very off-critical. We do not consider a binary case with higher concentration than $\omega_0 = 0.5$ because the chemical potential is symmetric and this is captured if we consider the second component instead.

We start with $\omega_0 = 0.5$. In Fig. D.2 the phase distribution is shown for 4 different times. The phases are indicated by black and white while black corresponds to the phase calculated (ω_1). We start with a qualitative view on the phase distribution and find that at the beginning the mass fraction is mainly noisy (Fig. D.2a). After very short time small patches are formed that grow with time. The global equilibrium configuration is reached only after very long time and will be a circle in two dimensions. For critical phase decomposition a meta stable state (as shown

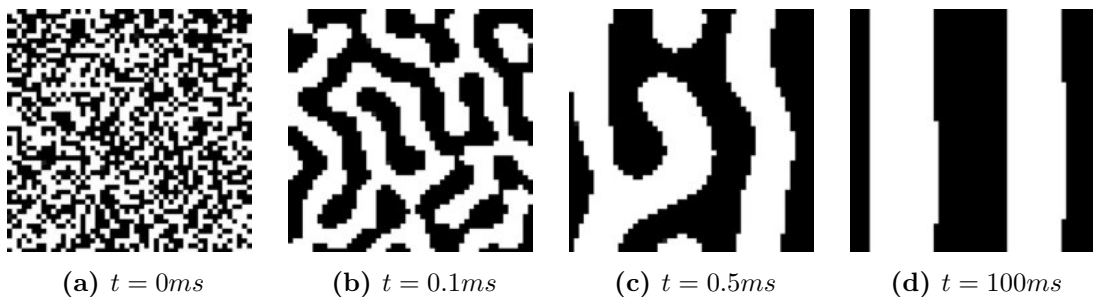


Figure D.2: Time series of phase decomposition with $\omega_0 = 0.5$ and $M = const.$.

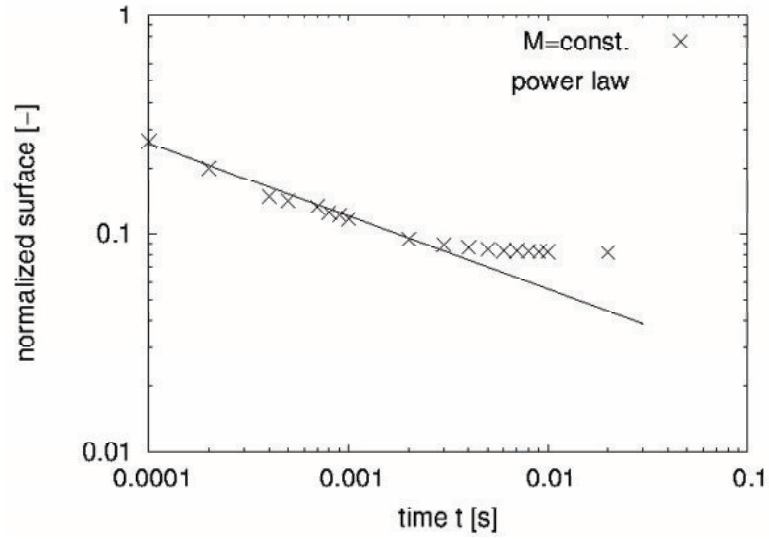
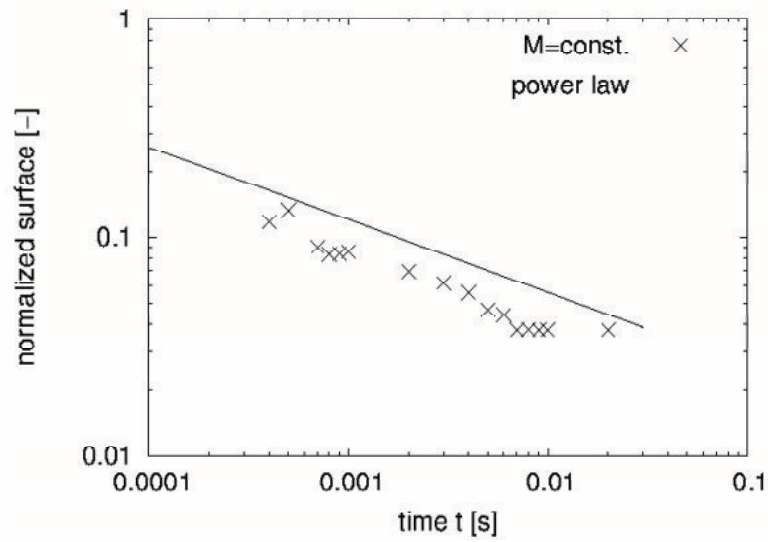
in Fig. D.2d) with a strip structure is possible. This can be proven by simple mathematical analysis considering the minimum of interface size, see [Hir14].

We get more quantitative analysis by comparison of surface area with the power law (Eq. D.1). The surface area in the simulation is measured graphically from an image of the current time-step by first identifying the interface between both phases (the iso line $\omega_0 = 0.5$) using the Canny algorithm [Can86] and then summing up the surface elements. The Canny algorithm is a method to identify gradients in a color field. These gradients correspond to the interfaces between the phases. As a result we get a normalized surface area (surface length per element length). The surface area is plotted over time in Fig. D.3a for the critical phase decomposition and $M = const.$ We see in Fig. D.3a that the surface area decreases very close to the power law. At $t \approx 0.003s$ the surface area decreases slower than the power law predicts. The reason is that stripes begin to form at this time. This is seen in Fig. D.2c. Therefore the surface area reduces slower than expected in the case of droplets. For late times the surface area is almost constant because of the local equilibrium (stripes, see Fig. D.2d) of the system. This is caused by numerical errors.

Now we turn to off-critical phase decomposition. The initial mean concentration is $\omega_0 = 0.25$. This means that there is less amount of one component in the system. Therefore we expect that droplets are formed that grow without coalescence until the final stable state, a circle in 2D, is reached. As before we start with a qualitative view on the phase distribution. In Fig. D.4 a time series of the off-critical case is shown. From the initially noisy pattern (Fig. D.4a) first elongated and then spherical patches are formed. Finally one single circle is formed that remains stable because the equilibrium state is reached.

The decreasing surface area over time is plotted in Fig. D.3b for $M = const.$ We find that after some initial time the slope of the power law and the results of the simulation are in agreement with small deviations caused by the method to determine the interface area.

These results confirm that the proposed discrete Cahn-Hilliard equation is promising. Therefore we continue by a detail investigation of the impact of the numerical parameters. The numerical parameters are the smoothing length h , the numerical resolution represented by the initial particle spacing L_0 and the value of the energy parameter κ' . Additional influences are the particle distribution and boundary conditions. Here we consider only symmetric boundary conditions because they are

(a) surface area vs. time with $\omega_0 = 0.5$ (b) surface area vs. time with $\omega_0 = 0.25$ **Figure D.3:** Time dependent surface area during phase decomposition.

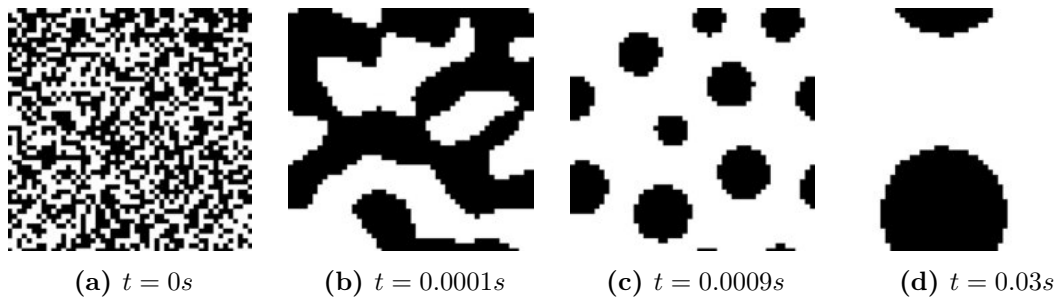


Figure D.4: Time series of phase decomposition with $\omega_0 = 0.25$ and $M = \text{const.}$

important for immersion precipitation. As a last point we consider the effect of consistent permanent fluctuations on the dynamics of the coarsening. As mentioned earlier, fluctuations of the mean concentration is a result of the reduction of molecular degrees of freedom and are necessary for consistent thermodynamics on mesoscale.

D.1.1 Influence of smoothing length

In this section we show the effect of different smoothing lengths on the morphology of the phase separating fluid mixture. The smoothing length is a measure for the amount of particles considered for the calculation of a quantity. With increasing smoothing length the amount of particles increases linear, quadratic or cubic in 1D, 2D or 3D because the kernel function is symmetric. An increase of the smoothing length also increases the smoothing of a gradient in space and therefore a sharp gradient is smoothed out.

We consider the same simulation as before with 50×50 particles and $\omega_0 = 0.5$. We now vary only the smoothing length and keep all other parameters constant. The smoothing length is varied from $h = 1.55L_0$ to $h = 3.05L_0$. The range considered here represents the lower limit as minimum for a good SPH approximation and the upper limit as maximum acceptable computational cost.

The phase distribution for 4 different smoothing lengths at the same time step are shown in Fig. D.5. To highlight the effect of the smoothing length on the interface width between the phases we plot the phase distribution with a continuous grey scale. The range of the scale is between black and white with the bulk mass fraction $\omega_1 = 0.063$ and $\omega_2 = 0.937$.

For a larger smoothing length we would expect that the interface gets wider because the concentration is smoothed out in a wider area. This gets obvious if we for

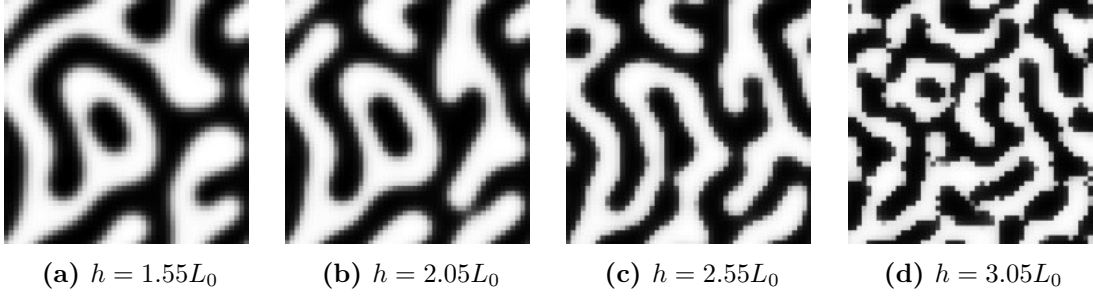


Figure D.5: Phase distribution with $\omega_0 = 0.5$ and $M = \text{const.}$ for different smoothing lengths at time $t = 0.2ms$. The phase color is diffuse to highlight the differences between the different smoothing lengths.

example consider the density field around the interface of two fluids with different densities and masses respectively. Assume the density is calculated as

$$\rho_a = \sum_b m_b W_{ab}. \quad (\text{D.3})$$

The density is continuous across the interface because near the interface the different masses of the particles are considered. The width of this transition from one to the other density is controlled by the smoothing length. With a larger smoothing length the transition region increases too. This is also the case for the gradient or the Laplacian of a quantity. Therefore we would expect that it is also true for the 4th order derivative. In Fig. D.5 we see, because of the grey scale, that the transition between the phases is larger for small smoothing lengths. This is in contrast to what we expect. It is not an error. The reason is that we have not kept all input parameters constant. The gradient energy term in the chemical potential depends on the smoothing length too because of the biharmonic formulation for the 4th order derivative. In Fig. D.5 we see two effects superposed. The first effect is that the concentration is smoothed out with increasing smoothing length as we expected. The other effect is that due to a larger smoothing length the gradient energy contribution is also smoothed out. As a result gradient energy contribution, responsible for phase separation, is lower for small smoothing lengths. This results in a lower contribution of the gradient energy term to the total chemical potential at the interface because the local part of the chemical potential does not change. We interpret this as a lower surface energy. We will see in Sec. D.1.3 that this leads to a thinner interface that we do not resolve here.

We conclude that convergence with higher smoothing length is crucial because it also effects the gradient energy contribution. Another possibility to show numerical convergence is by increasing the particle number and keep the smoothing length constant. In this way we do not have two effects superposed.

D.1.2 Influence of resolution

In the last section we decreased the ratio of the initial particle spacing and the smoothing length from $L_0/h = 0.65$ to $L_0/h = 0.33$ and found that the gradient energy contribution depends on this ratio. Now we keep L_0/h constant.

We investigate the influence of the particle number on the morphology of the phase separating fluid. Analog to a grid convergence study in a grid-based method like the Finite-Volume method we increase the particle number, and therefore the initial particle spacing L_0 , in SPH and keep the smoothing length constant. We decrease L_0 from $20nm$ to $5nm$. Therefore the particles in the domain increase from 50×50 to 200×200 particles. We use a smoothing length $h = 2.05L_0$ and $\omega_0 = 0.5$. All other parameters are the same as in the reference.

In Fig. D.6 the phase distribution at time $t = 0.1ms$ is shown for the different resolutions. The phase color is sharp and clipped at $\omega_0 = 0.5$. Since the L_0/h ratio is constant the interface width is also constant.

Qualitatively we see that with increasing resolution the interface contour is smoother. For a quantitative comparison we compare the decrease of the interface size over time with the power law. The normalized surface area is plotted in Fig. D.7. As explained for the reference simulation we graphically measure the interface size. Since the particle number is different in each simulation we have to normalize the

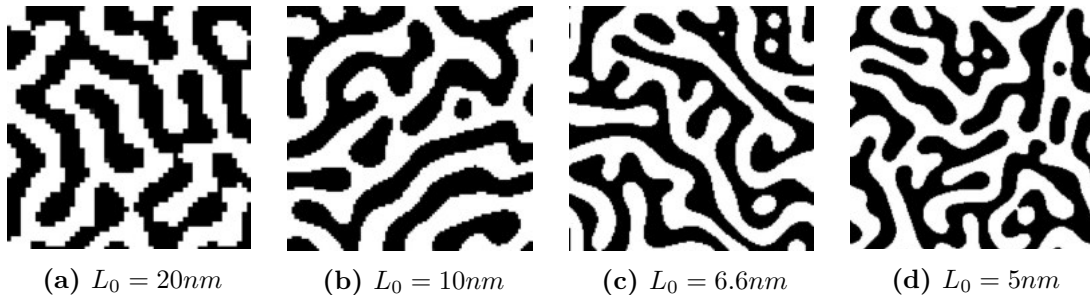


Figure D.6: Phase distribution with $\omega_0 = 0.5$ and $M = const.$ for different resolutions indicated by the initial particle distance. The diffuse interface is clipped at $\omega_0 = 0.5$. The time is $t = 0.1ms$

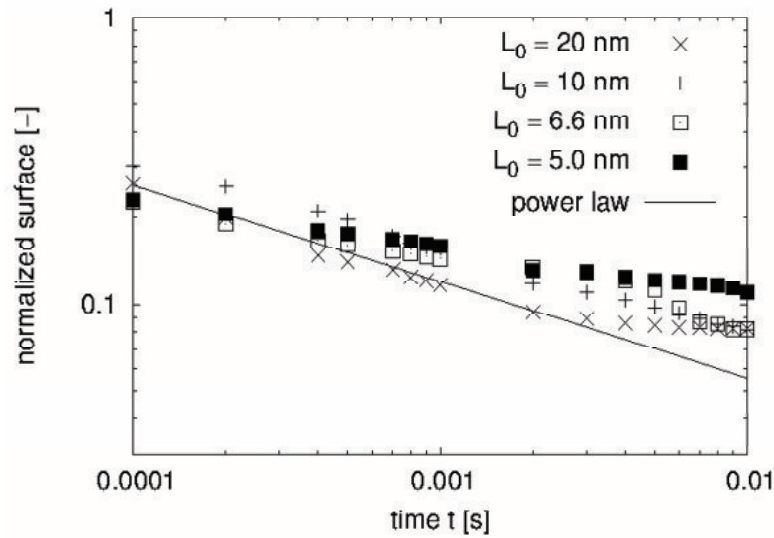


Figure D.7: Surface area vs. time with $\omega_0 = 0.5$ and different resolutions.

calculated interface size by the total amount of particles in the domain. Then the normalized interface size is compared as shown in Fig. D.7. We see that the trend of the power law is fulfilled for all simulations. There are some small deviations between the different resolutions because the dynamics at the interface differ for the different resolutions. The deviation at large time results from an almost phase separated mixture where the power law is no longer valid. The most representative part in Fig. D.7 is in the time between $t = 0.1ms$ and $t = 2ms$. In this regime the power law is valid. We show also the later regime because it is seen that at all resolutions the deviation from the power law occur at approximately the same time $t = 3ms$. With the exception of $L_0 = 10nm$ we identify a convergence of the surface area with higher resolution in the regime where the power law is valid. It is known that in SPH results may depend on the particle number used and this may also be the case for $L_0 = 10nm$ [Sha15].

We conclude that we found convergence for higher resolution. The power law is also fulfilled for higher resolutions. Next we have a closer look on the gradient energy parameter κ' .

D.1.3 Influence of energy parameter κ'

The gradient energy term in the Cahn-Hilliard equation results from the presence of an interface with a change of the partial mass density in the mixture. The change of

density leads to a change in the energy at the interface. This change of energy is proportional to the change in the density and an energy parameter κ' . As shown in Eq. 3.2 the energy parameter is directly linked to the surface tension. As seen in Eq. 3.2 if κ' is reduced and the interface energy should be constant then the Laplacian of the density function has to be increased. This means that the transition from one phase to the other phase should be sharper. Numerically speaking the interface is thinner but has to be resolved accordingly to guarantee a smooth transition.

With this relation in mind we turn to the influence of the energy parameter κ' on the morphology. In principle the energy parameter may be calculated from the surface tension using an equation of state, e.g. PC-SAFT [Mou11]. But this would imply that the interface has to be resolved physically which means on a scale of DFT (density functional theory). This scale is much smaller than the scale of interest for immersion precipitation. An alternative approach to fix the energy parameter is used in phase field simulations. As long as the dynamics of the interface is captured in the same ratio than in the real system the energy parameter can be adjusted. For example, if the interface energy differs by a factor of 1000 from the bulk energy it is still valid to use an interface energy that is only a factor of 100 lower than the bulk energy because it is still much smaller than the bulk energy. On the other hand the interface between the fluids has to be smooth enough to account for accurate discretization of the gradient energy term in the Cahn-Hilliard equation. In literature the choice of the energy parameter according to the characteristic length scale [Kim12] that in SPH is

$$\kappa' \propto L_0^2 \tag{D.4}$$

or

$$\kappa' \propto h^2 \tag{D.5}$$

respectively. We arbitrarily choose the first relation with a constant parameter α

$$\kappa' = \alpha L_0^2. \tag{D.6}$$

In literature we find that κ' controls the width of the interface [Kim05]. Since we choose κ' proportional to L_0^2 the interface width scales with the resolution. α is a

constant and we will show below that $\alpha = 2$ is a good choice. Values in the same range are found in literature [Kim05].

We keep all simulation parameters equal to the reference simulation but now vary κ' . The initial composition is $\omega_0 = 0.5$. The energy parameter varies from $\kappa' = 0.2L_0^2$ to $\kappa' = 8L_0^2$.

We consider three different energy parameters, $\kappa' = 0.2L_0^2$, $\kappa' = 2L_0^2$ and $\kappa' = 8L_0^2$, as shown in Fig. D.8. We again show the phase distribution with a continuous transition from black to white to highlight the interface width in grey scale. We see that the interface width increases with higher κ' . If κ' is decreased, here by a factor of 10, the smooth interface is no longer resolved and we don't get phase decomposition because the Cahn-Hilliard equation is not resolved correctly. These results confirm the choice of $\kappa' = 2L_0^2$. In Fig. D.8 we find an interesting result. For larger κ' the phase separation is faster than for lower κ' . This indicates that phase separation is faster for larger surface tension because the Laplacian $\nabla^2\omega$ is kept constant.

We also investigated the dependence of κ' on the resolution and the physical domain size and found that this choice is good in a large range of physical length scales. It is also applicable in 3D. Therefore we conclude that $\kappa' = 2L_0^2$ is valid and resolves the interface smoothly enough.

D.1.4 Influence of particle distribution

In literature it is shown that some operators tend to diverge for perturbed particle distribution [Fat11]. In this section we demonstrate that the proposed approach for the 4th order derivative produces the correct dynamics for perturbed particle

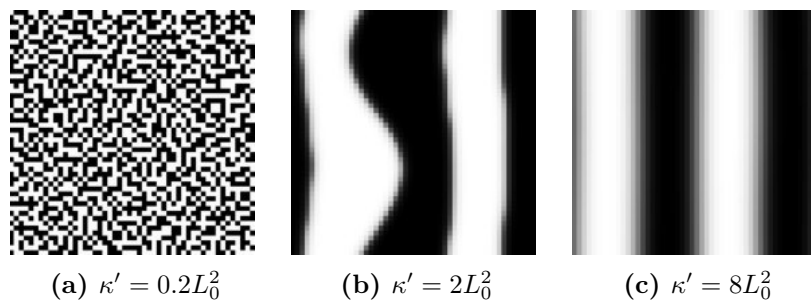


Figure D.8: Phase distribution at $t = 2.5ms$ for different energy parameters κ' with $\omega_0 = 0.5$ and $M = const.$ The phase color is diffuse to highlight the differences between the different energy parameters.

distribution. We perform the same simulation as in the reference but with different particle distribution. The particle distribution is generated by performing a Taylor-Green vortex simulation with Reynolds number $Re = 100$ as presented by Xu et al. [Xu09] and taking the particle distribution at equilibrium. The initial composition is $\omega_0 = 0.5$.

The particle distribution and the phase distribution at three different times are shown in Fig. D.9. In contrast to previous phase distributions shown in this chapter we plot the particles as small circles to highlight the perturbed particle distribution. In Fig. D.9a we see the initial particle distribution that is very similar to the reference in Fig. D.2a but differs in the particle positions. In Fig. D.9b-d different times are shown including the equilibrium phase distribution. Qualitatively the phase distribution is similar to the reference simulation but differs in the equilibrium (Fig. D.9d). Instead of two layers only one layer remains and therefore the system is closer to the equilibrium. This shows that a meta-stable state may depend on the particle distribution.

A more quantitative comparison is done by plotting the surface area over time and compare the decrease of the interfacial area with the power law. This is shown in Fig. D.10. The data labeled as symmetric corresponds to the reference simulation and the asymmetric data corresponds to the perturbed particles. Aside from a shift in the total surface size of the asymmetric simulation the decrease of interface size is in good agreement with the power law. The shift is due to the graphical analysis for the perturbed particles. There is some loss of information while mapping the particles on a regular grid. This leads to the shift in the total interface size.

With the present results we showed that the proposed formulation does not diverge

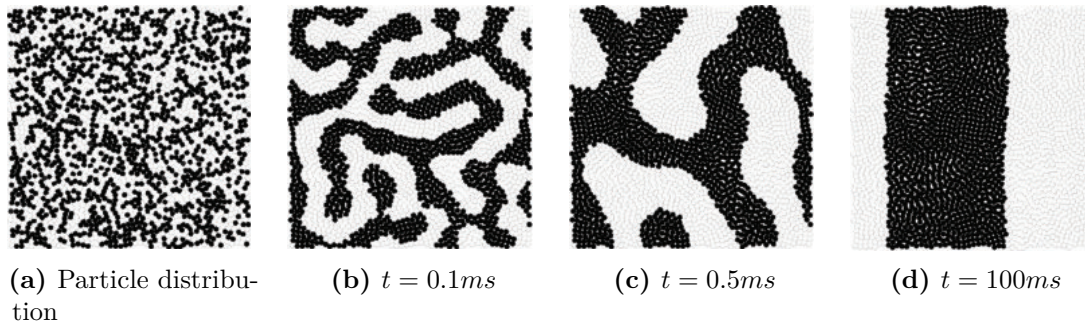


Figure D.9: Time series of phase decomposition with $\omega_0 = 0.5$ and $M = const..$ (a) Initial particle distribution (b) - (d) time series.

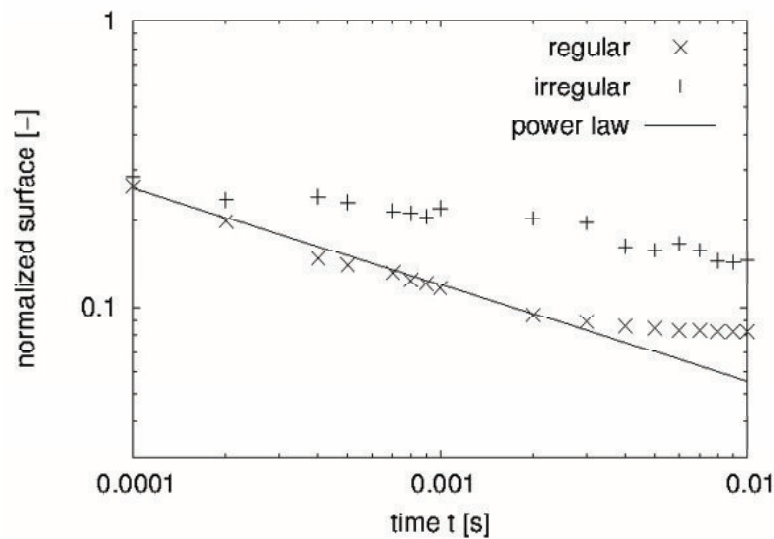


Figure D.10: surface area vs. time with $\omega_0 = 0.5$ for regular and irregular particle distribution.

for perturbed particle distributions. This is important because as soon as we couple the component balance to the momentum balance the particles are accelerated and the particle distribution gets irregular.

D.1.5 Consistent fluctuations in the Cahn-Hilliard model

In Sec. 6.6 we presented the thermodynamic consistent equations to account for fluctuations of the partial mass density. The fluctuations arise because a contracted physical system is described. As a result of neglecting all molecular degrees of freedom the average quantities fluctuate around their mean value. With decreasing size of the SPH particles or with higher resolution the fluctuations increase. In the limit of macroscopic scale the fluctuations become negligible small and it is justified to only consider the average quantity like in macroscopic Navier-Stokes equations. In this section we focus on the influence of the fluctuations on the morphology of a phase separating binary mixture. In Appendix C we present a validation of the concentration fluctuation used here and show that this model correctly predicts the concentration distribution near equilibrium. Validation for non-equilibrium cases was shown in literature, e.g. [Kor14], using giant fluctuations.

We consider the same parameters as in the reference simulation. Now we consider permanent fluctuations instead of artificial initial fluctuations. The temperature in

the system is $T = 298.15K$. The mobility is

$$M = M_0 \cdot (1 - \omega) \omega \quad (\text{D.7})$$

with $M_0 = 10^{-10} \frac{m^2}{s}$. This guarantees that the amplitude of the fluctuations are zero for $\omega = 0$ and therefore negative, nonphysical values of ω , caused by large random fluctuations, are avoided.

The initial phase distribution for this simulation is similar to the reference. That's why we only show the phase distribution for 3 times in Fig. D.11. The phase distribution is shown for the same times as in the reference simulation to directly compare the morphology (see Fig. D.2). We see that the qualitative characteristics of the morphology is very similar. The effect of the fluctuations on the phase distribution (which means a small kick out of a local equilibrium) is seen in the equilibrium state at time $t = 100ms$. Instead of two layers we get a single layer that represents the global equilibrium of the system [Hir14]. Therefore we conclude that permanent fluctuations enable the system to reach the global equilibrium. This is one of the realistic features of the thermodynamic consistent fluctuations and in the end may lead to more realistic morphology of polymer membranes.

For a quantitative comparison we consider the decrease of surface size over time in Fig. D.12. We also consider an asymmetric particle distribution here because it represents the common particle distribution in SPH simulations. In this diagram we first compare the cases with and without fluctuations with symmetric particle distribution. We find that the curves are very similar except for large times. Here we quantitatively see that the normalized surface is smaller in the simulation with fluctuations and the global equilibrium of the system is reached. We already found

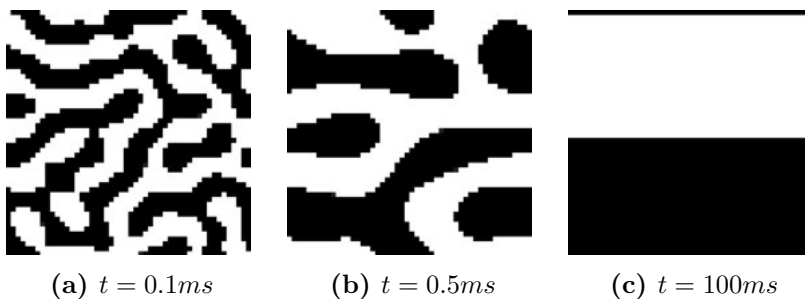


Figure D.11: Time series of phase decomposition with $\omega_0 = 0.5$ and $M = const.$ with permanent fluctuations that are consistent with the dissipation-fluctuation theorem.

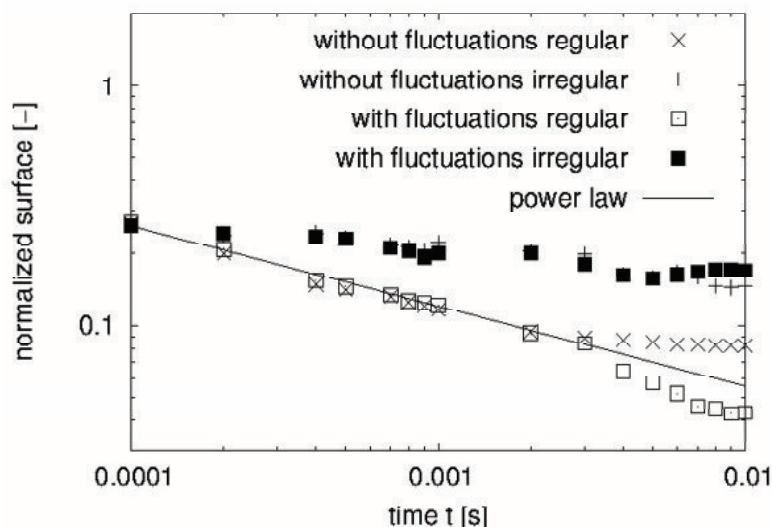


Figure D.12: surface area vs. time with $\omega_0 = 0.5$ with and without permanent fluctuations and for symmetric (regular) and asymmetric (irregular) particle distribution.

that in Fig. D.11 in the phase distribution.

Now we compare the cases of the asymmetric particle distribution with and without fluctuations. Again, we find that the curves with and without fluctuations are very similar except for very large times. But as we mentioned in the reference simulations this large time is no longer covered by the power law.

An increase of the temperature by a factor of 100, where the magnitude of the fluctuations also increases, only slightly influences the phase distribution. Therefore we do not discuss these results here.

We conclude that fluctuations only influence early stage of phase decomposition. They only have an effect in the beginning and the end of the coarsening process. They have an effect at the beginning because they thermodynamic consistently perturb the system so that the system phase separates if unstable. And they have an effect in the end of coarsening because a system does not stick to a local equilibrium but is perturbed to reach the global equilibrium. This is necessary for realistic simulations. Nevertheless we have seen that major insight into phase separating systems is possible without fluctuations. In the remainder of this thesis we neglect permanent fluctuations except when explicitly stated.

D.1.6 Influence of symmetric boundary conditions

Till now we have not discussed boundary conditions different from periodic boundary conditions. Periodic boundary conditions have the advantage that we only investigate the new approach for the Cahn-Hilliard equation without possible effects from boundary conditions. For a real application of the model we apply different boundary conditions because most of the systems cannot be considered periodic. This is the case for immersion precipitation.

As mentioned in Sec. 4.4, aside from periodic boundary conditions we need to consider wall boundary conditions and open boundary conditions. For both kind of boundary conditions we can assume that the boundary has no influence on the fluid. This results in so-called symmetric boundary conditions. The symmetric boundary does not prefer wetting with either of the fluid phases. For a solid wall this means that the contact angle between fluid and wall is 90° . If we want to consider different wetting behavior of the fluid phases we need to model the free energy of the wall. This is beyond the scope of this thesis because it is not important for immersion precipitation. An approach how this may be done is presented in [Hir14].

Proper boundary conditions for the Cahn-Hilliard equation in SPH with the bi-harmonic formulation include a boundary condition for the concentration and the chemical potential.

Boundary conditions for the concentration are necessary because the Laplacian of the concentration is calculated for the gradient energy term. For symmetric boundary conditions we need to apply Neumann boundary conditions for the concentration because there should be no contribution from the boundary to the gradient energy. Boundary conditions for the chemical potential are necessary because the Laplacian of the chemical potential is calculated. Again, for symmetric boundary conditions Neumann boundary conditions for the chemical potential are valid because the boundary should not prefer one of the two phases during phase separation. We also apply these boundary conditions throughout the thesis if symmetric boundary conditions are used.

We illustrate the effect of symmetric boundary conditions on critical phase decomposition. For off-critical phase decomposition the results are similar to those with periodic boundary conditions because one of the phases is present in excess and therefore the morphology observed is very similar, resulting in a droplet centered in

the middle of the domain.

The simulation parameters are the same as for the reference simulation with $\omega_0 = 0.5$ but with symmetric boundary conditions instead of periodic boundary conditions at all boundaries.

A time series of the phase distribution for critical phase decomposition is shown in Fig. D.13. The main difference between phase separation with periodic boundary conditions and symmetric boundary condition gets obvious in Fig. D.13b (at time $t = 0.1ms$). In detail, at the boundaries, we find that the patches are always ordered in a way that a contact angle of 90° is formed. We also see that in Fig. D.13d. On the bottom left a quarter circle is formed in the corner while at the right side of the domain a layer is formed. At this time the global equilibrium isn't reached. The global equilibrium in this case (for $\omega_0 = 0.5$) is layering because the circumference of a circle is larger than the intersection of the domain.

We conclude that symmetric boundary conditions lead to reasonable phase distributions.

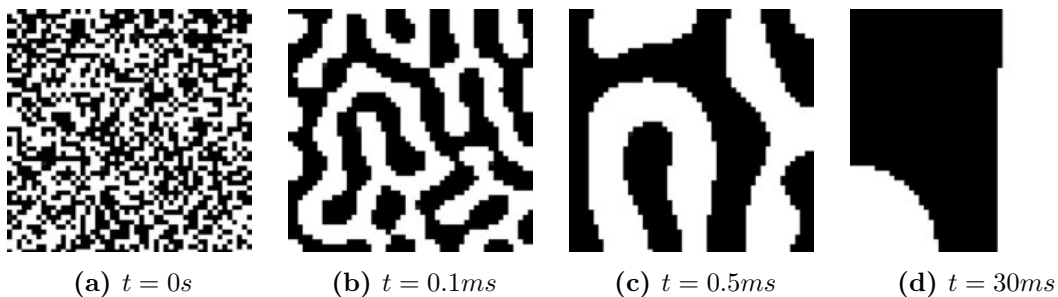


Figure D.13: Time series of phase decomposition with $\omega_0 = 0.5$ and $M = const.$ with symmetric boundary conditions.

APPENDIX E

Ternary phase separation and Stefan–Maxwell Diffusion in SPH

In Chap. D we considered a binary phase separating mixture. This is sufficient for qualitative results about phase separating fluid mixtures but it limits the model to mixtures where the mass transport described as an effective field variable is covered by the Cahn-Hilliard equation. Such kind of effective field variables are frequently used in phase field models which SPH represents to a certain degree. For more quantitative insight into phase separating fluid mixtures at least ternary systems need to be considered.

In principle there exist two approaches for mass transfer in multi-component systems [Tay93]. Both approaches cover coupled mass transfer where the gradient of the chemical potential of every component is considered in every transport equation. This is similar to the Onsager cross coupling where gradients of mass and heat are considered as driving forces in mass flux respectively.

E.1 Generalized Fickian approach

The first approach is called the Generalized Fickian approach. According to [Tay93], the second law of thermodynamics requires a positive entropy production due to mass transfer in an isotherm, isobaric process. We find that for a system of N components there are $N - 1$ independent fluxes and driving forces. This can be

written as

$$\vec{j}_i = - \sum_{j=1}^{N-1} M_{ij} \nabla (\mu_j - \mu_N) \quad (\text{E.1})$$

for $i \in [1, N - 1]$. In contrast to the general formulation of the Fickian approach in terms of gradients of the composition we write the mass flux j_i in terms of the chemical potential because this is more convenient for phase separating fluid mixtures. If one prefers the formulation of the transport equation in terms of gradients of the composition the Hessian matrix of the Gibbs free energy needs to be calculated using models for activity coefficients. For phase separating fluid mixtures one needs to consider the total chemical potential including the gradient term with a diffuse interface to determine the correct Hessian.

The transport coefficients M_{ij} are elements of the inverse transport coefficient matrix \mathbf{M}^{-1} with dimension $N - 1 \times N - 1$. This matrix needs to be symmetric and positive definite to fulfill the second law of thermodynamics. The driving force $\nabla (\mu_j - \mu_N)$ is relative to the gradient of the chemical potential of component N according to [Tay93]. The component balance equations for a ternary system (1=nonsolvent, 2=solvent, 3=polymer) using the generalized Fickian law is

$$\frac{D\omega_1}{Dt} = \nabla \cdot (M_{11} \nabla (\mu_1 - \mu_3) + M_{12} \nabla (\mu_2 - \mu_3)) \quad (\text{E.2})$$

$$\frac{D\omega_2}{Dt} = \nabla \cdot (M_{21} \nabla (\mu_1 - \mu_3) + M_{22} \nabla (\mu_2 - \mu_3)) \quad (\text{E.3})$$

with the chemical potential calculated using the Flory–Huggins free energy for a ternary mixture with one polymer component (m_p is the number of segments of the polymer)

$$\mu_1 = \varphi_2^2 \chi_{12} + \varphi_3^2 \chi_{13} + \varphi_3 \left(1 - \frac{1}{m_p} + \varphi_2 (\chi_{12} + \chi_{13} - \chi_{23}) \right) + \log(\varphi_1) \quad (\text{E.4})$$

$$\begin{aligned} \mu_2 = & (\varphi_2 - 1)^2 \chi_{12} + \varphi_3^2 \chi_{13} - \frac{\varphi_3}{m_p} \\ & + \varphi_3 (1 + (\varphi_2 - 1) (\chi_{12} + \chi_{13}) + \chi_{23} - \varphi_2 \chi_{23}) + \log(\varphi_2) \end{aligned} \quad (\text{E.5})$$

$$\begin{aligned} \mu_3 = & \log(\varphi_3) + 1 - \varphi_3 + m_p (\chi_{13} + \varphi_3^2 \chi_{13} - 1) + m_p \\ & (\varphi_3 (1 - 2\chi_{13} + \varphi_2 (\chi_{12} + \chi_{13} - \chi_{23})) + \varphi_2 (\chi_{12} (\varphi_2 - 1) - \chi_{13} + \chi_{23})) \end{aligned} \quad (\text{E.6})$$

For the present phase separating fluid mixture we choose $\chi_{12} = \chi_{23} = 1$ and $\chi_{13} = 3$. With these interaction parameters the ternary mixture has a miscibility gap between large and small polymer concentrations. Therefore, like in the real PSf-NMP-water mixture, the system phase separates into a polymer lean and a polymer rich phase. The parameters are chosen arbitrarily to reduce numerical cost and obtain good numerical stability. Nevertheless, the system qualitatively represents the properties of the real system and therefore gives insight into the dynamics and phase distribution. The balance equations for the ternary system are discretized in the same way as for the binary system using the fourth-order derivative. As long as the molar mass of the components are equal it doesn't matter if we balance mass fractions (ω_j), volume fractions (ϕ_j) or molar fractions (X_j). Here we balance volume fractions and choose the units of the mobility to be consistent. For the following case we choose the mobility as

$$M_{11}^0 = 64 \cdot 10^{-10} \quad (\text{E.7})$$

$$M_{12}^0 = 64 \cdot 10^{-11} \quad (\text{E.8})$$

$$M_{21}^0 = 64 \cdot 10^{-11} \quad (\text{E.9})$$

$$M_{22}^0 = 64 \cdot 8 \cdot 10^{-11} \quad (\text{E.10})$$

The mobility is multiplied by the volume fraction to ensure non-negative values of the volume fraction, as introduced in Appendix D,

$$M_{ij} = M_{ij}^0 (1 - \varphi_1) \varphi_1 (1 - \varphi_2) \varphi_2 (1 - \varphi_3) \varphi_3. \quad (\text{E.11})$$

The mobility was chosen in a way that the mobility matrix is symmetric and positive definite. The transport coefficients in the generalized Fickian approach have no

physical significance [Tay93] rather than characterizing the system. The mobility reflects that a flux depends mainly on the part of the considered component and the cross coupling is small.

Now we consider a phase separating ternary system with the same setup as in the reference Sec. D.1. Instead of a binary fluid mixture we use the transport equations and mobility for a ternary system discussed in this section. We use 2 initial compositions that correspond to critical and off-critical phase decomposition. For the critical case we initialize the system with $\omega_1 = 0.45$, $\omega_2 = 0.1$ and $\omega_3 = 0.45$. For the off-critical case we use $\omega_1 = 0.6$, $\omega_2 = 0.08$ and $\omega_3 = 0.32$. We only disturb the system initially as in the reference simulation in Sec. D.1. Permanent fluctuations are not present here.

A time series of the composition of the ternary critical phase decomposition is shown in Fig. E.1. In Fig. E.1 each column represents one component and each row represents one time. From left to right non-solvent, solvent and polymer composition is shown. The composition of the polymer is calculated with the concentration of non-solvent and solvent using the fact that they sum up to unit.

We get 3 major results from Fig. E.1. First it is eye-catching that the composition of non-solvent and polymer are complementary. The reason is that the miscibility gap in the system is symmetrically between polymer and non-solvent. Therefore the equilibrium composition is also symmetric which leads to complementary composition. The second conspicuousness is seen in the solvent composition. The concentration of solvent is large near the interface but low in the polymer rich and polymer lean phase. This is a result of the free energy of the ternary system and the finite width of the interface. Therefore the solvent concentration is an indicator of the interface. This may be a feature of the potential used here and may be different in a real polymer system. The last but very important fact is that the equilibrium distribution is reached which is a single layer for the critical phase decomposition.

Before we investigate the quantitative results using the power law, we first analyse off-critical phase decomposition. A time series of the composition of the ternary off-critical phase decomposition is shown in Fig. E.2. There we see the 3 eye-catching characteristics as in the critical case. The non-solvent composition is again complementary to the polymer composition. The solvent concentration is high near the interface and low in the bulk. In contrast to the case of critical phase decomposition, the solvent concentration differs between the bulk phases.

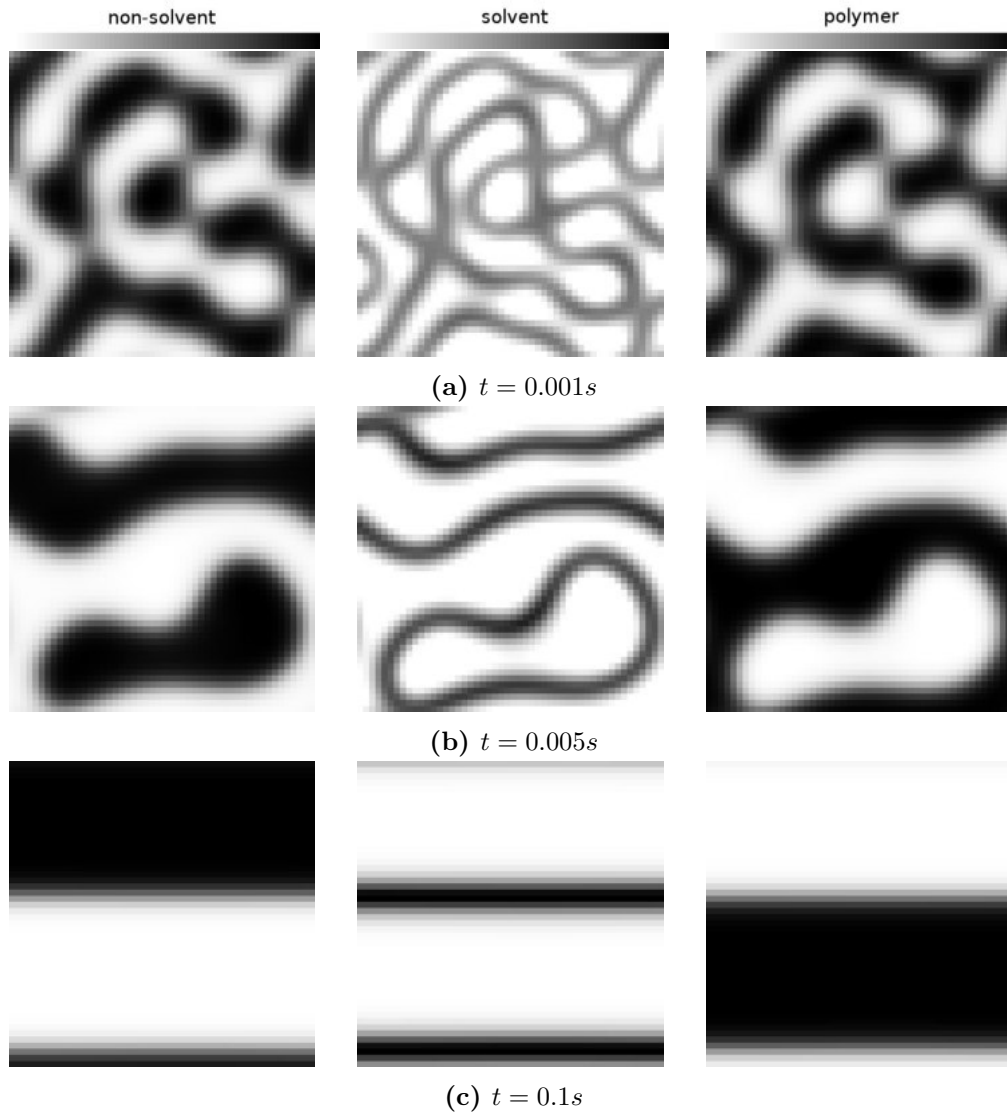


Figure E.1: Time series of ternary phase decomposition. Left column represents non-solvent composition, middle column represents solvent composition and right column represents polymer composition. Black indicates high concentration, white indicates low concentration. Initial composition: $\omega_1 = 0.45$, $\omega_2 = 0.1$, $\omega_3 = 0.45$.

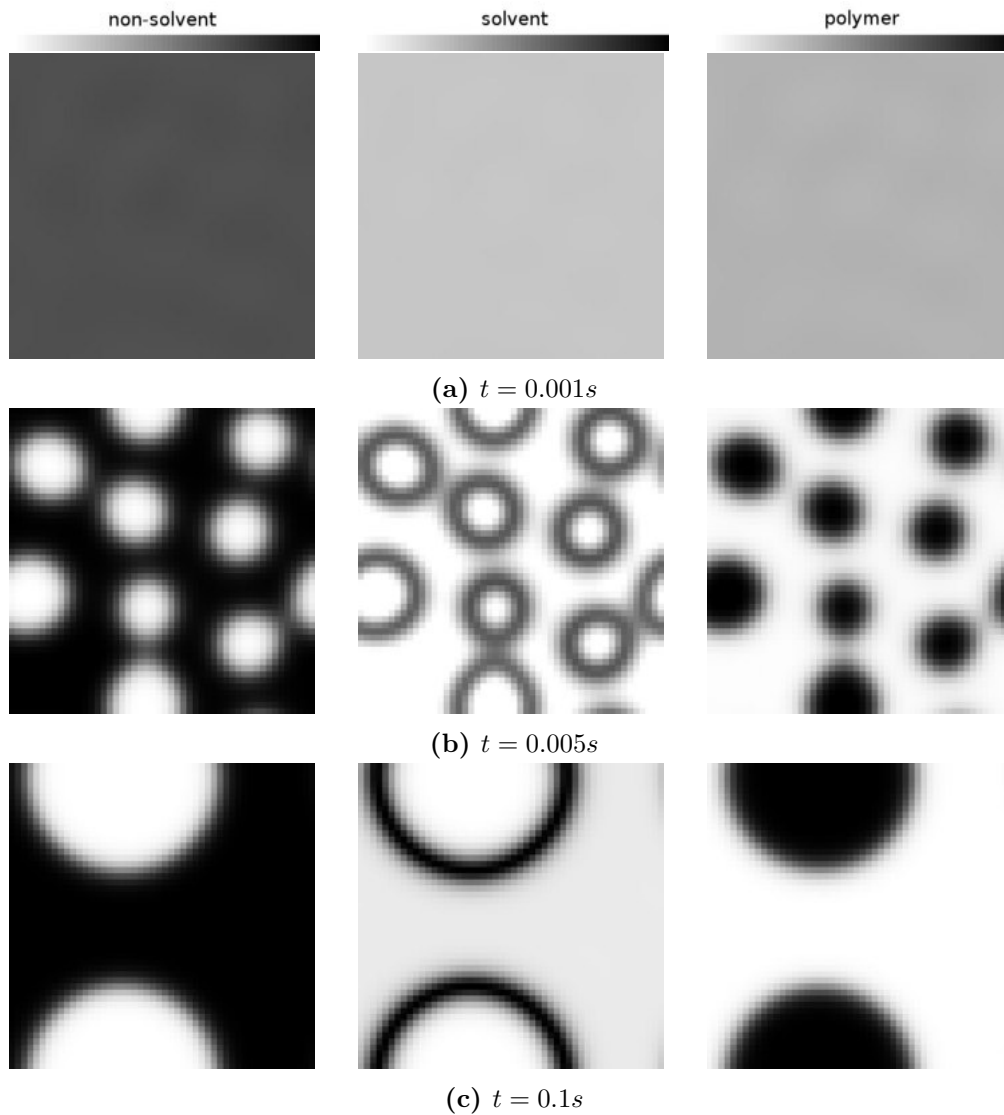


Figure E.2: Time series of ternary phase decomposition. Left column represents non-solvent composition, middle column represents solvent composition and right column represents polymer composition. Black indicates high concentration, white indicates low concentration. Initial composition: $\omega_1 = 0.6$, $\omega_2 = 0.08$, $\omega_3 = 0.32$.

Quantitative results for the dynamic of critical and off-critical phase decomposition of the ternary system is shown in Fig. E.3. We consider the normalized surface versus time and compare the decrease of the interface size over time. The decrease of the interface size is in agreement with the power law of Lifshitz and Slyosov for both the critical and off-critical initial composition. This demonstrates that the dynamics of phase decomposition is well captured with the generalized Fickian approach for a ternary system.

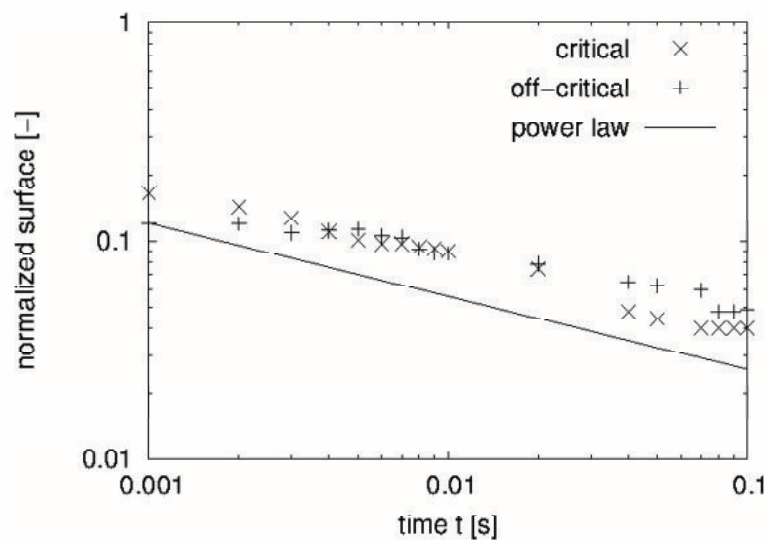


Figure E.3: surface area vs. time for critical and off-critical ternary phase decomposition using the generalized Fickian law.

E.2 Stefan-Maxwell approach

In literature a second approach for multi-component diffusion is discussed. This approach is called Stefan-Maxwell Diffusion. In contrast to the generalized Fickian law binary interactions between components are explicitly considered using binary diffusion coefficients. This is a way to directly use binary diffusion coefficients in a coupled mass transfer model. The Stefan-Maxwell approach is state-of-the-art in many numerical discretization methods but was not discussed in the context of SPH. During the preparation of this thesis we first published a Stefan-Maxwell approach for SPH. In this section refer to Hirschler et al. [Hir16b] for an application of the Stefan-Maxwell approach to phase decomposition. Summarizing, the Stefan-Maxwell approach can be implemented in SPH in a straight forward way but we need caution if the molar mass of the components are different. This may be also the case for the generalized Fickian approach for different molar weights. A detailed discussion is found in [Hir16b].

APPENDIX F

Validation of diffusive transport of a scalar property in SPH

Diffusive transport of a scalar property

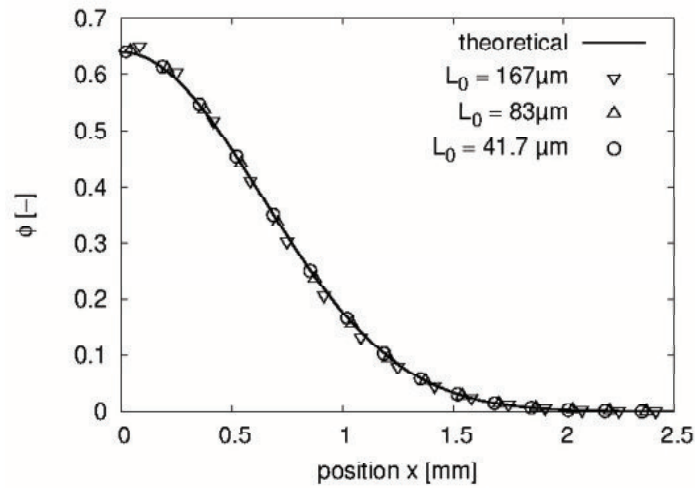
$$\frac{D\phi}{Dt} = \nabla (\alpha \nabla \phi) \quad (\text{F.1})$$

with ϕ as a scalar property and α as a transport coefficient appear in the component equation (Eq. 3.14) in the bulk phase and in the energy equation (Eq. F.5). Since the transport of heat and mass are similar, we validate diffusive transport for a general scalar property ϕ representing the temperature and concentration, respectively. The discrete form of Eq. F.1 was introduced in Eq. 4.15 and in terms of the scalar variable ϕ is

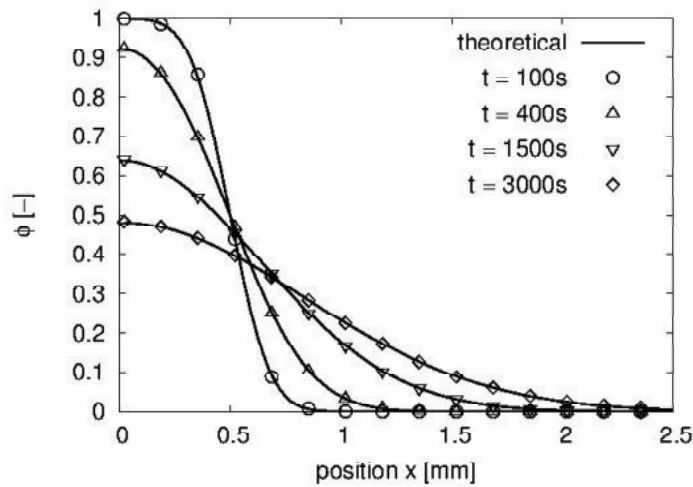
$$(\nabla \cdot \alpha \nabla \phi)_a = \sum_b \frac{m_b}{\rho_b} (\alpha_a + \alpha_b) \frac{\vec{r}_{ab}}{r_{ab}^2} \nabla_a W_{ab} \cdot (\phi_a - \phi_b). \quad (\text{F.2})$$

In literature this discrete form for diffusive transport of a scalar variable was validated, e.g. in [Ada10b; Cle99; Zhu01]. Here we demonstrate convergence of the present model. A very common test case is diffusion of a solute in one direction. This is similar to heat conduction in a bar. For this test case a theoretical solution is available [Cra75]

$$\phi = \frac{1}{2} \phi_0 \left(\text{erf} \left(\frac{x_0 - x}{2\sqrt{\alpha t}} \right) + \text{erf} \left(\frac{x_0 + x}{2\sqrt{\alpha t}} \right) \right) \quad (\text{F.3})$$



(a) Profile of ϕ at time $t = 1500s$ for different resolutions.



(b) Profile of ϕ at different times for $L_0 = 41.7\mu m$.

Figure F.1: Profile of ϕ along the x direction. (Left) The profile for different resolutions at time $t = 1500s$ and the theoretical profile are shown. (Right) The profile of ϕ at different times with $L_0 = 41.7\mu m$ and the theoretical profiles are shown.

where x_0 defines the region of concentrated solute ϕ_0 at time $t = 0$. We choose a transport coefficient $\alpha = 10^{-10} m^2/s$, $\rho = 1000 kg/m^3$, $x_0 = 0.5 mm$ and

$$\phi_0 = \begin{cases} 1 & x < x_0 \\ 0 & \text{else.} \end{cases} \quad (\text{F.4})$$

The length of the domain is $x_{max} = 2.5 mm$.

We show numerical convergence of the present model by increasing the resolution for a smoothing length $h = 2.05 L_0$. We consider 3 different resolutions with $L_0 = 167 \mu m$, $L_0 = 83 \mu m$ and $L_0 = 41.7 \mu m$. This corresponds to 15, 30 and 60 particles along x_{max} . We apply Neumann boundary condition at the boundaries.

The profile of ϕ at time $t = 1500 s$ is shown in Fig. F.1a. For the lowest resolution we see deviations from the theoretical profile especially near $x = 0$. The profile for the highest resolution matches the theoretical profile very well.

The profile of ϕ for $L_0 = 0.25 mm$ at different times is shown in Fig. F.1b. For all times the agreement is very good. Therefore we conclude that the implementation and the discrete form of the second order derivative are valid, and therefore the heat transfer as well as mass transport in the bulk is valid.

In appendix G we use the energy balance in the Lagrangian form

$$\rho c_p \frac{DT}{Dt} = \nabla (k \nabla T) \quad (\text{F.5})$$

with the conductivity of temperature k , the thermal conductivity λ

$$k = \frac{\lambda}{\rho c_p} \quad (\text{F.6})$$

and the specific heat capacity at constant pressure c_p . The discrete energy equation (Eq. F.5) for convective and diffusive heat transfer is

$$\left(\frac{DT}{Dt} \right)_a = \sum_b \frac{m_b}{\rho_b} (\lambda_a + \lambda_b) \frac{\vec{r}_{ab}}{r_{ab}^2} \nabla_a W_{ab} \cdot (T_a - T_b) \quad (\text{F.7})$$

using the second-order derivative (Eq. 4.15). T_a and λ_a are the temperature and heat conductivity of particle a .

APPENDIX G

Surface tension

In this appendix we validate the momentum balance of the proposed model and its discrete formulation using the SPH method. Since the SPH method itself is well validated in literature we focus on the validation of the modifications made in this thesis. We start with the very common isotherm lid-driven cavity test case [Ghi82; Sch83] to demonstrate accurate implementation of the momentum balance, boundary conditions and numerical stability approaches. It is one of the standard test cases of computational fluid dynamics simulation codes. It enables us to validate no-slip boundary conditions for velocity as well as the wall velocity.

Afterwards we couple the momentum equation with the energy equation. We consider a buoyancy-driven flow in a cavity where the density of the fluid is temperature-dependent. In this test case a circular flow is induced due to a temperature gradient [Haj14; LeQ81; Pen82]. Note that the validation of diffusive heat transport is shown in Appendix F for completeness.

Then we validate the model for multi-phase applications. We discuss the formulation of surface tension including gradients of the surface tension tangential to the interface. We assume that the surface tension is temperature-dependent. Because of the similarity between heat and mass transfer we can easily substitute the temperature dependence by a concentration dependence in chapter 6 as long as the interface between the phases is diffuse. We analyze the surface force in a static and dynamic case to highlight features of the discretization. The normal part of the surface tension is investigated using a spherical droplet. The tangential part of the surface tension is investigated using a planar interface.

Finally we consider the complete model to investigate thermocapillary flow. We consider the migration of a spherical droplet [Ma11; Nas03; Ton14] and investigate the stationary migration velocity. We show numerical convergence and compare the SPH method to reference simulations taken from literature.

G.1 Lid-driven cavity

Circular flow in a cavity was theoretically and numerically studied by many researchers e.g. [Bur66; Ghi82; Lee08; Poz02; Raf08; Sch83; Xu09] to mention a few of them. An isotherm flow inside a wall bounded cavity, as schematically shown in Fig. G.1, driven by a constant velocity on the top of the cavity is considered. Due to the no-slip condition on the top wall the fluid is accelerated and a circular flow is initiated. In the following we perform simulations for different Reynolds numbers and compare the axial velocity profiles with results from the well validated grid-based solver OpenFOAM [15] version 2.4.0. We investigate different resolutions to show numerical convergence of the solution of SPH.

The Reynolds number for the lid-driven cavity is defined as

$$Re = \frac{\rho L u_w}{\eta}. \quad (\text{G.1})$$

L is the length of the cavity, u_w is the absolute velocity of the wall and ρ and η are the density and the dynamic viscosity of the fluid. We perform simulations for $Re = 10$, $Re = 100$ and $Re = 1000$ where we alter the Reynolds number by changing

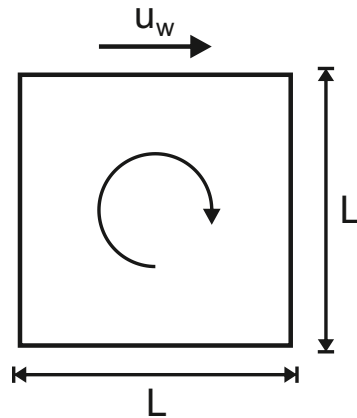


Figure G.1: Scheme of lid-driven cavity example.

the wall velocity only. The size of the cavity is quadratic and the length is $L = 1mm$. The density and viscosity are $\rho = 1000kg/m^3$ and $\eta = 0.01Pas$. For each Reynolds number we vary the resolution from $L_0 = 16.67\mu m$ to $L_0 = 4.17\mu m$ that corresponds to 60 and 240 particles across L . For this test case we use the DIDF and particle shifting approach to avoid void spaces in the stagnation points in the upper corners. The boundary conditions for the velocity at the impenetrable walls are no-slip boundary conditions. From physical point of view the boundary conditions for pressure at the wall are Neumann boundary conditions. As a result the reference pressure is not set in the linear equation system (LES). Therefore infinite solutions exist and an additional bootstrap is necessary. There are two valid options to specify it. One option is to use a constant null space of the krylov subspace solver. If we use this option we cannot use the algebraic multigrid method as preconditioner in the PETSc library. Instead we may use a Jacobi preconditioner. Therefore the stability of the solution for disturbed particle configuration decreases because the condition of the matrix for the krylov subspace method gets worse. The number of iterations also increases by a factor of 100.

Another option is to specify a reference pressure, e.g. $p = 0$, at a point in the domain where the pressure gradient is very low or zero. For the lid-driven cavity such a point may be at the bottom corners. A result of that is a spurious pressure in this corner because specified pressure may not be the best choice. Since the velocity in the corner is nearly zero the effect of this spurious pressure vanishes but the stability of the solution is much better because the algebraic multigrid preconditioner can be used. For that reason we choose the latter option. We show the pressure field later in the discussion. Note that instead of choosing a corner we may choose the bottom wall and apply a constant pressure on the wall. The difference, between specifying the pressure in the corner or the bottom wall, on the pressure is small. Therefore we choose the bottom left corner here to minimize numerical artifacts with a reference pressure $p = 0Pa$.

We use the grid-based solver OpenFOAM [15] version 2.4.0 to prepare a reference solution with two different meshes, a 192x192 regular mesh for $Re = 10$ and $Re = 100$ and a 240x240 regular mesh for $Re = 1000$. The mesh size was chosen after investigation of convergence of the solution. For finer meshes the solution was unchanged for the selected Reynolds number.

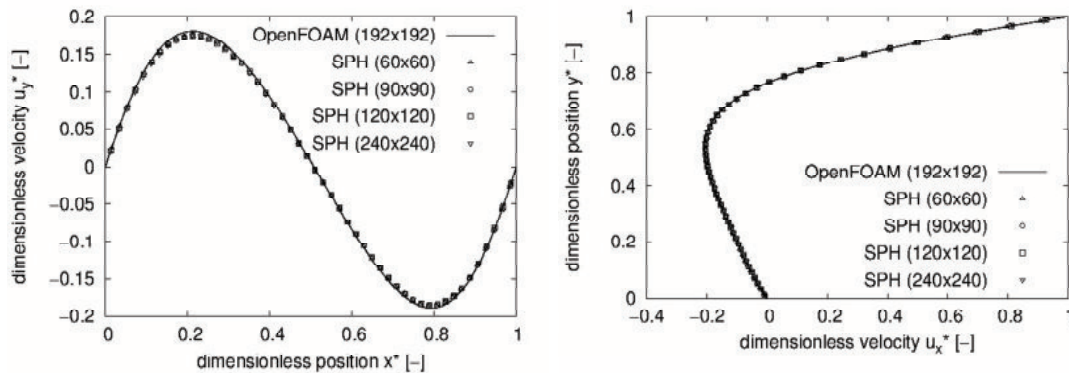
The dimensionless velocity profiles $u_y^* = \frac{u_y}{u_w}$ and $u_x^* = \frac{u_x}{u_w}$ at dimensionless position

$x^* = \frac{x}{L}$ and $y^* = \frac{y}{L}$ are shown in Figs. G.2, G.3 and G.4. For each Reynolds number we investigate convergence for the present SPH model by varying the resolution and compare the velocity profiles to a reference solution from OpenFOAM. For $Re = 10$ (Fig. G.2) the velocity along the vertical and horizontal axis is almost independent of the resolution. We find good agreement between SPH and OpenFOAM for the horizontal velocity (Fig. G.2b) but small deviations at the extreme value for the vertical velocity (Fig. G.2a). One indication for convergence is the position of the center of the vortex. The relative error between the position of the vortex for the highest resolution in SPH and the reference is $\varepsilon = [0.60\%, 0.42\%]$ with respect to the reference solution.

For $Re = 100$ (Fig. G.3) we find good agreement in the velocity profiles between different resolutions in SPH and the reference solution. The relative error in the position of the vortex for the highest resolution in SPH is $\varepsilon = [0.24\%, 0.31\%]$ with respect to the reference solution.

For $Re = 1000$ (Fig. G.4) the effect of finer resolution is more obvious. The change in the velocity profiles is sharper than before. Therefore good agreement between SPH and reference solution is only obtained for high resolution. We see convergence of the vertical and horizontal velocity to the reference solution for higher resolution. The relative error in the position of the vortex for the highest resolution is $\varepsilon = [0.60\%, 0.32\%]$ with respect to the reference solution.

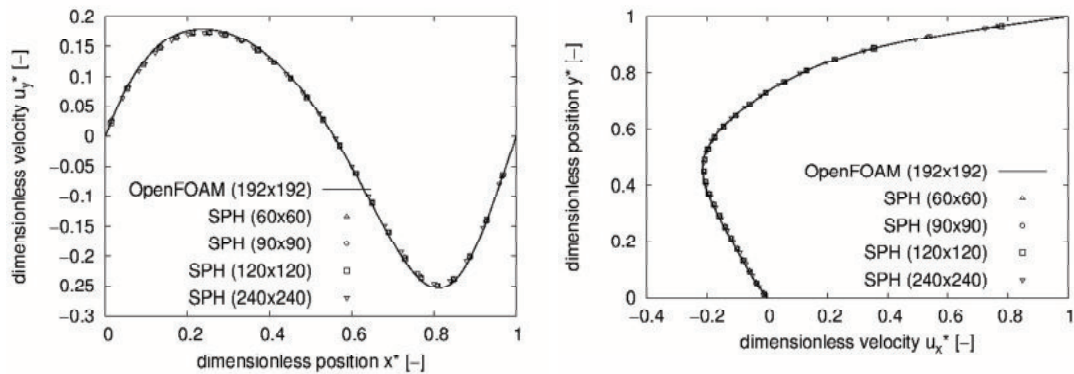
The 2D lid-driven cavity is investigated in the context of SPH in literature as well



(a) vertical velocity vs. x^* at $y = 0.5$

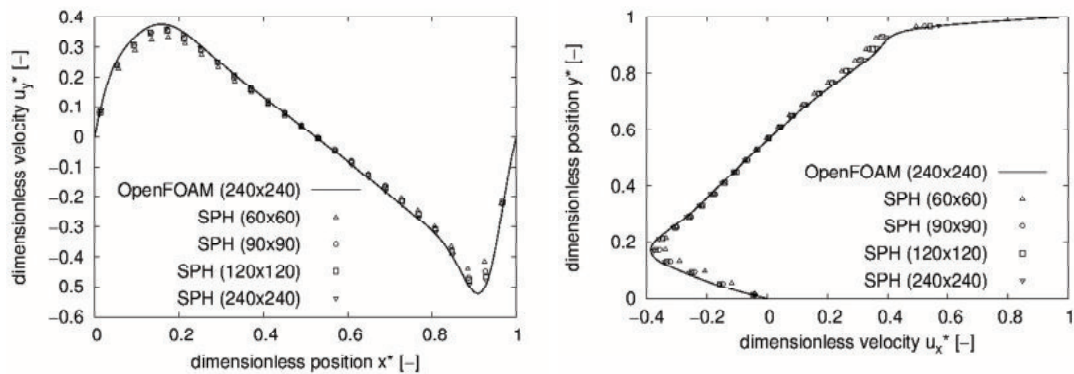
(b) horizontal velocity vs. y^* at $x = 0.5$

Figure G.2: Velocity profiles for $Re = 10$ of a lid-driven cavity.



(a) vertical velocity vs. x^* at $y^* = 0.5$ (b) horizontal velocity vs. y^* at $x^* = 0.5$

Figure G.3: Velocity profiles for $Re = 100$ of a lid-driven cavity.



(a) vertical velocity vs. x^* at $y^* = 0.5$ (b) horizontal velocity vs. y^* at $x^* = 0.5$

Figure G.4: Velocity profiles for $Re = 1000$ of a lid-driven cavity.

[Bas09; Ghi82; Kho14; Lee08; Xu09; Yil09]. Compared to literature the present results are within an expected range of error and therefore we assume that the viscous and pressure force as well as the no-slip boundary conditions for the velocity at the wall and numerical stability approaches (DIDF and particle shifting) are well implemented.

At the beginning of the section we mentioned that an arbitrary bootstrap for the solution of the Pressure Poisson Equation is needed. We note that the velocity or pressure field is not affected by the artificial bootstrap as shown in Fig. G.5. The reason is that the gradient of the pressure in the bottom left corner is very small (Fig. G.5b). Even if the pressure near the corner is different from the specified

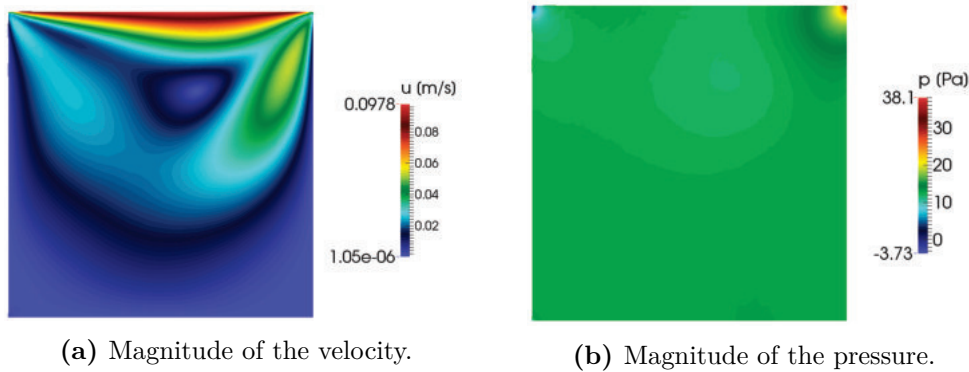


Figure G.5: Velocity field and pressure field for $Re = 100$ with a resolution of $L_0 = 8.33\mu m$.

bootstrap we obtain a good solution. This highlights that the bootstrap is only necessary for algorithmic reasons during the solution of the linear equation system.

G.2 Buoyancy-driven cavity

Next we investigate non-isotherm single-phase flow to validate the coupling of momentum and energy equation. In the context of this thesis, non-isotherm flow is not relevant. But in Chap. 6 we investigate gradients of the surface tension caused by gradients in the concentration tangential to the interface. Because of the similarity of heat and (Fickian) mass transfer, a validation of the numerical framework using heat conduction for common test-cases represents a validation for coupling component and momentum equation.

Buoyancy-driven flow was investigated in the context of SPH in a few articles [Ler15; Sze11; V13]. Here we investigate a buoyancy-driven cavity. In contrast to a lid-driven cavity, where the fluid is driven by a velocity of the wall, the fluid is accelerated due to a temperature difference between two walls. A schematic sketch is shown in Fig. G.6. The left wall is heated, the right wall is cooled and the top and bottom walls are adiabatic. Due to the change in temperature the density decreases with increasing temperature. Because of a gravitational force, a circular flow is initiated because denser fluid is accelerated downwards and lighter fluid moves upwards. For small density variations the Boussinesq approximation [Bou97] is valid and the system can be regarded as incompressible since the pressure is still independent of the density [Lan87; Sze11]. Therefore the only coupling term between momentum

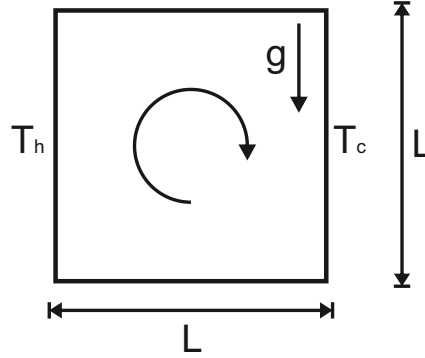


Figure G.6: Scheme for buoyancy-driven cavity example.

balance and energy balance is the gravitational acceleration \vec{g} . According to Landau and Lifshitz [Lan87] the difference in the acceleration between two fluid portions with different temperature is

$$\frac{\vec{F}_{body}}{\rho} = -\beta\vec{g}\Delta T \quad (\text{G.2})$$

with the thermal expansion coefficient

$$\beta = -\frac{1}{\rho} \frac{\partial \rho}{\partial T_p}, \quad (\text{G.3})$$

in the range of $10^{-4}[1/K]$ for polymers, and the temperature difference

$$\Delta T = T - T_0 \quad (\text{G.4})$$

with a reference temperature T_0 . Note that the hydro-static part of the pressure is neglected here because it should be negligible per definition. Therefore we directly use Eq. G.2 as an effective external force in the momentum balance Eq. 3.23.

For natural convection the dimensionless numbers are the Prandtl number Pr

$$Pr = \frac{\nu}{k}, \quad (\text{G.5})$$

the Rayleigh number Ra

$$Ra = \frac{g\beta L^3 \Delta T}{\nu k} \quad (\text{G.6})$$

and the Gay-Lussac number

$$Ga = \beta \Delta T. \quad (\text{G.7})$$

The characteristic length L is the size of the cavity. ν and $k = \frac{\lambda}{\rho c_p}$ are the kinematic viscosity of the fluid and the thermal diffusivity with the heat capacity c_p and the thermal conductivity λ . The Gay-Lussac number Ga describes the level of density variations caused by temperature [Sze11]. For $Ga \rightarrow 0$ the Boussinesq approximation holds [Pes09]. In our case the temperature difference is $\Delta T = T_h - T_c$ with T_h and T_c as the temperature at the hot and cold wall (see Fig G.6).

We consider a square cavity of length L under the influence of gravity $\vec{g} = [0 - 9.81]$. In the direction of gravity the cavity is adiabatic. In the other direction a constant temperature is applied at the boundary. On the left side we set the hot temperature to $T_h = 274.15K$ and on the right side the cold temperature to $T_c = 273.15K$. We apply no-slip boundary conditions for the velocity at all boundaries. Initially temperature in the systems is homogeneous $T_0 = 273.15K$. The dynamic viscosity of the fluid is $\mu = 0.01Pas$ and the density is $\rho = 10 \frac{kg}{m^3}$. The thermal diffusion coefficient is $k = \frac{\lambda}{\rho c_p} = 0.00141 \frac{m^2}{s}$ and the thermal expansion coefficient is $\beta = 0.071$. We investigate the flow in the cavity for two different Rayleigh numbers. The size of the cavity varies with the Rayleigh number and is $L = 126.4555mm$ and $L = 272.44mm$ for $Ra = 10^3$ and $Ra = 10^4$. We vary the resolution to show convergence.

We compare the profile of the velocity and temperature along the vertical and horizontal axis of the cavity with reference simulations using OpenFOAM [15]. After investigation of the different resolutions in OpenFOAM we choose a 120x120 regular grid for all reference simulations.

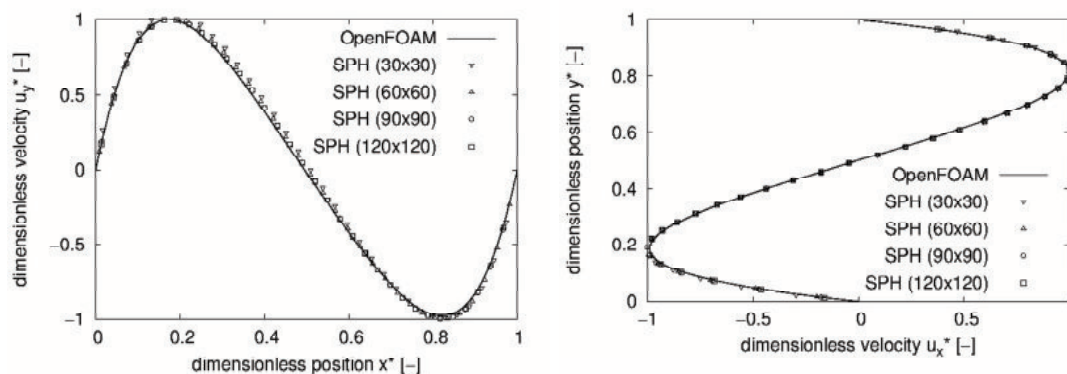
As already discussed in the last section we need to set a bootstrap for the pressure to solve the linear equation system (LES). In this case it is more difficult to identify a point with very small gradient in the pressure. Therefore it was more stable to fix the pressure along the bottom wall to $p = 0Pa$. We used the DIDF and

particle shifting approach as for lid-driven cavity. The dimensionless velocities are $u_y^* = \frac{u_y}{u_{y,max}}$ and $u_x^* = \frac{u_x}{u_{x,max}}$ at dimensionless positions $x^* = \frac{x}{L}$ and $y^* = \frac{y}{L}$. The dimensionless temperature is $T^* = \frac{T-T_0}{T_{max}-T_0}$ with $T_0 = T_c$ and $T_{max} = T_h$.

First we investigate a buoyancy-driven cavity at $Ra = 1000$. We vary the resolution from $L_0 = 4.2mm$ to $L_0 = 1.05mm$. The vertical and horizontal velocity profiles along the axis at $x^* = 0.5$ and $y^* = 0.5$ are shown in Fig. G.7. The velocity profiles are almost independent of the resolution and in good agreement with the reference solution. The temperature profile along x^* is shown in Fig. G.9a. Even with higher resolution we see a small deviation from the reference solution. The deviation is in a reasonable range compared to literature [Ler15; Sze11; V13].

Next we investigate the buoyancy-driven cavity at $Ra = 10000$. We again vary the resolution. The vertical and horizontal velocity profiles along the axis are shown in Fig. G.8. For higher Rayleigh numbers the buoyancy force is stronger. We see more deviations of the velocity in SPH compared to the reference solution for coarse resolutions. With increasing resolution we find convergence and good agreement to the reference solution. The temperature profile shown in Fig. G.9b also converges and is in very good agreement with the reference solution.

In Fig. G.10 we demonstrate for $Ra = 10000$ that the velocity and temperature field is smooth. We don't see an effect of the artificial bootstrap for the pressure and therefore skip the plot of the pressure here. The velocity and temperature seems to be unaffected because we see a symmetric velocity distribution in Fig. G.10a.

(a) vertical velocity vs. x^* at $y^* = 0.5$ (b) horizontal velocity vs. y^* at $x^* = 0.5$ **Figure G.7:** Velocity profile for $Ra = 1000$

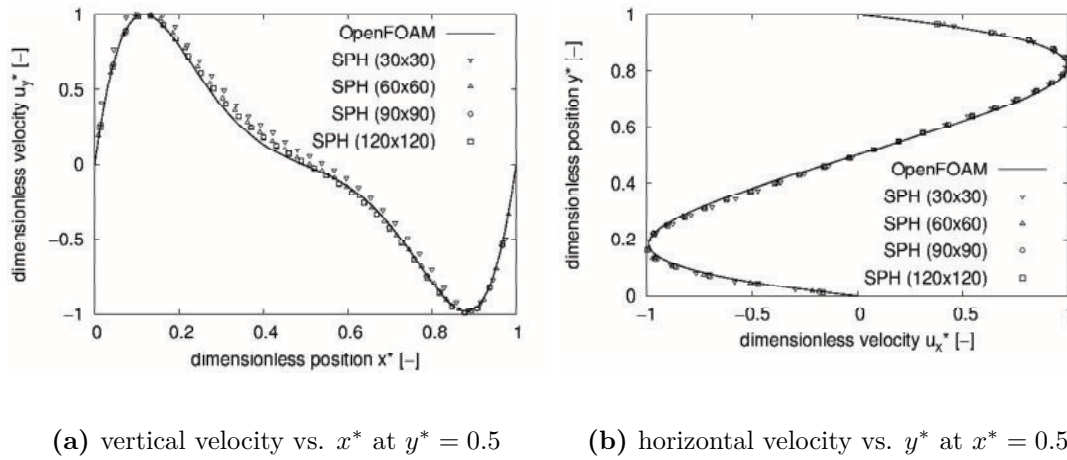


Figure G.8: Velocity profile for $Ra = 10000$

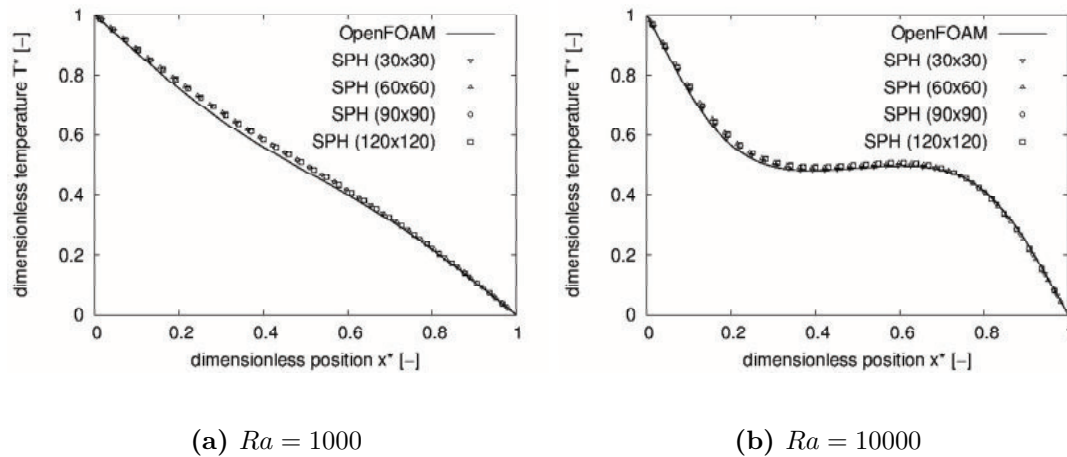


Figure G.9: Temperature profile vs. x^* at $y^* = 0.5$ for $Ra = 1000$ and $Ra = 10000$

The temperature distribution is also in good agreement with literature [Sze11]. Therefore we conclude that the coupling of the momentum and energy equation is valid. Throughout this thesis we only need buoyancy flow with low and moderate Rayleigh numbers. Therefore we don't show results for higher Rayleigh numbers here. The application of the SPH method to large Rayleigh numbers is shown in [Ler15; Sze11].

G.3 Validation of surface tension

In a multi-phase system we get a contribution of the interface to the momentum balance. This contribution is called capillary stress in general or surface tension in

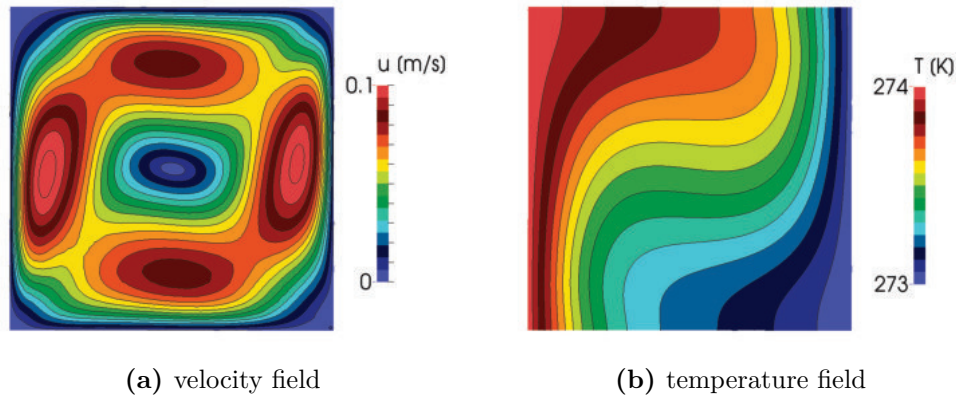


Figure G.10: Velocity and temperature distribution in a buoyancy-driven cavity for $Ra = 10000$.

an immiscible system. The form of the capillary stress tensor in the momentum balance is similar to the form of the viscous stress tensor as it accounts for a normal and tangential stress. Therefore we may split the capillary stress into a normal and tangential part. The tangential part is known as the Marangoni force and accounts for gradients in the surface energy along the interface.

In this thesis we use the CSF model [Bra92; Mor00] to discretize the capillary stress. This model is well validated in literature for SPH [Ada10b; Gre09; Hu06; Hub16; Mon12; Mor00; Sze13; Sze15]. In this section we focus on the validation of the implementation. We note that using the CSF model is not the rigorous way to include surface tension for a diffuse interface. For a rigorous formulation of the surface tension we should discretize the capillary stress using the same potential as in the component equation for the chemical potential (see chap. 3 in Eq. 3.18). Unfortunately there is no numerically stable formulation of the capillary stress available for a diffuse interface in literature for SPH. Therefore, we use the CSF model where the interface is numerically smoothed. As we will see later this enables us to model capillary stress in miscible systems when the color function is identical to the composition. Capillary stress arises due to local gradients in the partial density. Note that the corrected SPH approach and particle shifting is used every time when capillary stress is considered.

As introduced in Sec. 4.3.3 we use a color function to calculate the normal at the interface between two phases. The color function may be sharp or diffuse and arbitrary or physically meaningful. A common choice in literature is an arbitrary

sharp color function

$$C_a = \begin{cases} 0 & \text{if fluid 1} \\ 1 & \text{if fluid 2.} \end{cases} \quad (\text{G.8})$$

where each particle of a fluid has a constant color C_a . In a few literature the arbitrary color function is diffuse too [Sha12a]

$$\bar{C}_a = \sum_b \frac{m_b}{\rho_b} C_b W_{ab}. \quad (\text{G.9})$$

In this section we use both arbitrary color functions for a sharp and diffuse interface. Examples for a physically meaningful sharp and diffuse color function are the density of the fluids in an immiscible system and the mass fraction or concentration in a diffuse interface. We will use the latter one for the diffuse interface in Chap. 5 and 6.

G.3.1 Static capillary stress normal to interface

We first investigate the normal part of the capillary stress in a static test case. We consider a spherical droplet in a second fluid at rest and compare the pressure jump over the interface with the Young-Laplace equation [You59]. In 2D the Young-Laplace equation for a pressure jump is

$$\Delta p_{YL} = \frac{\sigma}{R_d} \quad (\text{G.10})$$

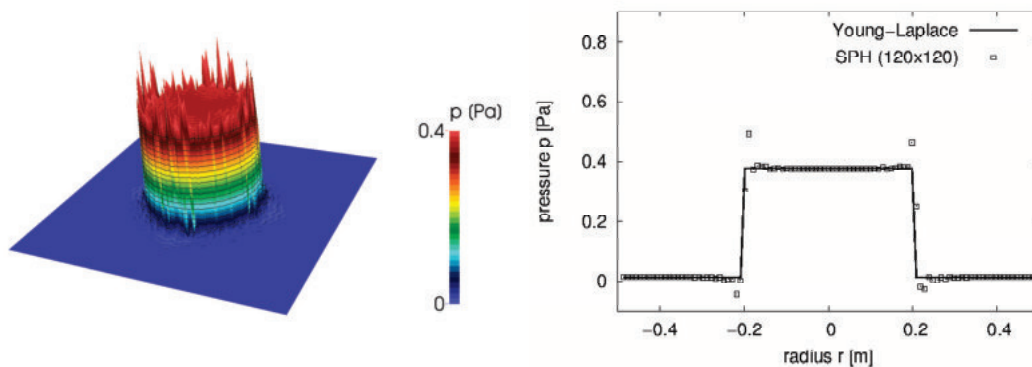
with the radius of the droplet R_d . We consider a droplet with a radius $R_d = 0.2m$ inside a quadratic box with size $L = 1m$ filled with a second fluid. Both fluids have the same physical properties. The density, dynamic viscosity and surface tension are $\rho = 1000 \frac{kg}{m^3}$, $\eta = 0.01 Pa \cdot s$ and $\sigma = 72.75 \frac{mN}{m}$. The resolution of the box is 120x120 particles and 24 particles per droplet radius respectively. Initially the particles are in regular Cartesian order. At the boundary we apply no-slip conditions for the velocity. At the top of the box we use Dirichlet boundary conditions and at the other three boundaries Neumann boundary conditions for the pressure. The theoretical pressure jump in the present case is $\Delta p = 0.36375 Pa$.

We first investigate the sharp color function (Eq. G.8). At the beginning the order

of the particles of the droplet isn't smooth because of the Cartesian order. We wait until an equilibrium configuration of the particles and then investigate the pressure jump. Fig. G.11a shows a 3-dimensional graph of the pressure distribution in the box at an equilibrium configuration. We see that the pressure jump isn't smooth. At the interface we observe fluctuations where the pressure is higher or lower than the pressure in the bulk phases. This is more obvious in the pressure profile along the radius of the droplet (Fig. G.11b). These pressure fluctuations are also observed and discussed in literature [Ada10b; Sze15]. The reason for the pressure fluctuations are the spurious currents at the interface caused by unfavorable energetic configuration of the particles [Heß10]. The pressure in the bulk phase is constant. Therefore we quantify the pressure jump across the interface using the constant pressure in the bulk phases. The pressure jump in the simulation is $\Delta p_{SPH} = 0.3601 Pa$. The relative error is

$$\varepsilon = \frac{\Delta p_{YL} - \Delta p_{SPH}}{\Delta p_{YL}} \cdot 100\% \quad (\text{G.11})$$

of $\varepsilon = 0.99\%$. This error is in the same order than in literature [Ada10b; Mor00]. Next we use a diffuse color function to calculate the normal. Initially the color of each particle is set using Eq. G.8. Then the color is smoothed at the begin of every time step using Eq. G.9. Therefore we get a smooth transition of the color function



(a) 3D graph of the pressure distribution.

(b) Pressure profile along the radius of the droplet.

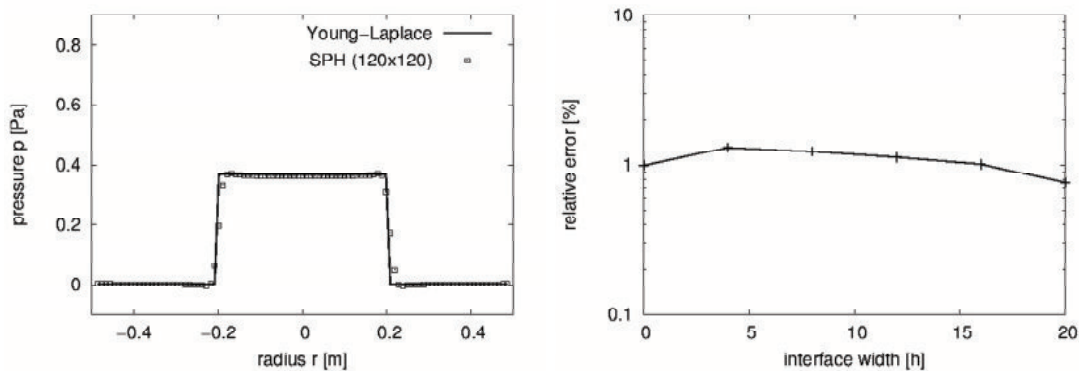
Figure G.11: Graph and plot of a single droplet in rest in a square box with surface tension $\sigma = 72.75 \frac{mN}{m}$. A sharp color function is used.

between both phases in a range of $2r_c$ or $4h$ for the Wendland kernel, respectively. We may repeat smoothing the color function to get a wider transition that lead to $8h$, $12h$, $16h$ and $20h$ for 2, 3, 4 and 5 smoothing cycles.

Again, we investigate a droplet at rest with the same properties as for the sharp color function. We estimate the error in the pressure jump for different widths of the interface. In Fig. G.12a we show the pressure profile along the radius for a color function with one smoothing cycle. At the interface between both phases the transition is smooth. The pressure jump is well approximated. The relative error of the pressure jump compared to the Young-Laplace equation is $\varepsilon = 1.30\%$. In contrast to the pressure profile using a sharp color function (Fig. G.11b) the pressure fluctuations are smaller but don't vanish.

In Fig. G.12b we show the error in the pressure jump with increasing width of the color function. In addition the value at zero interface width indicates the error of the sharp color function. We see a decrease of the error in the pressure jump with increasing width of the color function. For a width of the color function of approximately $16h$ the error of the pressure jump using a smoothed color function is in the same range as for a sharp color function.

Finally note that the error in the pressure jump between both phases is very similar



(a) Pressure profile along the radius of the droplet using a smoothed color function with width $4h$.

(b) Error of calculated pressure jump of a droplet using a smoothed color field with different width of the color field. For $h = 0$ a sharp color function is used.

Figure G.12: (Left) Plot of pressure profile using a smoothed color function. Surface tension is $\sigma = 72.75 \frac{mN}{m}$. (Right) Error of pressure jump for different widths of the interface.

for both color functions. Therefore we conclude that we can either use a sharp or a smoothed color function. We will use a sharp color function in immiscible systems without mass transfer. In all other cases we will use the concentration as a smoothed color field.

G.3.2 Dynamic capillary stress normal to interface

Next we demonstrate that the dynamics of the fluid due to capillary stress is valid. A common test case is an oscillating droplet, where an analytic solution of the oscillation period is only available in the limit of a large density ratio [Ray79]. It was shown in literature that the CSF model using a sharp color function accurately reproduces the oscillation period of a droplet for different surface tensions [Ada10b; Hu06; Mor00; Sze15]. Numerical reference data for a density ratio of 1 is also available in literature [Ada10b]. In this section, we focus on the effect of the smoothed color function on the oscillation of the droplet for a density ratio of 1.

The test case consists of a spherical droplet with radius $R = 0.2m$ in the center of a square box with length $L = 1m$. At the boundaries we use no-slip conditions for the velocity. The pressure is fixed at the top of the box and Neumann boundary conditions for the pressure are applied at the other boundaries. In both phases, the density, dynamic viscosity and surface tension are $\rho = 1kg/m^3$, $\eta = 0.05Pas$ and $\sigma = 1N/m$. Initially we impose a divergence-free velocity field [Ada10b; Mor00]

$$u_x = U_0 \frac{x}{r_0} \left(1 - \frac{y^2}{r_0 r} \right) \exp \left(-\frac{r}{r_0} \right) \quad (G.12)$$

$$u_y = -U_0 \frac{y}{r_0} \left(1 - \frac{x^2}{r_0 r} \right) \exp \left(-\frac{r}{r_0} \right) \quad (G.13)$$

with $u_0 = 10m/s$, $r_0 = 0.05m$. The amplitude of the oscillation is damped by the viscous force but for small viscosity the oscillation period is not influenced.

We investigate the oscillation period for a sharp color function and different smoothed color functions. The results are shown in Tab. G.1. For comparison we give the estimated period from [Ada10b] as a reference. We estimate the period as the mean of x and y position of Fig. 7a in [Ada10b] with highest resolution. The mean is approximately $t = 0.4s$.

Table G.1: Oscillation periods of droplet with density ratio 1. Different color functions used. Comparison with estimated period from Adami et al. [Ada10b].

color function	t [s]
[Ada10b]	≈ 0.4
sharp	0.409
$4h$	0.437
$8h$	0.441
$12h$	0.440
$16h$	0.440
$20h$	0.443

For a sharp color function we are very close to the period of the reference. For the smoothed color function the period is approximately 10% higher. This is larger than we would expect according to literature [Ada10b; Hu06; Mor00] where an error in the range of 5% is common. For different widths of the smoothed color function we get very similar periods.

In addition we compare the contour of the oscillating droplet with a smoothed color function at different times with a contour from literature [Ada10b]. The particle distribution of the droplet is shown in Fig. G.13. Only the particles of the droplet are shown. The surrounding particles are not shown. The particles in the upper half are taken from [Ada10b]. The particles in the bottom half correspond to the simulation with a smoothed color function of width $4h$. The contours match with small deviation for larger times. Even if in [Ada10b] a weakly compressible SPH is used, the particle distribution is very similar. This is in disagreement with the estimated oscillation periods in Tab. G.1 but within an accuracy of 10%.

Finally we give the maximum position of the droplet in x and y direction over time in Fig. G.14. On the left and right side of Fig. G.14 we see the variation of position for a sharp and a smoothed color function. In both plots we compare the variation with results from [Ada10b]. There is a difference between the amplitude of the present results and the literature. The reason for the difference in the amplitude is that in the reference [Ada10b] the variation of position is calculated in a different way than in the present simulations. They take the average of the mean position in a quarter of the droplet and plot it over time. Here we take the maximum position of a particle in x and y direction. Therefore the variation is larger in the present simulation but both kind of analysis indicate the frequency. We see in both figures

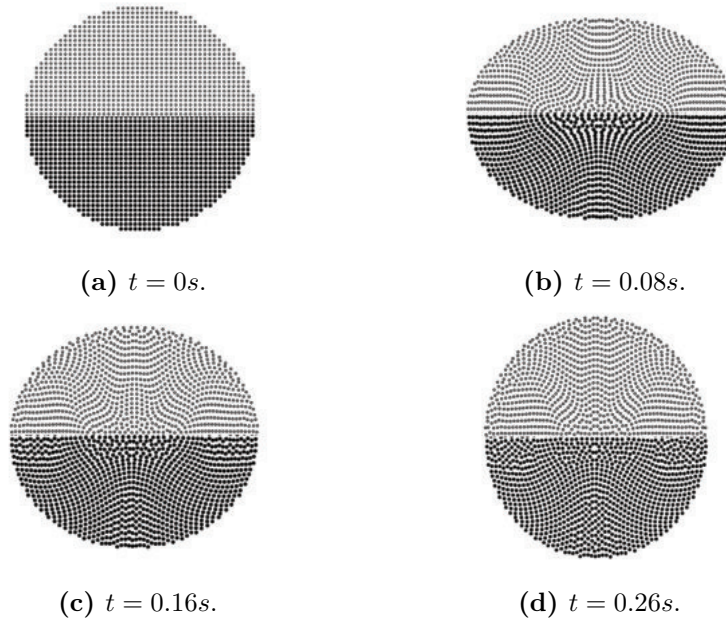
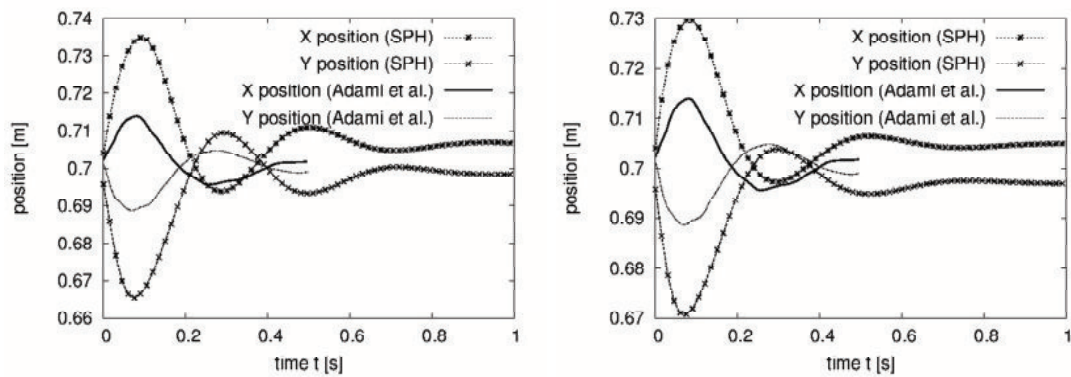


Figure G.13: Particle distribution of an oscillating droplet. Top half of every image is taken from [Ada10b]. The bottom half of every image are present results. The surface tension is $\sigma = 1 \frac{N}{m}$. A smoothed color function with a width $4h$ is used.



(a) Sharp color function.

(b) Smoothed color function.

Figure G.14: Position variations over time for a droplet with $R = 0.2m$ and $\sigma = 1 \frac{N}{m}$. (Left) A sharp color function is used. (Right) A smoothed color function with a width of $4h$ is used.

that the position oscillates around the average position $x = 0.7m$ and $y = 0.7m$ respectively. In comparison to the reference, the oscillation profile in the present simulations are very smooth. A very small drift of the position is seen for $t \rightarrow 1s$ because the droplet moves a little bit out of the center of the box. This is caused by small fluctuations of the pressure.

In Fig. G.14 we see that the oscillation periods in Tab. G.1 and the contours in Fig. G.13 are correct. For the smoothed color function the second half of the first oscillation period is larger than the first one. The reason may be that the surface force is slightly different because the shape of the droplet is smoothed due to the smoothed color function. We conclude that the capillary stress in dynamic cases for a smoothed color function deviates from that of a sharp color function by approximately 10%.

G.3.3 Static capillary stress tangential to interface

The surface tension may depend on the temperature or concentration. If there is a temperature or concentration gradient tangential to the interface between two fluids then an additional force, the Marangoni force, arises.

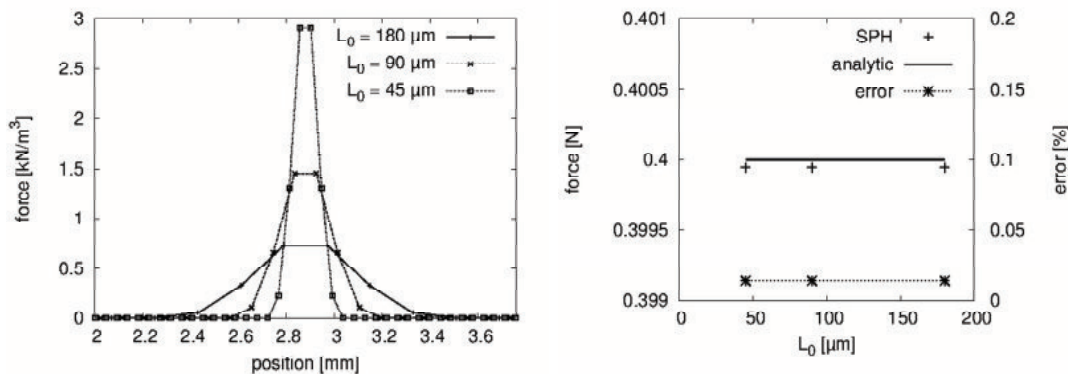
In literature there are only a few publications on Marangoni force in the context of SPH. Marangoni force due to a concentration gradient at the interface was first discussed by Adami et al. [Ada10a]. He used the conservative formulation of the CSF model (the continuum surface stress (CSS) model) and investigated the motion and surface concentration of a bubble. For thermocapillary flow Tong et al. [Ton14] presented a model based on the non-conservative formulation of the CSF model (the same that we use here). He investigated thermocapillary migration of a droplet. Heat transfer was included using an enthalpy balance. Our model is similar to the model of Tong et al. [Ton14] except that we use the energy balance in temperature form.

First we investigate the Marangoni force in a static test case. We consider two layered fluids in an infinitely long channel of width $5.76mm$ in 2D. The interface between the fluids is planar. We apply a linear temperature profile along the channel with a slope of $\nabla T = 200K/m$. We assume that the surface tension coefficient depends linear by temperature

$$\sigma = \sigma_0 + \sigma_T (T - T_0) \tag{G.14}$$

with the surface tension coefficient σ_0 at T_0 and the coefficient $\sigma_T = -2mN/(mK)$. With these parameters the theoretical Marangoni force is $\nabla_S \sigma = 0.4N/m^2$. In the following simulations we use a sharp color function to calculate the normal. The only force in the system is the thermocapillary force tangential to the planar interface. We investigate the Marangoni force for different resolutions to show numerical convergence. We investigate the resolutions $L_0 = 180\mu m$, $L_0 = 90\mu m$ and $L_0 = 45\mu m$.

Because SPH is a smoothed discretization method the Marangoni force is smoothed out around the interface between the fluids. In Fig. G.15a we see the profile of the Marangoni force perpendicular to the interface in the channel. We see that the Marangoni force is wider for low resolution and narrower for higher resolution. In the limit of infinite resolution the profile tends to a Dirac function with the magnitude of the Marangoni force. The calculated integral of the smoothed Marangoni force of the simulation is shown in Fig. G.15b. The Marangoni force in SPH is only slightly different from the theoretical value. The relative error is $\varepsilon = 0.014\%$ based on the theoretical value. The calculated Marangoni force is independent of the resolution because we used the corrected SPH approach with regular order of the particles and therefore the force is as accurate as possible. In [Ton14] a similar case is presented. The relative error was also constant but with $\varepsilon = 3.65\%$ very large. The reason may



(a) Profile of Marangoni force along the width of the channel.

(b) Integrated Marangoni force and relative error for different resolutions.

Figure G.15: (Left) Profile of Marangoni force in normal direction to the interface using a resolution of $L_0 = 180\mu m$, $L_0 = 90\mu m$ and $L_0 = 45\mu m$. (Right) Integrated force and relative error of the Marangoni force for different resolutions.

be an incorrect application of the corrected SPH approach in [Ton14]. One major difference is that we calculate the shepard kernel using only particles with a normal larger than $0.01/h$.

We conclude that the Marangoni force is very accurate in the present model.

G.4 Thermocapillary droplet migration

In this section we combine the normal and tangential surface force and investigate thermocapillary migration of a droplet. In thermocapillary flow, a droplet moves because of gradients of the surface tension tangential to the interface, caused by a gradient of the temperature, in the absence of gravity. For sufficiently low Reynolds numbers, the shape of the droplet is spherical and constant during motion.

Thermocapillary motion was studied for several decades theoretically [Bal87; Bal96; Fed13; You59], numerically [Fat15; Ma11; Nas03; Tho80; Zha10] and experimentally [Had99; Kan08; Kan06; Woz01; Xie05]. An overview about the work of the 20th century is found in [Sub01] and the references therein. In the context of SPH, thermocapillary motion was only recently studied by Tong et al. [Ton14] in 2D. Tong et al. presented results for the migration velocity of a single droplet in thermocapillary flow. In this case a droplet is accelerated by gradients in the surface tension coefficients. For a very low resolution the migration velocity presented by Tong et al. match results of Ma & Bothe [Ma11] but they didn't provide a convergence study. In this section we investigate thermocapillary migration of a droplet in 2D and 3D. We first show numerical convergence with increasing resolution, investigate the effect of a bounded domain and compare our results to [Ton14] and [Ma11]. Young et al. [You59] derived an analytic solution for the steady-state migration velocity of a droplet in 3D. We compare the present results for 3D migration velocity to the analytic solution.

The setup of the test case is shown in Fig. G.16. Initially a spherical droplet (phase 1) with radius R is located in the center of a square box with length L . In x direction we apply Neumann boundary conditions for the temperature and free slip conditions for the velocity. In y direction we apply Dirichlet boundary conditions for temperature and no-slip conditions for the velocity. The density, viscosity and thermal diffusion coefficient of the droplet are $\rho_1 = 250\text{kg}/\text{m}^3$, $\eta_1 = 0.012\text{Pas}$ and $\lambda_1 = 1.2 \cdot 10^{-6}\text{W}/(\text{mK})$. The density, viscosity and thermal diffusion coefficient of

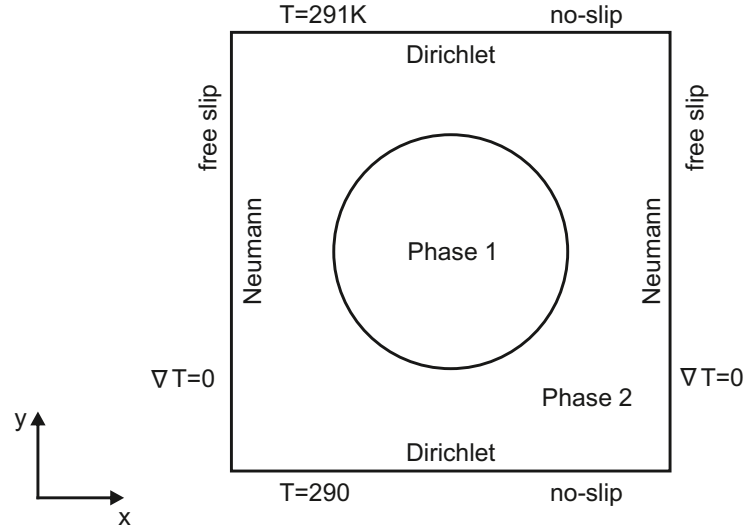


Figure G.16: Schematic setup of thermocapillary migration of a droplet.

the continuous phase are $\rho_2 = 500 \text{ kg/m}^3$, $\eta_2 = 0.024 \text{ Pas}$ and $\lambda_2 = 2.4 \cdot 10^{-6} \text{ W/(mK)}$. The specific heat capacities are $c_{p,1} = 0.5 \cdot 10^{-4} \text{ J/(kgK)}$ and $c_{p,2} = 10^{-4} \text{ J/(kgK)}$. The surface tension is

$$\sigma = \sigma_0 + \sigma_T (T - T_0) \quad (\text{G.15})$$

with $\sigma_0 = 10 \text{ mN/m}$ and $\sigma_T = 2 \text{ mN/(mK)}$. The temperature at the bottom of the box is the reference temperature $T_1 = T_0 = 290 \text{ K}$. The temperature gradient in y direction is $\nabla T = 200 \text{ K/m}$. The radius of the droplet is $R = 1.44 \text{ mm}$. The dimensionless numbers to characterize thermocapillary migration are the Reynolds number

$$Re = \frac{\rho_2 R U_R}{\eta_2} = 0.72 \quad (\text{G.16})$$

Marangoni number

$$Ma = \frac{\rho_2 c_{p,2} R U_R}{\lambda_2} = 0.72 \quad (\text{G.17})$$

and Capillary number

$$Ca = \frac{\eta_2 U_R}{\sigma_0} = 0.0576 \quad (\text{G.18})$$

with the characteristic velocity

$$U_R = \frac{\sigma_T |\nabla T| R}{\eta_2} = 0.024 \frac{m}{s}. \quad (\text{G.19})$$

The dimensionless time is

$$t^* = \frac{t \cdot U_R}{R} \quad (\text{G.20})$$

and the dimensionless velocity is

$$U^* = \frac{U}{U_R}. \quad (\text{G.21})$$

First we investigate numerical convergence of the migration velocity in 2D. We choose a box length $L = 5.76 \text{ mm}$ which corresponds to a ratio $L/R = 4$. We vary the resolution from $L_0 = 180 \mu\text{m}$ to $L_0 = 45 \mu\text{m}$. The dimensionless migration velocity U^* over dimensionless time t^* is shown in Fig. G.17. We compare the migration

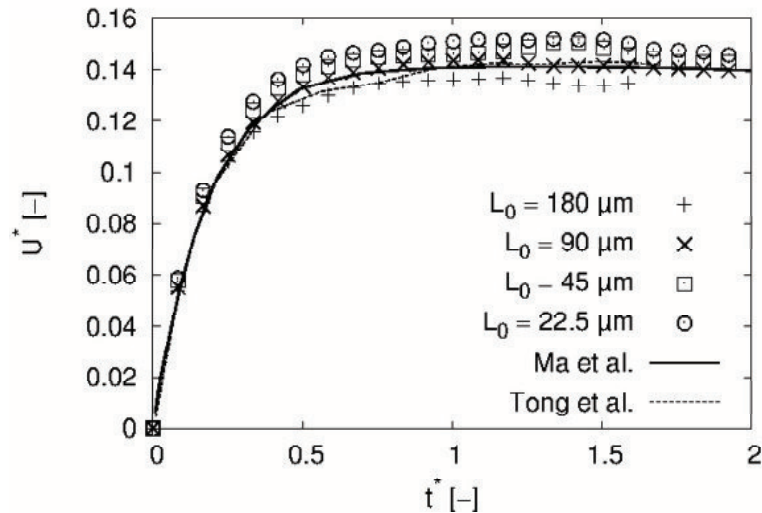


Figure G.17: Droplet migration using different resolutions compared to solution from [Ma11] and [Ton14]. The box length to radius ratio is $L/R = 4$.

velocity to the results of Tong et al. and Ma et al. In literature [Ma11; Ton14] a resolution similar to $L_0 = 90\mu m$ is used.

In Fig. G.17 we find two major results. First, we see that the migration velocity of the present model is very similar to the migration velocity of Ma & Bothe [Ma11]. Compared to Tong et al. [Ton14] the present results are more accurate. The reason is that the error in the Marangoni force is lower in the present model.

Second, we see that with increasing or decreasing resolution we over- and underestimate the data of Ma & Bothe. The present model converges with increasing resolution indicating that the results presented in literature are not yet converged. If analytic solutions of migration velocity are available, the box size is always assumed infinitely large. This means that the wall effects do not disturb the flow field. In a simulation we always have a bounded domain. Next we investigate the influence of the bounded domain on the migration velocity of the droplet in 2D. We consider the same setup and properties of the fluids as before. Then we increase the box size from $L = 5.76mm$ to $L = 46.08mm$. The resolution is $L_0 = 90\mu m$ or 16 particles per droplet radius. Initially the droplet is placed in the center of the box.

The migration velocity U^* over time t^* is shown in Fig. G.18. We see that with increasing box size the steady-state migration velocity increases and converges to a limit of $U^* \approx 0.18$. For L/R ratios larger than 16 the migration velocity is converged

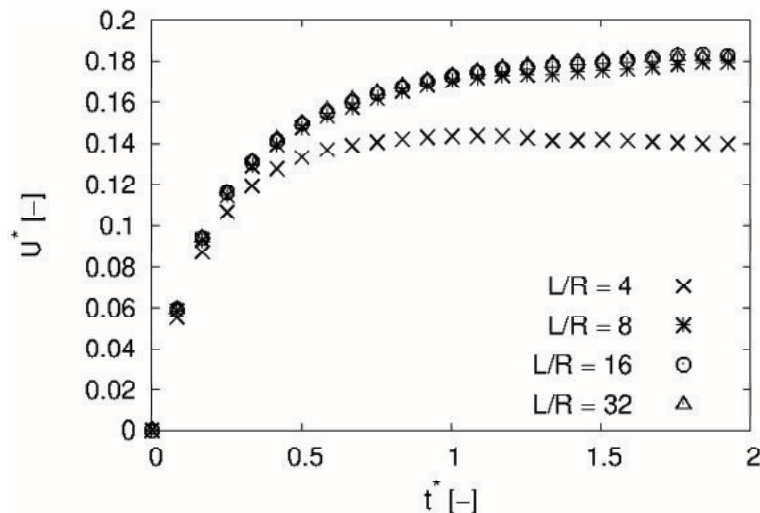


Figure G.18: Influence of box size on the migration velocity of a droplet in 2D. The droplet radius is resolved with 16 particles.

and we may assume that the flow field is approximately unaffected by the boundaries. A similar value but for the 3D case was presented by Ma & Bothe [Ma11] where the steady-state migration velocity is constant for L/R ratios larger than 16.

Finally we consider thermocapillary migration of a spherical droplet in 3D. For the steady-state migration velocity of a spherical droplet in 3D Young et al. [You59] derived an theoretical value

$$U^* = \frac{2}{\left(2 + \frac{\lambda_1}{\lambda_2}\right) \left(2 + 3\frac{\eta_1}{\eta_2}\right)} \quad (\text{G.22})$$

with the ratio of the thermal conductivity and dynamic viscosity of the droplet and the continuous phase. Young et al. assumed that the domain is unbounded. But in the simulation we have a bounded domain and therefore we will reach the theoretical value only in the limit of a large L/R ratio.

In the 3D model we consider a spherical droplet in a closed box. We use slip boundary conditions for velocity in x and z direction and no-slip boundary conditions in y direction. Similarly we use Neumann boundary conditions for the temperature in x and z direction and Dirichlet boundary conditions in y direction. The properties of the fluids are the same as in the previous simulations. Initially a spherical droplet is centered in the box. To reduce the numerical effort we use 16 particles per droplet radius with $L_0 = 90\mu m$. The smoothing length is reduced to $h = 1.55L_0$ because there are more particles in the vicinity in 3D than in 2D and therefore the SPH approximation is already good for lower smoothing lengths.

In Fig. G.19 we demonstrate that we converge against the theoretical value by increasing the L/R ratio. We see that the steady-state migration velocity increases with increasing L/R ratio. We underestimate the theoretical value because the domain is still bounded but we are very close for $L/R = 8$. As we have seen at the beginning of this section the influence of the bounded domain is only negligible for L/R ratio larger than 16.

We also compare the results of the present simulations with results of Ma et al. [Ma11]. The present results are slightly closer to the theoretical value than the results of Ma and Bothe. We have not performed simulations for very large L/R ratios because the numerical effort is very high. In the results of Ma and Bothe it seems that there is a constant offset in the migration velocity because the migration

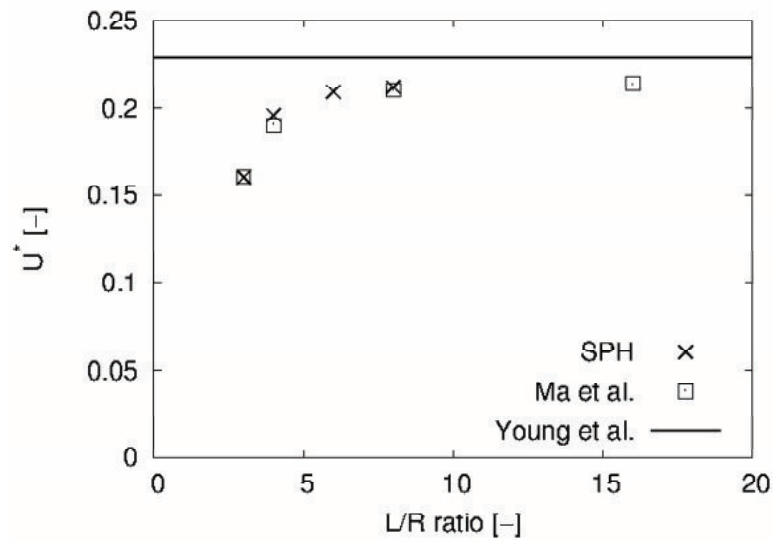


Figure G.19: Influence of box length to droplet diameter ratio for 3D simulation where the droplet diameter is resolved with 32 particles. Comparison with analytic migration velocity [Fed13; You59]

velocity is very similar for $L/R = 8$ and $L/R = 16$. We expect similar behavior of the present model because we use a very similar formulation of the CSF model. We conclude that the present model predicts thermocapillary flow very accurate compared to literature.

APPENDIX H

Review of limit of instability in immiscible viscous fingering

Here we review the derivation of the limit of instability for an immiscible system. The detailed derivation is found in Chuoke et al. [Chu59].

We consider two fluids 1 and 2 in a thin channel between closely spaced parallel plates. The interface between the fluids is assumed planar. The flow direction is perpendicular to the interface between the fluids and parallel to the plates of the channel. Thus the considered flow is mainly one dimensional along the z axis in positive direction. The gravitational acceleration g is assumed to be parallel to the z axis.

We define a moving coordinate system with the velocity of the interface. The z axis is positive parallel to the flow direction. The z axis in the fixed and moving coordinate system are identical. The displacing velocity is W and positive if fluid 1 displaces fluid 2. For this system the equation of motion is

$$\vec{u} = -\nabla \left(\frac{k}{\eta} p + \frac{k}{\eta} W z + \rho g z \right) = -\nabla X \quad (\text{H.1})$$

and

$$\nabla \cdot \vec{u} = -\nabla^2 X = 0. \quad (\text{H.2})$$

Here $k = b^2/12$ and g is the gravitational acceleration. The latter equation is a Poisson equation. If we consider only first-order effects, e.g. neglect tangential

velocities, integration of these equations lead to

$$p = \frac{\eta}{k}X - \frac{\eta}{k}Wz - \rho gz + P(t) \quad (\text{H.3})$$

with $P(t)$ as an arbitrary function of time. Next arbitrary deformations of the interface are decomposed into fundamental Fourier perturbation modes ζ with a propagation vector $\vec{\alpha}$ in the x,y plane with a magnitude α . The condition for the pressure discontinuity at the interface $z = \zeta$ is

$$(p_1 - p_2)_{z=\zeta} = \sigma (\kappa_1 + \kappa_2) + P_c(t) \quad (\text{H.4})$$

with a curvature-independent pressure $P_c(t)$. κ and σ are the curvature and surface tension. The kinematic conditions at the interface $z = \zeta$ are

$$\frac{\partial \zeta}{\partial t} = -\frac{\partial X_1}{\partial z} = -\frac{\partial X_2}{\partial z}, \quad (\text{H.5})$$

neglecting higher order terms. If we assume that $\alpha\zeta$ is small we can write

$$\kappa_1 \sim -\frac{\partial^2 \zeta}{\partial x^2} \quad (\text{H.6})$$

and

$$\kappa_2 \sim -\frac{\partial^2 \zeta}{\partial y^2}. \quad (\text{H.7})$$

We combine Eqs. H.3 and H.4 and get

$$\frac{\eta_2}{k_2}(X_2)_{z=\zeta} - \frac{\eta_1}{k_1}(X_1)_{z=\zeta} - \left[\left(\frac{\eta_2}{k_2} - \frac{\eta_1}{k_1} \right) W + (\rho_2 - \rho_1) g \right] \zeta \quad (\text{H.8})$$

$$- \sigma \left(\frac{\partial^2 \zeta}{\partial x^2} + \frac{\partial^2 \zeta}{\partial y^2} \right) + P_2(t) - P_1(t) + P_c(t) = 0. \quad (\text{H.9})$$

This equation reduces to

$$P_1(t) - P_2(t) = P_c(t) \quad (\text{H.10})$$

for small $\alpha\zeta$ as is shown in [Chu59]. Therefore the characteristic equation with the magnitude α of the propagation vector is

$$\left(\frac{\eta_2}{k_2} + \frac{\eta_1}{k_1}\right)n - \left[\left(\frac{\eta_2}{k_2} - \frac{\eta_1}{k_1}\right)W + (\rho_2 - \rho_1)g\right]\alpha + \sigma\alpha^3 = 0. \quad (\text{H.11})$$

n is a positive value indicating the index of instability. From Eq. H.11 we find that for $\alpha > 0$ the condition for instability (Eq. H.11 <0) is

$$\left(\frac{\eta_2}{k_2} - \frac{\eta_1}{k_1}\right)W + (\rho_2 - \rho_1)g - \sigma\alpha > 0. \quad (\text{H.12})$$

Now, if there is an instability for all velocities $U > U_c$, defined as

$$\left(\frac{\eta_2}{k_2} - \frac{\eta_1}{k_1}\right)U_c + (\rho_2 - \rho_1)g = 0, \quad (\text{H.13})$$

and if we write the wavelength of perturbation as $\lambda = 2\pi/\alpha$, then the critical wavelength λ_c is

$$\lambda_c = 2\pi \left[\frac{\sigma}{\left(\frac{\eta_2}{k_2} - \frac{\eta_1}{k_1}\right)(U - U_c)} \right]^{0.5}. \quad (\text{H.14})$$

For $k = b^2/12$ and $U_c = 0$ we get Eq. 5.4. The wavelength of maximum growth rate is found at the maximum of α .

APPENDIX I

Reduction of dimension of the shear stress

The general form of a balance equation for a quantity ψ is

$$\frac{\partial \psi}{\partial t} + \langle \nabla \cdot \psi \vec{u} \rangle + \langle \nabla \phi_\psi \rangle = \sigma_\psi^P + \sigma_\psi^F \quad (\text{I.1})$$

where the first term on the left hand side is the accumulation, the second term is the convective transport, the third term is the diffusive transport term. The terms on the right hand side represent the volume and surface source terms. For the momentum balance of a single phase and single component system we get

$$\frac{\partial \rho \vec{u}}{\partial t} + \langle \nabla \cdot \rho \vec{u} \vec{u} \rangle + \langle \nabla \cdot \mathbf{\Pi} \rangle = \rho \vec{f} \quad (\text{I.2})$$

with the stress tensor

$$\mathbf{\Pi} = p\mathbf{I} + \tau. \quad (\text{I.3})$$

Here p is the pressure and τ is the shear stress with the elements τ_{ij} . For a Newtonian incompressible fluid the elements of the shear stress are

$$\tau_{ij} = \eta \left(\frac{\partial u_j}{\partial x_i} + \frac{\partial u_i}{\partial x_j} \right). \quad (\text{I.4})$$

Since the reduction of dimension of the convective and source term is straight forward we focus on the reduction of dimensions of the shear stress

$$\nabla \cdot \tau = \begin{pmatrix} \tau_{xx} & \tau_{yx} & \tau_{zx} \\ \tau_{xy} & \tau_{yy} & \tau_{zy} \\ \tau_{xz} & \tau_{yz} & \tau_{zz} \end{pmatrix}. \quad (\text{I.5})$$

The divergence of the shear stress tensor is

$$\nabla \cdot \tau = \begin{pmatrix} \frac{\partial \tau_{xx}}{\partial x} + \frac{\partial \tau_{yx}}{\partial y} + \frac{\partial \tau_{zx}}{\partial z} \\ \frac{\partial \tau_{xy}}{\partial x} + \frac{\partial \tau_{yy}}{\partial y} + \frac{\partial \tau_{zy}}{\partial z} \\ \frac{\partial \tau_{xz}}{\partial x} + \frac{\partial \tau_{yz}}{\partial y} + \frac{\partial \tau_{zz}}{\partial z} \end{pmatrix}. \quad (\text{I.6})$$

We want to reduce the dimensions assuming that we have a channel flow along the x coordinate as shown in Fig. I.1. For the reduction from 3D to 2D we still have shear stress in the xy plane. For further reduction to 1D shear stress reduces to a single friction force. The velocity profile of the fluid is parabolic and we are in steady-state. Therefore for a reduction of dimensions some of the elements in Eq. I.5 vanish due to reasons of symmetry or zero gradient of the velocity. If we reduce from 3D to 2D $\tau_{zz} = 0$ because the flow profile is unidirectional in the x direction. The stresses in the xy plane remain. There are 4 stresses τ_{xz} , τ_{yz} , τ_{zx} , τ_{zy} left that need to be reduced. The general integral to reduce the diffusion term of the momentum equation from 3D (x,y,z) to 2D (x,y) is

$$\int_{z_{min}}^{z_{max}} \nabla \phi_{\psi} dz. \quad (\text{I.7})$$

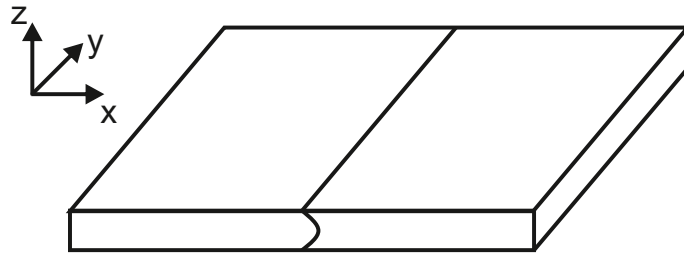


Figure I.1: Scheme

With $\phi_\psi = \mathbf{\Pi}$ we get

$$\int_{z_{min}}^{z_{max}} \nabla \cdot \mathbf{\Pi} dz. \quad (\text{I.8})$$

Next we split up the integral into parts of the stress tensor neglecting the pressure because its reduction is straight forward. For each component of the gradient of the shear stress tensor we use Eq. I.4. The first element of the gradient of the shear stress is

$$\nabla_x \cdot \tau = \frac{\partial \tau_{xx}}{\partial x} + \frac{\partial \tau_{yx}}{\partial y} + \frac{\partial \tau_{zx}}{\partial z}. \quad (\text{I.9})$$

The first term is

$$\frac{\partial \tau_{xx}}{\partial x} = \frac{\partial}{\partial x} \left(\eta \left(\frac{\partial u_x}{\partial x} + \frac{\partial u_x}{\partial x} \right) \right) \quad (\text{I.10})$$

and the integral is

$$\int_{z_{min}}^{z_{max}} \frac{\partial \tau_{xx}}{\partial x} dz = \frac{\partial \tau_{xx}}{\partial x} (z_{max} - z_{min}) \quad (\text{I.11})$$

τ_{xx} is independent of the z coordinate because the flow profile is constant in x direction.

The second term in Eq. I.9 is

$$\frac{\partial \tau_{yx}}{\partial y} = \frac{\partial}{\partial y} \left(\eta \left(\frac{\partial u_y}{\partial x} + \frac{\partial u_x}{\partial y} \right) \right) \quad (\text{I.12})$$

and the integral is

$$\int_{z_{min}}^{z_{max}} \frac{\partial \tau_{yx}}{\partial y} dz = \frac{\partial \tau_{yx}}{\partial y} (z_{max} - z_{min}) \quad (\text{I.13})$$

because it is independent of z coordinate.

The last term in Eq. I.9 is

$$\frac{\partial \tau_{zx}}{\partial z} = \frac{\partial}{\partial z} \left(\eta \left(\frac{\partial u_z}{\partial x} + \frac{\partial u_x}{\partial z} \right) \right) \quad (\text{I.14})$$

and the integral is

$$\int_{z_{min}}^{z_{max}} \frac{\partial \tau_{zx}}{\partial z} dz = \int_{z_{min}}^{z_{max}} \frac{\partial}{\partial z} \left(\eta \left(\frac{\partial u_z}{\partial x} + \frac{\partial u_x}{\partial z} \right) \right) dz. \quad (\text{I.15})$$

We split the integral into

$$\eta \int_{z_{min}}^{z_{max}} \frac{\partial}{\partial z} \left(\frac{\partial u_z}{\partial x} \right) dz = \eta \left[\frac{\partial u_z}{\partial x} \right]_{z_{min}}^{z_{max}} = 0 \quad (\text{I.16})$$

and

$$\eta \int_{z_{min}}^{z_{max}} \frac{\partial}{\partial z} \left(\frac{\partial u_x}{\partial z} \right) dz = \eta \left[\frac{\partial u_x}{\partial z} \right]_{z_{min}}^{z_{max}}. \quad (\text{I.17})$$

We assume a parabolic flow profile in a channel in the x direction. The velocity u_z at z_{max} and z_{min} is zero because of the impenetrable wall. Therefore the first integral vanishes. The second integral doesn't vanish. We keep it for the moment.

The second element of the gradient of the shear stress is

$$\nabla_y \cdot \tau = \frac{\partial \tau_{xy}}{\partial x} + \frac{\partial \tau_{yy}}{\partial y} + \frac{\partial \tau_{zy}}{\partial z}. \quad (\text{I.18})$$

The first term is

$$\frac{\partial \tau_{xy}}{\partial x} = \frac{\partial}{\partial x} \left(\eta \left(\frac{\partial u_x}{\partial y} + \frac{\partial u_y}{\partial x} \right) \right) \quad (\text{I.19})$$

and the integral is

$$\int_{z_{min}}^{z_{max}} \frac{\partial \tau_{xy}}{\partial x} dz = \frac{\partial \tau_{xy}}{\partial x} (z_{max} - z_{min}) \quad (\text{I.20})$$

The second term in Eq. I.18 is

$$\frac{\partial \tau_{yy}}{\partial y} = \frac{\partial}{\partial y} \left(\eta \left(\frac{\partial u_y}{\partial y} + \frac{\partial u_y}{\partial y} \right) \right) \quad (\text{I.21})$$

and the integral is

$$\int_{z_{min}}^{z_{max}} \frac{\partial \tau_{yy}}{\partial y} dz = \frac{\partial \tau_{yy}}{\partial y} (z_{max} - z_{min}) \quad (\text{I.22})$$

Both terms are independent of the z coordinate.

The last term in Eq. I.18 is

$$\frac{\partial \tau_{zy}}{\partial z} = \frac{\partial}{\partial z} \left(\eta \left(\frac{\partial u_z}{\partial y} + \frac{\partial u_y}{\partial z} \right) \right) \quad (\text{I.23})$$

and the integral is

$$\int_{z_{min}}^{z_{max}} \frac{\partial \tau_{zy}}{\partial z} dz = \int_{z_{min}}^{z_{max}} \frac{\partial}{\partial z} \left(\eta \left(\frac{\partial u_z}{\partial y} + \frac{\partial u_y}{\partial z} \right) \right) dz. \quad (\text{I.24})$$

We split the integral into

$$\eta \int_{z_{min}}^{z_{max}} \frac{\partial}{\partial z} \left(\frac{\partial u_z}{\partial y} \right) dz = \eta \left[\frac{\partial u_z}{\partial y} \right]_{z_{min}}^{z_{max}} = 0 \quad (\text{I.25})$$

and

$$\eta \int_{z_{min}}^{z_{max}} \frac{\partial}{\partial z} \left(\frac{\partial u_y}{\partial z} \right) dz = \eta \left[\frac{\partial u_y}{\partial z} \right]_{z_{min}}^{z_{max}} \quad (\text{I.26})$$

At the boundaries z_{max} and z_{min} the velocity in z direction is zero. Therefore the first integral vanishes. The second integral remains for the moment.

The last element of the gradient of the shear stress is

$$\nabla_z \cdot \tau = \frac{\partial \tau_{xz}}{\partial x} + \frac{\partial \tau_{yz}}{\partial y} + \frac{\partial \tau_{zz}}{\partial z}. \quad (\text{I.27})$$

The first term is

$$\frac{\partial \tau_{xz}}{\partial x} = \frac{\partial}{\partial x} \left(\eta \left(\frac{\partial u_x}{\partial z} + \frac{\partial u_z}{\partial x} \right) \right) \quad (\text{I.28})$$

and the integral is

$$\int_{z_{min}}^{z_{max}} \frac{\partial \tau_{xz}}{\partial x} dz = \int_{z_{min}}^{z_{max}} \frac{\partial}{\partial x} \left(\eta \left(\frac{\partial u_x}{\partial z} + \frac{\partial u_z}{\partial x} \right) \right) dz. \quad (\text{I.29})$$

We split up into two integrals

$$\eta \int_{z_{min}}^{z_{max}} \frac{\partial}{\partial x} \left(\frac{\partial u_z}{\partial x} \right) dz = \eta \left[\frac{\partial}{\partial x} \left(\frac{\partial u_z}{\partial x} \right) z \right]_{z_{min}}^{z_{max}} = 0 \quad (\text{I.30})$$

and

$$\eta \int_{z_{min}}^{z_{max}} \frac{\partial}{\partial x} \left(\frac{\partial u_x}{\partial z} \right) dz = \eta \left[\frac{\partial u_x}{\partial x} \right]_{z_{min}}^{z_{max}} \quad (\text{I.31})$$

The first integral is zero because the velocity u_z is zero at the boundary. The second integral remains. The second term in Eq. I.27 is

$$\frac{\partial \tau_{yz}}{\partial y} = \frac{\partial}{\partial y} \left(\eta \left(\frac{\partial u_y}{\partial z} + \frac{\partial u_z}{\partial y} \right) \right) \quad (\text{I.32})$$

and the integral is

$$\int_{z_{min}}^{z_{max}} \frac{\partial \tau_{yz}}{\partial y} dz = \frac{\partial \tau_{yz}}{\partial y} (z_{max} - z_{min}) \quad (\text{I.33})$$

We split up into two integrals

$$\eta \int_{z_{min}}^{z_{max}} \frac{\partial}{\partial y} \left(\frac{\partial u_z}{\partial y} \right) dz = \eta \left[\frac{\partial}{\partial y} \left(\frac{\partial u_z}{\partial y} \right) z \right]_{z_{min}}^{z_{max}} = 0 \quad (\text{I.34})$$

and

$$\eta \int_{z_{min}}^{z_{max}} \frac{\partial}{\partial y} \left(\frac{\partial u_y}{\partial z} \right) dz = \eta \left[\frac{\partial u_y}{\partial y} \right]_{z_{min}}^{z_{max}} \quad (\text{I.35})$$

The first integral is zero because the velocity u_z is zero at the boundary. The second integral remains. The last term in Eq. I.27 is

$$\frac{\partial \tau_{zz}}{\partial z} = \frac{\partial}{\partial z} \left(\eta \left(\frac{\partial u_z}{\partial z} + \frac{\partial u_z}{\partial z} \right) \right) \quad (\text{I.36})$$

and the integral is

$$\int_{z_{min}}^{z_{max}} \frac{\partial \tau_{zz}}{\partial z} dz = \int_{z_{min}}^{z_{max}} \frac{\partial}{\partial z} \left(\eta \left(\frac{\partial u_z}{\partial z} + \frac{\partial u_z}{\partial z} \right) \right) dz = 0 \quad (\text{I.37})$$

At the boundaries z_{max} and z_{min} the velocity in z direction is zero. Therefore the integral vanishes.

Finally the reduced shear stress matrix in two dimensions is

$$\nabla \cdot \tau = \begin{pmatrix} \tau_{xx} & \tau_{yx} \\ \tau_{xy} & \tau_{yy} \end{pmatrix}. \quad (\text{I.38})$$

In addition we need to explicitly formulate the effective friction due to the reduction of dimensions for

$$\eta \left[\frac{\partial u_x}{\partial z} \right]_{zmin}^{zmax} \quad (\text{I.39})$$

$$\eta \left[\frac{\partial u_y}{\partial z} \right]_{zmin}^{zmax} \quad (\text{I.40})$$

$$\eta \left[\frac{\partial u_x}{\partial x} \right]_{zmin}^{zmax} \quad (\text{I.41})$$

and

$$\eta \left[\frac{\partial u_y}{\partial y} \right]_{zmin}^{zmax}. \quad (\text{I.42})$$

In a channel we assume a parabolic velocity profile along the z direction that may be aligned in x or y direction. The parabolic flow profile for steady flow of a Newtonian fluid is [Lan87]

$$\vec{u}(z) = -\frac{1}{2\eta} \nabla p (H - z) z \quad (\text{I.43})$$

and its derivative is

$$\frac{\partial \vec{u}(z)}{\partial z} = -\frac{1}{2\eta} \nabla p (H - 2z) \quad (\text{I.44})$$

with the height of the channel H and the pressure gradient in flow direction ∇p . We combine Eqs. I.39 and I.40 to

$$\eta \left[\frac{\partial \vec{u}(z)}{\partial z} \right]_{z_{min}}^{z_{max}}, \quad (\text{I.45})$$

and insert Eq. I.44 with $z_{max} = H$ and $z_{min} = 0$ and get

$$\eta \left[-\frac{1}{2\eta} \nabla p (H - 2z) \right]_{z_{min}}^{z_{max}} = H \Delta p \quad (\text{I.46})$$

Analog we find that combining Eqs. I.41 and I.42

$$\eta \left[\frac{\partial u_x}{\partial x} + \frac{\partial u_y}{\partial y} \right]_{z_{min}}^{z_{max}} = \eta [\nabla \cdot \vec{u}]_{z_{min}}^{z_{max}} = 0 \quad (\text{I.47})$$

because the fluid is incompressible and $\nabla \cdot \vec{u} = 0$.

We get the friction force due to dimensional reduction from 3D to 2D by multiplying the friction (Eq. I.46) with the area of contact A

$$\vec{F} = AH \nabla p \quad (\text{I.48})$$

In the Navier-Stokes equation we want to formulate the additional friction in terms of the velocity instead of the pressure gradient. The acceleration due to the friction force is

$$\vec{a} = \frac{\vec{F}}{m} = \frac{AH \nabla p}{m}. \quad (\text{I.49})$$

with the mass m . The average velocity in a channel at steady-state is $2/3 \cdot \vec{u}_{max}$ where the maximum velocity of the flow is located at $z = H/2$. We reformulate Eq. I.43 and insert it for the pressure gradient in Eq. I.49 to get

$$\vec{a} = -\frac{2\eta AH \vec{u}}{m(H-z)z} = -\frac{2\eta m H \vec{u}}{\rho H m (H-z)z} = -\frac{2\eta \vec{u}}{\rho(H-z)z} \quad (\text{I.50})$$

with the contact area $A = V/H$ and the volume $V = m/\rho$. At $z = H/2$ the velocity is $\vec{u}(z = H/2) = \vec{u}_{max}$ we get

$$\vec{a} = -\frac{2 \cdot 2\eta\vec{u}}{\rho(H - H/2)H} = -\frac{8\eta\vec{u}}{\rho H^2}. \quad (\text{I.51})$$

The acceleration \vec{a} corresponds to the maximum velocity in the channel. Since the average velocity is $2/3 \cdot \vec{u}(z = H/2)$, we need to correct with the reciprocal constant $3/2$ to get the average acceleration in the channel. Finally, the additional friction force in the Navier-Stokes equation is

$$\rho\vec{a} = \vec{F} = -\frac{12\eta\vec{u}}{H^2}. \quad (\text{I.52})$$

In case of a viscoplastic Bingham fluid (not used in this thesis) we need to formulate Eqs. I.39 and I.40. The theoretical velocity profile at the boundaries $z = z_{max}$ and $z = z_{min}$ is

$$\vec{u}(z) = -u_{ref} \cdot (0.5b(0.25 - z^2) - Bn(0.5 - z)). \quad (\text{I.53})$$

$b = \frac{\nabla p H^2}{\eta_\infty u_{ref}}$ is the dimensionless pressure and $Bn = \frac{\tau_0 H}{\eta_\infty u_{ref}}$ is the Bingham number with the reference velocity u_{ref} (that is the maximum velocity of a Newtonian fluid in the channel), the dynamic viscosity at infinite shear rate η_∞ and the height of the channel H . The derivative of Eq. I.53 is

$$\frac{\partial \vec{u}(z)}{\partial z} = -u_{ref}(-bz + Bn). \quad (\text{I.54})$$

Using this equation with $z = z_{max} = H/2$ and $z = z_{min} = -H/2$ we get

$$\eta_\infty \left[\frac{\partial \vec{u}(z)}{\partial z} \right]_{z_{min}}^{z_{max}} = \eta_\infty [-bz + Bn]_{z_{min}}^{z_{max}} = \eta_\infty H b u_{ref}. \quad (\text{I.55})$$

We get the dimensionless pressure from Eq. I.53 for $z = 0$ (maximum of velocity)

$$b = -\frac{1}{u_{ref}} (8\vec{u} + 4Bn). \quad (\text{I.56})$$

With the definition of the dimensionless pressure $b = \frac{\nabla p H^2}{\eta_\infty u_{ref}}$ we find

$$\nabla p = -\frac{4\eta_\infty}{H^2} (2\vec{u} + Bn). \quad (\text{I.57})$$

Analog to the Newtonian fluid we derive the acceleration (Eq. I.49)

$$\vec{a} = \frac{AH\nabla p}{m} = -\frac{4A\eta_\infty}{mH} (2\vec{u} + Bn) \quad (\text{I.58})$$

and finally with $V = m/\rho$ and $A = V/H$ we get

$$\vec{a} = -\frac{4\eta_\infty}{\rho H^2} (2\vec{u} + Bn) \quad (\text{I.59})$$

Finally we introduce the mean velocity as we did for the Newtonian because \vec{a} should be identical to Eq. I.51 in the case of $Bn = 0$. Therefore we end up with

$$\rho\vec{a} = \vec{F} = -\frac{6\eta_\infty}{\rho H^2} (2\vec{u} + Bn). \quad (\text{I.60})$$

APPENDIX J

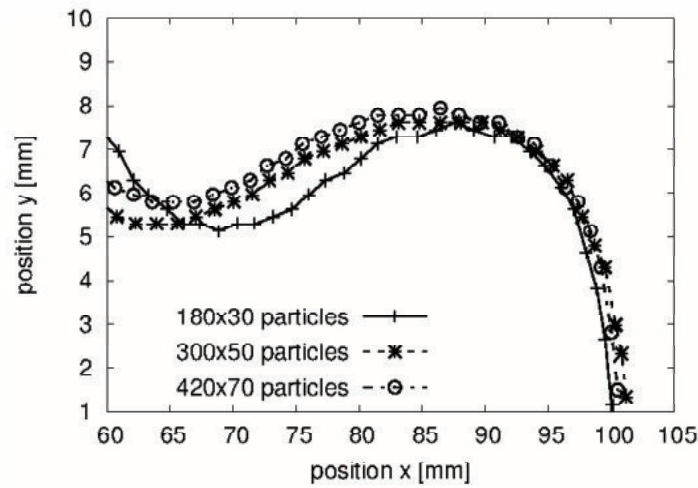
Numerical convergence in immiscible viscous fingering

In addition to the discussion of immiscible viscous fingering in the context of SPH we demonstrate numerical convergence of the solution for a single viscous fingering in the Hele-Shaw cell.

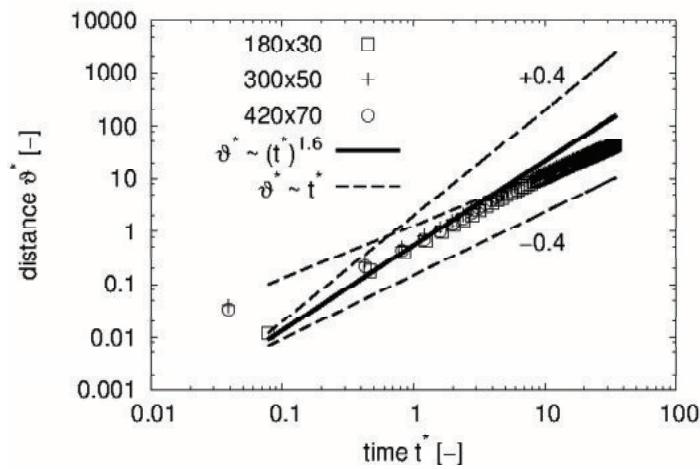
We consider the case of maximum growth rate $\lambda = \lambda_m$ presented in Sec. 5.3. The parameters are summarized in Tab. 5.1. In contrast to simulations presented in Sec. 5.3 we increase the resolution to proof convergence of the solution. We perform 3 simulations with a resolution of 180x30, 300x50 and 420x70 particles and investigate the shape and position of the tip of the finger as well as the dynamics of the growth of the finger.

The shape and position of the tip of the finger are plotted in Fig. J.1a. We see that the position of the tip of the finger converges with increasing resolution. The result for the coarsest resolution is already very good. The shape of the finger (Fig. J.1a) at the coarsest resolution deviates from the result for higher resolution. The contraction at lower resolution is shifted to the tip of the finger.

The growth of the finger (Fig. J.1b) deviates for very early times but converges with higher resolution. For times $t^* > 1$ the size of the finger is very similar for all resolutions.



(a) Contour of the finger tip for different resolutions, $t^* = 10$.



(b) Comparison of growth of fingering to power law.

Figure J.1: Left: Convergence of the finger tip with increasing resolution at $t^* = 10$. Right: Comparison of finger growth over time with power law for viscous fingering and flow in a channel for $\lambda = \lambda_m$.

APPENDIX K

Derivation of phase separation front velocity

In this appendix we derive an equation for the phase separation velocity. We use the following assumptions to enable classical balancing of the component at the interface between two phases (PGF). We assume that

- only solvent (S) diffuses across the interface.
- the interface between the stable polymer solution and unstable region is infinitesimal small, e.g. in the sharp interface limit,
- the driving force μ_j is continuous at the interface,
- there is no source at the interface,
- there is a jump in ρ_j at the interface,
- there is only unidirectional diffusive transport across the interface.

A sketch up is shown in Fig. K.1. We start with the general balance equation at the interface (PGF)

$$0 = - \langle [\Psi^+ \vec{u}^+ + \phi_{\Psi}^+ - \Psi^- \vec{u}^- + \phi_{\Psi}^- - (\Psi^+ - \Psi^-) \vec{u}^T] \cdot \vec{n} \rangle + \sigma_{\Psi}^T. \quad (\text{K.1})$$

For a component j the component balance in terms of the partial density $\Psi = \rho_j$ and the mass flux $\phi_{\Psi} = \vec{j}_j$ is

$$0 = \left[\rho_j^+ \vec{u}^+ + \vec{j}_j^+ - \rho_j^- \vec{u}^- - \vec{j}_j^- - (\rho_j^+ - \rho_j^-) \vec{u}^T \right] \cdot \vec{n} \quad (\text{K.2})$$

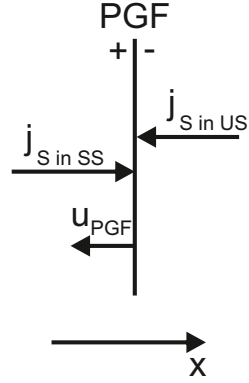


Figure K.1: Sketch up at the PGF.

neglecting the source term $\sigma_\psi^\Gamma = 0$. We assume the mass transfer across the interface unidirectional in normal direction. The normal at the interface points into the same direction as the coordinate x . Therefore

$$\vec{n} = n_x = 1, \quad (\text{K.3})$$

$$\nabla = \frac{\partial}{\partial x}, \quad (\text{K.4})$$

$$\vec{u} = u_x \quad (\text{K.5})$$

and

$$\vec{j}_j = j_{j,x}. \quad (\text{K.6})$$

Eq. K.2 reduces to

$$0 = \rho_j^+ u_x^+ + j_{j,x}^+ - \rho_j^- u_x^- - j_{j,x}^- - (\rho_j^+ - \rho_j^-) u_x^\Gamma. \quad (\text{K.7})$$

We assume a linear driving force approach for the mass flux

$$\vec{j}_j = -D_j \nabla \mu_j \quad (\text{K.8})$$

with the diffusion coefficient D_j and the chemical potential μ_j . In x direction it reduces to

$$j_{j,x} = -D_j \frac{\partial \mu_j}{\partial x}. \quad (\text{K.9})$$

Plugging in Eq. K.7 leads to

$$0 = \rho_j^+ u_x^+ - D_j^+ \frac{\partial \mu_j^+}{\partial x} - \rho_j^- u_x^- + D_j^- \frac{\partial \mu_j^-}{\partial x} - (\rho_j^+ - \rho_j^-) u_x^\Gamma. \quad (\text{K.10})$$

Now we assume that there is no convective transport which is valid for very low Reynolds numbers. Then Eq. K.10 reduces to

$$0 = -D_j^+ \frac{\partial \mu_j^+}{\partial x} + D_j^- \frac{\partial \mu_j^-}{\partial x} - (\rho_j^+ - \rho_j^-) u_x^\Gamma. \quad (\text{K.11})$$

Next we reformulate Eq. K.11 and get

$$u_x^\Gamma = \frac{D_j^- \frac{\partial \mu_j^-}{\partial x} - D_j^+ \frac{\partial \mu_j^+}{\partial x}}{\rho_j^+ - \rho_j^-} \quad (\text{K.12})$$

or

$$u_x^\Gamma = \frac{D_j^- \frac{\partial \mu_j^-}{\partial x}}{\rho_j^+ - \rho_j^-} \left(1 - \frac{D_j^+ \frac{\partial \mu_j^+}{\partial x}}{D_j^- \frac{\partial \mu_j^-}{\partial x}} \right) \quad (\text{K.13})$$

respectively. Physically we don't have a sharp interface and we know that the chemical potential is continuous across the interface. For simplicity, we may assume that the gradient of the chemical potential is continuous at the interface

$$\frac{\partial \mu_j^+}{\partial x} = \frac{\partial \mu_j^-}{\partial x} \quad (\text{K.14})$$

to eliminate the diffusive flux in the coagulation bath. Then Eq. K.13 reduces to

$$u_x^\Gamma = \frac{D_j^- \frac{\partial \mu_j^-}{\partial x}}{\rho_j^+ - \rho_j^-} \left(1 - \frac{D_j^+}{D_j^-} \right). \quad (\text{K.15})$$

We introduce the quantities shown in Fig. K.1. Then Eq. K.15 is

$$u_{PGF} = \frac{D_{(S \text{ in } US)} \frac{\partial \mu_{(S \text{ in } SS)}}{\partial x}}{\rho_{(S \text{ in } SS)}^+ - \rho_{(S \text{ in } US)}^-} \left(1 + \frac{D_{(S \text{ in } SS)}}{D_{(S \text{ in } US)}} \right). \quad (\text{K.16})$$

Here we changed the sign of $D_{(S \text{ in } SS)}$ because of Fig. K.1. We reformulate this equation to

$$u_{PGF} = \frac{D_{(S \text{ in } SS)} \frac{\partial \mu_{(S \text{ in } SS)}}{\partial x}}{\rho_{(S \text{ in } SS)}^+ - \rho_{(S \text{ in } US)}^-} \left(\frac{D_{(S \text{ in } US)}}{D_{(S \text{ in } SS)}} + 1 \right). \quad (\text{K.17})$$

The latter ratio is the dimensionless number Hi

$$\frac{D_{(S \text{ in } US)}}{D_{(S \text{ in } SS)}} = Hi. \quad (\text{K.18})$$

We note that if the partial mass density ρ_S is continuous this kind of balancing fails (because $\rho_{(S \text{ in } SS)}^+ = \rho_{(S \text{ in } US)}^-$). Finally we introduced the factor Φ

$$\Phi = \frac{D_{(S \text{ in } SS)} \frac{\partial \mu_{(S \text{ in } SS)}}{\partial x}}{\rho_{(S \text{ in } SS)}^+ - \rho_{(S \text{ in } US)}^-} \quad (\text{K.19})$$

and get the final equation for the phase separation front velocity

$$u_{PGF} = \Phi (Hi + 1). \quad (\text{K.20})$$

We check plausibility considering known cases of Hi . In the case of $Hi \rightarrow \infty$ the phase separation front velocity limits to $u_{PGF} = \Phi \cdot Hi \sim D_{(S \text{ in } US)}$. This means that the phase separation front velocity may move very fast into the polymer solution. In the case of $Hi \rightarrow 0$ we get $u_{PGF} = \Phi \sim D_{(S \text{ in } SS)}$. This means that the front moves very slow into the polymer solution. Since Hi cannot be negative the phase separation front always moves into the polymer solution.

Publications

Some parts of this thesis were previously published in international journals or were presented at national and international conferences and workshops. These publications are listed below.

Journal publications

1. **Hirschler, Manuel**, FRANZ KELLER, MANUEL HUBER, WINFRIED SÄCKEL, and ULRICH NIEKEN: ‘Ein gitterfreies Berechnungsverfahren zur Simulation von Koaleszenz in Mehrphasensystemen’. *Chemie Ingenieur Technik* (2013), vol. 85(7): pp. 1099–1106.
2. **Hirschler, Manuel**, MANUEL HUBER, WINFRIED SÄCKEL, PHILIP KUNZ, and ULRICH NIEKEN: ‘An Application of the Cahn-Hilliard Approach to Smoothed Particle Hydrodynamics’. *Mathematical Problems in Engineering* (2014), vol. 2014: p. 694894.
3. KRONE, MICHAEL, MARKUS HUBER, KATRIN SCHARNOWSKI, **Manuel Hirschler**, DANIEL KAUKER, GUIDO REINA, ULRICH NIEKEN, DANIEL WEISKOPF, and THOMAS ERTL: ‘Evaluation of Visualizations for Interface Analysis of SPH’. *Euro Vis 2014 Short Papers 3* (2014), vol. 2014.
4. **Hirschler, Manuel**, PHILIP KUNZ, MANUEL HUBER, FRIEDEMANN HAHN, and ULRICH NIEKEN: ‘Open boundary conditions for ISPH and their application to micro-flow’. *Journal of Computational Physics* (2016), vol. 307: pp. 614–633.
5. **Hirschler, Manuel**, WINFRIED SÄCKEL, and ULRICH NIEKEN: ‘On Maxwell-Stefan diffusion in Smoothed Particle Hydrodynamics’. *International Journal of Heat and Mass Transfer* (2016), vol. 103: pp. 548–554.

Submissions to conferences and workshops

1. **Hirschler, Manuel**, MANUEL HUBER, WINFRIED SÄCKEL, and ULRICH NIEKEN: ‘A Fourth-Order Derivation for Smoothed Particle Hydrodynamics to Model Thermodynamically-Based Phase Decomposition’. *Proceedings of the 3th International Conference on Particle-Based Methods, Particles*. University of Stuttgart, Germany. 2013.
2. **Hirschler, Manuel**, MANUEL HUBER, WINFRIED SÄCKEL, and ULRICH NIEKEN: ‘Modeling of Phase Decomposition Using a Fourth-Order Derivation for SPH’. *Proceedings of the 8th Interantional SPHERIC Workshop*. 2013.
3. **Hirschler, Manuel**, WINFRIED SÄCKEL, MANUEL HUBER, and ULRICH NIEKEN: ‘A Fourth-order Derivation for Smoothed Particle Hydrodynamics to Model Thermodynamically-based Phase Decomposition’. *Interpore - 5th International Conference on Porous Media*. 2013.
4. BECK, FLORIAN, **Manuel Hirschler**, ULRICH NIEKEN, and PETER EBERHARD: ‘A study of truly incompressible and weakly compressible Smoothed Particle Hydrodynamics methods to model incompressible flows with free surfaces’. *Proceedings of the 85th Annual Meeting of the International Association of Applied Mathematics and Mechanis*. 2014.
5. **Hirschler, Manuel**, PHILIP KUNZ, MANUEL HUBER, WINFRIED SÄCKEL, and ULRICH NIEKEN: ‘multiphase flow in porous media’. *Workshop on Application of Smoothed Particle Hydrodynamics in Environmental Engineering and Geoscience*. 2014.
6. **Hirschler, Manuel**, PHILIP KUNZ, MANUEL HUBER, WINFRIED SÄCKEL, and ULRICH NIEKEN: ‘Open Boundary Conditions without buffer zone for incompressible Smoothed Particle Hydrodynamics’. *11th WCCM and 5th ECCM and 6th ECFD*. 2014.
7. **Hirschler, Manuel**, MANUEL HUBER, GUILLAUME OGER, PHILIP KUNZ, DAVID LE TOUZÉ, and ULRICH NIEKEN: ‘Modeling of quantitative droplet dynamics with coalescence–bouncing transition in a pseudo–single–phase system using ISPH and WCSPH’. *Proceedings of the 10th International SPHERIC workshop*. 2015.

8. **Hirschler, Manuel**, PHILIP KUNZ, WINFRIED SÄCKEL, MANUEL HUBER, and ULRICH NIEKEN: ‘Droplet dynamics: Comparison of Smoothed Particle Hydrodynamics and experimental results’. *Proceedings of the 7th International Berlin Workshop on Transport Phenomena with Moving Boundaries and More*. Fortschr.Ber. VDI Reihe 3 Nr. 947, VDI Verlag 2015, 2015.
9. **Hirschler, Manuel** and ULRICH NIEKEN: ‘Modelling of polymer membrane formation using Smoothed Particle Hydrodynamics’. *Euromembrane 2015*. 2015.
10. **Hirschler, Manuel** and ULRICH NIEKEN: ‘Modelling of polymer membrane formation’. *Interpore - 8th International Conference on Porous Media*. 2016.
11. **Hirschler, Manuel**, CHRISTIAN ZANDER, and ULRICH NIEKEN: ‘Modelling of polymer membrane formation’. *Hydrodynamic Fluctuations in Soft-Matter Simulations, CECAM workshop, Prato, Italy*. 2016.
12. **Hirschler, Manuel**: ‘Mechanismus der Porenentstehung bei porösen Polymermembranen im Phaseninversionsprozess (invited)’. *Deutsche Gesellschaft für Membrantechnik - Stammtisch Süd*. 2017.
13. **Hirschler, Manuel** and ULRICH NIEKEN: ‘Modellierung der Strukturbildung von porösen Polymermembranen im Phaseninversionsprozess’. *Deutsche Gesellschaft für Membrantechnik - Jahrestagung*. 2017.
14. **Hirschler, Manuel** and ULRICH NIEKEN: ‘Modellierung der Strukturbildung von porösen Polymermembranen im Phaseninversionsprozess’. *ProcessNet Jahrestagung - Fachtagung Membrantechnik*. 2017.
15. **Hirschler, Manuel** and ULRICH NIEKEN: ‘Modelling of pore formation in porous polymer membranes during phase inversion process’. *Interpore - 9th International Conference on Porous Media*. 2017.

